Correlations between Meteorological Conditions and Power Loss in Wind Turbines Under Icing Conditions

By

Leidy Tatiana CONTRERAS MONTOYA

THESIS PRESENTED TO ÉCOLE DE TECHNOLOGIE SUPÉRIEURE IN PARTIAL FULFILLMENT OF THE REQUIREMENTS FOR THE DEGREE OF DOCTOR OF PHILOSOPHY
Ph. D.

MONTRÉAL, SEPTEMBER 8, 2026

ÉCOLE DE TECHNOLOGIE SUPÉRIEURE
UNIVERSITÉ DU QUÉBEC

BOARD OF EXAMINERS (THESIS PH.D.)

THIS THESIS HAS BEEN EVALUATED

BY THE FOLLOWING BOARD OF EXAMINERS

Mr. Adrian Ilinca, Thesis Supervisor
Mechanical Engineering Department at École de technologie supérieure

Mr. Santiago Lain, Thesis Co-supervisor
Energetics & Mechanics Department at Universidad Autónoma de Occidente

Mr. Wahid Maref, President of the Board of Examiners
Construction Engineering Department at École de technologie supérieure

Mr. François Morency, Member of the jury
Aerospace Engineering Department at École de technologie supérieure

Mr. Yves Gagnon, External member of the jury
Engineering Department at University of Moncton

THIS THESIS WAS PRESENTED AND DEFENDED

IN THE PRESENCE OF A BOARD OF EXAMINERS AND PUBLIC

1ST JUNE 2026

AT ÉCOLE DE TECHNOLOGIE SUPÉRIEURE

FOREWORD

Generating sustainable electrical power is considered a viable solution to address climate change and meet the growing demand for clean energy. Wind power is a central element of renewable energy and has gained prominence due to the abundance of wind resources and technological advances over the past few decades. However, wind resources are more abundant in cold regions, which present greater operational challenges.

This PhD thesis investigates the impact of icing on the performance of wind turbines. The research proposes relationships between meteorological conditions and output power, providing insight into the phenomenon of icing.

This research not only identifies relevant parameters affecting turbine performance under icing conditions but also proposes approaches to mitigate adverse effects. The results of this study may provide insights into the design, operation, and maintenance of wind turbines in cold climates.

With the ongoing global transition toward sustainable energy sources, it is crucial to emphasize the importance of enhancing wind energy systems. This thesis provides evidence of the development of new ideas to improve renewable energy technologies. I am delighted to provide this preface, acknowledging the importance of the work conducted and its potential to advance wind energy.

May this thesis serve as an impetus for further research and innovation, ultimately leading to a more environmentally sustainable future characterized by greater energy efficiency.

ACKNOWLEDGMENT

I want to thank my parents, Olga and Jorge, in Colombia, who, despite the distance, have supported and believed in me. To Professor Adrian Ilinca for providing me with the academic and financial opportunity to embark on this adventure. To Professor Santiago Lain for his advice, support, and guidance throughout the research. To Fahed Martini for his advice on completing this project. To the Nergica Research Center for providing the data that enabled me to validate my findings. To Patrick Rizk, José Paniagua, and Cristian Cadena for their collaboration in implementing and analyzing various machine learning methods. To my friends in Canada and Colombia, who made the tempestuous moments more bearable. Moreover, I thank my husband, Cesar Gonzalez, whose patience, care, and love supported me throughout this project, even when I did not.

CORRÉLATIONS ENTRE LES CONDITIONS MÉTÉOROLOGIQUES ET LA PERTE DE PUISSANCE DES ÉOLIENNES EN CAS DE GIVRAGE

Leidy Tatiana CONTRERAS MONTOYA

RÉSUMÉ

L'énergie éolienne est devenue une source d'énergie renouvelable majeure, jouant un rôle crucial dans la transition mondiale vers un avenir durable. Récemment, l'utilisation de cette énergie renouvelable s'est développée, en particulier dans les régions à climat froid, où les vents forts et la densité élevée de l'air à des températures plus basses sont prédominants. Cependant, les exploitants de parcs éoliens sont confrontés à un problème : le givrage. Le givrage se produit lorsque des températures négatives entraînent la formation de glace sur les composants des éoliennes, notamment les pales, la nacelle et la tour.

La présence de glace sur les éoliennes peut avoir de graves répercussions sur leurs propriétés aérodynamiques et compromettre leur capacité à capter efficacement l'énergie du vent. Les formations de glace augmentent le poids des pales et modifient leur forme, ce qui peut entraîner une réduction de la vitesse de rotation et de la production d'énergie. Par conséquent, les éoliennes fonctionnant dans des conditions de givre produisent moins d'électricité, ce qui limite leur contribution au réseau électrique et réduit leur efficacité globale. Il est essentiel que les exploitants de parcs éoliens surveillent et gèrent de près les conditions de givrage afin de garantir la sécurité du personnel et du public.

L'influence du givre sur les éoliennes nécessite une approche à multiples facettes. La nature fluctuante de la température, de l'humidité et de la vitesse du vent rend difficile la prévision des phénomènes de givrage. Les systèmes de surveillance météorologique, comprenant des capteurs et des modèles météorologiques, améliorent la précision des prévisions des phénomènes de givrage. En surveillant ces conditions, les opérateurs peuvent anticiper et se préparer à d'éventuels épisodes de givrage.

Cette étude vise à établir des corrélations permettant d'estimer la perte de puissance attendue des éoliennes en cas de givrage. Les corrélations proposées ici ont été développées à l'aide de l'analyse dimensionnelle, également appelée « théorème π », puis validées par trois méthodes d'apprentissage profond. Cette solution permet aux opérateurs d'améliorer l'efficacité de l'exploitation des éoliennes en conditions de givre, en évaluant systématiquement la gravité du givrage. L'originalité de la méthodologie proposée réside dans sa capacité à estimer les pertes de puissance directement à partir des paramètres météorologiques, géométriques et opérationnels des éoliennes. Une base de données a été créée à partir des résultats d'études de simulation sur le givrage, issus de la littérature, des données recueillies dans un centre de recherche et des résultats d'une étude de simulation CFD menée dans le cadre de la présente thèse.

Les corrélations obtenues ont été validées à l'aide de diverses méthodes d'apprentissage profond et ont démontré leur cohérence dans différents scénarios. La méthodologie proposée facilite l'utilisation de paramètres adimensionnels qui établissent des corrélations entre les paramètres météorologiques, géométriques et opérationnels. Des recommandations sont présentées pour l'utilisation de méthodes d'apprentissage profond et d'analyse dimensionnelle afin d'améliorer l'efficacité des éoliennes dans des conditions de givrage.

Un article de revue a été publié et intégré en tant que chapitre à la thèse. Cet article passe en revue les différentes méthodes de modélisation de la perte de puissance liée au givrage dans les éoliennes. Un second article de recherche a été publié, examinant l'impact de la modélisation de la rugosité de surface sur l'aérodynamique d'une éolienne givrée. Ce document constitue également un chapitre de la thèse.

Ce projet contribuera au développement de nouvelles connaissances sur le phénomène de givrage et à l'optimisation des performances des éoliennes dans les climats nordiques.

Mots-clés : accrétion de glace, pertes de puissance, outil d'apprentissage automatique, théorème Pi, modélisation et simulation.

CORRELATIONS BETWEEN METEOROLOGICAL CONDITIONS AND POWER LOSS IN WIND TURBINES UNDER ICING CONDITIONS

Leidy Tatiana CONTRERAS MONTOYA

ABSTRACT

Wind energy has become a significant renewable energy source, playing a crucial role in the global transition to a sustainable future. Recently, the use of this renewable energy has been expanding, particularly in cold-climate regions, where strong winds and higher air density at lower temperatures are prevalent. However, wind farm operators face a challenge: icing. Icing occurs when sub-zero temperatures cause ice to form on wind turbine components, including blades, the nacelle, and the tower.

The presence of ice on wind turbines can have serious repercussions on their aerodynamic properties and compromise their ability to capture wind energy efficiently. Ice formations increase the blades' weight and alter their shape, potentially reducing rotational speed and energy production. As a result, wind turbines operating under icing conditions produce less electricity, limiting their contribution to the power grid and reducing their overall efficiency. It is essential for wind farm operators to closely monitor and manage icing conditions to ensure the safety of personnel and the public.

Addressing the influence of icing on wind turbines necessitates a multifaceted approach. The variability of temperature, humidity, and wind speed predicts challenging icing events. Advanced weather monitoring systems, including sensors and meteorological models, improve the accuracy of forecasts for icing events. By monitoring these conditions, operators can anticipate and prepare for potential icing events.

This study aims to establish correlations for estimating the expected power loss of wind turbines during icing conditions. The correlations proposed here were developed using dimensional analysis, also known as the “π theorem,” and validated using three machine learning methods. This solution enables operators to improve the efficiency of wind turbine operations under icing conditions by systematically assessing icing severity. The originality of the proposed methodology lies in its ability to estimate power losses directly from meteorological, geometrical, and operational parameters of wind turbines. A database has been created using results from literature-based icing simulation studies, data collected at a research center, and results from a CFD simulation study conducted as part of this thesis.

The correlations obtained were validated using multiple machine learning methods and demonstrated consistency across different scenarios. The proposed methodology facilitates the utilization of dimensionless parameters that establish correlations among meteorological, geometrical, and operational parameters. Recommendations are presented for the utilization of machine learning methods and dimensionless analysis to improve the efficiency of wind turbines under icing conditions.

A review paper has been published and included as a chapter in the thesis. This paper reviews various methods for modeling power loss due to icing in wind turbines. A second research paper has been published, examining the impact of surface-roughness modeling on the aerodynamics of an iced wind turbine airfoil. This paper is also included as a chapter in the thesis.

This project will contribute to advancing knowledge on icing and to optimizing wind turbine performance in northern climates.

Keywords: ice accretion, power losses, π theorem, machine learning tool, modeling and simulation.

TABLE OF CONTENTS

Pages

LIST OF TABLES

Page

LIST OF FIGURES

LIST OF ALGORITHMS

Page

LIST OF ABBREVIATIONS

AEP	Annual Energy Production
ANN	Artificial Neural Networks
AoA	Angle of Attack
AQPER	Association Québécoise de la Production d'Énergie Renouvelable
SCADA	Supervisory Control and Data Acquisition
BEM	Blade Element Momentum
CFD	Computational Fluid Dynamics
CNN	Convolutional Neural Networks
DMP	Dispersed Multiphase Droplet Model
DT	Decision Trees
FEM	Finite Element Model
FENSAP-ICE	Finite Element Navier-Stokes Analysis Package – Ice
FNN	Fully connected Neural Networks
GRU	Gated Recurrent Units
HAWT	Horizontal-Axis Wind Turbine
LES	Large Eddy Simulation
LEWICE	Lewis Ice Accretion Prediction Code
LSTM	Long Short-Term Memory
LWC	Liquid Water Content
MCMS	Meteorological Conditions Monitoring Station
MSE	Mean Squared Error

MRF	Multiple Reference Frame
MVD	Median Volume Diameter
NASA	National Aeronautics and Space Administration
NREL	National Renewable Energy Laboratory
PCA	Principal Component Analysis
PCTG	Parallel CNN-TCN GRU
RANS	Reynolds-Averaged Navier-Stokes
RF	Random Forest
SST	Shear-Stress Transition
TCN	Temporal Convolutional Networks
TSR	Tip Speed Ratio
UDS	User-Defined Scalar

LIST OF SYMBOLS

w	Mass concentration.
v	Velocity relative to the object.
A	Cross-sectional area or swept area.
α_1	Collision efficiency.
α_2	Sticking efficiency.
α_3	Accretion efficiency.
ρ	Density.
U	Velocity.
T	Temperature.
σ^{ij}	Stress tensor.
E	Initial energy.
H	Enthalpy.
ϑ	Volume fraction.
$\dot{m}$	Mass transfer.
C_D	Drag coefficient.
Re	Reynolds number.
K	Inertial parameter.
Fr	Froude number.
μ_a	Air dynamic viscosity.
L_∞	Characteristic length.
h_f	Height of the water film.

β	Collection efficiency.
c	Airfoil chord.
k_s	Sand-grain roughness.
C_{Lmax}	Maximum Lift Coefficient.
C_L	Lift Coefficient.
y^+	Dimensionless wall thickness.
y	Initial height (wall distance).
u^*	Friction velocity.
τ_w	Wall shear stress.
C_f	Skin friction coefficient.
C_p	Pressure coefficient.
k	Thermal conductivity.
h	Convection coefficient.
Ω	Rotational speed.
P	Turbine power.
D	Turbine diameter.
R	Turbine radius.
t	Duration of the icing event.
M_{ice}	Mass of ice.
$\dot{q}_{conv}$	Cooling law.
T_s	Surface temperature.
T_∞	Fluid temperature.
Nu	Nusselt number.

Pr	Prandtl number.
ν	Molecular diffusivity of momentum.
α	Molecular diffusivity of heat.
C_P	Power coefficient.
p	Air pressure.
M	Molar mass.
R_g	Gas constant.
γ	Temperature gradient.
e	Water vapor pressure.
w^*	Effective LWC.
E_i	Ice thickness.
e_{ice}	Lateral thickness.
F	Flux density of water on the surface.
D_{max}	Maximum droplet diameter.
$C_{P\,max}$	Maximum power coefficient.

INTRODUCTION

0.1 Context and Problem Statement

The planet has experienced strong energy demand in recent years, so it is desirable and necessary to improve the efficiency of power-generating devices. Due to the scarcity and high cost of fossil fuels, as well as the high pollution levels in densely populated areas, attention in the energy sector has turned towards clean energy alternatives. Among them, one of the most booming in recent decades is wind energy. Within a short period, wind turbine capacity increased to 10 MW.

In recent years, wind turbines have been widely installed in cold climates, particularly in northern European countries such as Finland, Norway, Sweden, and Germany. According to the International Energy Agency Wind Technology Collaboration Program Task 19, by 2020, the installed wind power capacity in cold climates was 156 GW, and is expected to reach 224 GW by 2025 (IEA Wind TCP TASK, 2020). However, when blades are covered with ice, the aerodynamic properties (lift and drag coefficients) change, and as a result, power generation is reduced or the turbine can stop (Fu & Farzaneh, 2010; Jasinski, Noe, Selig, & Bragg, 1998; L. Makkonen, Laakso, Marjaniemi, & Finstad, 2001; Pedersen & Sørensen, 2016; Shu et al., 2018). Moreover, the ice layer on blades creates an undesirable load, increasing the fatigue of rotor components and posing safety hazards from ice thrown (Fu & Farzaneh, 2010; Jasinski et al., 1998; L. Makkonen et al., 2001; Shu et al., 2018). Annual icing losses were estimated at approximately 20% of the annual power output (Fu & Farzaneh, 2010; Jia Yi Jin & Virk, 2018) and between 20% and 50% in the aerodynamic performance (Jia Yi Jin & Virk, 2018). The best way to maximize energy production from a turbine operating under icing conditions is to understand the performance losses that may be predicted during the icing event (Jasinski et al., 1998).

Despite the importance of its study, the icing phenomenon has not been fully understood due to its complexity and its dependence on multiple factors (W. Han, Kim, & Kim, 2018; L.

Makkonen, 2000; Virk, Mughal, Hu, & Jiang, 2016; Zimnickas, Gecevičius, & Markevičius, 2016): air temperature, humidity, pressure, wind speed, blades angle of attack, size of water droplets, blade geometry, point of operation, among others. Until now, there have been no reliable icing prediction systems (Contreras Montoya, Lain, & Ilinca, 2022).

Different models have been developed and applied to both the analysis and optimization of wind turbines in response to the above. However, the implementation of any model depends on efficiency, accuracy, and computational cost. The available models range from low-cost, yet low-accuracy, computational models to three-dimensional CFD-based models that incorporate all relevant physical phenomena. Over the last decade, driven by significant advancements in computer performance, Computational Fluid Dynamics (CFD) has become a crucial tool for product design, prediction, and optimization of industrial and environmental processes and systems. In this sense, this technique could be applied to study the effect of icing in a horizontal-axis wind turbine.

CFD simulations do not require any external data, such as experimental drag and lift coefficients, for the profile under consideration. They may include flow separation and resistance induced by vortices detached from the blade tips and the axis of rotation. Due to limitations in turbulence models, this also partially accounts for the blade's dynamic losses during rotation. Additionally, CFD is well-suited to complex geometries. However, CFD simulations of wind turbines are computationally expensive and, therefore, have not yet been widely adopted as a standard tool for evaluation and design. From an energy-efficiency perspective, it is strategic to identify the impact of ice formation and accretion on wind turbine performance and to predict their presence.

This research project focused on establishing correlations between meteorological conditions and power losses in wind turbines operating under icing conditions. In this case, three questions were answered: 1) what is the influence of the blade geometry and turbine operation regime on the ice accretion, 2) what are the meteorological parameters that influence the most the process of ice accretion on wind turbine blades and how it affects the overall performance; and the last question, which summarizes the previous, 3) what are the correlations between the meteorological conditions, the operation regime and the power loss of the wind turbines under icing conditions? The Dimensional Analysis (π Theorem) was used to generate the correlatios and Machine Learning techniques such as neural networks, decision trees, and random forests, were used to validate the correlations from the dimensional analysis. Data required for the analysis and validation of the two methodologies were obtained from CFD simulations, experiments reported in the literature, and in situ measurements provided by NERGICA.

Despite the growing body of literature on wind turbine performance in cold climates, a significant research gap persists in quantitatively predicting power losses due to ice accretion, particularly under diverse meteorological and operational conditions. Most existing studies either focus on simplified icing scenarios or rely on empirical correlations that fail to capture the complex interaction between environmental variables, turbine geometry, and operating regimes. Furthermore, although ice detection and de-icing strategies have advanced, our understanding of how different types of ice (dry, wet, and mixed) affect aerodynamic performance across the rotor span remains limited. The lack of integrated, physics-informed predictive models that can directly link meteorological inputs to power degradation represents a barrier to optimizing wind turbine operation and maintenance in cold regions. This research addresses this gap by combining high-fidelity CFD simulations, dimensional analysis, and machine learning to develop predictive tools that are both accurate and generalizable.

0.2 General and Specific Objectives

The main objective of this research is to determine the correlations among meteorological conditions, operational regimes, and wind turbine performance, specifically, power loss under icing conditions. To address the overarching goal of accurately predicting wind turbine power loss due to ice accretion under varying atmospheric and operational conditions, this research is structured around the following sequential objectives:

1) Build a comprehensive database integrating CFD simulations, field measurements, and literature data to characterize types of ice accretion (wet, dry, and mixed) and their aerodynamic impacts on wind turbine blades under cold-climate operating conditions.
2) Identify the dominant physical parameters governing ice formation and power loss using the π theorem to establish universal, dimensionless groups that explain ice-turbine interaction across varying scenarios.
3) Develop and validate a data-driven predictive model informed by the database and physical insights to estimate ice accretion characteristics and their impact on turbine performance. The model aims to support real-time operational decisions and improve cold-climate wind energy forecasting.

0.3 Methodological Approach and Thesis Structure

To address these objectives, the research employs a multi-stage methodology that combines physical modeling, dimensional analysis, and data-driven techniques. First, a comprehensive database is developed using field measurements, CFD simulations, and published literature on wind turbine icing and performance degradation. Second, a dimensional analysis is conducted using the π theorem to identify the most influential meteorological, operational, and geometrical parameters affecting ice accretion and power loss. Finally, a predictive model is developed using machine learning techniques to estimate the type and severity of icing and their impact on the turbine power curve.

For the first objective, the database was created from the main results of simulations and experiments available in the literature. Some of the studies used were: Etemaddar, Hansen, et Moan (2014); Homola, Virk, Nicklasson, et Sundsbø (2012); Homola, Virk, Wallenius, Nicklasson, et Sundsbø (2010); Homola, Wallenius, Makkonen, Nicklasson, et Sundsbø (2010); Matthew C. Homola, Tomas Wallenius, Lasse Makkonen, Per J. Nicklassona, et Per A. Sundsbøa (2010); Muhammad S. Virk, Matthew C. Homola, et Per J. Nicklasson (2010a, 2010b). These studies enabled the determination of functional relations between meteorological conditions, wind turbine operating regimes, and ice accretion. They also enabled us to identify the meteorological parameters that most strongly influence the type, shape, and amount of ice accretion on wind turbine blades. Finally, they established a relationship between ice accretion and a loss in wind turbine performance.

Additionally, data from wind turbines operating under icing conditions were used to validate the proposed correlations derived from dimensional analysis and to train the machine learning models. Nergica provided data from its research center located in Murdochville, Québec, and analyzed 25 icing events that occurred between winter 2019 and winter 2021.

To validate the findings in the literature and improve the understanding of the ice accretion phenomenon, a series of CFD simulations using FENSAP-Ice software were conducted. These simulations provided a better understanding of the icing phenomenon at the airfoil level, thereby facilitating analysis of the relationship between meteorological parameters and ice accretion.

For the second objective, a dimensional analysis was conducted using the "π Theorem". This methodology was used in two parts. The first part involved estimating the mass of ice accumulated on the turbine rotor. In this case, the π Theorem allowed for the reduction of 12-dimensional variables into eight dimensionless groups. The second part involved estimating the power turbine performance while accounting for ice. In this case, six variables (wind turbine power, ice mass, turbine radius, wind speed, rotational speed, and air density) were reduced to three dimensionless groups. The primary objectives of these correlations are to reduce the number of variables and to predict energy losses for any combination of meteorological data and operating conditions, without requiring analysis of icing profiles.

Finally, for the third objective, three machine learning techniques were used to evaluate the proposed correlations with the π Theorem. These techniques included decision trees, random forests, and neural networks. The different techniques were compared to determine which performed best in predicting turbine performance under icing conditions.

The following flowchart (Figure 0. 1) explains, in a general way, the methodology used to achieve the objectives proposed in the research project:

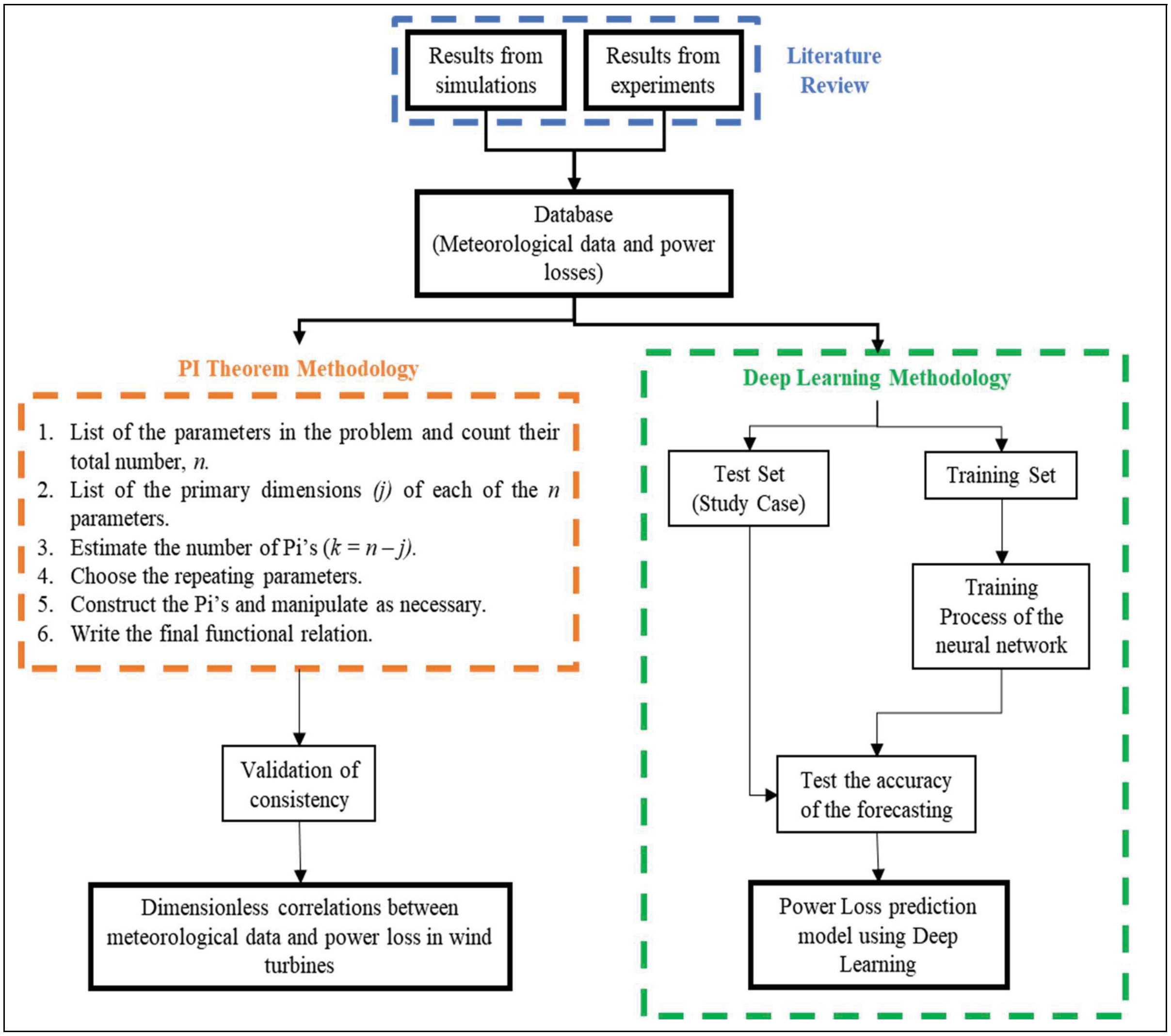

Figure 0. 1 Objectives and methodological plan of the research project

The thesis is structured as follows:

- Chapter 1 covers a literature review of CFD approaches to modeling wind turbine icing and machine learning methods applied to wind turbine icing. As a result of the literature review on CFD simulation, a paper was published in the journal "Energies".

- Chapter 2 presents a CFD simulation of ice accretion on a wind turbine blade airfoil (S809). The paper derived from this study was published in the journal "*Processes*".
- Chapter 3 focuses on database construction.
- Chapter 4 focuses on the correlations proposed to predict wind power losses under icing conditions using dimensional analysis (π theorem).
- Chapter 5 focuses on validating the correlations proposed in Chapter 4 using various machine learning methods.

0.4 Original Contribution of the Thesis

Ice accretion on wind turbines remains among the most challenging operational issues in cold climate regions. While its occurrence and adverse effects have been documented through field observations and performance data, current research predominantly uses descriptive or case-specific modeling approaches. A predictive, generalizable understanding of the complex interactions between meteorological conditions, turbine operating parameters, and blade geometry remains lacking. This thesis aims to bridge that gap by developing a comprehensive, data-driven framework to predict performance losses from icing across varying environmental and operational conditions.

The original contributions of this thesis are threefold:

1) Development of a Predictive Framework Based on Dimensional Analysis: Unlike existing studies that focus primarily on specific icing events or aerodynamic impacts on blade profiles, this work applies the π theorem to identify dimensionless groups governing ice formation and performance degradation. This approach systematically correlates ice-induced power losses with key factors, including air temperature, humidity, wind speed, blade geometry, and operational regimes. To the author's knowledge, this is one of the first attempts to establish a general mathematical framework for ice accretion analysis based on dimensional analysis across diverse icing scenarios.

2) Construction of a Multisource Ice Accretion and Power Loss Database: A distinctive aspect of this thesis is the creation of a robust database that combines results from computational fluid dynamics (CFD) simulations, on-site measurements, and existing literature. This database supports both dimensional analysis and subsequent training of the machine learning model, ensuring that the conclusions are grounded in diverse and representative data.
3) Utilization of computational fluid dynamics (CFD) simulations to understand the effect of roughness in the ice accretion on an airfoil: Two models were evaluated to assess the advantages and disadvantages of each. This assessment demonstrated the importance of accounting for roughness in predicting the aerodynamic performance of an airfoil and, consequently, its overall impact on a wind turbine.
4) Application of Machine Learning for Ice Accretion and Power Loss Prediction: While machine learning has found wide applications in areas such as autonomous driving, medical diagnostics, and image recognition, its use in wind turbine icing prediction remains unexplored. This thesis pioneers the use of machine learning methods to predict ice type (wet, dry, or mixed), accreted ice mass, and associated changes in turbine power curves from meteorological and operational inputs. This approach offers significant potential for real-time forecasting, proactive turbine control, and improved reliability of wind energy production in cold climates.

Together, these contributions provide a novel, integrated methodology for understanding, modeling, and ultimately mitigating the impacts of ice accretion on wind turbine performance, thereby advancing the broader goal of enhancing wind energy reliability in cold regions.

CHAPTER 1

A REVIEW OF THE ESTIMATION OF POWER LOSS DUE TO ICING IN WIND TURBINES

Leidy Tatiana Contreras Montoya [a,b], Santiago Lain [b], and Adrian Ilinca [a]

[a] Wind Energy Research Laboratory (WERL), University of Québec at Rimouski, 300, allée des Ursulines, Rimouski, QC G5L 3A1, Canada
[b] PAI+ Group, Energetics & Mechanics Department, Faculty of Engineering, Universidad Autónoma de Occidente, Cll 25 # 115-85 Km 2 Vía Cali - Jamundí, Cali, Valle del Cauca 760030, Colombia.

Article published in Energies, vol. 15 (2022), available at
https://doi.org/10.3390/en15031083

1.1 Ice Accretion Phenomenon

Wind farms in cold climates are exposed to severe conditions, resulting in high annual production losses (Pedersen & Yin, 2014). These production losses result from atmospheric icing, defined as the effect of moisture on a surface at temperatures below 0°C, leading to ice accretion. However, periods during which accreted ice remains on the structure, also known as instrumental icing, are crucial for numerical analysis (Pedersen & Sørensen, 2016).

Atmospheric icing can be divided into three main categories: in-cloud icing, freezing rain, and wet snow icing. During in-cloud icing, supercooled droplets are present in a cloud or fog at low temperatures, resulting in the formation of hard rime, soft rime, and glaze ice (Pedersen & Sørensen, 2016). The parameters that influence the formation of each icing type are ambient temperature, the size of the water drops (median volume diameter – MVD), the water content in the air (liquid water content – LWC), wind speed, and precipitation type.

Studying this phenomenon is also essential for designing and optimizing anti-icing and de-icing systems and strategies. For example, heating a surface can allow relatively dry ice pieces to adhere, shifting the icing process from dry to moist and unfavourably modifying the aerodynamics of ice deposition. On the other hand, de-icing at the incorrect time will cause catastrophic systemic dynamic responses. In general, improperly designed or uncontrolled ice prevention can increase ice loads and lead to ice incidents that would not typically occur, potentially resulting in direct structural damage (L. Makkonen, 2000).

1.1.1 Fundamentals of Ice Accretion Modeling

The icing phenomenon occurs when particles in the air collide with an object's surface. These particles can be either liquid, solid, or a mixture of water and ice. In any case, the maximum rate of icing per unit area of the surface is determined by the flux density of these particles. The flux density is a product of the mass concentration (w) and the particles' velocity relative to the object (v). Consequently, the icing rate is obtained from the equation (1.1) (L. Makkonen, 2000):

$$\frac{dM}{dt} = \alpha_1 \alpha_2 \alpha_3 w v A \tag{1.1}$$

Where A is the cross-sectional area (relative to the direction of the particle velocity vector v), the correction factors α_1, α_2 and α_3 represent processes that may reduce $\frac{dM}{dt}$ and vary between 0 and 1. α_1 denotes the *collision efficiency*, α_2 the *sticking efficiency*, and α_3 the *accretion efficiency*.

- **Collision efficiency** is the ratio of the particles' flux density that hits the object to the maximum flux density. It is reduced because small particles tend to follow the air streamlines and may be deflected from their path toward the object. The collision efficiency depends strongly on the particle size, as represented by the MVD. Hence, for large MVDs, such as those encountered in freezing rain or wet snow, α_1 is typically estimated to be 1 in most applications unless the structure is extremely large. Therefore, α_1 is usually calculated when icing occurs due to cloud droplets (L. Makkonen, 2000).

- **Sticking efficiency** represents the efficiency of collecting particles that hit the object, i.e., the ratio of particles that stick to the object to the flux density of particles hitting the object. It is reduced when particles bounce off the surface (e.g., dry snow at ambient temperatures below 0°C). Particles are considered to adhere when they are permanently collected or when their residence time on the surface is sufficient to affect the icing rate, specifically for supercooled water droplets. α_2 is affected by air temperature and humidity (L. Makkonen, 2000).

- **Accretion efficiency** is the ratio of the rate of icing to the flux density of the particles that stick to the surface. It is reduced when the heat flux from the accretion is too small (part of the particle flow is lost from the surface due to run-off caused by gravity or wind drag) to cause sufficient freezing to incorporate all the sticking particles in the accretion. During wet-snow accretion, snow melting may occur. This may reduce the accretion rate, i.e., the extra water in the snow may disrupt the network of interconnected ice grains that hold the snow structure together (L. Makkonen, 2000).

In addition to the parameters that determine the icing rate, the duration of icing events is crucial for modeling and developing a comprehensive understanding of the phenomenon. Ice begins to settle on the exposed structure over time; therefore, time-dependent models often require simulating the density of accreted ice. This is because the icing rate for the next time step depends on the object dimensions; thus, the relationship between the modelled ice load and the iced structure's dimensions is necessary (L. Makkonen, 2000).

When calculating accretion, it is essential to note that roughness changes as ice continues to settle on the blade’s surface. The surface roughness of ice significantly affects heat transfer from a blade. It also determines the transition from laminar to turbulent flow (L. Makkonen et al., 2001; Pedersen & Sørensen, 2016). This is an essential factor in the simulation setup that will help select the optimal turbulence model and mesh refinement.

1.1.2 Icing Types

Rime Ice, or ‘**dry growth**’, occurs when there are no liquid layer and no runoff ($\alpha_3 = 1$). **Erreur ! Source du renvoi introuvable.** represents this type of ice (L. Makkonen, 2000). It can be divided into two categories: **Hard Rime Ice** and **Soft Rime Ice**. The first one appears at higher MVD and LWC, which are common at high altitudes and at temperatures below -10°C. The most severe rime icing occurs on freely exposed mountains or hilltops, where humid air is forced upward and consequently cooled, or in mountain valleys, where moist air is forced through passes, thereby increasing wind speed. It has a density between 600 and 900 kg/m^3 and a strong adhesion (L. Makkonen et al., 2001; Zimnickas et al., 2016). The second type of rime ice also occurs at high altitudes when air temperature is below 0°C, and MVD and LWC are relatively small. It has a low density of 200-600 kg/m3 and low-to-medium adhesion (Zimnickas et al., 2016).

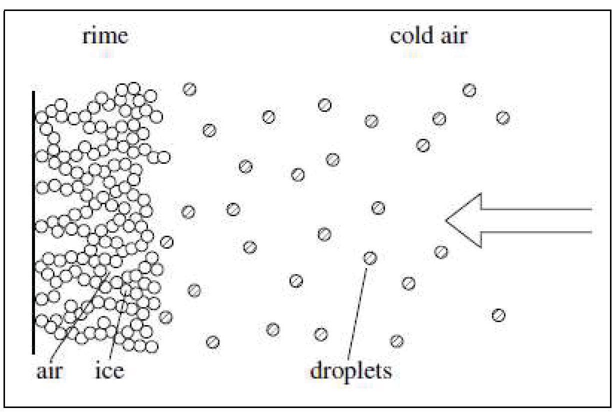

Figure 1.1 Representation of Rime Ice
Taken from L. Makkonen (2000)

Glaze ice, also known as ‘wet growth,’ occurs when the air temperature is between 0°C and -10°C. It forms when not all water drops freeze immediately after hitting the surface, i.e., when α_3 is lower than 1, a liquid layer is present on the accretion’s surface, and freezing occurs beneath this layer (L. Makkonen, 2000; L. Makkonen et al., 2001). The water on the surface freezes, and the other part runs back and freezes later (see Figure 1.2). Glaze ice has a high density of approximately 900 kg/m3 and strong adhesion. For that reason, it is difficult to remove (Zimnickas et al., 2016).

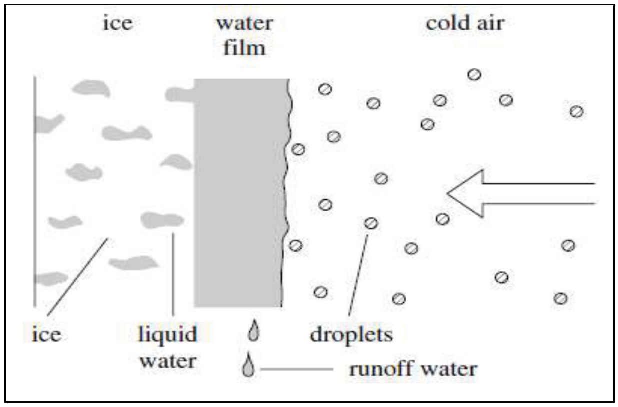

Figure 1.2 Representation of Glaze Ice
Taken from L. Makkonen (2000)

Finally, freezing rain occurs when raindrops fall onto a surface at temperatures below 0°C; it is dense and exhibits strong adhesion. Wet snow is the accretion process in which snowflakes partially contain liquid water and can adhere to a surface. This process occurs only when the ambient temperature is just above the freezing point (Zimnickas et al., 2016).

1.2 CFD-Based Models Icing Conditions

Despite the importance of its study, the icing phenomenon has not been fully understood due to its complexity and its dependence on multiple factors, such as (W. Han et al., 2018; L. Makkonen, 2000; Virk et al., 2016; Zimnickas et al., 2016): Air temperature, humidity, pressure, wind speed, blades' angle of attack, size of water droplets, blade geometry, point of operation, among others. Until now, there have been no reliable icing prediction systems. However, many models simulate rime ice formation on wind turbine blades, whereas only a few predict glaze ice formation (Zimnickas et al., 2016).

For years, the estimation of ice accretion impact on wind turbines has been restricted to two dimensions, i.e., the problem has been simplified to an airfoil section of the blade. However, a typical horizontal-axis wind turbine (HAWT) typically has a twisted-blade geometry with several different section forms (Abbadi, Mussa, Lin, & Wang, 2020). This blade geometry requires three-dimensional simulations for improved accuracy. However, icing affects not only the blade but also the entire wind turbine, producing various 3D effects, such as airflow along the radial direction caused by the blades' rotation (Abbadi et al., 2020; Fu & Farzaneh, 2010; Shu et al., 2018). As demonstrated by J. Y. Jin, Virk, Hu, et Jiang (2020), the flow-velocity magnitude in a 3D simulation involves a considerable non-zero component in the z-direction along the blade, which can lead to complex fluid-structure interactions and, consequently, a more complex flow pattern.

Numerical modeling of atmospheric ice accretion on wind turbines is a complex, coupled process that involves ice-shape prediction, airflow simulation, water-droplet behaviour, boundary-layer characteristics, and iced-surface thermodynamics with phase changes (L. Makkonen et al., 2001; Virk et al., 2016). The models used for the numerical analysis of wind turbine icing were originally developed for aeronautical applications. For example, in the case of LEWICE, FENSAP-ICE, the empirically tuned cylinder-based model by Makkonen, and TURBICE (Pedersen & Sørensen, 2016; Pedersen & Yin, 2014).

The modeling technique aims to integrate ice accretion and aerodynamic analysis of the iced object into a single CFD-based icing model. A series of integrated thermofluidic dynamic steps can be used to describe the numerical simulation (J. Y. Jin et al., 2020; Martini, Contreras, & Ilinca, 2021; M. C. Pedersen & H. Sørensen, 2016): (1) fluid flow simulation, (2) droplet behaviour, (3) surface thermodynamics, and (4) phase changes. For the last two steps, additional models should be used. All models will be updated at each time step to improve accuracy. Ultimately, mesh displacement occurs due to ice accretion. Thus, updating the multiphase flow solution after every surface boundary displacement guarantees that the solution reflects changes in geometry (see Figure 1.3).

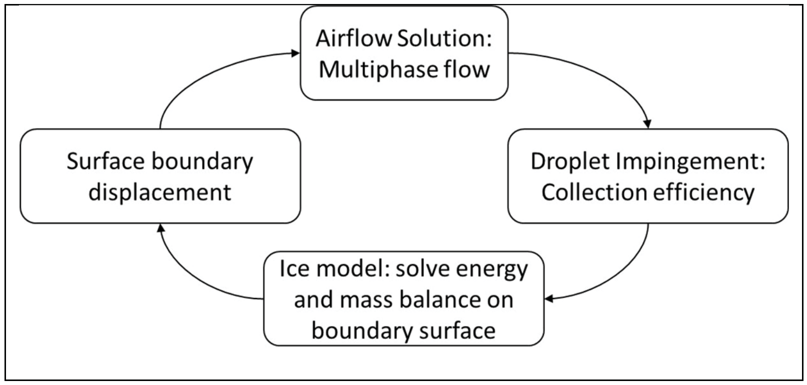

Figure 1.3 Diagram of ice accretion model based on CFD
Taken from Contreras Montoya et al. (2022)

1.2.1 Airflow Simulation

The airflow simulation consists of the discretization of the governing Partial Differential Equations for conservation of mass (continuity equation—Equation (1.2)), momentum (Navier–Stokes equation—Equation (1.3), and energy (Equation (1.4) (J. Y. Jin et al., 2020; Virk et al., 2016).

$$\frac{\partial \rho_a}{\partial t} + \vec{\nabla}(\rho_a \vec{U}) = 0 \tag{1.2}$$

$$\frac{\partial \rho_a \vec{U}}{\partial t} + \vec{\nabla}(\rho_a \vec{U}\vec{U}) = \vec{\nabla}\sigma^{ij} + \rho_a \vec{g} \tag{1.3}$$

$$\frac{\partial \rho_a E_a}{\partial t} + \vec{\nabla}(\rho_a \vec{U} H_a) = \vec{\nabla}(\kappa_a(\vec{\nabla} T_a) + \nu_i \tau^{ij} + \rho_a \vec{g}\vec{U} \tag{1.4}$$

In this context, ρ_a denotes air density, and U is the velocity vector. The subscript a refers to the air solution, T refers to the air static temperature measured in Kelvin, σ^{ij} signifies the stress tensor, κ_a is the thermal conduction coefficient, E is the total initial energy, and H is enthalpy. Such equations are supplemented by turbulence models that describe the flow fluctuations around wind turbine blades (Contreras Montoya, Ilinca, & Lain, 2023).

The airflow is considered turbulent; hence, to resolve the oscillations and eddies produced in the flow, time-dependent Navier-Stokes equations and fine spatial resolution are required. However, these eddies and oscillations become too small as the Reynolds number increases, so the Reynolds-Averaged Navier–Stokes (RANS) approach is more suitable. Based on observations, the RANS formulation averages the velocity variations in the flow field across time (Martini, Contreras, & Ilinca, 2021).

Given the above, several RANS models and modifications are available for different applications and differ in how turbulent eddy viscosity is computed. In response to the above, several turbulence models, including the k-ε, k-ω, Shear-Stress Transition (k-ω SST model), Spalart–Allmaras, and Large Eddy Simulation (LES) models, have been employed. However, four of them have been widely used in flows around airfoils and wind turbines (Martini, Contreras, & Ilinca, 2021; Sagol, Reggio, & Ilinca, 2012).

The **Spalart–Allmaras model** is a one-equation turbulence model. The one additional equation is used to model the transport of turbulent viscosity. This model is employed in aerodynamics because of its compromise between acceptable computational cost and accuracy (Contreras Montoya et al., 2023; Homola et al., 2012; Martini, Contreras, & Ilinca, 2021). Furthermore, several scientists have stated that this model is the most effective in simulating ice buildup on electrical cables, wind turbines, and aircraft (Hudecz, Koss, & Laver, 2013; L. Makkonen, Zhang, Karlsson, & Tiihonen, 2018). However, it has a limitation in describing boundary-layer behaviour under adverse pressure gradients (Martini, Ibrahim, Contreras M, Rizk, & Ilinca, 2022).

The **k-ε model** is a two-equation turbulence model that solves for the turbulent kinetic energy (k) and the rate of dissipation of kinetic energy (ε), under fully turbulent flow, yielding better results for ice accretion simulations (Martini, Contreras, & Ilinca, 2021). It has demonstrated adequate performance in simulating ice accretion, gaining widespread popularity owing to its numerical stability, efficiency in computational resources, and rapid convergence rate (Contreras Montoya et al., 2023; Fu & Farzaneh, 2010; Homola, Virk, et al., 2010; Martini, Contreras, & Ilinca, 2021). However, in some cases, it is inadequate for flows with high-pressure gradients (Taborda Ceballos, 2015). To correct this issue, the RNG k-ε model was developed. Based on the renormalization group, this new turbulence model incorporates correction terms for swirling, low-Reynolds-number, and high-velocity-gradient flows, and also predicts the smallest recirculation zone and the separation point closest to the trailing edge (Martini, Contreras, & Ilinca, 2021). Villalpando, Reggio, et Ilinca (2011) evaluated different turbulence models and concluded that this model was adequate for simulating icing on wind turbines.

The **k-ω model** is also a two-equation turbulence model. It is used when k-ε is insufficient and exhibits convergence difficulties, as it is more nonlinear (Bai & Wang, 2016). It solves the turbulent kinetic energy (k) and the specific rate of dissipation of kinetic energy (ω).

The **k-ω SST model** is a four-equation model presented by Menter (1993). It combines the standard k-ω and k-ε models. It uses both models in different flow regions, activating the k-ω model near the wall and the k-ε model away from the surface (Contreras Montoya et al., 2022; Martini, Contreras, & Ilinca, 2021). This model is more accurate than other turbulence models (Sagol et al., 2012) because it allows studying the laminar-turbulent transitions of the boundary layer at high angles of attack (Tardif d'Hamonville, 2009), handling the recirculation zones, accurately predicting flow separation, and describing the generation of specific vortices at the trailing and leading edges (Martini, Contreras, & Ilinca, 2021). However, this model has a high computational cost.

1.2.2 Droplets Behavior

The droplets' behaviour can be described by considering the icing phenomenon as a multiphase flow because the icing rate may be affected by a mixture of ice, air, and liquid water (L. Makkonen, 2000; Virk, Homola, & Nicklasson, 2012). The term "Multiphase Flow" refers to any fluid flow that involves more than one phase or component. They are categorized by the state of the different phases and hence apply to gas/solid, liquid/solid, or gas/liquid flows (Van Wachem & Almstedt, 2003).

With two extensions, the equations of multiphase flows in CFD are the same as those of single-phase flows applied to each fluid in the simulation. To begin, new equations for the volume fraction of each fluid are included. Second, additional terms are introduced into each phase's transport equation to simulate interphase transfers, including drag, heat, and mass transfer (ANSYS Inc., 2020; Fu & Farzaneh, 2010). When gravity and buoyancy are neglected, liquid water droplets in the air are influenced by drag and inertia. If drag dominates inertia, the droplets follow the streamline. However, if inertia dominates, the droplet hits the object (the wind turbine). The ratio of inertia to drag depends upon the droplet size, the velocity of the air stream, and the dimensions of the object in question (Virk et al., 2012).

The equations involved in multiphase (two-fluid interaction) computations are (Fu & Farzaneh, 2010):

- Mass conservation: the continuity equation for phase $\boldsymbol{q}$ can be expressed as:

$$\frac{\partial}{\partial t}\left(\vartheta_q \rho_q\right) + \nabla \cdot \left(\vartheta_q \rho_q \overrightarrow{v_q}\right) = \sum_{p=1}^{n}\left(\dot{m}_{pq} - \dot{m}_{qp}\right) \tag{1.5}$$

Where ϑ, ρ and v denote the volume fraction, density, and velocity for phase q, respectively, and $\dot{m}$ represents the mass transfer between two phases.

- Momentum Conservation: The equation of conservation of momentum for phase $\boldsymbol{q}$ can be written as:

$$\frac{\partial}{\partial t}\left(\vartheta_q \rho_q \overrightarrow{v_q}\right) + \nabla \cdot \left(\vartheta_q \rho_q \overrightarrow{v_q}\overrightarrow{v_q}\right) = -\vartheta_q \nabla p + \nabla \cdot \overline{\overline{\tau_q}} + \sum_{p=1}^{n}\left(\dot{R}_{pq}\dot{m}_{pq}\overrightarrow{v_{pq}} - \dot{m}_{qp}\overrightarrow{v_{qp}}\right) \tag{1.6}$$

Where $\overline{\overline{\tau_q}}$ is the qth phase stress–strain tensor, $\dot{R}_{pq}$ is an interaction force between phases, p is the pressure shared by all phases, and $\vec{v}$ is the velocity vector.

Two approaches have been developed for simulating the dispersed phase in multiphase flows: the Eulerian and Lagrangian methods. Each method can yield accurate results, and its use will depend on the type of study, flow characteristics, and particle properties (ANSYS Inc., 2020). However, the more robust method will entail a higher computational cost and require more time to obtain reliable results (Martini, Contreras, & Ilinca, 2021). For the icing, several software codes have been developed, including FENSAP-ICE, LEWICE, TURBICE, and ANSYS-Fluent, and both approaches have been implemented. For instance, FENSAP-ICE employs an Eulerian approach, whereas TURBICE and LEWICE employ a Lagrangian approach (Ayabakan, 2013).

1.2.2.1 Eulerian Multiphase Model

In this model, the dispersed phase, like the continuous phase, is described as a continuous fluid. This approach employs phasic volume fractions, which describe the space occupied by each phase (solid-liquid, gas-liquid, or liquid-liquid) (Laín & Aliod, 2000). The laws of mass and momentum conservation are satisfied individually for each phase; the properties of each dispersed particle or droplet are averaged; and mass transfer between phases is not assumed (ANSYS Inc., 2020; M. C. Pedersen & H. Sørensen, 2016; Pedersen & Yin, 2014; Van Wachem & Almstedt, 2003). The presence of the dispersed phase significantly affects the continuous phase, manifesting as viscous drag (Jia Yi Jin & Virk, 2018). Similarly, there is a contribution to the lift force, which arises from transverse forces associated with rotational strain, velocity gradients, or wall effects (Van Wachem & Almstedt, 2003).

The droplet drag coefficient could be based on the empirical correlation for the flow around spherical droplets described by Clift et al. 1978 (Jia Yi Jin & Virk, 2018; J. Y. Jin et al., 2020):

$$\frac{\partial \alpha}{\partial t} + \vec{\nabla}\left(\vartheta \vec{U}_d\right) = 0 \tag{1.7}$$

$$\frac{\partial\left(\vartheta \vec{U}_d\right)}{\partial t} + \vec{\nabla}\left(\rho_a \vec{U}_d \otimes \vec{U}_d\right) = C_D Re_d / 24K\, \vartheta\left(\vec{U} - \vec{U}_d\right) + \frac{\vartheta(1 - \rho_a/\rho_d)1}{Fr^2 \vec{g}} \tag{1.8}$$

Where ϑ is the water volume fraction, $\vec{U}_d$ is the droplet velocity, C_D is the droplet drag coefficient, Re_d is the droplets' Reynolds number (Equation (1.9)), K is the inertial parameter (Equation (1.10)), and Fr is the Froude number $\left(Fr = \vec{U}/\sqrt{gd}\right)$.

$$Re_d = \frac{\rho_a d \left\|\vec{U} - \vec{U}_d\right\|}{\mu_a} \tag{1.9}$$

$$K = \frac{\rho_d d^2 U}{18 L_\infty \mu_a} \tag{1.10}$$

Where d is the droplet diameter, $\vec{U}$ the wind speed, $\vec{U}_d$ the droplet's speed, μ_a the air dynamic viscosity, and L_∞ the characteristic length.

To imitate in-cloud icing conditions, the Eulerian Multiphase Flow Model has been used. The droplet solution of this model provides, in all computational domains, the velocity, volume fractions, density, and temperature variables for the phases at any time (Martini, Contreras, & Ilinca, 2021; M. C. Pedersen & H. Sørensen, 2016). Another advantage is that we can use the same mesh to calculate multiphase flow and predict ice shape (Fu & Farzaneh, 2010; Martini, Contreras, & Ilinca, 2021).

1.2.2.2 Lagrangian Multiphase Model

This model solves the Newtonian motion equations for each particle or droplet and employs a collision model to account for particle interactions. The calculation of particle paths consists of two steps: (1) calculation of the particle motion and (2) treatment of the collision between a particle and another particle. For particle motion, Newton's second law is applicable, and the forces acting on each particle, distinct from collisions, include gravity and the traction force exerted by the fluid phase on the particle (Van Wachem & Almstedt, 2003). This approach is often used in 2D icing analysis, where the velocities of water droplets required for icing-rate evaluation can be obtained by numerically tracking many droplets in the vicinity of the icing object. However, in 3D, it becomes computationally expensive to track sufficient droplets to generate the ice-layer geometry (Fu & Farzaneh, 2010).

1.2.3 Ice Accretion

The ice accretion involves heat and mass transfer. It is traditionally based on the first-order differential equations of mass conservation and heat transfer developed by Messinger (1953) and on the work of Lozowski, Stallabrass, et Hearty (1983a); (1983b). The contamination caused by the water droplets is modelled as a thin film of liquid running along the blade surface. Part of this film may freeze, evaporate, or sublimate (Martini, Contreras, & Ilinca, 2021). Hence, the ice accretion model is based on thermodynamic equilibrium and involves different heat fluxes, including convective and evaporative cooling, fusion heat, viscous and kinetic heating (J. Y. Jin et al., 2020; Martini, Contreras, & Ilinca, 2021; Virk et al., 2016). For the mass conservation, the partial differential equation on solid surfaces will be (Jia Yi Jin & Virk, 2018; J. Y. Jin et al., 2020):

$$\rho_f \left[\frac{\partial h_f}{\partial t} + \vec{\nabla}\left(\vec{U}_f h_f\right)\right] = U(LWC)\beta - \dot{m}_{evap} - \dot{m}_{ice} \tag{1.11}$$

Where h_f is the height of the water film, $\vec{U_f}$ is the velocity of the water film, and LWC denotes liquid water content. The terms on the right-hand side represent mass transfer through water droplet impingement (source for the film), evaporation, and ice accretion (sinks for the film). The collection efficiency is represented by β, which is given by Equation (1.12).

$$\beta = -\frac{\vartheta\overrightarrow{U_d} \cdot \vec{n}}{(LWC)U} \tag{1.12}$$

For the conservation of energy, the equation is:

$$\begin{aligned} \rho_f \left[\frac{\partial h_f c_f \dot{T}_f}{\partial t} + \dot{\nabla}\left(U_f h_f c_f \dot{T}_f\right)\right] \\ = \left[c_f\left(T - \tilde{T}_f\right) + \frac{\left\|\vec{U}_d^2\right\|}{2}\right] U(LWC)\beta - L_{evap}\dot{m}_{evap} \\ + \left(L_{fusion} - c_s\tilde{T}\right)\dot{m}_{ice} + \sigma\varepsilon\left(T^4 - {T_f}^4\right) \\ - c_h\left(\tilde{T}_f - \tilde{T}_{ice.rec}\right) + Q_{anti-icing} \end{aligned} \tag{1.13}$$

Where c_f, L_{evap}, L_{fusion}, and c_s are physical properties of the fluid and the solid, σ is the Boltzmann constant, ε is the solid emissivity, and $\tilde{T}_f$ is the equilibrium temperature at the air/water-film/ice/wall interface.

For the ice accretion calculation, it is common to consider the effect of ice roughness that can reduce energy production by 20% (Blasco, Palacios, & Schmitz, 2017; Jasinski et al., 1998; Martini, Contreras, & Ilinca, 2021; Sagol, 2014), and which also affects the heat transfer (L. Makkonen et al., 2001; Martini, Contreras, & Ilinca, 2021), especially when rime ice is considered (Zanon, De Gennaro, & Kühnelt, 2018). Ice accretion is usually at the leading edge. Still, for icing calculations, the flow solution is computed with roughness applied to all surfaces as droplet impingement, and icing limits are unknown a priori (Abbadi et al., 2020). On this basis, Shin, Berkowitz, Chen, et Cebeci (1991) developed, from empirical data based on experiments, an equivalent sand-grain roughness (k_s), expressed as a function of the LWC, static air temperature (T), airspeed (U) and the MVD to determine the ice shapes. With c denoting the airfoil chord and $\left(\frac{k_s}{c}\right)_{base} = 0.001177$, it is expressed in the following form:

$$k_s = \left[\frac{\frac{k_s}{c}}{\left(\frac{k_s}{c}\right)_{base}}\right]_{LWC} \cdot \left[\frac{\frac{k_s}{c}}{\left(\frac{k_s}{c}\right)_{base}}\right]_{T} \cdot \left[\frac{\frac{k_s}{c}}{\left(\frac{k_s}{c}\right)_{base}}\right]_{U} \cdot \left[\frac{\frac{k_s}{c}}{\left(\frac{k_s}{c}\right)_{base}}\right]_{MVD} \cdot \left(\frac{k_s}{c}\right)_{base} \cdot c \tag{1.14}$$

Where each sand-grain roughness parameter is given by Shin et al. (1991):

$$\left[\frac{\frac{k_s}{c}}{\left(\frac{k_s}{c}\right)_{base}}\right]_{LWC} = 0.5714 + 0.2457(LWC) + 1.2571(LWC)^2 \text{ for LWCs greater than 1 g/m}^3 \tag{1.15}$$

$$\left[\frac{\frac{k_s}{c}}{\left(\frac{k_s}{c}\right)_{base}}\right]_{T} = 0.047(T) - 11.27 \tag{1.16}$$

$$\left[\frac{\frac{k_s}{c}}{\left(\frac{k_s}{c}\right)_{base}}\right]_{U} = 0.4286 + 0.0044139(U) \tag{1.17}$$

$$\left[\frac{\frac{k_s}{c}}{\left(\frac{k_s}{c}\right)_{base}}\right]_{MVD} = \begin{cases} 1 & MVD \leq 20 \\ 1.667 - 0.0333(MVD) & MVD > 20 \end{cases} \tag{1.18}$$

Bragg (1982) describes in detail a method to correct the drag coefficient due to ice accretion and small-scale surface roughness, which can be expressed by Equations (1.19) and (1.20).

$$\Delta C_D = 0.01\left[(-15.8 \times \ln\left(\frac{k_s}{c}\right) + 23.2\right] \tag{1.19}$$

$$C_{D\,iced} = (1 + \Delta C_D)C_D \tag{1.20}$$

Where $\frac{k_s}{c}$ can be determined by the method of Shin et al. (1991).

1.3 Blade Element Momentum (BEM) Theory

Blade Element Momentum Theory (BEM) has become the standard approach for evaluating and designing wind turbines (Homola et al., 2012). It combines the momentum theory (analysis of the forces based on the conservation of linear and angular momentum) and the blade element theory (analysis of the forces at a section of the blade based on the blade geometry) (Manwell, McGowan, & Rogers, 2010; Martini, Contreras, Ilinca, & Awada, 2021). It involves dividing the turbine blade into N sections (see Figure 1.4) applying the following assumptions: (1) there is no aerodynamic interaction between sections; (2) the lift determines the forces on the blades and drag characteristics of the airfoil shape using an angle of attack calculated from the incident resultant velocity in the element's cross-sectional plane; (3) the velocity component in the span-wise direction is ignored; (4) three-dimensional effects are also ignored (Burton, Jenkins, Sharpe, & Bossanyi, 2011; Manwell et al., 2010; Martini, Contreras, Ilinca, et al., 2021).

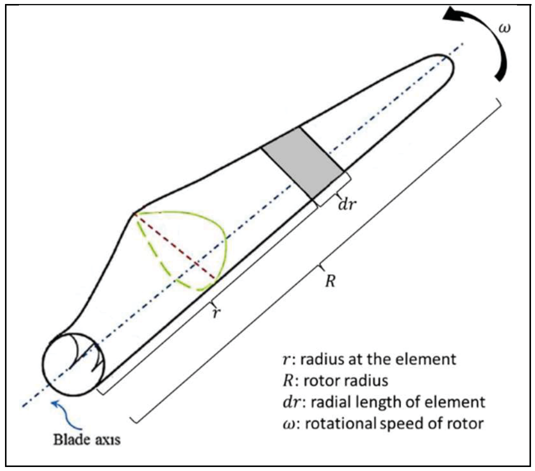

Figure 1.4 Diagram of blade elements
Taken from Contreras Montoya et al. (2022)

As mentioned before, from the momentum theory, we obtain the thrust (dT) and torque (dQ) on an annular section of the rotor as a function of the axial (a) and tangential (a') induction factors of the flow conditions (Manwell et al., 2010; Martini, Contreras, Ilinca, et al., 2021):

$$dT = \rho U^2 4a(1-a)\pi r dr \tag{1.21}$$

$$dQ = 4a'(1-a)\rho U \omega \pi r^3 dr \tag{1.22}$$

Where U is the air velocity and ω the rotational speed of the rotor.

In blade element theory, both forces are obtained. However, in this case, they are a function of the flow angles at the blades and airfoil characteristics (see Figure 1.5):

$$dT = \frac{1}{2} B \rho U_{rel}^2 (C_l \cos\phi + C_d \sin\phi) c dr \tag{1.23}$$

$$dQ = \frac{1}{2} B \rho U_{rel}^2 (C_l \sin\phi - C_d \cos\phi) c r dr \tag{1.24}$$

Where B is the number of the blades, c is the airfoil chord, U_{rel} is the relative wind speed, which is the vector sum of the wind velocity at the rotor $\big(U(1-a)\big)$, and the wind velocity due to the rotation of the blade $(\omega r(1+a'))$, C_l is the lift coefficient, C_d is the drag coefficient, and ϕ is the angle between the wind speed and the plane of rotation.

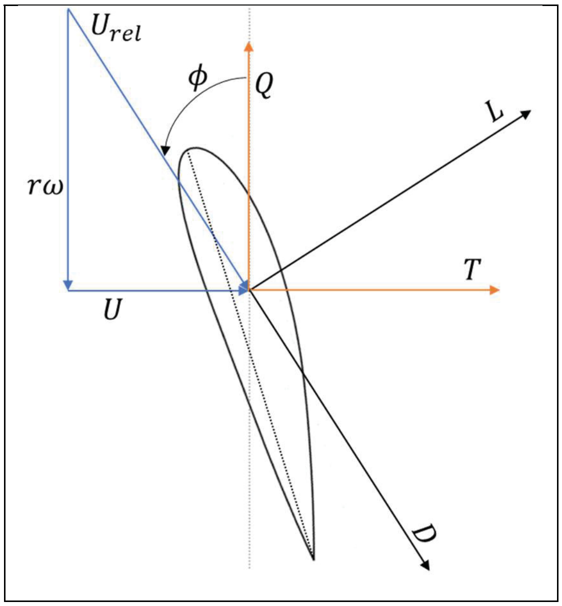

Figure 1.5 Blade Element Velocities and Forces
Taken from Contreras Montoya et al. (2022)

Determining the complete performance characteristics of a wind turbine requires an iterative solution, which consists of initializing a and a' to zero, assuming $C_d = 0$. Drag is excluded from the calculation of the flow induction factors because, in attached flows, drag arises from skin friction and does not affect the pressure drop across the rotor (Burton et al., 2011; Martini, Contreras, Ilinca, et al., 2021). Once the induction factors have been obtained, ϕ , C_l and C_d are calculated. The process is then repeated until convergence is obtained. With the results for a, a', ϕ, C_l and C_d, the torque can be calculated by the equations (1.22) and (1.24):

$$dQ = 4a'(1-a)\rho U\omega\pi r^3 dr - \frac{1}{2}B\rho U_{rel}^2(C_l \sin\phi - C_d \cos\phi)crdr \tag{1.25}$$

Finally, the power contribution from each annulus is given by (Manwell et al., 2010; Martini, Contreras, Ilinca, et al., 2021):

$$P = \int_{0}^{R} \omega \, dQ \tag{1.26}$$

And the power coefficient is given by (Manwell et al., 2010; Martini, Contreras, Ilinca, et al., 2021):

$$C_P = \frac{P}{P_{wind}} = \frac{\int_r^R \omega \, dQ}{\frac{1}{2}\rho\pi R^2 U^3} \tag{1.27}$$

The wind turbine power coefficient depends on the number of blades B, the aerodynamic characteristics of the airfoils, their position r, their pitch angle β, the angle of incidence α, the upstream wind speed U, and the rotational speed ω . The previous velocity triangle (see Figure 1.5) for an airfoil can be simplified to the relative velocity, U_{rel}, and the angle of attack, α, which are used as input parameters for the CFD calculations (Martini, Contreras, Ilinca, et al., 2021).

The power output of a turbine analyzed using BEM is typically underestimated due to assumptions, particularly at low tip speed ratios. Nevertheless, the power coefficient is often overestimated in high-solidity rotors (Burton et al., 2011; Martini, Contreras, Ilinca, et al., 2021). However, span-wise flow exists and is caused by the centrifugal force generated by blade rotation. Therefore, the radial crossflow is unstable, generating steady and trailing vortices that delay flow separation, reduce drag, increase lift, and, at large angles of attack, yield lift and drag coefficients that differ significantly from those obtained from 2D computations and measurements (Laín, Contreras, & López, 2019).

Some corrections have been proposed to this model to enhance the calculations and account for the 3D phenomenon. Some examples include Prandtl’s tip loss factor, the Stall–Delay model, the Viterna–Corrigan Stall model, and Spera’s correction.

1.3.1 Prandtl's Tip Loss Factor

This factor accounts for the flow around the blade tip from the lower to the upper surface. This flow results from the different pressures on the blade's sides: the suction side has lower pressure than the pressure side, reducing lift and, thus, power near the tip. The tip loss is more pronounced in turbines with fewer, wider blades. The correction factor (F), introduced into the equations discussed previously, mainly affects the forces derived from momentum theory (Martínez, Bernabini, Probst, & Rodríguez, 2005; Martini, Contreras, Ilinca, et al., 2021).

$$F = \left(\frac{2}{\pi}\right) \cos^{-1} exp\left(-\left\{\frac{\left(\frac{B}{2}\right)\left[1-\left(\frac{r}{R}\right)\right]}{\left(\frac{r}{R}\right)\sin\phi}\right\}\right) \tag{1.28}$$

1.3.2 Stall – Delay Model

This model accounts for the stall–delay phenomenon. The stall region in rotating blades begins in regions of higher angle of attack. However, the effects of centrifugal force help reduce the adverse pressure gradient that causes an airfoil to stall. This phenomenon can be described mathematically using laminar boundary layer theory as follows (Bai & Wang, 2016; Martini, Contreras, Ilinca, et al., 2021):

$$C_{l,\text{stall}} = C_l + 3\left(\frac{c}{r}\right)^2 \Delta C_l \tag{1.29}$$

$$C_{d,\text{stall}} = C_d + 3\left(\frac{c}{r}\right)^2 \Delta C_d \tag{1.30}$$

Where ΔC_l and ΔC_d are the differences in lift and drag coefficients obtained from the flow with no separation, $\frac{c}{r}$is the local chord length normalized according to the radial direction.

Considering the tip loss and the stall delay, the induction factors can be rewritten as (Bai & Wang, 2016; Martini, Contreras, Ilinca, et al., 2021):

$$a = \frac{C_x \sigma_r}{4F \sin^2 \phi + C_x \sigma_r} \tag{1.31}$$

$$a' = \frac{C_y \sigma_r (1 - a)}{4F\lambda \sin^2 \phi} \tag{1.32}$$

Where $C_x = C_l \cos\phi + C_d \sin\phi$, $C_y = C_l \sin\phi - C_d \cos\phi$, λ is the tip speed ratio ($\lambda = \omega R/U$), σ_r is the chord solidity, defined as the total blade chord length (c) at a given radius (r) divided by the circumferential length at that radius:

$$\sigma_r = \frac{B}{2\pi}\frac{c}{r} \tag{1.33}$$

1.3.3 Viterna – Corrigan Stall Model

This model assumes that a horizontal-axis wind turbine has a high aspect ratio and a flow field that is comparable to that of a 2D airfoil. Consequently, lifting-line theory has been applied to compute the lift coefficient up to the stall angle of attack. But when the flow enters the fully developed stall zone (angle of attack higher than the angle of attack for which the maximum lift coefficients are observed (α_s)), the Viterna–Corrigan model is used to estimate the aerodynamic coefficients (equations (1.34) and (1.35)) (Bai & Wang, 2016; Martini, Contreras, Ilinca, et al., 2021).

$$C_l = \frac{1}{2} C_{d,max} \sin 2\alpha + \frac{K_L \cos^2 \alpha}{\sin \alpha} \tag{1.34}$$

$$C_d = C_{d,max} \sin^2 \alpha + K_B \cos \alpha \tag{1.35}$$

Where K_L and the K_D are:

$$K_L = \left[C_{l,s} - C_{d,max} \sin \alpha_s \cos \alpha_s\right] \frac{\sin \alpha_s}{\cos^2 \alpha_s} \tag{1.36}$$

$$K_D = \frac{C_{d,s} - C_{d,max} \sin^2 \alpha_s}{\cos \alpha_s} \tag{1.37}$$

$C_{l,s}$ and $C_{d,s}$ are, respectively, the lift and drag coefficients at an angle of attack α_s of 20º in which $C_{d,max}$ depends on the aspect ratio (AR), as follows (Bai & Wang, 2016; Martini, Contreras, Ilinca, et al., 2021):

$$C_{d,max} = \begin{cases} 1.11 + 0.018\,AR, & AR \leq 50 \\ 3.01, & AR > 50 \end{cases} \tag{1.38}$$

1.3.4 Spera's Correction

With Spera's correction, the effect of the turbulent wake is considered using an empirical relation between the angle of attack and the thrust coefficient (C_T) (Bai & Wang, 2016; Martini, Contreras, Ilinca, et al., 2021). The correlation is presented in equation (1.39):

$$C_T = \frac{\sigma_r (1-a)^2 C_x}{\sin^2 \phi} \tag{1.39}$$

If $C_T > 0.96$, the axial induction factor is:

$$a = 0.143 + \sqrt{0.0203 - 0.6427(0.889 - C_T)} \tag{1.40}$$

Whereas, if $C_T < 0.96$, then the axial induction factor is solved using Equation (1.31).

1.4 Estimating Power Loss in Wind Turbines under Icing Conditions

Numerous studies have examined ice formation and how ice accretion varies with meteorological parameters. Some examples can be found in references (Abbadi et al., 2020; Barber, Wang, Jafari, Chokani, & Abhari, 2010; Bhatia & Wahaibi, 2019; Homola, Virk, et al., 2010; Homola, Wallenius, et al., 2010; Ibrahim, Pope, & Muzychka, 2018; Jian Liang, Maolian Liu, Ruiqi Wang, & Wang, 2018; Jia Yi Jin & Virk, 2018, 2019; J. Y. Jin et al., 2020; Knobbe-Eschen et al., 2019; Li, Sun, et al., 2018; Li, Sun, Jiang, Yi, & Zhang, 2019; Liang, An, Liu, Wang, & Lv, 2019; L. Makkonen et al., 2018; Muhammad S. Virk et al., 2010a, 2010b; Pallarol, Sunden, & Wu, 2014; Son & Kim, 2020; Wang et al., 2020; YAN LI et al., 2017), and the consequences for energy production in (Barber et al., 2010; Homola, Virk, et al., 2010; Hu, Zhu, Chen, Shen, & Du, 2018; Reid, Baruzzi, Ozcer, Switchenko, & Habashi, 2013; Tabatabaei, Gantasala, & Cervantes, 2019). Better comprehension and quantification of losses due to icing are crucial for developers and investors in wind farms, who must accurately estimate a project's expected energy generation to quantify its risks and evaluate its financial viability (Barber et al., 2010). As a result, this section provides an overview of recent research on methodologies for estimating power loss under icing conditions using computational fluid dynamics (CFD). **APPENDIX A** summarizes the atmospheric conditions, simulation setup, and output parameters of the reviewed articles.

1.4.1 CFD – BEM Approach

This approach involves both methodologies described in Section 1.2 and Section 1.3. Here, the CFD is performed in two dimensions, specifically for each blade section. The results from the CFD simulation include ice accretion (ice shape, mass, thickness, among others) and aerodynamic coefficients (lift and drag). The latter is the input data for the BEM model. A more detailed explanation of the methodology can be found in Martini, Contreras, Ilinca, et al. (2021). Figure 1.6 presents a diagram that visualizes the implementation of this approach.

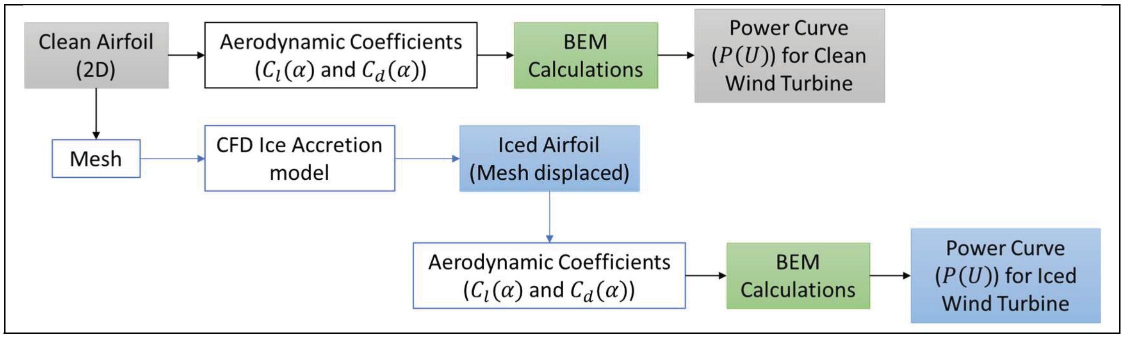

Figure 1.6 Diagram of CFD – BEM Method
Taken from Contreras Montoya et al. (2022)

One of the first studies involving the CFD–BEM methodology was made in 1998 by Jasinski et al. (1998). They conducted a study to estimate the effects of rime ice on the performance of a horizontal-axis wind turbine. They predicted four rime-ice accretions on the S809 wind turbine airfoil using the LEWICE code. The icing conditions used were a relative velocity of 65.2 m/s at an angle of attack of 5°, an air temperature of −10 °C, and LWC of 0.1 g/m3 at MVDs of 15 and 35 µm. The icing event durations were 3 and 7 h. The resulting iced profile combinations were tested in a wind tunnel to determine the lift, drag, and pitching-moment coefficients. Subsequently, the coefficients were used with the PROPID code to predict the effects of rime ice on a 450-kW, 28.7-m-diameter, three-bladed turbine operated under both stall-regulated and variable-speed/variable-pitch rotors. For the stall-regulated case, a rotor speed of 48 rpm and a blade pitch of 1.36° were employed, whereas for the variable-speed/variable-pitch case, a tip speed ratio of 7 and the same blade pitch angle were utilized.

The results obtained by Jasinski et al. (1998) showed performance losses ranging from 14.5% to 20% for the variable-speed/variable-pitch rotor at wind speeds below the rated power. A relatively small rime ice profile (0.025 c-long protrusion) produced significantly larger performance losses for the stall-regulated rotor. The rated peak power was exceeded by 16% for a 0.08-c-long rime-ice protrusion because, at high angles, the rime-ice shape behaved like a leading-edge flap, increasing the airfoil C_{lmax} and delaying stall. This might result in generator failure and excessive blade loads.

Dimitrova (2009) conducted a study to predict wind turbine energy losses under light icing conditions numerically. For this purpose, she developed the numerical model PROICET, which combines three software programs: CIRALIMA, XFOIL, and PROPID. Data from a Vestas V80 1.8 MW wind turbine with a NACA 63415 airfoil were used to validate the results obtained from the PROICET simulations. The atmospheric conditions were from Murdochville's site (Quebec), and some approximations were made, leading to the following conditions: LWC of 0.05 g/m^3, MVD of 20 μm, an airspeed of 8 m/s, temperatures of −6 and −2 °C, and two icing events of 6 and 4 h duration.

The simulations made by Dimitrova (2009) were at five different radial positions on the blade. For each section, CIRALIMA predicted the iced airfoil shape, XFOIL the lift and drag coefficients, and finally, PROPID estimated the wind turbine power curve. The author recommended replacing XFOIL with CFD simulations because it does not yield reliable results in cases involving large flow separation zones. Despite high uncertainty, the lift coefficient decreased by 30%, and the drag coefficient increased by 140%, values comparable to those reported in the literature. The deterioration in aerodynamic performance leads to an approximately 3.4% power loss. The reduction in annual energy production of the wind turbine due to light icing was estimated to be less than 1%. This is due to the assumed light ice conditions (low LWC and short event duration), which resulted in small ice accumulation on the blades (maximum of 1.33 kg/m at the blade tip).

Homola et al. (2012) conducted a numerical study of power performance losses on the NREL 5 MW wind turbine's blade under rime ice conditions. The atmospheric conditions were −10°C, an LWC of 0.22 g/m^3, and an MVD of 20 μm. For the CFD calculation, a structured-type numerical grid was used for each section (five in total), with a y+ value less than 1. The roughness height for the iced blade profiles was calculated according to Shin et al. (1991). The Spalart–Allmaras turbulence model was used. The results obtained by Homola et al. (2012) showed a gradual increase in the rate and shape of ice accretion as the blade moved from the root to the tip. This is due to a higher water-droplet collection efficiency along the blade as the relative velocity increases. They also found that the iced turbine incurred a significant penalty, resulting in a 27% power loss, and that the performance deterioration due to ice increased with increasing tip-speed ratios.

Homola et al. (2012) also evaluated the performance of the wind turbine using the actual turbine controller strategy to identify the operating point for both cases, i.e., a clean and iced rotor condition. The turbine generator controller was constructed to follow the torque-speed curve calculated by NREL. It consisted of a high tip speed ratio at start-up ($\lambda = 14$), which decreased linearly, and then was optimized for maximum power capture by following the torque–speed curve corresponding to a tip speed ratio of 7.55 (wind speed of 10 m/s) for the maximum power coefficient. By crossing both the controller curve and the rotor torque–speed curve in both cases, they found that the clean rotor's operating point matched the designed one. For the iced rotor, the operating point, at the same wind speed, was lower (rotor speed of 1.08 rad/s and $\lambda = 6.80$) than the optimal value.

To evaluate the improvement in this case, iced-rotor data were used to modify the turbine controller to adapt to the iced profiles; instead of operating along the torque-speed curve for the clean blade, the controller maintains the designed tip-speed ratio at each wind speed. Homola et al. (2012) demonstrated that modifying the control method can increase the energy capture of an iced turbine, resulting in a power gain for the improved iced case at wind speeds ranging from 7 to 13 m/s.

Turkia, Huttunen, et Wallenius (2013) developed a method for estimating wind turbine production losses due to icing. Three rime ice cases were simulated under the same meteorological conditions (−7 °C, a wind speed of 7 m/s, an LWC of 0.2 g/m^3, and an MVD of 25 μm). Still, the duration of the icing events varies across phases: the beginning of icing (19 min), a short icing event (3 h), and a long icing event (10 h). First, the authors used the code TURBICE to simulate the ice accretion on two blade sections (NACA 64618 airfoil). Then, they used ANSYS FLUENT to model the aerodynamic properties of the iced profiles, including lift and drag coefficients. Finally, power curves for a typical variable-speed pitch-controlled 3 MW wind turbine model, as well as for the same turbine with different ice accretions, were generated using the FAST software. They also considered the effect of roughness by analyzing the effect of small-scale surface roughness on the drag coefficient using the method described by Shin et al. (1991), and Bragg (1982).

As a result, Turkia et al. (2013) demonstrated that it is crucial to consider surface roughness when estimating the aerodynamic penalty caused by icing events, particularly for calculating the drag coefficient. Power production drops at the beginning of the icing event due to accumulated roughness. They also showed a relation between the ice mass and power production. As the mass increases, the power reduction was 18% for the short icing event and 24% for the long one.

Sagol (2014) compared both methods previously mentioned to predict ice shape and the corresponding rotor performance. The objective was to determine whether the improvement in the accuracy of the findings justifies the additional computational resources required by the Full CFD approach. The 2D and 3D analyses were performed in ANSYS FLUENT using the k-ω SST turbulence model. Here, the extended Messinger model was used to calculate ice accretion, and the roughness effect was accounted for. The reference turbine was the NREL Phase VI. Only one blade was simulated in 3D, adopting a periodic boundary condition and a rotating reference frame technique to account for the blade's rotation. The icing analyses were performed for a wind speed of 7 m/s, 60 min of ice accretion, an MVD of 20 µm, an LWC of 1 g/m^3, and a temperature of −15 °C.

According to the data obtained by Sagol (2014), the CFD–BEM analysis predicted a 40% power loss, whereas the full CFD analysis anticipated a 25% power loss. This was a foregone conclusion since the ice accumulation on the blade was most substantial when estimated using CFD–BEM. Although the full CFD approach entails substantially higher computational costs, 2D icing assessments may be inaccurate. Based on the clean-blade findings, the authors concluded that the entire CFD procedure yields more accurate results. Finally, using the CFD–BEM method, the ice shape and associated power loss are affected by neglecting the 3D features of the rotating flow.

Switchenko, Habashi, Reid, Ozcer, et Baruzzi (2014) simulated an industrial-scale wind turbine (WindPACT, a three-bladed 1.5 MW model) to demonstrate the impact of atmospheric icing using the CFD–BEM method. The selected icing event lasted 17 hours and was based on data collected at a wind farm located in Gaspé, Quebec, Canada. The FENSAP-ICE model was used for the 2D CFD calculations. The Spalart–Allmaras turbulence model was implemented, and for the ice accretion calculation, the authors utilized the multi-shot strategy available in the software. This strategy enables quasi-steady simulation of icing events by dividing the overall period of the event into shorter intervals during which ice builds on the blade. However, until the end of the period, the computational grid is not updated to account for ice accumulation (Switchenko et al., 2014). To reproduce the wind farm data, 34 atmospheric-icing shots were performed. The MVD and LWC were not measured, so three droplet sizes were assumed: 20, 50, and 200 µm. For the LWC, a constant value of 0.1 g/m^3 was used. Each shot was divided into 30-minute intervals, during which wind speed and temperature were adjusted based on on-site measurements. The impact of surface roughness was also investigated, with three values selected: 1, 3, and 10 mm.

When the authors Switchenko et al. (2014) compared the 2D CFD simulation of torque for the clean rotor with the 3D CFD simulation, they obtained good agreement at lower wind speeds for a fully attached flow. However, for wind speeds exceeding 15 m/s, the torque calculated using the 2D approach was underestimated due to larger flow-separation regions. Similar behaviour was documented by Reid et al. (2013). These discrepancies would affect the simulation of stall-regulated turbines more than those of pitch-regulated turbines.

Regarding the results for the iced rotor, as expected, Switchenko et al. (2014) found more accreted ice at the blade tip than at the blade root. After 17 hours, the ice shape at the tip developed a double-horn shape surrounding the stagnation region, with a maximum thickness of 21 cm and ice accretion at the trailing edge. The latter was associated with an increase in the pressure drag. Regarding the effect of roughness, they found that increasing surface roughness increases shear in the airflow, producing a separated region and subsequently lower power outputs; differences of more than 30% were observed. Regarding the influence of droplet size on power output, Switchenko et al. (2014) found that larger droplet sizes yielded lower power outputs due to increased ice accretion. Finally, Switchenko et al. (2014) compared the power loss and performance degradation to those measured on-site. A good agreement was found. However, when compared to the average power generated by the wind farm's turbines, the power produced by the simulated iced turbine was somewhat overpredicted during icing events of between 6 and 15 h.

Etemaddar et al. (2014) studied the atmospheric ice accumulation on a reference wind turbine blade (NREL 5 MW Virtual wind turbine with NACA 64618 airfoil) and its effect on the aerodynamic performance and structural response. Here, only the results related to aerodynamic performance will be presented. The authors evaluated atmospheric parameters (wind speed, LWC, MVD, and temperature) using the 2D software LEWICE for a 24-hour icing event. Each parameter changed hourly until the 24-hour mark was reached. The final iced profile was used as an input in Fluent to estimate the aerodynamic coefficients after icing, and the BEM code WT-Perf was used to quantify the degradation in performance curves (power and thrust coefficients as a function of TSR for four blade-pitch angles of 0°, 5°, 10°, and 15°). It is worth noting that the airfoil used corresponded to the outer part of the blade near the tip.

The domain was discretized using 2D quadrilateral elements for CFD modeling, employing an O-Grid topology. The relative wind speed was 50 m/s, the static temperature was −7 °C, a roughness height of 0.5 mm was considered, and the k-ε model was used as the turbulence model.

The results obtained by Etemaddar et al. (2014) showed that power loss increased by up to 35% below the rated wind speed, and the rated power shifted from 11 to 19 m/s. A similar behaviour at the operation point was obtained by Homola et al. (2012). Regarding the power coefficient, they found that the difference between clean and iced rotors increases with the TSR for a constant pitch angle. However, for constant TSRs, the difference decreases with increasing pitch angle. Based on these results, the authors concluded that the turbine could continue to operate at below-rated wind speeds under icing conditions. However, at wind speeds above the rated limit, the thrust on the iced turbine would be substantially higher than the nominal value, posing a risk to the structural components. Hence, they recommend two possible solutions: shut down the wind turbine or reduce the cut-out wind speed.

In 2016, (Yirtici, Tuncer, & Ozgen) carried out a study to determine the performance losses due to ice accretion on the Aeolos-H 30 kW wind turbine. The 2D ice accretion prediction tool employed the Hess–Smith Panel method, the extended Messinger model for thermodynamic balance, and the Lagrangian approach to determine the collection efficiency. The effects of splash and break-up were taken into consideration. The potential flow solver XFOIL was used to get the aerodynamic loads on each airfoil for the BEM implementation. The predicted ice shapes were validated with experimental and numerical data for two airfoils (NACA 64618 and S809). The results for this first part were in good agreement with those from the literature.

The power loss was analyzed at an 11 m/s wind speed and 120 RPM for a selected icing condition (LWC = 0.05 g/m3, MVD = 27 µm, temperature = −8 °C, and exposure time = 3 hours). The results from Yirtici et al. (2016) indicate that at wind speeds greater than 12 m/s, the XFOIL solution slightly underpredicted the power production compared to experimental data. Finally, the power loss during this icing event was 24%, consistent with similar studies.

W. Han et al. (2018) carried out a CFD simulation based on the Dispersed Multiphase Droplet Model (DMP), available in STAR-CCM+, to predict ice formation along the blade tip of an airfoil's leading edge. The simulation focused on the rime ice, and the profile analysis was divided into five cases corresponding to planes along the blade. The airfoil selected was the NACA 64618 used in the NREL 5-MW wind turbine. The meteorological conditions were −8 °C, a droplet size of 25 µm, and an LWC of 0.22 g/m^3. The authors incorporate the effect of roughness, utilizing the Shin et al. (1991) model and the Bragg (1982) method. The ice accretion was built by updating the mesh deformation for each time step. However, this remeshing process can cause issues with reliability and convergence. Thus, they conducted a 2D aerodynamic performance simulation using the final iced airfoil shape obtained from the ice accretion simulation. The lift and drag coefficients were estimated for all five cases, and power calculations were performed using BEM; for this, the BLADED software was employed. The results showed that ice formation on the blade tip of the airfoil's leading edge reduced wind turbine power performance by 8 to 29% at lower-than-rated wind speeds, indicating an evident correlation between the two parameters. However, at wind speeds above the rated value, only a slight power loss was attributable to the blade pitch control system, which stabilized power output. They also found that increasing the angle of attack (AoA) enhanced the rime ice accretion area while decreasing the lift coefficient (significantly at AoA ≥ 8°).

Finally, W. Han et al. (2018) suggested that aerodynamic performance control by pitch angle modification is possible at higher-than-rated wind speeds, even if ice has formed on the blade's leading edge, because it will maintain the power steady. Nevertheless, maximum wind turbine efficiency may be achieved at wind speeds below the rated value by integrating variable-speed operation via generator torque control.

Ebrahimi (2018) investigated the aerodynamic loads and energy losses of a small wind turbine (a 600 kW three-bladed turbine with an S816 airfoil blade and a 47 m diameter) under both wet and dry icing conditions. The wet regime was established with an MVD of 38.3 µm, an LWC of 0.218 g/m^3, a temperature of −1.4 °C, and an event duration of 360 s. The dry regime was set up with an MVD of 40.5 µm, an LWC of 0.242 g/m3, a temperature of −5.7 °C, and an event duration of 264 s. The ice accretion simulations were carried out using LEWICE for three-blade cross-sections. The airflow simulations were performed using ANSYS FLUENT with the k-ω SST turbulence model at three wind speeds (9.2, 18.1, and 27.1 m/s). The production losses were calculated using the BEM theory. For the latter, a tip-speed ratio of 7 was selected.

In Ebrahimi (2018), under the wet regime, the ice shape (in the form of a horn) accreted on the airfoil significantly affected the drag coefficient, which became excessively high relative to the lift, resulting in rotor stoppage. Under a dry regime, performance declined by approximately 30%.

Zanon et al. (2018) applied the CFD–BEM methodology to predict the performance of a reference turbine (NREL 5 MW) during and after an icing event (8 hours), including the possible increase in energy harnessing according to different operational strategies. The ice accretion was computed using ICEAC2D, while the airflow analysis was performed in ANSYS CFX with the k-ω SST turbulence model. The BEM code used was WT_Perf. The wind turbine's performance was evaluated at a wind speed of 10 m/s. Two icing conditions were evaluated: rime ice (20 μm, 0.22 g/m^3, and −10 °C) and glaze ice (14.36 μm, 0.1605 g/m^3, and −2 °C). Three operational strategies were evaluated for rime ice, whereas only one was evaluated for glaze ice.

The first operational strategy controlled rotational speed by following a precomputed torque–speed controller curve. It allowed the set-up of the TSR for the rime ice at 7.68 (IC-1-1) and 7.32 (IC-2-1) for the glaze ice. Therefore, this strategy was considered the baseline. The second operational strategy was the same as that proposed by Homola et al. (2012), which consisted of forcing the optimum TSR (7.55), which was evaluated for the rime ice (IC-1-2). Finally, the third operational strategy was to lower the turbine's TSR to reduce ice accumulation at the leading edge, thus delaying turbine shutdown and conserving the blade's aerodynamic performance. It was evaluated for the rime ice only (IC-1-3).

The results of Zanon et al. (2018) showed that during the icing event, the second strategy led to a negligible increase in wind energy (+0.16%). In comparison, the third strategy resulted in an 8.66% reduction in wind energy compared to the baseline. However, following the icing event, the third strategy performed best (+5.8%), whereas the second strategy performed worst (−3.0%). This finding was contrary to the results presented by Homola et al. (2012), which may be associated with the duration of the icing event considered by each author.

Continuing the research carried out by Yirtici et al. (2016), Yirtici, Ozgen, et Tuncer (2019) investigated the ice-induced power losses under different icing conditions on horizontal-axis wind turbines. Two turbines were used: the Aeolos-H 30 kW and the NREL 5 MW. The methodology was the same as described in Yirtici et al. (2016), except that in this case a second tool for the BEM implementation was used: the open-source Navier–Stokes solver SU2 with the k-ω SST turbulence model.

For the Aeolos-H 30 kW wind turbine, Yirtici, Ozgen, et al. (2019) simulated different icing conditions for LWC (0.05, 0.15, and 0.25 g/m^3), MVD (18, 27, and 35 μm), temperature (−5, −10, and −15 °C), and time (20, 40, 60, and 80 min) to see the effect on the power production. The operational conditions considered for the turbine were the same as in their previous work (Yirtici et al., 2016). They found that rime ice forms close to the hub, while glaze ice forms at the blade's tip. Studying the influence of MVD and temperature, they found that these parameters do not affect ice accretion as much as LWC. The predicted power losses ranged from 18% to 31%, with the maximum value corresponding to the higher LWC and longer time exposure to the icing event.

For the NREL 5 MW, Yirtici, Ozgen, et al. (2019) used the same conditions as Homola et al. (2012), resulting in a 17% power loss, which differs from the 27% power loss reported by Homola et al. (2012). This discrepancy was attributable to the different assumptions made in the two studies. For example, Homola et al. (2012) neglected the rotational effects and fixed the Reynolds number.

In conditions similar to those in Zanon et al. (2018), Hildebrandt et Sun (2021) conducted a comparative study of two operational strategies in terms of their overall influence on power production. The first strategy was powering through an icing event. In this case, wind speed was used to determine the airfoil model's angle of attack and relative airspeed. The second strategy involved stopping the turbine during the icing event and then resuming operation afterward. In this case, the rotor speed and the angle of attack were zero. The reference turbine (WindPACT 1.5 MW with a NACA 64618 airfoil) was evaluated for five 2-h icing events under varying atmospheric conditions. The 2D ice accretion was simulated with FENSAP-ICE and concentrated in the outer 30% of the blade. In the Droplets module (DROP3D), the authors utilized the Langmuir D distribution to enhance the accuracy of the collection efficiency. In the ice accretion (ICE3D) model, small-scale surface roughness was calculated using the Shin et al. (1991) method, and the multi-shot method was employed. The power curves for each icing event were generated using the Xturb-PSU code, which took the aerodynamic coefficients calculated in FENSAP-ICE as input.

The atmospheric parameters were: two wind speeds, 8 and 12 m/s; two temperatures, −8 and −1 °C; two LWC values, 0.2 and 0.48 g/m^3; and two MVD values, 30 and 33 µm. When validating the methodology, Hildebrandt et Sun (2021) found that the power curve was underestimated by around 6% in the above-rate wind zone.

In the case of short icing events, suspending the turbines reduces ice accretion. However, compared with powering through the event, the impact on power production was smaller. The former was associated with the pronounced effect of surface roughness from ice-crystal beading on blade aerodynamics, which occurs whether the blades are rotating or not. Still, for a severe short icing event with below-rated wind speeds, stopping the turbine during the event resulted in a 4.3% improvement in power production.

In summary, the simplicity and numerical stability of the setup are the significant benefits of the CFD–BEM method. However, a limitation of 2D CFD simulations is their inability to account for flow in the blade-span direction. This may be critical as other dynamic phenomena are expected to occur, potentially influencing the results (J. Y. Jin et al., 2020). For example, in Homola et al. (2012), the rotational effects on aerodynamic performance were not simplified, resulting in an underestimation of the lift coefficient. A similar phenomenon occurs with the BEM model, which can be unreliable when flow separation zones are significant. To conclude, this methodology can yield low-accuracy results and tends to underestimate the aerodynamic coefficients.

1.4.2 Full CFD Approach

Despite their enhanced accuracy, the adoption of fully CFD-based methods has been far less common; the primary issue is the high computational cost, which limits an interactive design process. This subsection presents an overview of recent studies on wind turbines operating under icing conditions using full 3D CFD. Each reviewed contribution briefly defines the computational domain, summarizes the essential points of the CFD study, and highlights the principal conclusions obtained. Figure 1.7 presents a diagram that visualizes the implementation of this approach.

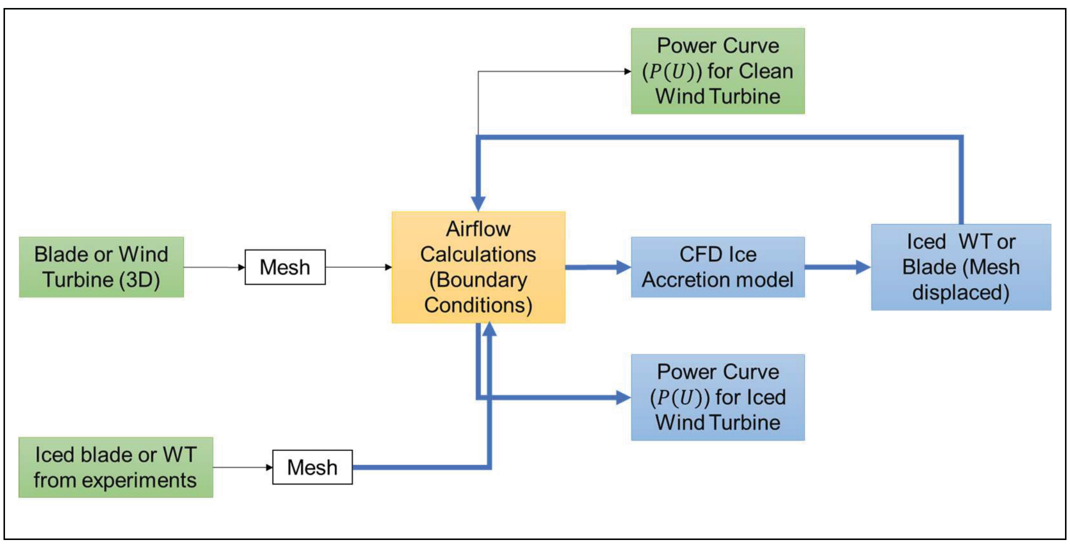

Figure 1.7 Diagram of Full CFD Method

Barber et al. (2010) experimentally and computationally studied the icing effects on the performance and aerodynamics of a three-bladed wind turbine. The scale-model wind turbine matched the NREL Phase VI rotor, consisting of two blades with the S809 profile. The icing effects were investigated by attaching simulated and observed ice shapes to the blades. The simulated ice shapes were obtained using the LEWICE software. The parameters used to predict the icing profiles were turbine diameter = 44 m; rotational speed = 15 rpm; wind speed = 4 m/s; temperature = −6 °C; LWC = 0.1 g/m3; MVD = 35 µm; and icing duration = 10 hours. With these data, six cases were studied: three cases with the same sharp ice shape at the leading edge but varying its span-wise distribution, considering 100%, 25%, and 5% location; two cases with a sawtooth ice shape, one located at the 90% of the span and the other between 80% and 95% of the span; and one extreme ice shape located at the 100% of the span.

The experimental test used a 0.3 m-diameter wind turbine model mounted on a carriage that moved through a water channel. The turbine's rotational speed was maintained at 800 rpm; by adjusting the carriage velocity between 1.5 and 2.8 m/s, the tip speed ratio (TSR) varied from 5 to 8. The experiments were conducted in a water tunnel by Barber et al. (2010), as the dynamically scaled model in their study more accurately replicated the full-scale Reynolds number than a wind tunnel. However, the measured power coefficient was corrected to account for the Reynolds-number difference between the sub-scale model and the full-scale turbine. Barber et al. (2010) used a single blade immersed in a domain consisting of a 120° arc-shaped region of 4R radius and length for the computational analysis. An unstructured tetrahedral mesh with 10 prism layers on the blade surface was constructed. The Y+ value on the blade surface ranged from 30 to 60. Accordingly, the k-ε turbulence model with a scalable wall function was selected. The boundary conditions included: velocity at the inlet (1.6–3.1 m/s), outlet pressure, an opening boundary with constant pressure at the top, free slip at the bottom wall, no-slip wall at the blade, and periodic boundaries with a rotational speed of 800 rpm.

In their experiments, Barber et al. (2010) demonstrate that the effect of icing on the power coefficient is greater at high TSRs. This was expected, given losses at high TSRs due to the blades' aerodynamic drag, which is altered by the ice shapes. They also found that ice in the last 25% of the span significantly affects performance, with the impact increasing in the last 5% of the blade's length, reducing the power coefficient by approximately 29%. They found a major effect on the power coefficient for the extreme ice shape. In this case, no power was generated at TSRs above 6, and the power at TSRs below 6 was smaller than in the other cases. From the Annual Energy Production (AEP) perspective, Barber et al. (2010) considered icing conditions for two months, obtaining an AEP reduction of up to 2% and 17% in extreme icing conditions. The CFD simulation results agreed well with the experimental data. However, the estimated power loss under extreme conditions was 100%. The analysis of streamlines explained this. In this case, many flow separation zones were observed across the span.

Reid et al. (2013) presented a numerical analysis of the performance degradation of a wind turbine operating under icing conditions using FENSAP-ICE software. They considered the NREL Phase VI rotor geometry, which features two tapered, twisted blades with an S809 airfoil, each 5 m in span. The computational domain consisted of a cylinder with a rotating frame of reference, allowing for steady-state modeling of rotating blades. The turbulence model was the Spalart–Allmaras model. Four icing conditions were evaluated to consider glaze and rime ice. Two wind speeds and temperatures were considered, 7 and 22 m/s, and −3 °C and −15 °C, respectively. The MVD and LWC were constant in all the cases and were 20 μm and 0.5 g/m^3, respectively. Three icing durations were considered: 10, 20, and 60 minutes.

Compared with experimental data from the clean turbine, the FENSAP-ICE calculations slightly overestimated turbine performance at a wind speed of 12 m/s. In the airflow simulations, this was related to a stall delay, which resulted in a shorter separation zone and higher torque levels Reid et al. (2013). However, the simulations agreed well with the experimental results for a wind speed of 7 m/s (fully attached flow) and 22 m/s (fully separated flow). Regarding the iced turbine, the authors found that ice was concentrated at the leading edge when rime ice was present. In contrast, the glaze ice (at a higher temperature) allowed the water to run back along the surface in the flow direction, resulting in a larger zone of contamination but with a lower ice thickness.

The authors observed power losses above 50% compared to a clean turbine. The losses are more severe in cases with an icing duration of 60 minutes, and wind speeds between 12 and 15 m/s, and are least severe at wind speeds above 20 m/s. This was explained by the fact that the ice shape could not expand the area of the separated flow due to the rime ice, which increased flow acceleration at the leading edge; the rime ice conditions resulted in lower power losses than the glaze ice conditions.

Shu et al. (2017) proposed a 3D ice accretion wind turbine model to simulate glaze ice to study the icing characteristics and output of a small horizontal-axis wind turbine (Twisted blade with a NACA 4409 airfoil along the blade). The simulation was performed under the icing test conditions using ANSYS FLUENT. The velocity and collision efficiency were obtained with the Eulerian method and a UDS (User-defined scalar) function. Subsequently, the ice accretion computation was performed in MATLAB using heat and mass transfer, and GAMBIT was used to generate the mesh. In this case, the authors also used a single blade with periodic conditions and a multiple reference frame (MRF) to simulate blade rotation. The standard k-ε turbulence model was used. The icing conditions were an LWC of 0.71 g/m^3, an MVD of 20 µm, and three temperatures (−3, −6, and −8 °C), as well as three wind speeds (5, 6, and 8 m/s).

The results obtained by Shu et al. (2017) showed that ice accretion reduces the turbine's rotation speed and load power. As a result, ice load has a greater impact on rotor performance than aerodynamic characteristic degradation. Additionally, as observed in other studies, ice mass increased linearly from the root to the tip and accumulated at the leading edge. They also found that the simulation predicted more severe ice at higher wind speeds and lower temperatures than the test did.

Continuing on this topic, Shu et al. (2018) carried out a steady-state 3D numerical simulation of a wind turbine rotor using a commercial CFD solver (ANSYS FLUENT) to estimate the blade's aerodynamic performance after icing. The multiple reference frame (MRF) model, Reynolds–Averaged Navier–Stokes equations, and k-ω SST turbulence model were employed. The computational domain consisted of two cylinders: the internal domain (rotating zone) and the external domain (stationary zone), which simulated the environmental conditions. A hybrid mesh was used. The internal domain was represented by unstructured tetrahedral cells, whereas the external domain was represented by a structured grid of hexahedral cells. The CFD results agreed well with the experimental results for clean and rime-iced rotors at rated wind speed but overestimated the values for glaze-iced rotors at high wind speeds. Under icing conditions, the rotor speed and output power of wind turbines decline sharply as wind speed increases.

The maximum power losses were 63% and 80% at wind speeds of 13 m/s and 14 m/s, respectively.

Moreover, the ice effect was smaller on the power coefficient at lower tip speed ratios and became more pronounced with increasing tip speed ratios (between 26% and 53% for tip speed ratios of 7 to 8). Additionally, ice shapes primarily affect pressure distribution along the leading edge of airfoils, significantly reducing normal and tangential forces at radial positions of approximately 62% to 89%. They also found that as wind speed increases, the impact of blade icing on pressure distributions and aerodynamic force loss becomes more pronounced, and that glaze has a greater effect on aerodynamic force. When influenced by ice shape, blades are more likely to stall at the same wind speed, resulting in greater reductions in lift. Additionally, flow separation around the frozen blade is more severe at higher wind speeds, leading to greater momentum and frictional losses, particularly for glaze ice.

It is worth noting that Shu et al. (2018) used experimental data to determine the ice shape on each section of the blade profile. The blade geometry was defined for rime- and glaze-ice conditions based on this information. An irregular horn and protrusion shape characterized the last one. This allowed the simulation to be reduced to an aerodynamic analysis, without considering the physics underlying the icing phenomenon.

Hu et al. (2018) simulated the rime ice on the rotating NREL Phase VI stall-regulated turbine. The icing event was treated as a quasi-steady process, and to calculate the rotating airflow, the moving reference frame (MRF) available in ANSYS FLUENT was used. In addition, the k-ω SST model was used as the turbulence model. The authors used the Eulerian method in conjunction with an additional UDS (user-defined scalar) function to estimate the collection efficiency. They used the dynamic mesh technique in ANSYS FLUENT to build the ice shape (see Hu et al. (2018) for further details). The icing conditions were a wind speed of 7 m/s, a rotational speed of 72 RPM, an MVD of 20 μm, an LWC of 1 g/m^3, a temperature of −15 °C, and an icing duration of 30 minutes. The boundary conditions consisted of a velocity inlet, a pressure outlet, and a periodic boundary condition throughout the domain. The blade and hub were treated as a moving rotational wall.

Based on the setup described above, Hu et al. (2018) found that ice accreted on the blade's leading edge and that the ice thickness and mass increased along the radial direction. The increase in the ice mass was up to 105%. The power decreased by up to 13%, primarily in the outer-blade region.

Tabatabaei et al. (2019) conducted a study comparing the CFD–BEM method with the Full CFD method. The computation was performed on the full-scale NREL 5 MW rotor, which has a rated wind speed of 11.4 m/s and a rotational speed of 12.1 RPM. In the computational domain for the CFD–BEM method, they used a discrete Fourier sine series to approximate an ice shape on the NACA 64618 airfoil, based on iced profiles available in the literature. In this case, a structured grid was used. The 2D simulations were performed for 15 airfoil sections. Because the airfoil rotation was not included in these simulations, the airfoil's relative velocity was considered. For the 3D simulations, the computational domain was a 120° pie-shaped domain, with a structured grid and periodic boundaries in the circumferential direction. Two domains were created to account for the rotation: the inner and far-field domains. The software used was ANSYS CFX, and the k-ω shear stress transport (SST) model was used as a turbulence model.

The total power calculated by the CFD–BEM method and the Full CFD for the clean rotor were in close agreement. However, the total power was underestimated by 28% for the iced rotor by the CFD–BEM method. In conclusion, the power coefficient loss due to ice was 32%, and the thrust coefficient was reduced by 11%. Furthermore, the power loss became more significant when the ice horn height exceeded 8% of the chord length.

Finally, for the Full CFD methodology, it is essential to note that, to date, the analyses have been conducted in a quasi-steady state. Therefore, uncertainty remains regarding how the behaviour of the coupling phenomenon would be if analyzed from a transient perspective.

Furthermore, the studies have been limited to a single rotating blade, assuming that ice accumulates in the same way on all the blades. It would be useful to determine whether this assumption is correct or whether there is a difference that could affect turbine power output.

1.4.3 Alternative Methods

In 2014, Lamraoui, Fortin, Benoit, Perron, et Masson (2014) proposed a new method based on a rotating helicopter blade analogy. In this study, Lamraoui et al. (2014) located the glaze and rime ice on the wind turbine blade (a V80-1.8 MW Vestas, with a diameter of 80 m, a rated wind speed of 14 m/s, a minimum wind speed of 4 m/s, a rotational speed of 16 RPM, a variable pitch angle, and a NACA 63415 airfoil). They identified the critical zones responsible for significant power loss. For this purpose, they used the experimental results obtained for a helicopter's blade (Fortin & Perron, 2009a). This approach introduced two concepts: The **freezing fraction** and the **power loss factor**. The **freezing fraction** indicates the rate at which supercooled water freezes upon impact with a solid surface; if equal to 1, it indicates complete freezing of liquid water and is therefore associated with rime ice. According to Fortin et Perron (2009a), the critical freezing fraction for a helicopter can be estimated as 0.88, which corresponds to a double-horn ice shape, characteristic of glaze ice.

On the other hand, the **power loss factor** quantifies the normalized changes in power requirements for rotor-blade helicopters under icing conditions. In the event of ice accumulation, the helicopter's rotor requires more power to maintain the rotational frequency, unlike in normal wind turbine operation, where it reduces expected power generation. To determine the power coefficient under icing conditions, the power coefficient for clean wind turbine blades was divided by the power loss factor. It is important to mention that this method does not consider the evaporation and sublimation of liquid water masses when calculating the ice mass's rate of accumulation.

Although the operation of a helicopter rotor and a wind turbine rotor differs, this approach enabled us to identify the parameters that maintain the freezing fraction (Lamraoui et al., 2014).

An MVD of 18 µm, different temperatures (−2.6, −4.5, −12, and −20 °C), and LWCs (0.04, 0.03, 0.2, and 0.36 g/m^3) were evaluated. From this evaluation, the parameter that maintained the freezing fraction at 0.88, and consequently maximum power loss, was an LWC of 0.2 g/m^3, a temperature of −12 °C, and the location was between 93% and 96% of the blade's radius. At this point, the power loss was estimated at approximately 40%. Compared with a temperature of −13.5 °C (rime ice along the entire blade), the power loss was slightly lower. As a result, even small temperature changes can alter power loss.

Finally, Lamraoui et al. (2014) found that the maximum mass rate and thickness of ice were located at 70% of the blade's radius and showed a strong dependence on LWC; higher values of LWC resulted in higher accumulations of ice and a shorter required icing duration to reach higher power loss values. Power degradation was governed by ice thickness across the entire blade, regardless of ice type.

1.4.4 Conclusions

Power losses are observed as soon as the icing conditions start. Consequently, annual production losses will depend on the intensity, duration, and frequency of the icing events. This literature review summarizes that both the CFD–BEM and Full CFD methodologies estimated power losses of between 8% and 30%. However, some discrepancies were observed, which could be attributed to assumptions in the CFD–BEM methodology and underscore the importance of considering the complex three-dimensional flow around the iced airfoil. Table 1.1 summarizes the advantages and disadvantages of the methodologies addressed in this section.

Simulation is an important verification tool that is less expensive than experimental testing and enables the study of multiple scenarios. However, one difficulty associated with full CFD simulations is their high computational cost. This review indicates that most studies have been conducted on a single blade or on blade sections, rather than on the entire turbine. Furthermore, some assumptions were made in the analysis: periodic boundary conditions and the assumption that the turbine blades behave identically regardless of their position. Another issue highlighted by Sagol (2014) and Tabatabaei et al. (2019) is that a lack of experimental data under real icing conditions makes it difficult to validate the accuracy of CFD solutions. Currently, validation is performed for the aerodynamic analysis under ice-free conditions, for which experimental data are available.

Table 1.1 Summary of advantages and disadvantages of BEM-CFD and Full CFD methodologies
Taken from Contreras Montoya et al. (2022)

Advantages	**Disadvantages**
BEM–CFD	
• Simplicity and numerical stability. • Low computational cost. • More interactive design process: Allows the study of multiple scenarios in less time. • Less expensive than experiments. • Good agreement with the experiments, especially with the ice shape.	• Fails to include information about the flow in the blade-span direction, as separation zones are neglected. • Underestimation of aerodynamic coefficients (lift and drag) and the power output. • Low accuracy: Depends on the software used for the BEM calculations. • Simulations are made only in Steady-State. • Extrapolation of the aerodynamic coefficients versus angle of attack.
Full CFD	
• Takes into account the flow in the span's z-direction. • High accuracy when compared to experimental data. • Possibility to carry out transient simulations. • Less expensive than experiments. • Multiple turbulence models available. • The ice break-up and shedding can be considered.	• HIGH CPU requirements. • High computational cost. • Overestimation of wind performance at wind speeds with the presence of transition zones in the boundary layer.

One factor that influences the CFD simulation process is the type of accreted ice. Most of the studies presented here concentrate on rime ice. It assumes that water droplets striking the blade surface freeze immediately due to rapid heat dissipation, thereby leading to ice accumulation.

However, the problem becomes more complex with glaze ice, as it involves an ice layer and a water film on the blade surface.

Most airflow simulations used the Spalart–Allmaras turbulence model due to its efficiency and low computational cost. However, when simulating in three dimensions (Full CFD), this model lacks accuracy when computing the stall phenomenon.

Likewise, power loss will depend on the type of ice. For example, in the case of rime ice, most of the losses are due to an increase in the drag coefficient. However, glaze ice is less studied due to its complexity and discrepancies between numerical predictions and experimental data. Thus, for the latter, its effect has not been widely documented.

Most available BEM codes use drag and lift coefficients as functions of angle of attack as input data. In all simulations, these coefficients were extrapolated to angles of attack beyond 15 °, as the calculations focused on angles of attack between 0° and 15°. However, the BEM model requires a more extensive range (±180°) to be considered. Therefore, some extrapolations were performed by hand by comparing similar curves obtained in the literature (Turkia et al., 2013). At the same time, other authors used models or modifications such as the Tagler model (W. Han et al., 2018) or the Viterna extrapolation method (Etemaddar et al., 2014; Sagol, 2014).

None of the simulations considered ice break-up or shedding. It was assumed that all the accumulated ice remained on the blade during the entire icing event. In reality, this does not happen, as some ice fragments can detach due to the turbine's rotation. Therefore, when validating simulation results against empirical data, it is essential to account for these factors.

The simulations were carried out in a stationary or quasi-stationary state, which also introduces inaccuracy in the calculations, as the icing phenomenon and turbine operation are transitory processes.

Currently, no sensors correctly measure LWC and MVD, which are fundamental parameters for numerical simulations. This lack of information also leads to significant uncertainty in the computationally generated results, as we resort to empirical correlations or to reusing values explored by other authors.

Ice growth was calculated only for the last 30–40% of the blade, as this region is estimated to most significantly influence turbine performance.

To conclude, progress has been made in applying CFD to understand the icing phenomenon and its impact on wind turbines' performance. However, there is still work to be done, for example, simulating the complete turbine using a transient methodology such as "sliding mesh," which is available in Ansys, to predict ice growth on each blade of the wind turbine and estimate its performance. This could help improve understanding of how icing affects the wind turbine, not only the blade's profile.

1.5 Dimensional Analysis

Dimensional analysis is a robust method used across engineering disciplines to analyze and interpret relationships among physical quantities and dimensionless variables. Specifically, it aids in describing physical processes through non-dimensional quantities (Volker Simon & Weigand, 2017).

The application of dimensional analysis eliminates irrelevant information from the regarded problem, thereby decreasing the number of variables and the complexity of experimental factors influencing a specific physical phenomenon through a dimensionally consistent equation (White, 2008; Zohuri, 2017), which enhances understanding of the fundamental physical mechanisms (Volker Simon & Weigand, 2017). Suppose a phenomenon depends on n-dimensional variables. In that case, dimensional analysis reduces the problem to k *dimensionless* variables. The reduction $n - k$ will depend on the problem's complexity and the number of fundamental dimensions (mass M or force F, length L, time T, and temperature Θ) that govern the problem (White, 2008; Zohuri, 2017).

Dimensional analysis has several side benefits, such as (White, 2008):

- Reduce the number of variables, resulting in significant time and resource savings when designing and planning an experiment or theory.
- It suggests dimensionless approaches to writing equations, eliminating the need for time-consuming computer analysis and experiments to find solutions. Correlations between multiple-dimensional variables are reduced to a single relation between dimensionless variables.
- It suggests variables that can be disregarded in the analysis as less significant; sometimes, dimensional analysis will eliminate a variable or a group of variables that are less influential under specific conditions.
- Often, it gives a great deal of insight into the form of the physical relationship we are trying to study.
- It provides scaling laws that can convert data from a cheap, small model to design information for an expensive, large prototype.

One of the most important principles to consider in dimensional analysis is **dimensional homogeneity (PDH)**. It states (White, 2008; Zohuri, 2017) "If an equation truly expresses a proper relationship between variables in a physical process, it will be **dimensionally homogeneous**; that is, each of its additive terms will have the same dimensions".

There are several methods to reduce the number of dimensional variables into smaller dimensionless groups. However, this thesis will focus on the **$\boldsymbol{\pi}$ (Pi) Theorem**, also called the **Buckingham-$\boldsymbol{\pi}$ Theorem.** The name "Pi" comes from the mathematical notation π, meaning a product of variables. The dimensionless groups found from the theorem are power products denoted by π_1, π_2, π_3, etc. According to White (2008) and Zohuri (2017), six steps are involved:

1) List and count the n variables involved in the problem.
2) List the dimensions of each variable according to MLTΘ or FLTΘ.
3) Find j. Initially, j can be assumed to equal the number of dimensions.
4) Select j scaling parameters that do not form a π product. These parameters must be sufficiently general and include all dimensions of the problem, as they will appear in every π group.
5) Add another variable to the j repeating variables and form a power product. Algebraically find the exponents that make the product dimensionless. Try to have the **dependent variables** (in this case, power loss) appear in the numerator and only one of the π products. Repeat this step, adding one new variable each time, and all the desired π products will be found.
6) Write the final dimensionless function and verify that all π groups are dimensionless.

As shown above, the π theorem provides a methodology for calculating dimensionless parameters, but it says nothing about their physical significance (Coderoni, 2020). Therefore, it is essential to clearly understand the physical phenomenon to interpret and correct the dimensionless groups.

1.5.1 Applications of the Buckingham π Theorem on Wind Turbines

As mentioned earlier, the Buckingham π Theorem has been applied in various fields of study, including mechanics, fluid mechanics, thermodynamics, electricity, and optics. In the case of wind energy, the dimensional analysis method has been used in wind turbine scaling studies (Iswahyudi, Sutrisno, & Prajitno, 2019; Sutrisno, Iswahyudi, & Wibowo, 2018). In this section, a brief overview of the application of this theorem to wind turbines is provided.

Ahmed H. Abdulaziz, Adel M. Elsabbagh, et Akl (2015) conducted a study to develop an approach that utilizes measurements and analysis of scaled-down models to predict the performance of full-scale horizontal-axis wind turbine blades. In this study, the authors employed the Buckingham π Theorem to predict the static and dynamic structural responses of large wind turbine blades using scaled-down models. The predictions were enabled by dimensionless groups developed, which correlated the behaviour of the scaled-down models with that of the full-scale blades. The variables correlated in the research included those that influence the static and dynamic behaviours of wind turbines, such as elastic modulus, moment of inertia, transverse force, cross-sectional area, blade length, and material density.

Ahmed H. Abdulaziz et al. (2015) used the previously defined variables to formulate dimensionless groups that correlate the tip deflections of the blades under steady aerodynamic forces. By establishing these correlations, the authors sought to predict the performance of full-scale blades using experimental data from the scaled models. The validation process consisted of three steps. The first involved developing a finite element model (FEM) to enable detailed analysis of the blade's structural behaviour under varying conditions. The second step consisted of validating the FEM model. In this case, the authors used a blade fabricated with a 3D printer and subjected it to various vibrations. The dynamic loads generated on the blade were recorded, and the frequencies at which the blade vibrated were identified as its natural frequencies. The comparison of the experimental and the numerical data yielded quite satisfactory results for the authors. Consequently, the FEM simulations were developed for a full-scale blade.

Finally, the third step used the natural frequencies obtained from the FEM model of the full-scale blade, together with the dimensionless groups derived from the π theorem, to predict the natural frequencies of the full-scale blade and thus its dynamic and static performance. Ahmed H. Abdulaziz et al. (2015) reported a good agreement between the predicted natural frequencies of the full-scale blade and the numerical solutions from the FEM analysis. This indicated that predictions from the scaled-down models were reliable and closely matched the full-scale blade's actual behaviour. Overall, the methodology proposed by Ahmed H. Abdulaziz et al. (2015) demonstrated a strong effectiveness and correlation between the predicted and actual performance of the blade.

In contrast to the previous case, this research by Sutrisno et al. (2018) did not focus only on one blade but on the entire turbine. Regarding the methodology employed, the authors developed an equation that presents the torque as a function of the turbine diameter, utilizing the TSR. Specifically, the authors propose an equation to estimate turbine power as a function of the TSR. Sutrisno et al. (2018) conducted a study on the power prediction of real-scale wind turbines using wind-tunnel torque measurements from small-scale models. This research explores the aerodynamic characteristics of HAWT and proposes the integration of small-scale experiments into large-scale applications.

The authors used the π theorem to analyze the torque measurements from two small turbines, with diameters of 0.14 and 0.19 m. The variables used to develop the dimensionless groups were the rotor diameter, air density, and wind speed. Through the analysis of new dimensionless groups, the authors were able to simplify complex relationships into simpler forms and establish similarities between small-scale and large-scale turbines. To validate the methodology, Sutrisno et al. (2018) conducted torque measurements on the two small turbines. With the collected data, they derived a correlation equation between the torque produced by the small turbines to their rotor diameters. Once the correlation was established, the authors applied the equation to predict the torque for a larger turbine with a radius of 1,2 m.

Sutrisno et al. (2018) reported that the errors between the predictions made using the proposed approach and the field measurements of the large-scale turbine were lower than expected, i.e., the error in the field measurements was about 161 Watts, while the maximum error from the new method was 92 Watts at a wind speed of 10 m/s. This indicates that this method provided a more accurate estimation of the power output for the large-scale turbine than the field measurements, illustrating the efficacy of the dimensional analysis methodology in predicting turbine performance. However, the authors emphasize that the scaling factor should be within a reasonable range, in this study was 8.57; and that the power coefficient was estimated consistently across a specific range of wind speeds (5 to 12 m/s) for accurate predictions.

In another study conducted by Iswahyudi et al. (2019), the authors present a technique that consisted of applying the Buckingham π theorem to predict the power and thrust of large wind turbines based on the small-scale one. The methodology proposed by the authors consisted of mixing three techniques traditionally used in the design of wind turbines. The first approach consisted of conducting tests on a small wind turbine (2.4 m) in a wind tunnel. This approach allowed the measurement of aerodynamic characteristics under controlled conditions. The wind tunnel test provided data on torque and thrust at different wind speeds (7, 10, and 12 m/s). The second approach was the BEM theory, which allowed to compute the geometry of the rotor blades and to generate the torque and thrust data for wind turbines of various diameters (2.4, 10, 50, and 75 m) at the same wind speeds evaluated in the wind tunnel. Finally, the third approach was the π theorem, which allowed for the establishment of relationships between parameters such as torque, thrust, rotor diameter, air density, wind speed, and rotor rotation speed. In summary, BEM theory was used for theoretical predictions and design optimization of wind turbine performance. In contrast, the wind tunnel served as a tool for experimental validation and data collection to support the predictions made with the π theorem.

The analysis made by Iswahyudi et al. (2019) revealed how the rotor diameter and other variables influence torque and thrust. The results indicated that as the rotor size increases, the scaling effects on torque and thrust must be carefully considered to ensure accurate predictions of performance for larger turbines. Iswahyudi et al. (2019) emphasized the need to obtain experimental data, particularly for designs with low TSR. This data is crucial before applying dimensional analysis for up-scaling wind turbine designs, as it ensures that the scaling laws derived from smaller models are valid for larger applications; especially as it relates to the Reynolds number, since large wind turbines operate at a higher Re. This difference can lead to discrepancies in performance predictions, as larger Re generally allows for a better lift-to-drag ratio, and the flow remains attached longer, thereby delaying stall and improving the overall aerodynamic efficiency of the turbine.

The proposed methodology by Iswahyudi et al. (2019) reported that a deviation of the estimated power values from those calculated by the BEM theory is only 0.09% for powers and 0.19% for thrusts. This allows us to conclude that the study has a high level of accuracy; however, the method is reliable for scaling up to a maximum of 31.25 and for TSR greater than 6.

The above studies are some examples of how the π theorem has been used in the field of wind energy. However, producing energy from wind in cold regions presents even more challenges. In these cases, there is a significant impact on turbine performance, mainly due to the amount of ice that accumulates on the blades. In that order of ideas, the following studies are focused on the application of the π theorem to predict ice accretion on turbines.

Ibrahim, Pope, et Naterer (2023b) investigate the scaling and similitude methods for modeling rime ice accretion on rotating wind turbine blades. The authors address the challenges posed by wind tunnel size limitations, which restrict the testing of full-scale wind turbine components under realistic icing conditions. To overcome these limitations, the authors formulated a scaling methodology that ensured the equivalence of flow fields, droplet trajectories, and ice accumulation between scaled models and full-size blades. The methodology consisted of the development of non-dimensional groups that govern the dynamics of the flow and ice accretion processes, emphasizing the importance of geometric similarity and maintaining consistent parameters such as airfoil curvature and surface roughness. The significant scaling dimensionless groups included Reynolds number, two performance speed ratios for the rotational forces, droplet inertia, droplet's drag coefficient, and ice accumulation parameter.

The methodology proposed by Ibrahim et al. (2023b) was validated using numerical simulations carried out with FENSAP-ICE software. The validation results demonstrated an accurate prediction of rime ice accretion on large wind turbine blade sections based on smaller blades tested under laboratory conditions. The predicted ice characteristics, including thickness and mass, were in good alignment with experimental data. Hence, the results indicated a successful scaling of ice accretion. The study did not evaluate turbine performance under icing conditions.

However, the authors continued the research, and in this second study, Ibrahim, Pope, et Naterer (2023a) examined the advanced methodologies developed for scaling ice accretion on rotating wind turbine blades, with a specific focus on glaze ice conditions. For this case, the analysis considered the thermodynamic effects, as in the case of glaze ice, the heat flux directly contributes to the icing process. Specifically, some droplets impacting the blade's surface will freeze, while others will run back and then freeze, forming horns or feathers. Therefore, in addition to the six significant dimensionless scaling groups mentioned in Ibrahim et al. (2023b), a new dimensionless parameter was proposed and called "relative heat factor" which relates the energy of impingement droplets and convection energy terms. With the addition of this parameter and following the previous CFD validation methodology, the authors carried out accurate predictions of ice accretion characteristics, such as thickness and shape, based on a smaller blade model tested under controlled glaze ice conditions.

However, Ibrahim et al. (2023a, 2023b) emphasize that for dimensionless parameters to be useful for prediction in real-size models, the scaled blade geometry should be identical to the reference blade geometry and other geometrical design parameters, such as the blade surface roughness, material, chord length, airfoil curvature thickness, span-wise length, and tilt/twist angle.

In all the studies reviewed, the authors agree that for the theorem to function effectively, it requires: reliable and accurate experimental, field or numerical data (a robust database); the dimensionless groups must accurately represent the relationships between the different physical phenomena, including that the parameters correlate well with the experimental data; validation of predictions against established theoretical models to confirm consistency with known aerodynamic principles; finally, the derived correlations must be robust enough to handle variations in turbine design and operating conditions without significant loss in accuracy. Additionally, when applying the π theorem to scale from a smaller model to a larger one, it is crucial that the prototype accurately represents reality in terms of both geometric and aerodynamic characteristics. The operating conditions for comparison must be identical for both the prototype and the actual turbine.

In conclusion, most of the studies found during the literature review correspond to similarity analysis and the application of the π theorem in scaling the results of a small-scale model to a large-scale one, which saves both time and money. However, to the best of our knowledge, the π theorem has not been used to propose dimensionless parameters for quantifying or predicting the power output of a wind turbine under icing conditions. Herein lies the importance of the present thesis.

1.6 Machine Learning

Machine Learning, also known as deep neural networks, is a technique that teaches computers by example. In other words, the computer model learns to perform tasks by analyzing images, text, or sound. In this technique, models are trained using a large set of labeled data and neural network architectures that contain many layers, learning features directly from the data without requiring manual feature extraction (Géron, 2019; MathWorks, 2020).

Some examples of the applications of Machine Learning are (MathWorks, 2020): automated driving (detection of pedestrians, stop signs, traffic lights, etc.), aerospace and defence, medical research (detection of cancer cells), industrial automation (detecting when people or objects are within an unsafe distance of machines), and electronics (automated hearing and speech translation).

Machine learning systems can be categorized based on the amount and type of supervision they receive during training (Géron, 2019). The four main categories are *supervised learning, unsupervised learning, semi-supervised learning*, and *reinforcement learning.*

- Supervised Learning: The algorithm is trained to produce desired outputs in response to sample inputs. This technique is well-suited for modeling and controlling dynamic systems, classifying noisy data, and predicting future events (Géron, 2019).

Classification: The algorithm learns to classify new observations based on examples of labeled data.

Regression: These models describe the relationship between a response variable (output) and one or more predictor variables (inputs).

Pattern Recognition: It classifies input data into objects or classes based on key features. It is essential in applications such as computer vision, radar processing, speech recognition, and text classification.

- Unsupervised Learning: Since the training data is unlabeled, the system attempts to learn without guidance (Géron, 2019). They are used to draw inferences from data sets consisting of input data without labelled responses. You can use them to discover natural distributions, categories, and category relationships within data.

Clustering: The algorithm can be used for exploratory data analysis to identify hidden patterns or group data by similarity. Some applications include gene sequence analysis, market research, and object recognition.

Anomaly detection and novelty detection: This allows the removal of outliers from a dataset before feeding it to another learning algorithm.

Visualization: The algorithm processes complex and unlabeled data to generate 2D or 3D representations. These representations aim to maintain the underlying structure of the data, such as preventing clusters from overlapping, enabling users to comprehend the data's organization, and potentially discovering unexpected patterns (Géron, 2019).

Dimensionality reduction: The algorithm simplifies the data without losing information by utilizing correlations.

Association rule learning: It involves sifting through vast amounts of data to identify significant relationships between variables.

- Semi-supervised learning*:* the data used to train the algorithm is partially labeled. Most semi-supervised learning algorithms are a combination of unsupervised and supervised learning algorithms (Géron, 2019).

- Reinforcement learning: With this approach, the learning system, an "agent," interacts with an environment, making decisions and receiving rewards or penalties. The agent autonomously learns the optimal strategy, known as a "policy," to maximize cumulative rewards over time. The policy guides the agent in choosing actions based on its current situation in the environment (Géron, 2019).

Machine learning algorithms are increasingly used to predict power loss in wind turbines during icing conditions. Several studies have highlighted the effectiveness of machine learning in predicting ice-growth-induced production losses and assessing icing risk (Dai, Zhang, Rotea, & Kehtarnavaz, 2024). For example, one study proposed a statistical method based on random forest regression that considers regional weather forecasts and on-site measurements (Scher & Molinder, 2019). Another research aimed to develop a prediction system based on neural networks that uses real-time data (SCADA) to determine icing risk hours. This enables a more efficient operation of the anti-icing system (Kreutz et al., 2019). Machine learning algorithms have demonstrated higher accuracy than traditional methods in predicting power loss in wind turbines under icing conditions (Lidong, Yimin, & Yuze, 2023). This highlights the potential of machine learning for predicting wind turbine icing.

Different machine-learning algorithms have been applied to estimate power loss in wind turbines under icing conditions (Dai, Zhang, et al., 2024). Each approach has its strengths and limitations in terms of accuracy, interpretability, and computational efficiency. The selection of a suitable model depends on factors such as the complexity of the data, the specific requirements and constraints of the application, and the need for robustness against noise or outliers.

Among the various machine learning models, this thesis will focus on decision trees (DT), random forest (RF), and artificial neural networks (ANN). DT algorithms are frequently employed due to their interpretability and robustness in binary classification (icing/no icing) and regression tasks; RF models are especially effective for managing high-dimensional data and complex features; and ANN have been utilized for both classification and regression in icing-related wind turbine prediction. Fully connected neural networks (FNN) often perform well at shorter forecast horizons. In contrast, deeper structures, such as Convolutional Neural Networks (CNNs) and Long Short-Term Memory (LSTM) networks, outperform over longer horizons thanks to their ability to model temporal relationships in time-series SCADA datasets.

For example, Zhang et al. (2024) showed that RF outperforms other methods in predicting icing-related power losses after applying PCA to match machine learning algorithms with cleaned datasets. While the results are compelling, dependence on PCA might mask the physical significance of features, and further validation with real-world data and an assessment of model robustness would strengthen the study. Similarly, Solheim Haugen (2025) provides a strong comparison of RF, FNN, and LSTM for forecasting icing events and related production losses, with the RF classifier showing the most consistent and accurate results at up to 36 hours of icing event classification using historical SCADA and weather prediction data. The practical deployment of this method may struggle due to computational cost and dependency on accurately labelled data. Regarding the ANN, Dai, Rotea, et Kehtarnavaz (2024) introduced a hybrid model called PCTG (Parallel CNN-TCN GRU) that achieved impressive results, with over 97% prediction accuracy for forecasts 2 days ahead and at least 95% accuracy for up to 22 days. It outperformed individual CNN, LSTM, and TCN models. While the findings are robust, the study may face limitations due to a lack of validation on diverse datasets or turbines, which could affect their applicability in different contexts. Additionally, the model's complexity might make real-time deployment challenging, and operational issues such as sensor failures are not thoroughly explored.

Machine learning has proven effective for predicting wind-turbine power losses from icing, with multiple studies showing improvements over traditional methods when combining SCADA and weather data. Decision trees provide transparent, easily interpretable baselines; random forest offer robust, high-performing results on high-dimensional and preprocessed data; and neural networks, especially deeper architectures (CNN, LSTM, TCN and hybrid models), deliver the best long-horizon predictive performance when sufficient labelled data and compute are available. Reported top-performing hybrids achieve very high accuracy but introduce complexity, potential overfitting to specific datasets, and operational challenges for real-time deployment.

For this thesis, the strategy is to use three machine learning methods (decision trees, random forests, and neural networks) to validate a set of proposed dimensionless parameters using the π theorem. It should be noted that the author does not claim expertise in the field of machine learning; consequently, the selected algorithms are employed exclusively as methodological tools to assess the coherence, consistency, and predictive relevance of the proposed dimensionless groups, rather than to advance or contribute to the development of machine learning techniques themselves.

CHAPTER 2

INFLUENCE OF SURFACE ROUGHNESS MODELING ON THE AERODYNAMICS OF AN ICED WIND TURBINE S809 AIRFOIL

Leidy Tatiana Contreras Montoya [a,b], Adrian Ilinca [a], and Santiago Lain [b]

[a] Mechanical Engineering Department, Faculty of Engineering, École de Technologie Supérieur, University of Québec, 1100, rue Notre-Dame Ouest, Montréal, QC, H3C 1K3, Canada
[b] PAI+ Group, Energetics & Mechanics Department, Faculty of Engineering, Universidad Autónoma de Occidente, Cll 25 # 115-85 Km 2 Vía Cali - Jamundí, Cali, Valle del Cauca 760030, Colombia.

Article published in *Processes*, vol. 11 (2023), available at https://doi.org/10.3390/pr1112337

2.1 Introduction

Simulation and modeling techniques have become increasingly valuable in studying and analyzing ice accretion on wind turbines. These methods offer numerous advantages compared to experimental approaches, including cost-effectiveness, efficiency, and the ability to explore diverse icing events. Nonetheless, achieving accurate ice accretion modeling on wind turbines requires a comprehensive approach that involves multiple disciplines, encompassing thermodynamics, aerodynamics, heat transfer, and mass transfer (Contreras Montoya et al., 2023).

Computer-aided engineering techniques are commonly utilized to conduct these analyses, employing various tools and approaches to numerically solve coupled differential equations through finite element and finite volume methods (W. Han et al., 2018; O'Brien, Young, O'Mahoney, & Griffin, 2017; Pedersen & Sørensen, 2016). Additionally, emerging methodologies such as machine learning, genetic algorithms, and artificial intelligence have been utilized in some instances, as evidenced by a few examples in recent years (Chen, Feng, Teng, Lu, & Fei, 2022; Fei et al., 2023; Hacıefendioğlu, Başağa, Yavuz, & Karimi, 2022). In real terms, during the last twenty years, several investigations have been performed to study the influence of icing on wind turbines using simulation methods. These studies aim to enhance our understanding of the phenomenon and provide valuable insights for designing more resilient and efficient wind turbine systems (Fakorede et al., 2016; Hu et al., 2018; Hu, Zhu, Hu, Chen, & Du, 2017; Rizk, Younes, Ilinca, & Khoder, 2022).

CFD is a common tool used to simulate various phenomena in turbomachinery (Laín et al., 2019), including the accumulation of ice on specific blade sections of the wind turbine (Martini et al., 2022). The amount of ice accretion is predicted by numerical models, which can affect the airfoil geometry and decrease aerodynamic performance (Contreras Montoya et al., 2023).

Some examples of such studies include Etemaddar et al. (2014), Villalpando, Reggio, et Ilinca (2016), W. Han et al. (2018), Jia Yi Jin et Virk (2018), Jia Yi Jin et Virk (2019), Yirtici, Cengiz, Ozgen, et Tuncer (2019), and Yirtici, Ozgen, et al. (2019).

In most CFD studies focused on icing events in wind turbines, the flow along the blade span is often neglected due to its complexity and high computational costs. Instead, these studies usually focus on two-dimensional airfoil profiles placed at specific sections of the blade span (Contreras Montoya et al., 2023). The decision to simplify the analysis using 2D airfoil models and neglecting the 3D rotating effect is driven by practical considerations. Accounting for the full 3D rotational flow requires significantly more computational resources and time. By focusing on specific sections of the blade span, researchers can still gain valuable insights into the aerodynamic behaviour of the wind turbine under icing conditions while keeping the computational requirements within manageable limits (Contreras Montoya et al., 2023). While this approach may introduce some limitations in capturing the complete 3D flow physics, it still provides valuable insights into understanding the impact of ice accretion on wind turbine performance. Researchers continue to explore advancements in modeling techniques and computational capabilities to better address the complexities of 3D rotating flows in future studies (J. Y. Jin et al., 2020; Pedersen, 2018; Shu et al., 2018).

After reviewing the literature, it was observed that popular icing programs were initially developed for simulation icing in aeronautics (Contreras Montoya et al., 2022; IEA Wind, 2016; M. C. Pedersen & H. Sørensen, 2016; Pedersen & Yin, 2014). The icing programs, primarily developed for simulating aircraft icing, are not specifically tailored to account for the distinct operational and weather conditions of wind turbines. Wind turbines and aircraft exhibit distinct icing dynamics attributed to various factors. These factors encompass differences in operational altitude, angle of attack (AoA), airfoil positioning relative to the ground, the contrast between fixed-wing and rotary-wing aircraft, and the impact of air compressibility at varying airspeeds (Contreras Montoya et al., 2023; Contreras Montoya et al., 2022).

Indeed, a few programs for in-flight icing have undergone adaptations, testing, and validation to replicate the formation of ice on wind turbine blades. The primary focus of these adjustments is on integrating the distinctive atmospheric conditions during operation and accounting for the geometry and rotation of the wind turbine blades (Contreras Montoya et al., 2023). Consequently, models originally designed to simulate icing on aircraft may exhibit incongruent behaviour when applied to simulations of wind turbines. The distinctions in operational conditions and blade characteristics necessitate adjustments to the existing models. For instance, wind turbine blades experience different airspeeds, air temperatures, and humidity levels compared to aircraft wings. The rotation of wind turbine blades introduces a time-varying flow field, resulting in variations in ice accretion patterns (Contreras Montoya et al., 2023).

Additionally, the complex geometry of wind turbine blades, including their twist and taper along the span, requires specific considerations for accurate simulation. By adapting, testing, and validating these in-flight icing programs for wind turbines, researchers and engineers aim to address these incompatibilities and develop models that effectively capture the icing behaviour unique to wind turbines (Contreras Montoya et al., 2023). These modifications enable more reliable assessments of ice accretion effects, aiding in the design and optimization of wind turbine systems for safe and efficient operation in icy conditions (Contreras Montoya et al., 2022; Martini et al., 2022; Villalpando et al., 2016). For instance, Etemaddar et al. (2014) concluded that wind turbines could operate under icy conditions by reducing their cut-off speed to minimize the risk of damage to components. The authors utilized LEWICE 1.6 software, and the Blade Element Momentum (BEM) code WT-Perf to arrive at this conclusion. Another example is the study by W. Han et al. (2018), which used a CFD model to suggest that modifying the pitch angle is necessary for maintaining steady power in wind turbines during icing periods. However, the study concluded that maximum turbine efficiency under these conditions can be achieved by operating at a variable speed via generator torque control, even below the rated speed.

While software packages like NASA's LEWICE and FENSAP-ICE (currently part of ANSYS) are commonly employed for investigating icing, they have predominantly been utilized in aeronautical applications (Contreras Montoya et al., 2023). LEWICE and FENSAP-ICE have been extensively used and validated for simulating ice accretion on aircraft surfaces. These packages incorporate specialized algorithms and models tailored to aircraft icing phenomena, considering droplet impingement, ice shape evolution, and ice shedding. However, their application to wind turbine icing simulations requires careful evaluation and adaptation to account for the unique characteristics and operational conditions of wind turbines (Contreras Montoya et al., 2023).

To effectively utilize these software packages for wind turbine icing studies, it is essential to validate their performance against experimental data and real-world observations specific to wind turbines (Contreras Montoya et al., 2023). This process involves assessing their ability to capture ice accretion patterns, evaluating the effects on aerodynamic performance, and accounting for the complex interactions between rotating blades, atmospheric conditions, and ice-shedding dynamics. By conducting thorough testing and validation, researchers and engineers can enhance the reliability and accuracy of these software packages for wind turbine icing simulations, enabling a better understanding and mitigation of icing-related challenges in the wind energy industry (ANSYS Inc., 2016; Pedersen, 2018).

However, using these two programs, various investigations have devised approaches for replicating ice accumulation on wind turbine blades (Hann, Hearst, Sætran, & Bracchi, 2020; Jia Yi Jin & Virk, 2018; Knobbe-Eschen et al., 2019; Li, Wang, et al., 2018). Homola et al. (2012) employed FENSAP-ICE to anticipate the formation of ice on the airfoils of the NREL 5MW benchmark wind turbine. In the study by Etemaddar et al. (2014), FLUENT was utilized for aerodynamic computations and ice accretion was simulated using LEWICE. The resultant lift and drag coefficients, C_L and C_D, were computed using ANSYS FLUENT and then corroborated against experimental measurements from the wind tunnel at LM Wind Power.

As mentioned in section 1.2, the simulation of ice accretion usually comprises a sequence of four primary modules (Contreras Montoya et al., 2022; L. Makkonen et al., 2001; Virk et al., 2016). The first module involves aerodynamic calculations to determine the flow characteristics around the wind turbine blade. This is achieved by solving the Navier–Stokes equations, which include the continuity equation (1.2), the momentum equation (1.3), and the energy equation (1.4).

The second module focuses on calculating the trajectory of water droplets in the airflow (see section 1.2.2). This can be performed using either a Lagrangian approach, which tracks individual droplets, or a Eulerian approach, which considers the behaviour of droplets as a continuous phase. Simulating the droplet trajectories, the module determines where the droplets impinge on the blade surface. The third module involves thermodynamic computations to assess the rate of ice accumulation in a specific location over a designated period (see Section 1.2.3). These calculations consider air temperature, humidity, and droplet properties to estimate how ice accumulates on the wind turbine blade surface. The fourth module addresses the geometry of the wind turbine blade, enabling the updating of the blade shape as the ice accumulates. This is important because ice accretion alters the blade's geometry and surface roughness, affecting its aerodynamic performance. The module ensures that the evolving geometry due to ice growth is accurately represented in the simulation. By integrating these four modules into a comprehensive simulation framework, researchers and engineers can obtain insights into the aerodynamic effects of ice accretion on wind turbine blades and make informed decisions regarding turbine design, operation, and ice protection strategies (Contreras Montoya et al., 2023).

This layer of ice enhances the likelihood of boundary layer detachment on the suction side of the airfoil, known as the extrados, resulting in an aerodynamic stall that occurs at a lower AoA compared to a clean scenario without ice. Given the intricate nature of this phenomenon, predicting fluctuations in flow velocity and the formation of eddies becomes exceedingly challenging (Contreras Montoya et al., 2023). Addressing these disturbances at a small scale necessitates employing an unsteady Navier–Stokes equation and incorporating a high level of detail. However, these vortices and fluctuations diminish in size at higher Reynolds numbers. Hence, the RANS approach becomes more appropriate where the velocity fluctuations in the flow field are averaged over time (Contreras Montoya et al., 2022).

Various RANS models and adaptations are accessible, depending on the specific application, each relying on distinct methodologies for computing turbulent eddy viscosity. Addressing this diversity, numerous turbulence models, including but not limited to the Spalart–Allmaras, k-ε, k-ω, shear stress transport (k-ω SST model), and large eddy simulation (LES) models, are typically employed. These models are extensively applied in studying flows surrounding airfoils and wind turbines (Contreras Montoya et al., 2022), and they are explained in section 1.2.1.

Contreras Montoya et al. (2022) addressed the various modeling approaches and simulation techniques available for wind turbine icing. This article specifically highlighted the distinct characteristics of wind turbine icing simulations, including the unique operational conditions and software capabilities required. Furthermore, the potential and suitability of various software tools for wind turbine icing simulations were thoroughly discussed. In particular, the adaptability of software FENSAP-ICE for wind turbine icing simulations, its integration with ANSYS, and the insights provided by previously published articles collectively contribute to the growing understanding and progress in modeling and simulating icing on wind turbines. These developments enable more accurate assessments of the impact of icing on wind turbine performance, facilitating the design of mitigation strategies to ensure safe and efficient wind turbine operations.

Recently, Martini et al. (2022) performed a computational analysis on a NACA 64618 airfoil of the iced NREL 5MW benchmark wind turbine, utilizing ANSYS FLUENT and FENSAP-ICE. The investigation focused on evaluating the precision of aerodynamic loss estimation for airfoils affected by icing using two turbulence models (Spalart–Allmaras and k-ω SST) and the effect of surface roughness distribution using the Shin et al. (1991) model available in the ICE3D module of FENSAP-ICE. Etemaddar et al. (2014) and Homola et al. (2012) used published research, numerical investigations, and experimental studies in the existing literature for comparison. These authors found that neglecting surface roughness from calculations underestimates the effect of ice on aerodynamic performance. On the other hand, they concluded that the choice of turbulence model had a limited influence on the resulting aerodynamic losses caused by icing, compared to the impact of considering roughness. A similar conclusion was reached by Caccia et Guardone (2023), who found that the extent of ice-induced roughness and its height drove the decrease in the aerodynamic performance of the studied airfoils as the angle of attack increased.

The previous discussion demonstrates that the accuracy of icing modeling depends heavily on roughness, which has been emphasized by various authors in the field (ANSYS Inc., 2017; Blasco et al., 2017; Contreras Montoya et al., 2022; Hildebrandt & Sun, 2021). Roughness plays a significant role in airfoil performance, as it affects the boundary layer transition and flow separation, both of which are critical factors in aerodynamic efficiency (Blasco et al., 2017; Hildebrandt & Sun, 2021; Turkia et al., 2013). Even small amounts of ice can significantly affect an airfoil's performance. Therefore, it is crucial to consider the effects of roughness at every step of the ice growth calculation (Caccia & Guardone, 2023; Turkia et al., 2013). Considering the roughness height as a parameter in heat transfer analysis ensures that the effects of surface roughness on convective heat transfer are adequately accounted for, leading to more reliable and precise thermal assessments and design considerations (Fortin & Perron, 2009b; Sagol, 2014). For example, modellers studying aircraft icing extensively utilized CFD to analyze the local heat transfer coefficient across various aircraft components. The findings suggested that surface roughness could substantially amplify local heat transmission, even in the presence of a thin layer of ice (Farzaneh, 2008).

However, determining the roughness height of structures such as wind turbine blades necessitates conducting experiments, as detailed in the study by Blasco et al. (2017). These experiments can be tedious and costly, and their applicability is limited due to their dependence on the airfoil type and wind tunnel configuration. In response to the above, different research centers employ different methods for describing roughness (Contreras Montoya et al., 2022). For instance, the traditional NACA roughness model originated by distributing typical grain sizes uniformly from the leading edge downstream on both the pressure and suction surfaces (Battisti, 2015). The sand-grain roughness model of Shin et al. (1991), originally developed for aeronautics, is the most commonly employed correlation for predicting ice surface roughness along wind turbine blades. This model was specifically designed to match the ice shapes predicted by the LEWICE code with experimental ones, and for the atmospheric conditions typical of aviation, which limits the model's generality (Caccia & Guardone, 2023). This empirical correlation relies on the Shin and Bond formula, which computes the non-dimensional height of small-scale surface roughness: $\frac{k_s}{c}$ as a function of static temperature, airfoil chord length c, MVD, LWC, and the relative wind speed (see equation (1.14)).

An alternative to the previous roughness model is the so-called beading model available in ANSYS-FENSAP-ICE. This model considers both constant and varying distributions of sand-grain roughness and integrates them into the existing turbulence models. After activation of the beading model, the prediction of sand-grain roughness height on the surface caused by moving and freezing beds is enabled (ANSYS Inc., 2017); i.e., there is an automatic transfer of the spatially and temporally evolving roughness data to the airflow module at the end of each shot. As a result, the roughness height changes dynamically and depends on the contaminated area.

In fact, the sand-grain roughness model proposed by Shin et al. (1991) is used in nearly every CFD investigation focused on icing, where it is employed to gauge the roughness of the ice-covered surfaces on wind turbine blades (Caccia & Guardone, 2023; Contreras Montoya et al., 2022). However, as far as we know, there is a scarcity of icing studies in the literature comparing the influence of the surface roughness model, particularly the beading model, on the aerodynamic performance of wind turbine airfoils.

Therefore, this paper presents a numerical study conducted in the iced S809 airfoil where the impact of the surface roughness model on its aerodynamic coefficients is addressed. Moreover, the influence of the employed turbulence model is also evaluated. The results for the clean airfoil were validated against experiments reported by Somers (1997) and simulations by Tan (2020). The predicted rime ice shape was validated with the experimental studies of Y. Han, Palacios, et Schmitz (2012). Two methodologies for estimating roughness, the Shin et al. (1991) model and the beading model, are compared, as well as the effects of icing types — rime ice and the less studied case of glaze ice — on aerodynamic performance. The influence of icing conditions and roughness is evaluated and discussed by examining the lift and drag coefficients, as well as the skin friction and pressure coefficients.

2.2 Geometrical Configuration and Mesh Generation

The geometrical model was based on an airfoil used by the National Renewable Energy Laboratory (NREL). The S809 airfoil is used in the two-bladed NREL Phase VI turbine (Hand et al., 2001), which is present along the entire blade length. This study will focus on the section at 95% radius of the blade, primarily because it corresponds to the area closest to the blade tip, where ice accumulation is most prevalent. Furthermore, this region of the blade is primarily responsible for turbine performance (Burton et al., 2011; Li et al., 2019). The chord of the S809 at this radius is 0.358 m, and the airfoil has the following specifications (Airfoil Tools):

- Max thickness: 21% at 39.5% of the chord from the leading edge.
- Max camber: 1% at 82.3% of the chord from the leading edge.

The geometric model was constructed using DesignModeler 2022 R1 software, a component of the ANSYS suite. Figure 2.1 illustrates the model, highlighting a substantial computational domain encompassing significant flow disturbances, particularly downstream. The positioning of boundaries and the size of the domain were determined based on prior studies that demonstrated satisfactory agreement with experimental and numerical data. For example, the computational domain used by Villalpando et al. (2016) and Hildebrandt et Sun (2021) was extended by 12.5 chords in front of the airfoil and 20 chords behind; in the case of Zanon et al. (2018), the domain boundaries were located at 20 chord lengths. Considering the above, the chosen dimensions of the computational domain were identical to those used by Zanon et al. (2018). This guarantees that the boundary conditions applied to the external domain do not disrupt the flow in the neighbouring region or compromise the accuracy of the results.

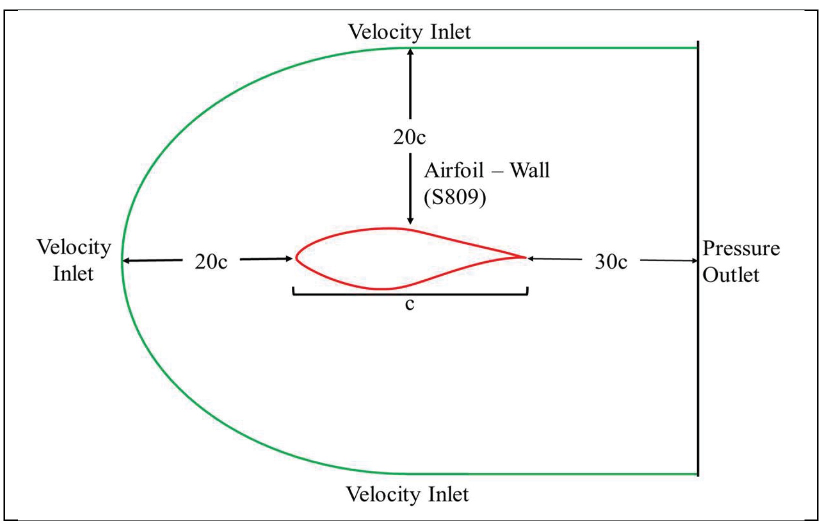

Figure 2.1 Illustration of the computational domain geometry
Taken from Contreras Montoya et al. (2023)

The computational domains have been discretized using a non-structured grid generated with ANSYS Meshing 2022 R1 software. Figure 2.2 provides an overview of the utilized meshes. To adequately describe the boundary layer development, the mesh around the airfoil has an O-grid topology, including 25 prism layers (see Figure 2.3). Beyond the prisms zone, a non-structured mesh based on tetrahedra was created, ensuring that its aspect ratio is close to the prisms to guarantee a smooth transition between the two mesh regions. The following sections present the calculations for ice accretion, including an estimation of the aerodynamic characteristics of clean and iced airfoils. Additionally, the performance losses occurring under specific icing scenarios are evaluated.

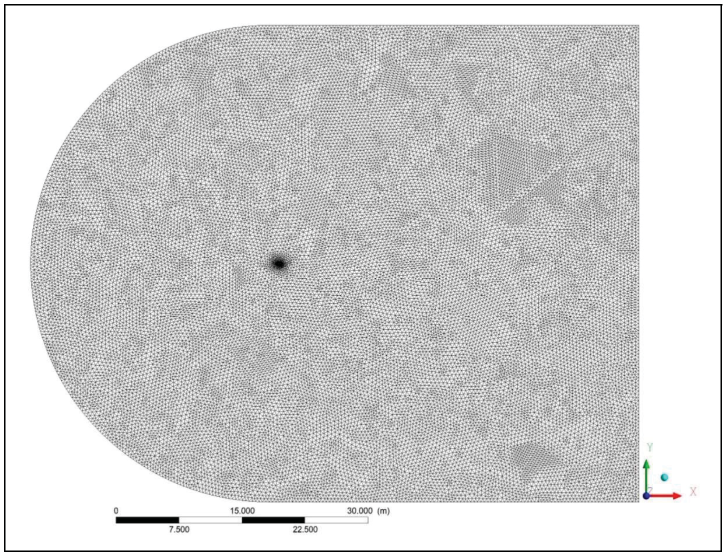

Figure 2.2 Overview of the mess in the computational domain
Taken from Contreras Montoya et al. (2023)

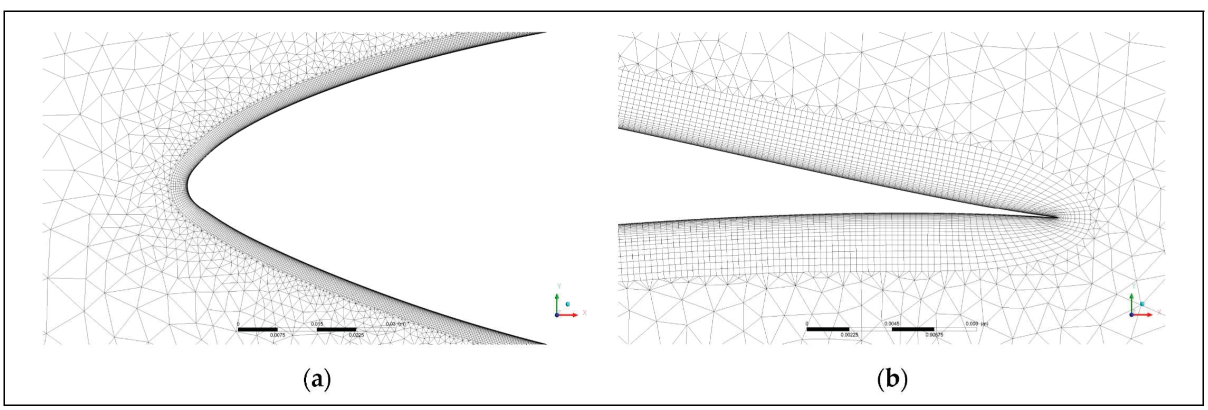

Figure 2.3 Detail of the prism layers around the airfoil. **(a)** Leading edge. **(b)** Trailing edge
Taken from Contreras Montoya et al. (2023)

2.3 Numerical Simulation Setup and Verification Study

Simulations of ice accretion on the S089 airfoil were conducted using the FENSAP-ICE software integrated into the ANSYS platform. They were performed on a desktop computer with a Windows 11 operating system, an Intel Core i5 10th-generation processor at 2.90 GHz, and 24 GB of RAM.

FENSAP-ICE operates within a modular system (see Figure 2.4) comprising three components: the FENSAP module is utilized for aerodynamic calculations, DROP3D is employed for droplet impingement, and ICE3D is used for ice growth calculations. Moreover, FENSAP-ICE has two methods for estimating roughness due to ice accretion: the beading model and the Shin et al. (1991) model. Both methods were used to compare their effect on the airfoil aerodynamic coefficients. Data regarding the simulation setup can be found in Table 2.1 1 for two ice conditions: rime (dry regime) and glaze (wet regime).

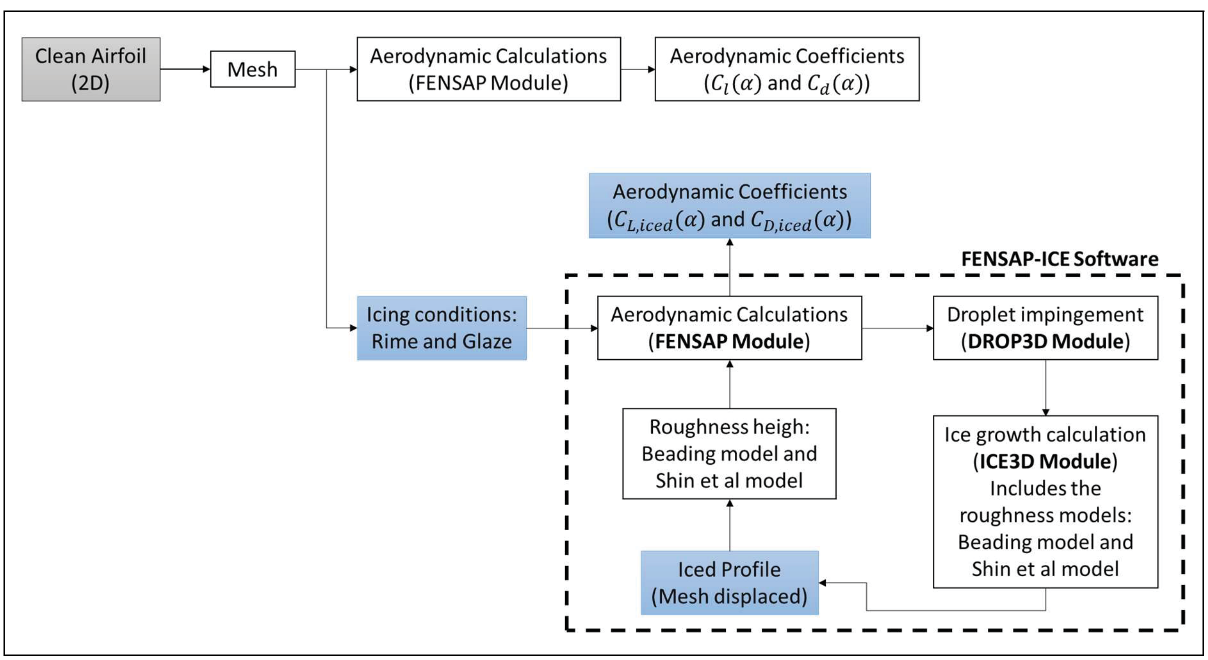

Figure 2.4 Flow chart of the CFD simulation using FENSAP-ICE
Taken from Contreras Montoya et al. (2023)

Table 2.1 Overview of the simulation parameters
Taken from Contreras Montoya et al. (2023)

Parameters	Rime	Glaze
Airspeed [m/s]	9.5	9.5
Angle of attack [°]	4	4
Relative velocity [m/s]	42	42
Reynolds number	$3.4x10^6$	$3.4x10^6$
MVD [µm]	20	27
LWC [g/m^3]	0.05	0.12
Ice density [kg/m^3]	750	917
Accretion time [min]	30	30
Temperature [°C]	-10	-5
Turbulence model	Spalart – Allmaras / k-ω SST	Spalart – Allmaras / k- ω SST
Converge criterion	$1x10^{-5}$	$1x10^{-5}$

Note: The parameters for the rime condition were taken from Y. Han et al. (2012) to validate and compare the results. The glaze ice condition parameters were estimated using in situ measurements from the non-profit applied research center “Nergica” in Québec, Canada.

The flow validation around the clean airfoil was conducted using the two turbulence models under the same conditions outlined in Table 2.1. The Spalart–Allmaras (SA) model was chosen because it is widely used in aerodynamics and has a good computational cost-to-accuracy performance ratio. The k-ω SST model was chosen because it is more robust and performs better in flows with strong adverse pressure gradients (Contreras Montoya et al., 2023).

A spatial verification test, also known as a mesh independence study, was performed under no-ice conditions. Three distinct grids were created to verify mesh convergence, adjusting the number of elements. Localized mesh refinement was opted for, indicating that variations in spatial discretization are concentrated around the airfoil. The procedure commenced with a coarse discretization at the outer limit of the boundary layer and progressed to a finer discretization along the profile wall (see Table 2.2).

Table 2.2 Number of elements in the considered meshes
Taken from Contreras Montoya et al. (2023)

Mesh	Number of Elements
1	870726
2	1235620
3	1655379

Intending to resolve the boundary layer development, all the grids use a thin layer around the airfoil, which is discretized by 25 layers of prisms. The initial height of these layers was set at 7.6×10^{-6} m, a value determined to maintain $y^+ < 2$. This value of the variable y^+ is suggested by the numerical requirements imposed by the k-ω SST turbulence model.

The CFD grid independency study involved calculations in successively refined meshes, evaluating the convergence of the most relevant variables. The lift coefficient (equation (2.1)) and drag coefficient (equation (2.2)), C_L and C_D, were chosen in this case. They are defined as:

$$C_L = \frac{L}{\frac{1}{2}\rho c U^2} \tag{2.1}$$

$$C_D = \frac{D}{\frac{1}{2}\rho c U^2} \tag{2.2}$$

L and D represent the dimensional lift and drag forces, and c is the airfoil chord length.

Table 2.3 showcases the verification outcomes for the generated meshes. The convergence error, expressed as a percentage, was calculated by comparing the difference in the aerodynamic coefficient for each mesh with that of the most refined mesh, i.e., mesh no. 3.

Table 2.3 Convergence errors for each mesh
Taken from Contreras Montoya et al. (2023)

	K-ω SST model				Spalart – Allmaras Model			
Mesh No.	**C_L**	**C_L Error**	**C_D**	**C_D Error**	**C_L**	**C_L Error**	**C_D**	**C_D Error**
1	0.5405	1.66%	0.014877	5.81%	0.5617	3.81%	0.013611	3.55%
2	0.5506	0.18%	0.015824	0.19%	0.5459	0.89%	0.014540	2.84%
3	0.5496		0.015794		0.5411		0.014058	

As can be seen in Table 2.3, the maximum difference between mesh no. 2 and 3 is less than 3%. Either mesh could be used for the study, so the computational cost was also a factor in the decision. Although mesh no. 3 has 33% more elements, the difference in computational time was minimal, so it was decided to work with it. For example, the complete simulation (i.e., of the three modules FENSAP, DROP3D, and ICE3D) took 24 hours for mesh no. 2 and 26 hours for mesh no. 3. The convergence study was performed using the two turbulence models, with the k-ω SST model yielding the lowest error percentage. In addition, as depicted in Figure 2.5, the lift and drag coefficients attain a nearly constant value, demonstrating that the achieved solution is mesh independent.

As previously mentioned, FENSAP-ICE comprises three modules: FENSAP, DROP3D, and ICE3D. Table 2.4 provides the relevant variable values for each module.

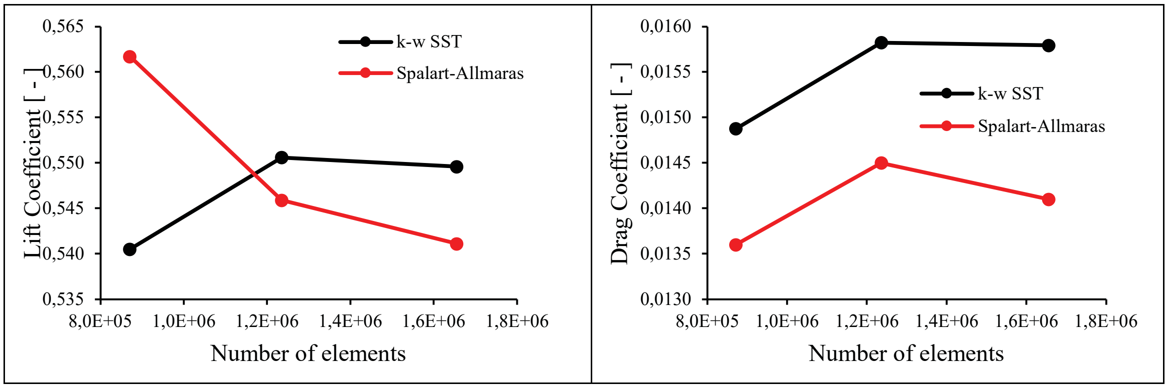

Figure 2.5 Aerodynamic coefficients vs. the number of elements. Lift coefficient (**left**) and drag coefficient (**right**)

Taken from Contreras Montoya et al. (2023)

Table 2.4 Parameter values in each ANSYS FENSAP-ICE module

Taken from Contreras Montoya et al. (2023)

Parameters	**FENSAP**	**DROP3D**	**ICE3D**
Characteristic length		0.358 m	
Relative air velocity		42 m/s	
Air static pressure		101325 Pa	
Air static temperature		-10 °C (rime) -5 °C (glaze)	
Velocity angle of attack		4°	
Liquid water content (LWC)	n. a	0.05 g/m^3 (rime) 0.12 g/m^3 (glaze)	0.05 g/m^3 (rime) 0.12 g/m^3 (glaze)
Droplet diameter (MVD)	n. a	20 µm (rime) 27 µm (glaze)	n. a
Droplet distribution	n. a	Monodisperse	n. a
Total time of ice accretion	n. a		1800s
Roughness model	n. a		Beading model / Shin et al. (1991) model

Upon completing the simulation, ICE3D generated the geometry of the iced airfoil, creating a computational mesh that was subsequently used to estimate aerodynamic lift and drag coefficients under rime and glaze ice conditions.

2.4 Results and Discussion

The results presented here validate the obtained aerodynamic parameters for the S809, comparing them with experimental data and findings from prior numerical studies on this airfoil (Y. Han et al., 2012; Somers, 1997; Tan, 2020). The performed CFD simulations consider two turbulence models in conjunction with two roughness scenarios and two different types of icing: rime and glaze.

2.4.1 Clean Airfoil

The drag and lift coefficients of the clean airfoil were estimated to assess the aerodynamic loss caused by icing. Subsequently, these results were compared with measured coefficients for the same airfoil at different angles of attack, providing validation for the simulation. The CFD simulation results of the S809 airfoil were validated with experimental data from Somers (1997). The numerical flow coefficients were also compared with those from the CFD study by Tan (2020) using the same turbulence model (Spalart–Allmaras).

The experimental study carried out by Somers (1997) took place at the low-turbulence wind tunnel of the Delft University of Technology Low-Speed Laboratory in the Netherlands. The study’s primary objectives were to achieve a maximum lift coefficient insensitive to roughness and obtain low-profile drag coefficients within a specific range of lift coefficients and Reynolds numbers. The airfoil model used in the experimental study was made of aluminum, with a chord length of 600 mm and a span of 1248 mm. The model was tested at various Reynolds numbers based on the airfoil chord, ranging from 1.0×10^6 to 3.0×10^6. The tests were conducted with the airfoil surface both smooth (without roughness) and with roughness introduced at specific locations (0.02c on the upper surface and 0.05c on the lower surface) to promote the transition of the boundary layer from laminar to turbulent.

Regarding Reynolds number effects, at the design Reynolds number (2.0×10^6), the maximum lift coefficient achieved was approximately 1.01, which met the design objective of 1.0 (Somers, 1997). The trailing-edge stall behaviour was gentle and occurred at approximately 20° angle of attack. Minimal hysteresis was observed at angles of attack beyond the maximum lift and below the minimum lift. Concerning the effect of roughness, Somers (1997) found that the maximum lift coefficient was not significantly affected by the addition of roughness at any of the Reynolds numbers tested. However, when using fixed transition, the drag coefficients tended to be excessively high at both low and high lift coefficients. This fact was primarily attributed to the roughness height being comparable to the boundary-layer thickness on the upper surface at low lift coefficients and on the lower surface at high lift coefficients. This resulted in an additional contribution to drag, known as pressure drag, caused by the roughness of the surface itself. The impact of roughness on drag was more pronounced at a higher Reynolds number.

The simulations by Tan (2020) assessed the aerodynamic performance of the NREL S809 airfoil with a trailing-edge flap. The length of the airfoil chord was 1 m, and a structured mesh of 150.000 cells was used around the airfoil. The simulations were performed using the commercial CFD software ANSYS Fluent 2022 R1 to solve the RANS equations in conjunction with three turbulence models (Spalart–Allmaras, SST k-ω, and Wray–Agarwal) at Reynolds number 10^6 (free stream velocity equal to 15 m/s) at angles of attack from 0° to 20°. The computations were performed with double precision, utilizing a second-order upwind scheme for the convection terms and a second-order central difference scheme for the diffusion terms. The SIMPLE algorithm was employed for the pressure-velocity coupling. Only the results of the unmodified profile with the Spalart–Allmaras turbulence model were used to validate this study.

As shown in Figure 2.6, the lift coefficients estimated using the two turbulence models are close to those obtained experimentally by Somers (1997); however, at an AoA of 15°, the CFD results slightly overpredict the experimental values. The disagreement between computations and experimental data at this AoA can be attributed to the stall experienced by the airfoil, a challenging phenomenon to model computationally.

In the case of the drag coefficient (see Figure 2.7), both turbulence models presented a slight overestimation for angles of attack of 0° and 5° and an underestimation for angles of attack of 10° and 15°. This behaviour is similar to that of Martini et al. (2022) and is associated with the stall phenomenon. The difference between the present SA computations and those of Tan (2020) is only significant at an AoA of 15°, which is attributed to the known drawbacks of the SA turbulence model in regions characterized by high-pressure gradients (O'Brien et al., 2017). Nevertheless, the disparity noted at elevated angles of attack between the experimental data and numerical drag outcomes for the no-iced airfoil was deemed less critical because it appears beyond the operational ranges of the considered wind turbine (Hand et al., 2001; Hu et al., 2018).

Figure 2.8 and Figure 2.9 depict the streamlines around the S809 airfoil, showing the flow recirculation zone (enclosed in the red circle) at an angle of attack of 15° for both turbulence models. The presence of such zones generates a decrease in lift and an increase in drag for the airfoil. The maximum error obtained with the k-ω SST model in C_L was below 10%, while the same error obtained with the Spalart–Allmaras model was 15%. This indicates that the k-ω SST model provides a more accurate estimate of the lift coefficient. On the other hand, when comparing the present C_L curve obtained with the SA turbulence model with the results of Tan (2020), a maximum difference of 6% is observed even though the same turbulence model was used; this may be associated with the fact that this author used a much coarser structured mesh and the ANSYS Fluent software.

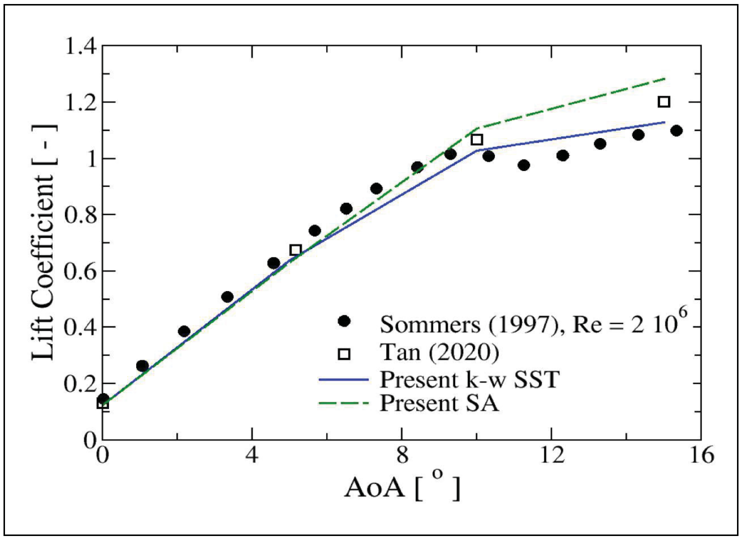

Figure 2.6 Lift coefficient versus AoA for the S809 airfoil, Somers's data from Somers (1997), Tan's data from Tan (2020)

Taken from Contreras Montoya et al. (2023)

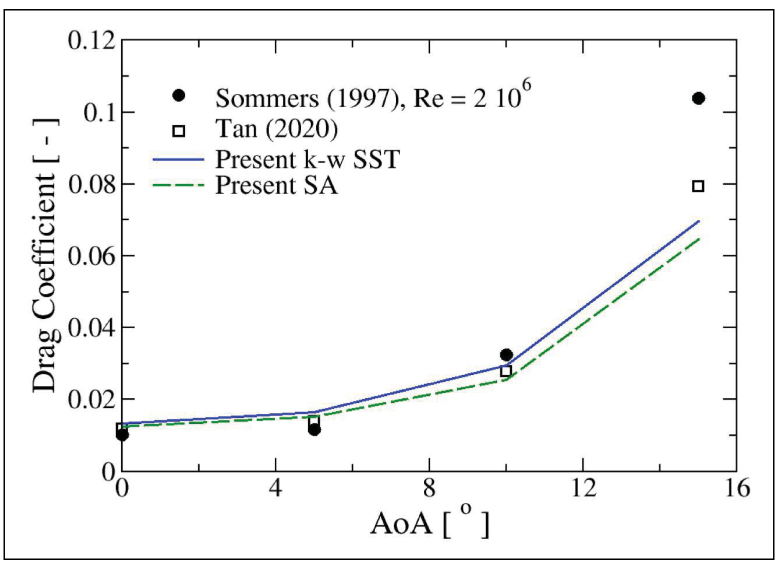

Figure 2.7 Drag coefficient versus AoA for the S809 airfoil, Somers's data from Somers (1997), Tan's data from Tan (2020)

Taken from Contreras Montoya et al. (2023)

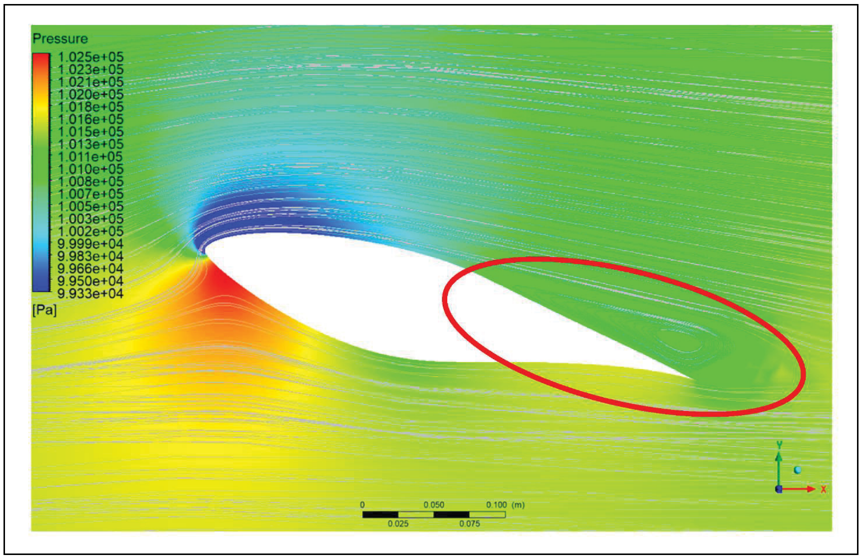

Figure 2.8 Pressure contours and streamlines at AoA of 15° of the clean profile using Spalart–Allmaras turbulence model

Taken from Contreras Montoya et al. (2023)

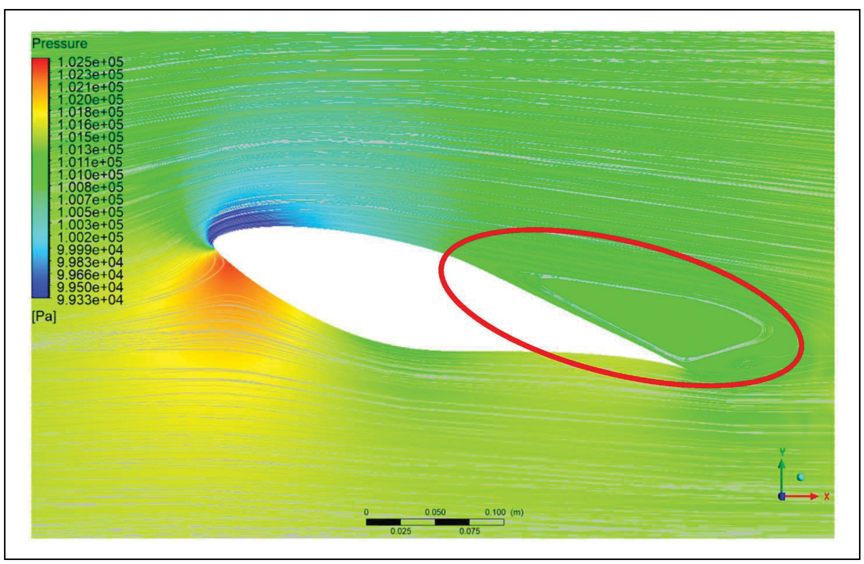

Figure 2.9 Pressure contours and streamlines at AoA of 15° of the clean profile using k-ω SST turbulence model

Taken from Contreras Montoya et al. (2023)

Comparing the outcomes of both turbulence models, the lift coefficient estimate obtained with the Spalart–Allmaras model was approximately 5% higher on average than that obtained with k-ω SST. Consistently, the drag coefficient for the Spalart–Allmaras estimate was approximately 10% lower than that obtained with the k-ω SST model. Further insights about the flow behaviour around the airfoil under separated conditions can be devised by analyzing the skin friction, C_f, and pressure, C_p, coefficients. They are defined as:

$$C_f = \frac{\tau_w}{\frac{1}{2}\rho U^2} \tag{2.3}$$

$$C_p = \frac{p_g}{\frac{1}{2}\rho U^2} \tag{2.4}$$

$$\tau_w = \rho u^{*2} \tag{2.5}$$

Where τ_w is the wall shear stress, and p_g is the local gauge pressure.

Figure 2.10 shows the skin friction coefficient, C_f at AoA of 15°. The trends of both turbulence models are very similar, showing overlapping curves along the intrados (pressure side) and slight differences in the extrados (suction side). The stagnation and separation points in the figure can be identified as those with $C_f = 0$; the first ones are located close to the leading edge, while the second ones are approximately placed at half of the chord. It is observed that the Spalart–Allmaras model predicts a later boundary layer separation than the k-ω SST model, which is consistent with the streamlines depicted in Figure 2.8 and Figure 2.9.

Figure 2.11 displays the pressure coefficients C_p, also at an AoA of 15°. The upper side curves correspond to the suction side (extrados) and those of the lower side to the pressure side (intrados). Both turbulence models predict similar C_p values in the intrados. However, the SA model provides more negative pressure coefficients than the k-ω SST model along the first half of the chord in the extrados. The two models provide similar values in the second half of the chord. The higher suction forecasted by the SA model reflects a higher lift coefficient than that obtained with the k-ω SST model, as confirmed in Figure 2.6. Consequently, the SA also yields a lower drag coefficient than the two-equation model.

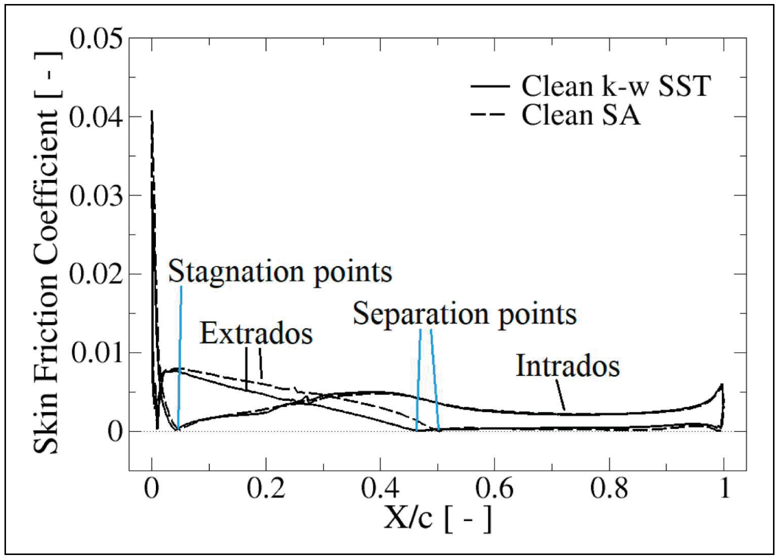

Figure 2.10 Skin friction coefficient at an AoA of 15° for the clean profile using both turbulence models

Taken from Contreras Montoya et al. (2023)

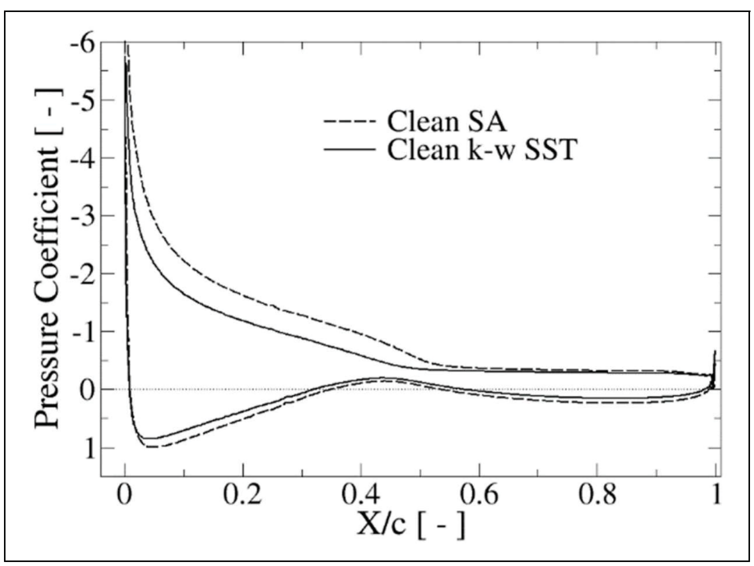

Figure 2.11 Pressure coefficient at an AoA of 15° for the clean profile using both turbulence models

Taken from Contreras Montoya et al. (2023).

In the subsequent analysis, considering that icing increases the likelihood of flow separation, the performance of both turbulence models in the presence of rime and glaze ice was investigated by comparing their results with those of the clean airfoil. Moreover, the effect of the roughness modeling on the aerodynamic coefficients is also studied.

2.4.2 Iced Airfoil

Figure 2.12 illustrates the accumulation of ice at the leading edge. A minor portion of the collected supercooled water does not instantly freeze upon contact with the airfoil's leading edge, leading the water to subsequently flow back and freeze at the trailing edge beyond the impingement zone, a phenomenon observed in the study by Fortin et Perron (2009b).

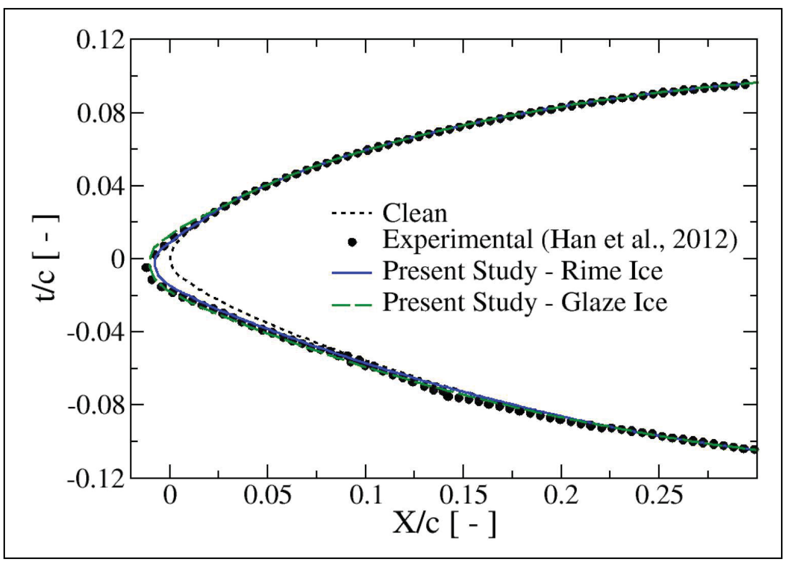

Figure 2.12 Comparison of the predicted ice shape (non-dimensional thickness versus non-dimensional chord) with Y. Han et al. (2012) experimental results

Taken from Contreras Montoya et al. (2023).

Concerning the leading edge (see Figure 2.12), the ice shape closely resembled the one depicted by Y. Han et al. (2012). This similarity enables us to assert that the model and the simulation tools employed are adequate. However, the aerodynamic coefficients could not be validated because this study only showed the shape of the ice generated at the wind tunnel airfoil. However, since the alteration in the airfoil aerodynamic coefficients depends on the airfoil shape, it was decided that simulating a shape similar to that obtained experimentally would be sufficient. The validation was performed for both turbulence models.

Figure 2.12 shows that the ice shape for the two types of ice is quite similar, agreeing with Y. Han et al. (2012), which is remarkable. Despite a 50% increase in LWC and a 35% increase in MVD in the case of the glaze ice, the difference in the accumulated ice shape at the leading edge is minimal and even comparable to the results obtained experimentally under rime ice conditions.

Since FENSAP-ICE performs the remeshing for the iced airfoil, it was decided to verify if the condition imposed for the y^+ was still satisfied. This parameter is essential since the performance of the k-ω SST model depends on its ability to describe the boundary layer development, so this value should be below 5 (or even less than 1) for better accuracy (ANSYS Inc., 2013). Although not shown, the values of y^+ for the clean airfoil are less than 1 throughout the profile, except for the leading-edge zone (30% of the profile), which reaches a maximum value of 2.15. However, in the iced airfoil cases, the y^+ moderately increases, reaching a maximum value of 3.14, mainly at the airfoil's leading edge. This is to be expected since it is the area where the ice accumulates. Therefore, the corresponding elements experience a rearrangement or deformation.

Despite the increase in y^+, it can be stated that the remeshing process for the conditions studied is acceptable, and the meshes generated by the software satisfy the primary conditions for the turbulence model to provide accurate results. This, in turn, highlights the importance and attention that should be paid to the initial meshing process.

The results obtained for each simulated ice regime (dry and wet) are presented below. For each case, the effect of the turbulence and roughness models on the aerodynamic coefficients of the iced airfoil was evaluated.

2.4.2.1 Dry Regime – Rime Ice

Rime ice forms when supercooled water droplets, which are liquid droplets at temperatures well below freezing, i.e., lower than $-10\ ^\circ C$, come into contact with the cold surfaces of the turbine blades. These supercooled droplets freeze quickly upon contact, adhering to the blade surfaces. Following Battisti (2015), rime ice formation is favoured at low temperatures, low liquid water content, small mean volume diameter, and low air velocities.

Regarding the results for the lift coefficient (see Figure 2.13), the obtained C_L was slightly higher than in the case of the no-ice airfoil at an angle of attack of 5°, 1.04% with the Spalart–Allmaras model and less than 2% with the k-ω SST model. This fact happens at low angles of attack, and it has been observed previously (Blasco et al., 2017; Caccia & Guardone, 2023; Somers, 1997), probably because the ice-induced roughness at this AoA has a positive effect of triggering the transition from laminar to turbulent boundary layer, which is less prone to separation than the laminar one.

There is a noticeable increase in drag (Figure 2.14) at this incidence angle, promoted by both the ice shape and the induced roughness (Battisti, 2015; Fortin & Perron, 2009b). However, for larger angles of attack, C_L in the iced configurations is notably reduced, and C_D is vastly increased regarding the clean case; in fact, drag augments faster with growing AoA. This is because apparent roughness causes the stall phenomenon to be anticipated up to an angle of around 10°, as indicated in Figure 2.13. The most significant differences in lift between the different models are observed at an AoA of 10°. This fact can be explained by the sudden expansion of the separation zone, the uncertainty of the transition position, and the inaccuracy of the turbulence and roughness models in predicting them.

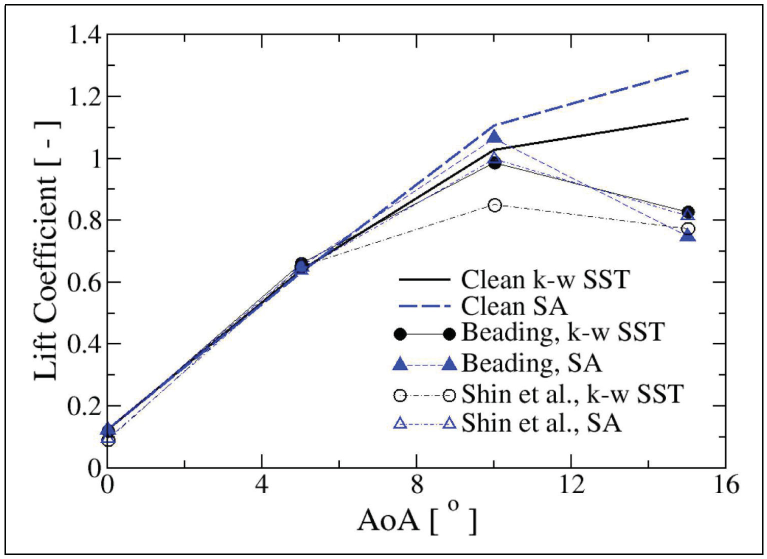

Figure 2.13 Lift coefficient for the rime ice, Shin's data from Shin et al. (1991)

Taken from Contreras Montoya et al. (2023)

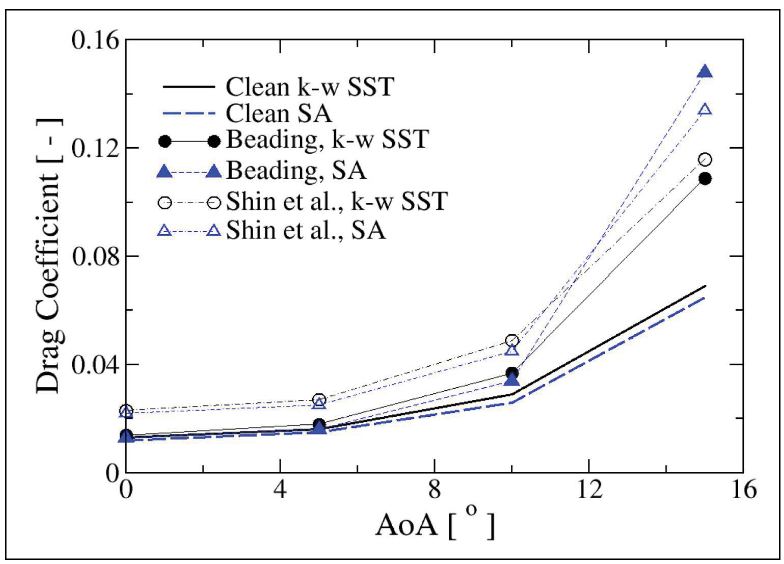

Figure 2.14 Drag coefficient for the rime ice, Shin's data from Shin et al. (1991)

Taken from Contreras Montoya et al. (2023)

Interestingly, the Shin et al. (1991) roughness model predicts a more significant lift decrease than the beading model at high angles of attack. However, in the case of the SA turbulence model at 15°, such a trend is inverted, and the C_L provided by the beading model is lower than for the Shin et al. (1991) model, a fact that does not happen for the k-ω SST formulation.

Figure 2.15 and Figure 2.16 show the behaviour of the skin friction (C_f) and pressure (C_p) coefficients in the iced configurations with rime ice at an AoA of 15°. Compared with Figure 2.10 and Figure 2.11, it can be seen that the peak of skin friction at the leading edge is higher in the case of ice than in the clean configuration; conversely, the maximum pressure coefficient magnitude at the exact location is lower in the iced scenario than in the clean situation. Moreover, the overpressure in intrados is higher in the clean profile than in the case with ice; at the same time, in the first half of the chord, the suction is also higher than in the iced configuration. As a result, the lift coefficient decreases with the presence of ice. Regarding the friction coefficient, rime ice occurrence increases C_f in the intrados and promotes an earlier boundary layer detachment than in the clean profile. Consequently, the separated flow region is the largest in the presence of rime ice, aggravating the stall phenomenon and implying lower lift and higher drag than in the no-ice configuration. Looking at Figure 2.15 and Figure 2.16, the performance of both turbulence models in the iced scenario is very similar, showing some differences only in the location of the flow separation point in the extrados, which is predicted earlier by the SA than by the k-ω SST model.

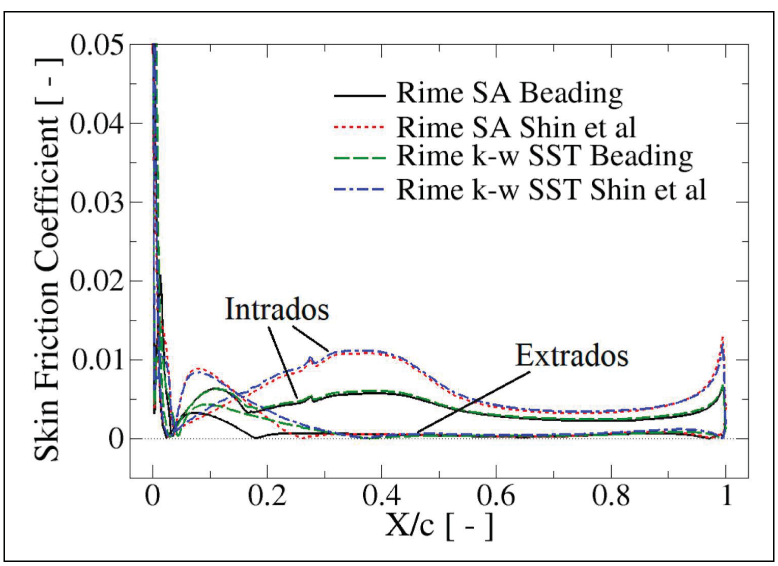

Figure 2.15 Rime ice: skin friction coefficient at an AoA of 15° of the iced profile with both turbulence and roughness models, Shin's data from Shin et al. (1991)

Taken from Contreras Montoya et al. (2023)

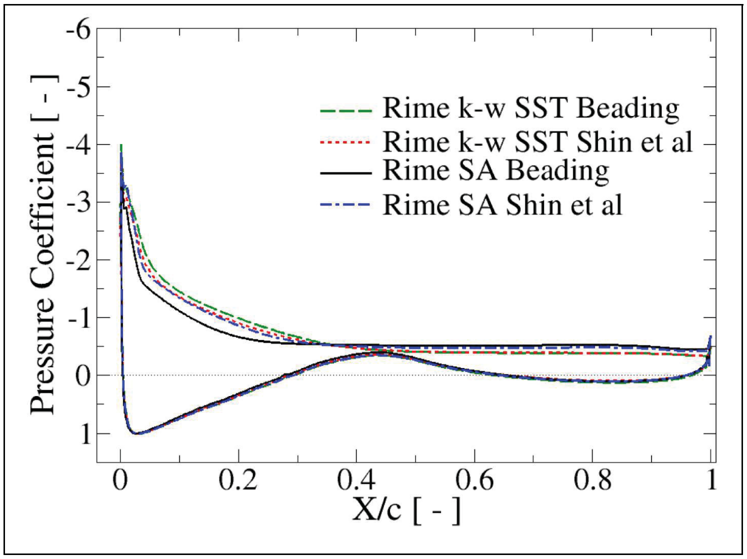

Figure 2.16 Rime ice: pressure coefficient at AoA of 15° of the clean profile with both turbulence and roughness models, Shin's data from Shin et al. (1991)

Taken from Contreras Montoya et al. (2023)

Regarding the influence of the roughness model, it is found that its larger influence happens in the skin friction coefficient (Figure 2.15), showing only a moderate effect on C_p distribution along the leading half chord of the profile extrados (Figure 2.16). In the intrados, the Shin et al. (1991) model predicts a noticeably higher C_f than the beading model, which is attributed to the extent of the rough region: the roughness height is uniform in the case of Shin et al. (1991), while in the beading model, it is higher close to the leading edge, where the ice layer develops. Therefore, the larger the rough surface, the larger the wall shear stress, as should be expected. A similar situation happens in the extrados; logically, the friction coefficient is close to zero behind the flow separation point. Here, the beading model predicts an earlier flow separation than in the Shin et al. (1991) model, which implies a larger recirculation bubble on the extrados; this is illustrated in Figure 2.17 and Figure 2.18 by the streamlines in the case of the SA turbulence model. Interestingly, the beading model in the intrados predicts a secondary maximum of C_f close to the leading edge, around 10% of the chord length, precisely where the ice generates the higher roughness height. On the other hand, owing to the regular roughness distribution, the Shin et al. model displays a maximum much later, around 40% of the chord.

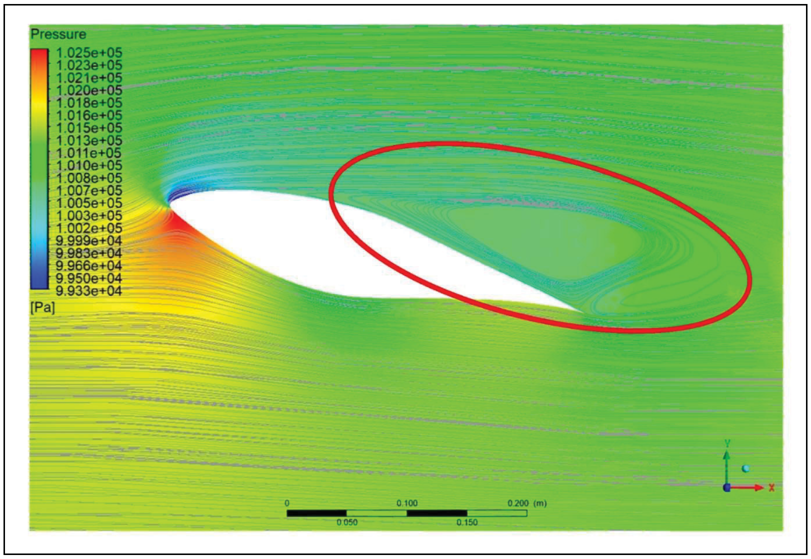

Figure 2.17 Rime ice: pressure contours and streamlines at AoA of 15°; beading model and Spalart – Allmaras model

Taken from Contreras Montoya et al. (2023)

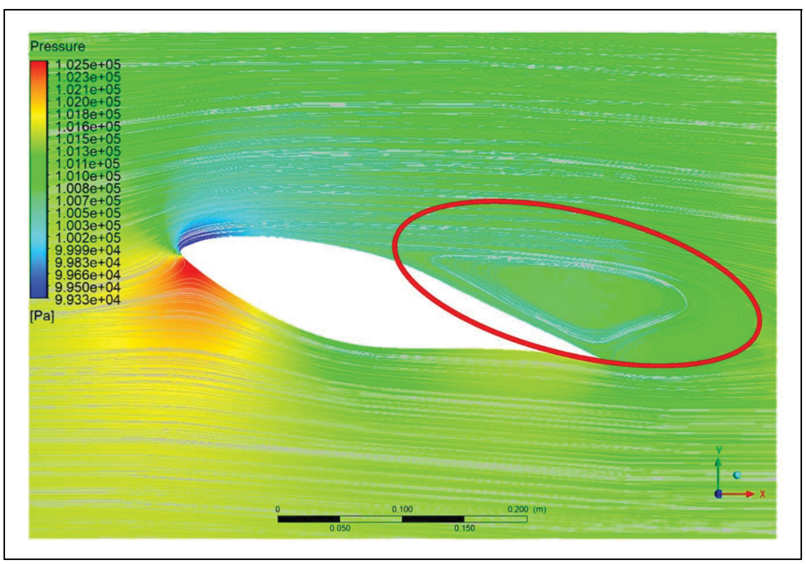

Figure 2.18 Rime ice: pressure contours and streamline at AoA of 15°; Shin et al. (1991) model and Spalart – Allmaras model

Taken from Contreras Montoya et al. (2023)

As shown in Figure 2.19, the roughness estimated by the beading model and caused by ice affects mainly the airfoil leading edge (17% of the chord in this case). In comparison, the roughness estimated by Shin et al. is a fixed value along the 100% of the airfoil. This may imply an underestimation of the lift coefficient since roughness may accelerate the separation of the boundary layer. As can be seen from Figure 2.19, the roughness estimated with the Spalart–Allmaras model is somewhat lower than that estimated by the k-ω SST model. From that figure, it can be seen that in the beading model, the ice roughness extends much more on the intrados than on the extrados.

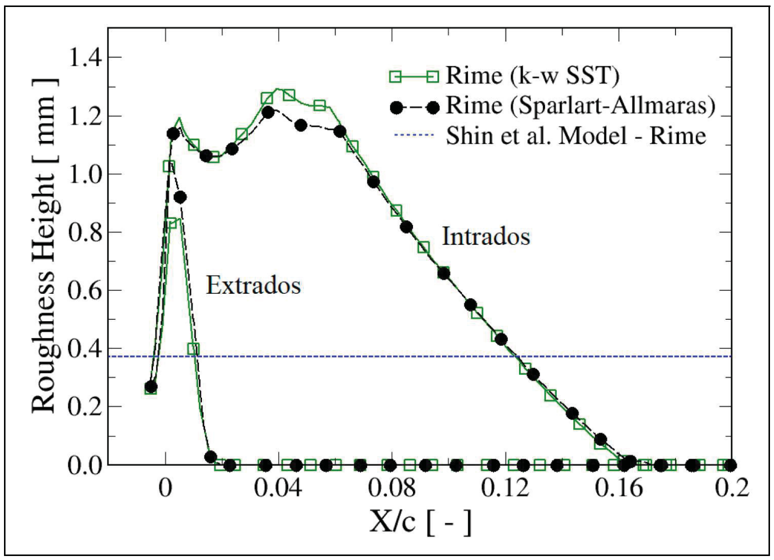

Figure 2.19 Distribution of the roughness height along the S809 airfoil for rime ice at an AoA of 15°, Shin's data from Shin et al. (1991)

Taken from Contreras Montoya et al. (2023)

Using the beading model (see Table 2.5), it was found that for angles of attack of 0° and 10°, the loss in lift coefficient using both turbulence models was less than 5%. For an angle of attack of 5°, around a 3% increase in the lift coefficient was obtained with the two turbulence models. However, for 15°, there was a loss of 41.74% with the Spalart–Allmaras model and 26.78% with the k-ω SST model. The average loss in the lift coefficient was 9.10% using the k-ω SST model and 12.59% using the Spalart–Allmaras model. Regarding the drag coefficient, the behaviour was as expected, and as the angle of attack increased, so did the drag coefficient, reaching its maximum at 15°. Again, the highest increase was estimated by the Spalart–Allmaras model, with an average value of 43.93%.

Table 2.5 The aerodynamic loss was estimated using the beading model with rime ice
Taken from Contreras Montoya et al. (2023)

	Clean				Iced (beading model)				% Loss (Iced to Clean)			
	Spalart–Allmaras		k-ω SST		Spalart–Allmaras		k-ω SST		Spalart–Allmaras		k-ω SST	
AOA (°)	C_L	C_D	C_L	C_D	C_L	C_D	C_L	C_D	C_L	C_D	C_L	C_D
0	0.124	0.012	0.123	0.013	0.124	0.013	0.120	0.014	-1.88%	6.73%	-2.16%	8.68%
5	0.632	0.015	0.639	0.016	0.651	0.016	0.662	0.018	3.13%	8.81%	3.43%	10.61%
10	1.106	0.026	1.029	0.029	1.066	0.034	0.988	0.037	-3.61%	31.67%	-4.04%	26.37%
15	1.284	0.065	1.129	0.069	0.748	0.148	0.827	0.109	-41.74%	128.51%	-26.78%	57.79%
Average:									**-12.59%**	**43.93%**	**-9.10%**	**25.86%**

The Shin et al. model, shown in Table 2.6, predicts a more pronounced drop in C_L regarding the beading model: an average value of 17% for the SA model and around 19% for the k-ω SST model. However, the trend at an AoA of 5° is maintained with a forecasted slight increment of around 1% by both turbulence models. Likewise, the Shin et al. (1991) model predicts a considerable augmentation in the drag coefficient, with mean increments of more than 80% and 68% for the SA and k-ω SST models, respectively.

Table 2.6 The aerodynamic loss was estimated using the Shin et al. (1991) model with rime ice
Taken from Contreras Montoya et al. (2023)

	Clean				Iced (Shin et al. model)				% Loss (Iced to Clean)			
	Spalart–Allmaras		k-ω SST		Spalart–Allmaras		k-ω SST		Spalart–Allmaras		k-ω SST	
AOA (°)	C_L	C_D	C_L	C_D	C_L	C_D	C_L	C_D	C_L	C_D	C_L	C_D
0	0.124	0.012	0.123	0.013	0.095	0.022	0.089	0.023	-22.96%	72.35%	-27.33%	72.70%
5	0.632	0.015	0.639	0.016	0.638	0.025	0.652	0.027	1.04%	66.96%	1.87%	68.00%
10	1.106	0.026	1.029	0.029	0.999	0.045	0.851	0.049	-9.61%	77.00%	-17.33%	65.94%
15	1.284	0.065	1.129	0.069	0.815	0.134	0.774	0.116	-36.50%	106.89%	-31.48%	66.70%
Average:									**-17.53%**	**80.80%**	**-19.50%**	**64.34%**

Therefore, looking at the numbers in Table 2.5 and Table 2.6, which are shown in Figure 2.13 and Figure 2.14, it can be stated that the Shin et al. model tends to predict lower C_L and higher C_D in the iced airfoil than the beading model. This fact is attributed to the Shin et al. model, which assumes that the entire profile is covered by ice. Therefore, the whole profile is considered to be a rough surface. On the contrary, the beading model assumes that the increase in roughness occurs only in areas contaminated by ice. In the case of the S809 profile, only the leading edge is contaminated (see Figure 2.12 and Figure 2.19).

Additionally, Figure 2.15 and Figure 2.16 show that turbulence modeling has a lower impact on the pressure and skin friction coefficients of the iced airfoil than the roughness model.

2.4.2.2 Wet Regime – Glaze Ice

Glaze ice is formed in temperatures between −10 and 0 °C. After impact, the droplet runs along the surface in the flow direction before freezing completely, occupying a wider surface than in the case of rime ice. The frozen liquid forms a smooth, transparent, and translucent layer of ice on the blade surface.

Regarding the results for the lift coefficient (see Figure 2.20), similarly to what happened for rime ice, the obtained C_L was a little bit over that of the clean airfoil at an angle of attack of 5°, between 2% and 3% depending on the turbulence and roughness models. However, the lift coefficient decreases noticeably for larger angles of attack, even more than in the case of rime ice. Moreover, the drag coefficient increases simultaneously, reaching higher values than in the case of rime ice (see Figure 2.21). Of course, this is again due to the anticipation of the stall phenomenon, which is illustrated by the streamline's behaviour shown in Figure 2.22 and Figure 2.23 in the case of the SA turbulence model and for the two considered roughness models.

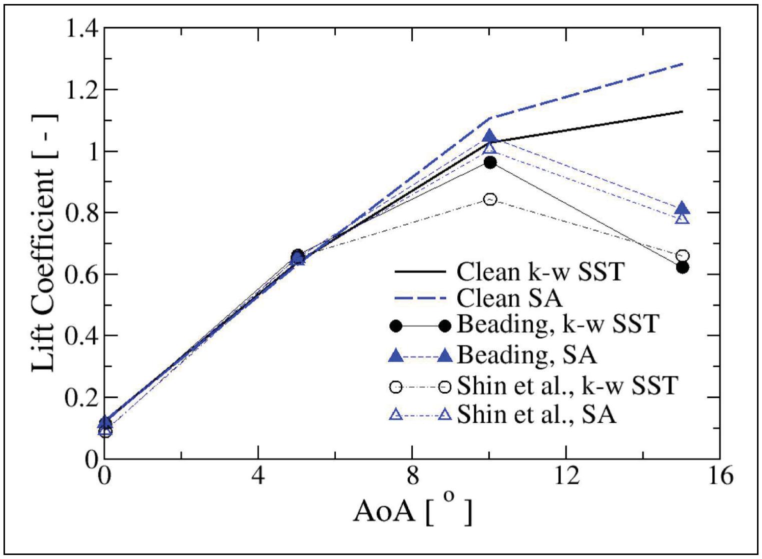

Figure 2.20 Lift coefficient for the glaze ice, Shin's data from Shin et al. (1991)

Taken from Contreras Montoya et al. (2023)

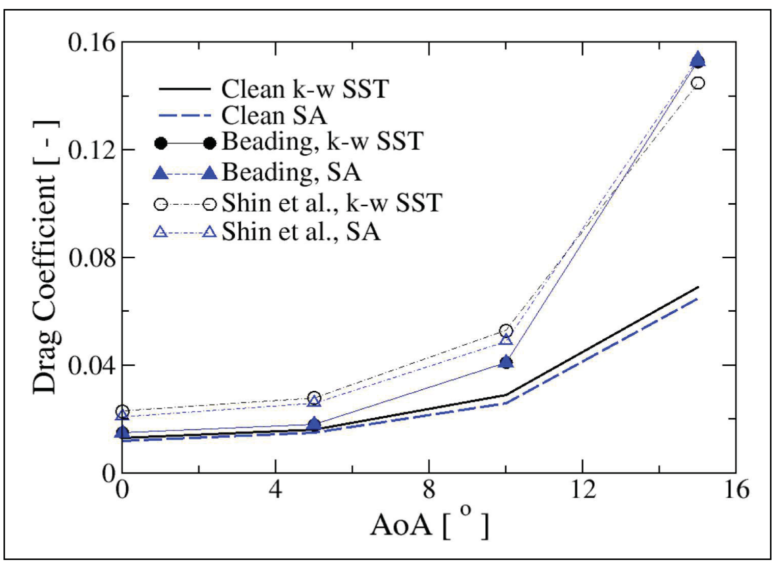

Figure 2.21 Drag coefficient for the glaze ice, Shin's data from Shin et al. (1991)

Taken from Contreras Montoya et al. (2023)

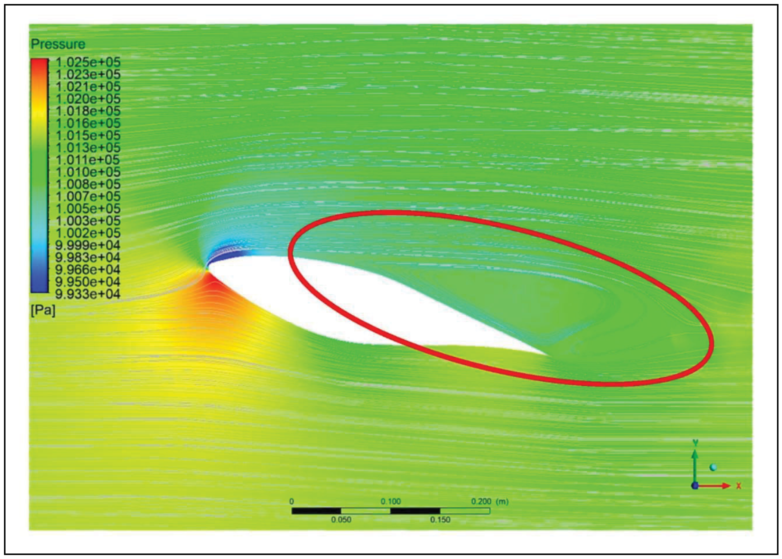

Figure 2.22 Glaze ice: pressure contours and streamlines at an AoA of 15°; beading and Spalart – Allmaras models

Taken from Contreras Montoya et al. (2023)

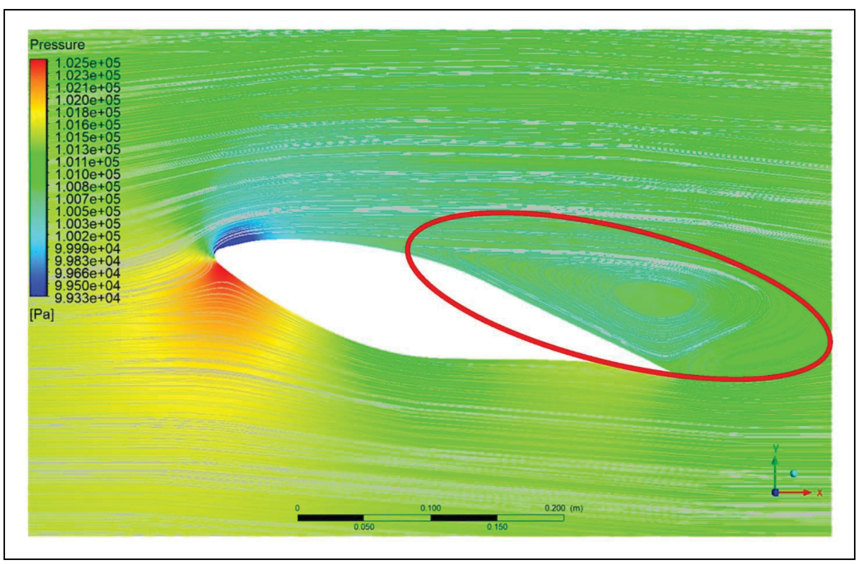

Figure 2.23 Glaze ice: pressure contours and streamlines at an AoA of 15°; Shin et al. (1991) model and Spalart – Allmaras model

Taken from Contreras Montoya et al. (2023)

Figure 2.24 and Figure 2.25 show the behaviour of the skin friction (C_f) and pressure (C_p) coefficients, respectively, in the iced configurations with glaze ice at an AoA of 15°. When comparing such coefficients with the clean profile scenario, the trends are similar to those observed with rime ice: the C_f peak at the leading edge is higher than in clean conditions, and C_p magnitude in the same position is lower than in the no-ice scenario, being even lower than in the case of rime ice (Figure 2.25). This observation is consistent with the lower C_L coefficients attained under glaze ice (Figure 2.20). In the case of the friction coefficient, shown in Figure 2.24, the separation points in the extrados are not so clearly identified as in the clean profile; the C_f curves show, for all the cases, a smooth decreasing shape reaching very low values already at 15% of the chord, suggesting a detached flow, as observed in Figure 2.22 and Figure 2.23. As for rime ice, both turbulence models provide very similar results for both coefficients, with the differences mainly located in the area between the leading edge and 20% of the chord. Here, the C_p and C_f predicted by the SA model are somewhat higher than those provided by the k-ω SST model.

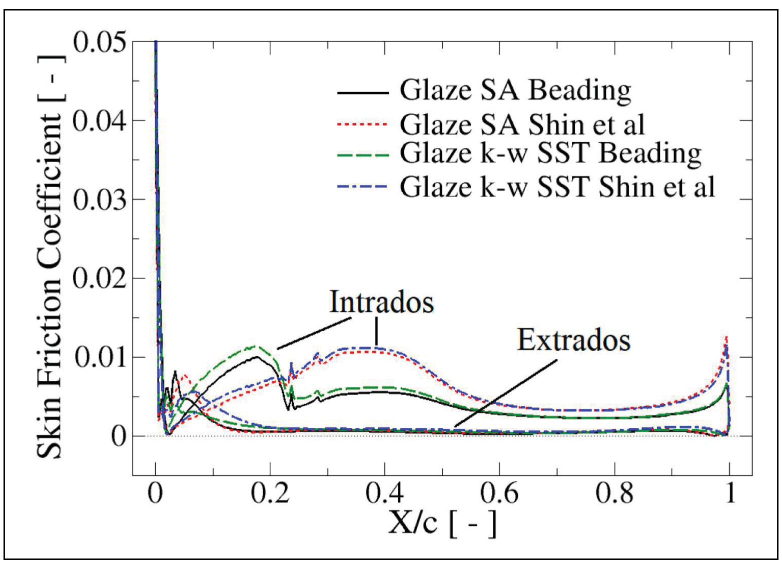

Figure 2.24 Glaze ice: skin friction coefficient at an AoA of 15° of the iced profile with both turbulence and roughness models, Shin's data from Shin et al. (1991)

Taken from Contreras Montoya et al. (2023)

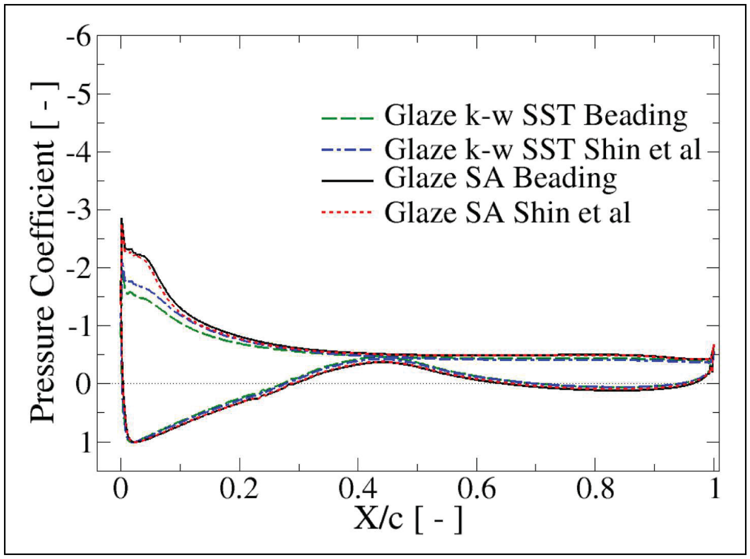

Figure 2.25 Glaze ice: pressure coefficient at an AoA of 15° of the iced profile with both turbulence and roughness models, Shin's data from Shin et al. (1991)

Taken from Contreras Montoya et al. (2023)

The influence on the same coefficients of the roughness model can also be seen in Figure 2.24 and Figure 2.25. Apparently, C_p is only slightly modified by the roughness model, being noticeable only in the leading 20% of the chord in the profile extrados for the k-ω SST model. However, differences are more evident in the skin friction coefficient. In the intrados, similar to what happened with rime ice, the secondary maximum of C_f predicted by the Shin et al. model is close to 40% of the chord, while the beading model predicts a bump near the leading edge with a maximum of around 20% of the chord; the extent of such a bump coincides with the region of the profile contaminated with ice (see Figure 2.26). In the extrados, the Shin et al. model predicts higher values of C_f than the beading model, except perhaps in the area very close to the leading edge. In summary, it can be stated that the Shin et al. model provides higher values of the skin friction coefficient than the beading model; however, the last one can concentrate the friction effects on the area where the ice is deposited, while the first model distributes such an influence along the whole profile. In this sense, it can be argued that the beading model responds better to the physics of the problem than the Shin et al. model, at least for the present application to wind turbine profiles.

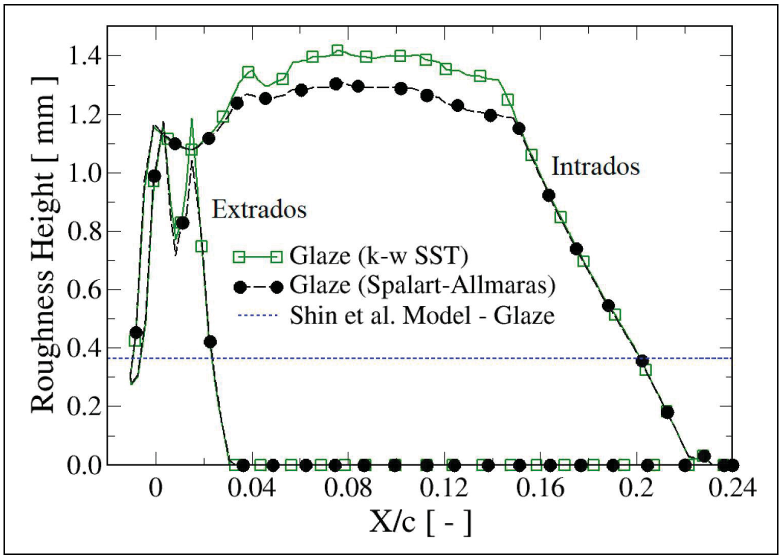

Figure 2.26 Distribution of the roughness height along the S809 airfoil for glaze ice at an AoA of 15°, Shin's data from Shin et al. (1991)

Taken from Contreras Montoya et al. (2023)

As shown in Figure 2.26, the roughness estimated by the beading model in the case of glaze ice affects approximately 24% of the airfoil. As seen from that figure, the roughness estimated with the Spalart–Allmaras model is lower than that estimated by the k-ω SST model (around 8%). On the contrary, the Shin et al. model predicts a uniform roughness along the profile with a very similar value to the case of rime ice.

Using the beading model (see Table 2.7), it was found that for angles of attack of 0° and 10°, the loss in lift coefficient using both turbulence models was less than 7%. For the angle of attack of 5°, a 3.5% increase in the lift coefficient was obtained with the two turbulence models. However, at 15°, there was a loss of 36.71% with the Spalart–Allmaras model and 44.65% with the k-ω SST model. The average loss in the lift coefficient was 15.10% using the k-ω SST model and 12.80% using the Spalart–Allmaras model. As in the rime ice conditions, the drag coefficient followed the expected behaviour, increasing monotonically with the angle of attack, reaching its maximum at 15°. Again, the highest increase was estimated by the Spalart–Allmaras model, with an average value of 59.34%.

Table 2.7 The aerodynamic loss was estimated using the beading model with glaze ice
Taken from Contreras Montoya et al. (2023)

	Clean				Iced (beading model)				% Loss (Iced to Clean)			
	Spalart–Allmaras		k-ω SST		Spalart–Allmaras		k-ω SST		Spalart–Allmaras		k-ω SST	
AOA (°)	C_L	C_D	C_L	C_D	C_L	C_D	C_L	C_D	C_L	C_D	C_L	C_D
0	0.124	0.012	0.123	0.013	0.117	0.015	0.116	0.015	-5.80%	18.25%	-6.04%	19.46%
5	0.632	0.015	0.639	0.016	0.653	0.018	0.663	0.018	3.32%	20.08%	3.55%	20.68%
10	1.106	0.026	1.029	0.029	1.047	0.041	0.966	0.041	-5.39%	61.91%	-6.15%	48.20%
15	1.284	0.065	1.129	0.069	0.812	0.153	0.625	0.153	-36.71%	137.12%	-44.65%	119.05%
Average:									**-12.80%**	**59.34%**	**-15.10%**	**51.85%**

The results obtained with the Shin et al. model in the wet regime are presented in Table 2.8 and follow similar trends as in rime ice. In this case, the average drop in the lift coefficient in the ice scenario is around 19% in the SA model and 23% in the k-ω SST model. A slight increase of about 2% in C_L is predicted for an AoA of 5°, similar to what happened with the beading model. At the same time, C_D increases with mean increments of around 94% and 83% for the one and two-equation turbulence models.

Table 2.8 Aerodynamic loss was estimated using the Shin et al. (1991) model with glaze ice
Taken from Contreras Montoya et al. (2023)

	Clean				Iced (Shin et al. model)				% Loss (Iced to Clean)			
	Spalart–Allmaras		k-ω SST		Spalart–Allmaras		k-ω SST		Spalart–Allmaras		k-ω SST	
AOA (°)	C_L	C_D	C_L	C_D	C_L	C_D	C_L	C_D	C_L	C_D	C_L	C_D
0	0.124	0.012	0.123	0.013	0.092	0.021	0.089	0.023	-25.39%	72.10%	-29.98%	72.81%
5	0.632	0.015	0.639	0.016	0.643	0.026	0.656	0.028	1.85%	70.89%	2.47%	71.71%
10	1.106	0.026	1.029	0.029	1.005	0.049	0.844	0.053	-9.12%	93.16%	-18.05%	78.95%
15	1.284	0.065	1.129	0.069	0.778	0.154	0.661	0.145	-39.37%	138.91%	-41.44%	109.14%
Average:									**-18.93%**	**93.77%**	**-22.98%**	**83.15%**

The Shin et al. model generally predicts lower C_L and higher C_D than the beading model, which is the same trend as in rime ice. Again, this difference is mainly attributed to the airfoil area covered by ice (see Figure 2.12 and Figure 2.26). On the other hand, the trends of the influence of the ice roughness model on the aerodynamic performance of the S809 airfoil are very similar for both turbulence models, SA and k-ω SST (see Table 2.7 and Table 2.8). This fact, together with the curves of C_f and C_p shown in Figure 2.24 and Figure 2.25, means that, in terms of the simulation outcomes, the modeling of ice-induced roughness is more critical than the election of turbulence model.

2.4.3 Analysis of the Aerodynamic Performance of the Iced Airfoils

As anticipated, ice on the S809 profile reduced the lift coefficient under both regimes, rime and glaze (Figure 2.13 and Figure 2.20), while C_D increased (Figure 2.14 and Figure 2.21). This agrees with the results in the literature (Bodenlle-Toral, García-Regodeseves, & Pandal-Blanco, 2022; Y. Han et al., 2012; Homola et al., 2012; Jasinski et al., 1998; Martini et al., 2022). The following tables compare the aerodynamic coefficients between the different ice scenarios considering the roughness and turbulence models employed.

The average difference in the lift coefficient (see Table 2.9) between the dry regime and the wet regime using the beading model was 7.67% with the k-ω SST model and 3.66% with the Spalart–Allmaras model, indicating a variation between the two turbulence models of less than 5%. However, for an angle of attack of 15°, the Spalart–Allmaras model estimates a gain in the lift coefficient of 8.63%, while the k-ω SST model estimates a loss of 24.41%. This difference can be attributed to the limitations of the Spalart–Allmaras model under adverse pressure gradient conditions.

The average difference in the drag coefficient (see Table 2.10) was higher, 18.78% with the k-ω SST and 11.97% with the Spalart–Allmaras models, indicating a difference between the two turbulence models of less than 7%. This increase in C_D is expected since the surface of the airfoil covered by ice was 5% greater in the wet regime than in the dry regime.

Table 2.9 Lift coefficient comparison of regimes using the beading model

Taken from Contreras Montoya et al. (2023)

AoA (°)	k-ω SST Model			Spalart-Allmaras Model		
	CL Rime	**CL Glaze**	**% Diff**	**CL Rime**	**CL Glaze**	**% Diff**
0	0.120	0.116	-3.97%	0.121	0.117	-3.99%
5	0.662	0.663	0.11%	0.652	0.653	0.18%
10	0.988	0.966	-2.20%	1.066	1.047	-1.84%
15	0.827	0.625	-24.41%	0.748	0.812	8.63%
Average			**7.67%**			**3.66%**

Table 2.10 Drag coefficient comparison of regimes using the beading model

Taken from Contreras Montoya et al. (2023)

AoA (°)	k-ω SST Model			Spalart-Allmaras Model		
	CD Rime	**CD Glaze**	**% Diff**	**CD Rime**	**CD Glaze**	**% Diff**
0	0.015	0.016	9.92%	0.013	0.015	10.80%
5	0.018	0.020	9.10%	0.017	0.018	10.36%
10	0.037	0.044	17.27%	0.034	0.041	22.96%
15	0.110	0.152	38.83%	0.148	0.153	3.77%
Average			**18.78%**			**11.97%**

The average difference in the lift coefficient (Table 2.11) between the dry and wet regimes using the Shin et al. model was 4.91% with the k-ω SST model and 2.25% with the Spalart–Allmaras model. The average difference in the drag coefficient (see Table 2.12) was slightly higher, being 8.89% with the k-ω SST model and 6.78% with the Spalart–Allmaras model. In these cases, the difference between the turbulence models was less than 3%. Similar findings were reported by Martini et al. (2022) for a different airfoil (NACA 64-618).

As can be observed from the previous values, the predictions of aerodynamic characteristics by the Shin et al. model are less sensitive to the type of ice regime than those by the beading model, presenting lower variations in both the lift and drag coefficients.

Table 2.11 Lift coefficient comparison of regimes using the Shin et al. model
Taken from Contreras Montoya et al. (2023)

AoA (°)	k-ω SST Model			Spalart-Allmaras Model		
	CL Rime	**CL Glaze**	**% Diff**	**CL Rime**	**CL Glaze**	**% Diff**
0	0.089	0.086	-3.65%	0.095	0.092	-3.15%
5	0.652	0.656	0.60%	0.638	0.643	0.80%
10	0.851	0.844	-0.87%	1.000	1.005	0.54%
15	0.774	0.661	-14.53%	0.815	0.778	-4.52%
Average			**4.91%**			**2.25%**

Table 2.12 Drag coefficient comparison of regimes using the Shin et al. model
Taken from Contreras Montoya et al. (2023)

AoA (°)	k-ω SST Model			Spalart-Allmaras Model		
	CD Rime	**CD Glaze**	**% Diff**	**CD Rime**	**CD Glaze**	**% Diff**
0	0.023	0.023	0.06%	0.022	0.022	-0.14%
5	0.028	0.028	2.21%	0.025	0.026	2.36%
10	0.049	0.053	7.84%	0.045	0.049	9.13%
15	0.116	0.146	25.46%	0.134	0.155	15.48%
Average			**8.89%**			**6.78%**

Regarding the ice type, the present results indicate that the wet regime negatively impacts the aerodynamic performance of the airfoil. Comparing the aerodynamic coefficients of the airfoil evaluated under glaze ice versus the clean airfoil, the lift loss using the k-ω SST model and the beading model was 6% higher than that obtained with the rime ice (compare values in Table 2.5 and Table 2.7). In contrast, with the Shin et al. model, the increase was 3.48% (compare values in Table 2.6 and Table 2.8). However, when evaluating the Spalart–Allmaras model, the increase in lift loss between the two regimes using either roughness model was less than 2%. In the case of the drag coefficient, the difference between the regimes was more evident.

Regarding the combination of k-ω SST and the beading model, the increase was 25.99% (compare values in Table 2.5 and Table 2.7), while with the Shin et al. model, it was 14.82% (compare values in Table 2.6 and Table 2.8). As with the lift coefficient, the increase was lower using the Spalart–Allmaras model, 15.41% combined with the beading model and 12.97% with the Shin et al. model. The above affirms that the airfoil performance will be more affected under conditions of glaze ice.

The combination of the k-ω SST turbulence model and the Shin et al. model for the roughness modeling generated the highest loss of lift coefficient for both regimes (19.50% for rime ice and 22.98% for glaze ice). Similar findings were reported by Martini et al. (2022) for a NACA 64-618 airfoil where the C_L loss was 22.54% under rime ice conditions. The combination of the Spalart–Allmaras turbulence model and the Shin et al. model generated the highest drag coefficient increase for both regimes (80.80% for rime ice and 93.77% for glaze ice). The findings reported by Martini et al. (2022) under rime ice using the same models are notably higher, with some exceeding 120%. Differences in the airfoil design can account for these variations. For instance, the S809 profile has been specifically designed to obtain lower drag coefficients and maximum lift and to be insensitive to roughness (Somers, 1997). The clean airfoil yielded comparable outcomes with a slight discrepancy in drag estimation at a 15° angle of attack when employing both turbulence models. This variation is attributed to the proximity to conditions of flow separation on the airfoil's suction side. As previously explained, the Spalart–Allmaras turbulence model exhibits limitations in boundary layer separation scenarios, which are accentuated when ice accumulates on the airfoil.

A related study was carried out by Caccia et Guardone (2023), in which the authors searched to verify whether the adverse effect on the aerodynamic performance of the profiles was due to the ice shape or the roughness. The roughness model of Shin et al. was employed by Caccia et Guardone (2023), and the model known as Wright's relation was determined from experimental measurements of the roughness height as a function of the freezing fraction at the stagnation point. The analysis was performed only for the dry regime (freezing fraction equal to 1) in different sections of the NREL 5MW turbine blade (Jonkman, Butterfield, Musial, & Scott, 2009) composed at the base by DU profiles and, at the tip, by NACA 643-618 profiles. Using the Spalart–Allmaras turbulence model, the roughness values were evaluated in two ways: the first one only in the area where ice accumulated (similar to what the FENSAP-ICE beading model does) and the second one at 0.44 m along the leading edge of the profile on both the suction and pressure sides. Caccia et Guardone (2023) found that ice caused a degradation in profile aerodynamic performance in all the evaluated cases due to ice shape and roughness. Regarding the ice shape, the icing condition evaluated generated a “horn” on the leading edge of the NACA 643-618 profiles. In contrast, in the DU profiles, the ice followed the shape of the profile. This horn shape produced a significant decrease in the performance of the NACA profiles. In the case of roughness, the effect of the extent of roughness and the value of its height became more critical as the angle of attack increased.

From the results presented in the previous sections and the performed discussions, it is seen that there is a close agreement between the attained conclusions in the present study and those of Caccia et Guardone (2023), i.e., the stall was anticipated, the lift coefficient slope decreased, and the drag coefficient increased in the case of iced airfoil. Furthermore, both studies found that the most significant difference occurred when the roughness height was higher and covered a larger airfoil area. The present results extend the same conclusions for the glaze ice scenario.

2.5 Conclusions

This study examines the impact of two surface roughness models, combined with two turbulence models, on the aerodynamic performance of the S809 wind turbine airfoil during rime and glaze ice via CFD simulation with FENSAP-ICE software. It has been shown that computational results of the aerodynamic parameters and ice shape were in reasonable agreement with the experimental and numerical data for clean and iced airfoils. The main conclusions of the study are summarized as follows:

1) Iced airfoil analysis revealed increased drag and reduced lift, consistent with the literature. Under the rime ice condition, C_D increased by around 50%, and C_L decreased by approximately 15%. These aerodynamic coefficients showed a higher impact in the glaze ice condition, increasing to 70% for C_D and decreasing to 20% for C_L, emphasizing further investigation into glaze ice conditions.
2) The modification of the airfoil lift and drag characteristics in the presence of ice is explained by the behaviour of the skin friction and pressure coefficients. The occurrence of the ice layer and its induced roughness promote an alteration in the pressure and wall shear stress around the profile, which increases skin friction and decreases the pressure coefficient. Also, it has been shown that the airfoil experiences an earlier flow separation with accreted ice compared to clean conditions, with the effect of increasing drag and reducing lift.
3) Conversely, the turbulence model selection did not significantly affect outcomes for aerodynamic coefficients. Average differences were around 3% for rime ice conditions and 2% for glaze ice conditions.
4) However, surface roughness was crucial, requiring consideration at each growth stage during ice accretion simulations. Validation of data obtained with experiments is recommended to determine which roughness model yields better results.
5) The beading model has shown excellent handling of the roughness variation along the ice accretion process. However, further validation of the model is needed to evaluate accuracy fully.
6) The widely used Shin et al. model may underestimate the lift coefficient and overestimate the drag coefficient compared to the beading model. This suggests that the first, which assumes that roughness is uniformly distributed along the entire airfoil, does not accurately reflect the actual physical nature of roughness distribution in the wind turbine simulated conditions.

7) Accurate predictions cannot rely solely on empirical correlations from the aeronautics domain. In this context, on-site roughness measurements are imperative to eliminate uncertainties.

The validated modeling methods and simulation utilities presented in this research would benefit scholars and engineers conducting reliable simulations for icing on wind turbine blades. However, it is essential to emphasize that the analysis was limited to two-dimensional aerodynamic performance; future analyses should be carried out to understand the effect of icing from a three-dimensional point of view that includes other phenomena, such as the influence of airflow along the blade span induced by its rotation.

CHAPTER 3

CONSTRUCTION OF THE ICING AND POWER LOSS DATABASES

Accurately assessing wind turbine performance under icing conditions requires more than isolated observations or simulations; it demands a comprehensive, harmonized database that captures the complex relationships among meteorological factors, operational parameters, and ice accretion dynamics. The objective of this chapter is therefore to document the development of such a database, which forms the backbone of the subsequent dimensional analysis (Chapter 4) and predictive modeling (Chapter 5).

The database was constructed by systematically integrating three complementary sources of information:

- Field measurements provide direct observations of ice accumulation and turbine performance under real operating conditions.
- CFD simulations provide controlled insights into aerodynamic and thermodynamic processes that are difficult to isolate in practice.
- Published data from peer-reviewed literature, extending the representativeness of the dataset and filling gaps not covered by measurements or simulations.

Special attention was given to data harmonization and quality control, since the different sources vary in format, resolution, and reliability. This required careful unit standardization, handling of missing and outlier values, and consistent classification of ice types (wet, dry, mixed). The resulting dataset provides both statistical robustness and physical consistency, making it suitable for analyzing correlations between meteorological conditions and turbine power loss.

This chapter is organized as follows. Section 3.1 presents the different data sources and their respective roles in the database. Section 3.2 describes the selection of relevant features, the rationale behind their inclusion, and the classification of ice regimes. Section 3.3 details the procedures used for data cleaning, normalization, and harmonization across sources. Section 3.4 introduces the final integrated dataset, summarizing its main statistical properties, coverage, and limitations.

3.1 Overview of Available Data Sources

The construction of the database required integrating multiple, complementary data sources. Each source contributes unique strengths while also presenting inherent limitations. To ensure robustness, the database design follows a hierarchy of reliability, prioritizing field measurements, then CFD simulations, and finally peer-reviewed literature.

Field measurements: These constitute the primary source of data, offering direct evidence of wind turbine performance under icing conditions. They capture real-world operating environments, including atmospheric variability, turbine mechanical response, and actual ice accretion patterns. Their main limitations are restricted spatial coverage and occasional gaps or uncertainties in sensor data.

CFD simulations: Numerical simulations complement field data by isolating specific aerodynamic and thermodynamic phenomena that are difficult to capture in practice. They enable controlled variation of meteorological and geometric parameters, extending the database beyond observed cases. However, their validity depends on model assumptions, turbulence closure choices, and the accuracy of boundary conditions.

Peer-reviewed literature: Published results provide an additional layer of information, particularly when field or simulation data are limited. Literature sources extend the database's temporal and spatial scope and enrich it with diverse case studies. Their main limitation is heterogeneity, as different authors employ varying experimental protocols, reporting standards, and definitions of icing severity.

This multi-source integration ensures both representativeness of real operating conditions and coverage of regimes that are difficult to observe continuously in the field. Field data anchors the dataset in reality, CFD extends its range and interpretability, and literature ensures comprehensive coverage.

Table 3.1 summarizes the three primary data sources, their advantages and limitations, and their specific roles in the database.

Table 3.1 Advantages and limitations of the data sources

Source	**Advantages**	**Limitations**	**Role in Database**
Field measurements	Real-world observations; capture actual turbine response and ice accretion patterns	Limited spatial/temporal coverage; possible sensor errors	Primary reference and reliability benchmark
CFD simulations	Controlled parametric studies; extend data beyond measured cases; isolate physical processes	Dependent on assumptions and model accuracy	Complement field data, extend representativeness
Peer-reviewed literature	Broad range of case studies; adds diversity and temporal depth	Heterogeneous methodologies and reporting standards	Fill gaps and increase dataset coverage

3.1.1 Experimental and Measurement Campaigns

This research does not include an experimental component. Therefore, Nergica was requested to provide icing event information. Nergica is a center of applied research and innovation in the renewable energy industry. They own and operate a full-scale research facility equipped with wind turbines (two Senvion MM92 CCV rated 2.05MW), a solar array, met masts, lidars, a wind/solar/diesel microgrid, storage technologies, and a real-time simulation platform. The site is in Rivière-au-Renard (Quebec, Canada) at an elevation of 330 m. This infrastructure enables various research, development, and technology-transfer initiatives under cold-weather conditions and on complex terrain (Nergica, 2022a). The wind turbines' operational data is recorded and archived at 1-second intervals, and they have a rotor-mounted ice-monitoring camera and an ice detector (Nergica, 2022b).

Nergica provided information between the winter of 2019 (November 2019 – May 2020) and the winter of 2021 (December 2020 – May 2021). The only data transmitted were those recorded during icing events. The following conditions were met to qualify as an icing event:

- The icing event has a minimum duration of 2 hours.
- Two icing events separated by less than 2 hours are part of the same event.

The 3 hours preceding and following the icing event were also transmitted. The data were extracted at 1 Hz, but turbine icing and availability were reported every 10 minutes. Therefore, it was decided to work on a 10-minute basis to consider all measurements associated with the icing events. Table 3.2 lists the data provided.

As shown in Table 3.2, LWC and MVD are typically not monitored due to a lack of suitable sensors. As a result, these parameters were estimated using empirical correlations available in the literature. Section 4.2.2 concisely explains the methods used to estimate these variables.

Table 3.2 List of the data provided by Nergica

Data	Dimension	Validation	Analysis of Results
Ice Mass (for each blade)	Kg	✓	
Turbine Power	kW	✓	
Turbine Rotation Speed	RPM	✓	
Wind Speed	m/s	✓	
Temperature	°C	✓	
Turbine Availability	-		✓
Icing Intensity	-		✓
Pressure	hPa		✓
Cloud Height	m		✓
Cloud Thickness	m		✓
Ambient Relative Humidity	%	✓	

In total, Nergica provided information on 25 icing events (see Table 3.3). However, not all icing events could be used to validate the π theorem. For correct validation, it is necessary to have information about the amount of ice that accumulated on the rotor; however, due to unknown causes, this parameter was not measured by the sensors during all the events. Hence, events 4, 6, 12, 13, and 14 were not considered. Events 23 and 24 were also neglected. These cases are exceptional and require a more detailed analysis, since although the temperature range was above zero, ice sensors on the turbine blades indicated the presence of ice. This shows that even if the air temperature increases, the ice accumulated on the rotor can continue to affect the turbine's performance. It also shows that considering only temperature as a parameter to determine the effect on wind turbines is insufficient. The start time and date, the duration in hours, the end time and date, and the temperature range are all included in Table 3.3.

In the end, the validation will use 17 icing events. However, data with temperatures above zero degrees (Events 23, 24, and 25) and atypical data, such as negative or very high turbine power when the wind speed was below the turbine cut-in velocity, were disregarded.

Table 3.3 Icing events provided by Nergica

# Event	Beginning Date and time		Ending Date and time		Duration (h)	Air Temperature (°C) Min	Avg	Max
Event 1	21-Nov-19	19:20	22-Nov-19	21:10	26.50	-2.983	-2.020	-0.086
Event 2	25-Nov-19	18:30	26-Nov-19	13:20	19.00	-2.985	-1.938	-0.820
Event 3	28-Nov-19	09:40	29-Nov-19	13:40	28.17	-7.935	-2.590	-0.238
Event 4*	15-Dec-19	00:30	15-Dec-19	09:00	8.67	-0.422	1.404	7.626
Event 5	31-Dec-19	20:50	04-Jan-20	08:40	84.00	-6.628	-4.265	-0.152
Event 6*	04-Jan-20	10:50	04-Jan-20	13:40	3.00	-2.344	-2.021	-1.508
Event 7	27-Jan-20	00:20	01-Feb-20	02:50	122.50	-16.090	-9.503	-1.752
Event 8	02-Feb-20	13:20	02-Feb-20	15:10	2.00	-7.476	-7.350	-7.200
Event 9	28-Feb-20	08:10	02-Mar-20	20:00	84.00	-11.170	-7.730	-2.103
Event 10	04-Mar-20	12:30	04- Mar-20	15:10	2.83	-4.232	-3.909	-3.493
Event 11	05-Mar-20	17:00	05- Mar-20	21:30	4.67	-4.936	-4.700	-4.453
Event 12*	27-Mar-20	08:00	28- Mar-20	11:40	27.83	-6.076	-4.288	-2.626
Event 13*	01-Apr-20	04:20	02-Apr-20	05:30	25.33	-2.417	-0.507	3.459
Event 14*	10-Apr-20	22:30	11-Apr-20	19:50	21.50	-3.315	-2.556	1.203
Event 15	05-May-20	09:10	05-May-20	14:20	5.50	-2.098	-1.481	-1.192
Event 16	06-Dec-20	13:40	25-Dec-20	02:20	444.83	-13.340	-5.007	2.778
Event 17	24-Jan-21	08:30	25-Jan-21	01:00	16.67	-5.749	-3.312	-1.854
Event 18	26-Jan-21	15:50	07-Feb-21	13:20	285.67	-13.080	-6.183	0.316
Event 19	24-Feb-21	04:30	24-Feb-21	10:00	5.67	-3.966	-3.822	-3.610
Event 20	01-Mar-21	12:40	01- Mar-21	15:20	2.83	-4.121	-4.058	-3.929
Event 21	29-Mar-21	19:00	29- Mar-21	22:10	3.33	-2.320	-2.049	-1.771
Event 22	02-Apr-21	06:40	05-Apr-21	06:50	72.33	-6.374	-3.781	1.839
Event 23	11-Apr-21	11:30	11-Apr-21	16:00	4.67	0.261	2.697	5.092
Event 24	22-Apr-21	06:20	22-Apr-21	10:30	4.33	0.226	2.604	5.171
Event 25	06-May-21	15:20	07-May-21	16:00	24.83	-0.945	-0.358	1.180

* No ice mass information

Figure 3.1 shows the power curve for the turbine operated under icing events. As can be seen, there were periods when the turbine performed poorly or even stopped, as well as periods during icing events when performance matched the nominal power curve. The information about the power curve was taken from REPower Systems (2010).

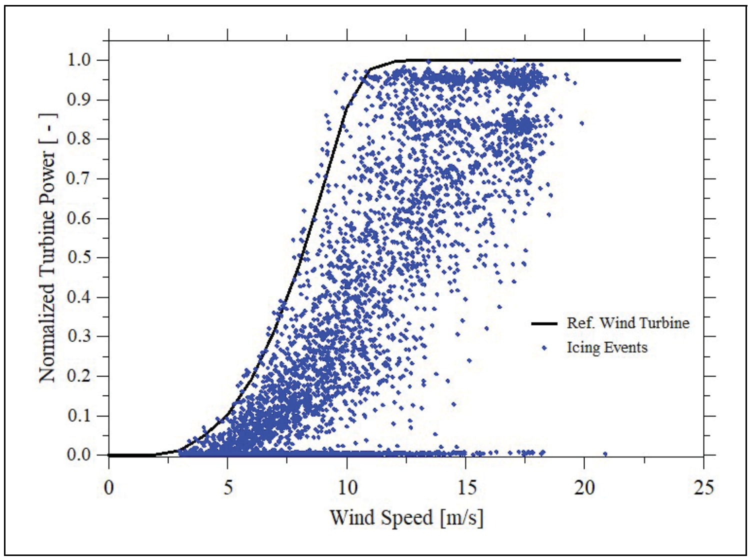

Figure 3.1 Power curve of the icing events

The measurements were conducted under various meteorological conditions, allowing the database to represent diverse icing scenarios.

3.1.2 CFD Simulation Outputs

To supplement the in-situ measurements and extend the analysis of icing beyond the constraints of field data, a series of CFD simulations were conducted using FENSAP-ICE (Contreras Montoya et al., 2023). The simulations focused on a better understanding of the influence of the different parameters (meteorological, geometrical, and operational) on the aerodynamic performance of a wind turbine airfoil under two types of ice (rime and glaze).

The simulations were conducted on the S809 airfoil, a commonly used airfoil in wind turbine blades, and environmental parameters representative of in-cloud icing conditions. The studied range of ambient temperatures, LWC values, MVD values, and ice density allowed for a representative simulation of glaze and rime ice types. The results from these simulations were presented in the previous chapter and published as a paper in MDPI-Processes: Contreras Montoya et al. (2023)

The principal objective of the CFD study was to evaluate the influence of surface roughness evolution and turbulence modeling on the predicted ice shape and its aerodynamic consequences. Two turbulence models (Spalart-Almaras and SST k-ω) were tested to assess their sensitivity in capturing flow separation and droplet impingement behavior under icing conditions. The resulting simulations provided high-resolution data on ice distribution along the airfoil, ice type classification (e.g., rime vs. glaze), and aerodynamic degradation metrics such as pressure coefficient (C_p) alterations, loss of lift, and drag increase (Contreras Montoya et al., 2023).

From these simulations, two primary types of output were used to enhance the database:

1) **Ice Type Classification**: The resulting ice morphology from each simulation was visually and quantitatively assessed to determine whether the accretion resembled rime, glaze ice. This classification was used to supplement the database with labels for physically realistic icing scenarios under varying meteorological conditions.
2) **Estimated Influence on Power Output**: The simulated ice shapes were used for post-processing to evaluate aerodynamic penalties, including changes in lift-to-drag ratio and stall behavior.

The CFD dataset thus serves as both a source of physically consistent ice-type labels and a means to infer power degradation trends that are not directly observable from field data. Combined with in-situ measurements and literature sources, the simulations provide a valuable interpolation framework for exploring under-sampled meteorological regimes and for validating icing-related power-loss estimates across a broader operating envelope.

The importance of simulations presented in Chapter 2 lies in the fact that surface-roughness effects are implicitly accounted for through the definition of different ice-accretion types (glaze, rime, and mixed ice). Each of these accretion regimes leads to distinct roughness characteristics, which in turn contribute to the different aerodynamic and thermal behaviors observed on the iced blade. Beyond the purely physical differences in accretion mechanisms and morphologies, these roughness-induced variations justify treating each ice type separately in the analysis. Consequently, the results and conclusions of Chapter 2 provide the physical basis for distinguishing between glaze, rime, and mixed ice throughout the thesis, even though roughness does not appear as an explicit parameter in the non-dimensional framework.

3.1.3 Literature data

A targeted literature review was conducted to identify existing studies that provided quantitative data on wind turbine icing and related power losses. Publications were selected based on their methodological transparency, geographic relevance, and data accessibility. Key criteria included the use of validated models or measurements, the availability of raw or aggregated data, and relevance to cold-climate turbine operation.

Data from literature sources included power losses due to icing, classifications of ice types, case studies of turbine behavior under extreme icing conditions, and wind turbine performance under degraded aerodynamic conditions. When possible, these external datasets were normalized and aligned with the in-situ dataset's structure to ensure consistency in feature representation and units. APPENDIX B provides a synthesis of the literature references and data characteristics.

3.2 Feature Selection and Labeling

Feature selection identifies the most relevant, non-redundant, and impactful variables (or features) from a dataset. These features are used as inputs for predictive modeling or analysis. The primary objective is to simplify the dataset while retaining the information necessary for accurate predictions or insights (Heavy.AI, 2024). The feature selection is an important process because (Hex, 2025):

1) **Improves model performance:** models become more accurate and efficient when removing irrelevant or redundant features.
2) **Reduces overfitting:** Simplifying the feature set minimizes the risk of overfitting, in which a model performs well on training data but poorly on unseen data.
3) **Decreases computational costs:** fewer features mean less data to process, reducing the time and resources required for computation.
4) **Enhances interpretability:** a smaller set of meaningful features makes it easier to understand and explain the model's behavior.

To achieve this, features were organized into three categories: meteorological variables, turbine operational variables, and environmental descriptors.

- <u>Meteorological variables</u>: Air temperature, relative humidity, wind speed and direction, and LWC were included as they directly govern the phase, amount, and morphology of accreted ice. Additional parameters, such as precipitation rate and atmospheric pressure, were considered when available. These features are essential for distinguishing between glaze, rime, and mixed icing regimes.
- <u>Turbine operational variables</u>: Rotor speed, blade pitch angle, generated power, and torque were selected to capture the turbine's response under icing. Blade geometry descriptors (e.g., chord length, twist angle at the section of interest) were also integrated where available, particularly from CFD data. These parameters are critical for linking meteorological conditions to aerodynamic losses and power degradation.
- <u>Environmental descriptors</u>: Site-specific variables, including elevation, turbine hub height, and exposure category, were included to account for geographic and topographic influences on icing frequency and severity.

Labeling refers to assigning meaningful annotations, or "labels," to data points in a dataset. These labels often represent the target variable, for example, "power coefficient" or "type of ice," that a model is trained to predict. These labels allow models to learn relationships between input features and outcomes and ensure reliable model predictions and insights (Toloka, 2023). Labeling of icing events followed a standardized framework to ensure comparability across datasets.

3.2.1 Meteorological Conditions

Table 3.4, below, illustrates the relevant meteorological variables in the database.

Table 3.4 Relevant meteorological variables in the database

Variables	**Significance**	**Availability across the different data sources**		
		In-situ	**CFD Simulation**	**Literature data**
Air Temperature	To classify the type of ice and to calculate the water vapor pressure.	A	A	A
Relative humidity	Used to estimate the LWC.	A	NA	NA
Air density	Used to estimate the LWC.	A	NA	NA
Air pressure	At the sea level and the nacelle level.	A	A	NA
Cloud height	Used to extrapolate the air temperature at the nacelle level (saturated conditions).	A	NA	NA
LWC	This variable was calculated using empirical equations from the literature for the in-situ data.	C	A	A
MVD	This variable was calculated using empirical equations from the literature for the in-situ data.	C	A	A
Air Wind Speed	To calculate the TSR	A	A	A

Note: A – Available, NA – Not Available, C – Calculated, As – Assumed

3.2.2 Geometrical Parameters

In Table 3.5, we present the geometrical parameters used in the database.

Table 3.5 Relevant geometrical parameters in the database

Variables	Significance	Availability across the different data sources		
		In-situ	CFD Simulation	Literature data
Turbine radius	To calculate the TSR	A	A	A
Airfoil profile	An airfoil was assumed for the in-situ data	As	A	A
Airfoil chord	The airfoil chord was estimated at 85 % of the turbine radius	C	A	A

Note: A – Available, NA – Not Available, C – Calculated, As – Assumed

3.2.3 Operational Variables

Table 3.6 presents the operational variables in the database.

Table 3.6 Relevant operational variables in the database

Variables	Significance	Availability across the different data sources		
		In-situ	CFD Simulation	Literature data
Rotational Speed	To estimate the TSR	A	A	A
TSR	To build the power curve and compare the models	C	C	C
Angle of attack	Important for the aerodynamics analysis in two dimensions	NA	A	A
Power Coefficient	Calculated from the lift and drag coefficient for the CFD simulation.	A	NA	A

Note: A – Available, NA – Not Available, C – Calculated, As – Assumed

3.2.4 Ice Type Classification

Accurate labeling of ice type was essential for interpreting the effects of icing on performance degradation.

For the in-situ measurements, the ice type was labeled based on air temperature, since the LWC and MVD values were estimated using empirical correlations that exhibited behavior consistent with theoretical expectations. For the CFD simulation, the classification was based on a combination of three variables: temperature, LWC, and MVD, following the definitions in section 1.1.2. For the literature data, the label was assigned based on the authors' information provided. However, there were cases where the authors claimed to have worked with glaze ice. However, when analyzing the combination of variables and the theoretical definition, it was rime ice. In cases where consistency was lacking, it was decided to reclassify the data according to the theoretical definition.

This classification was discretized into categorical labels “rime,” “glaze,” and “mixed,” which were used as target labels in supervised learning tasks and filters in descriptive statistics. Table 3.7 summarizes the characteristics of the three ice types.

Table 3.7 Characteristics to classify the three ice types

Ice type	Temperature range	LWC range	MVD range
Rime	Below -10°C	$< 0{,}5$ g/m^3	< 15 – 20 µm
Glaze	between 0°C and -3°C	> 0,8 – 1,3 g/m^3	> 20 – 50 µm
Mixed: conditions for both rime and glaze coexist.	between -3°C and -10°C	0,5 – 1,3 g/m^3	15 – 50 µm

3.3 Data Cleaning and Normalization

The integration of heterogeneous data sources required a systematic process of data cleaning and normalization to ensure the database's consistency, comparability, and reliability. The procedures were applied across four main stages: handling missing values; detecting and treating outliers; harmonizing units and formats; temporal and spatial alignment; and normalizing variables.

3.3.1 Handling Missing or Noisy Data

Due to the nature of in-situ measurements, data incompleteness and sensor artifacts were unavoidable. Missing values were handled using a combination of:

- **Interpolation:** linear and spline methods for short time gaps in meteorological variables.
- **Flagging and removal:** exclusion of segments with prolonged sensor failure or invalid power readings.

3.3.2 Outlier Detection

Outlier detection was performed using both statistical thresholds (values more than 3 standard deviations from the mean) and physical plausibility checks (e.g., negative wind speeds, unphysical temperatures, and unrealistic humidity levels > 100%). Outliers were corrected when sensor errors were evident; otherwise, they were removed from the dataset.

3.3.3 Unit and Format Harmonization

Data sources reported variables in different units (e.g., wind speed in m/s or km/h, temperature in °C or K). All meteorological data were converted into SI units to ensure consistency. Time resolution was standardized to 10-minute intervals to match the field dataset's operational format. CFD and literature data were aggregated or interpolated as needed.

3.3.4 Temporal / Spatial Alignment

To align the various data sources:

- **Time synchronization** was conducted using UTC timestamps, with a temporal resolution of 10-minute intervals. However, for the literature data, this synchronization was not always available, as the authors evaluated ice accretion durations ranging from 10 minutes to hours.
- **Spatial interpolation** was applied to align met mast data with turbine nacelle-level measurements for the in-situ data.

The alignment process enabled meaningful multi-source feature comparisons and ensured that icing and power losses were attributed to the correct environmental conditions.

3.3.5 Normalization

To facilitate integration into dimensional analysis and machine learning algorithms, variables were normalized. Continuous variables (temperature, wind speed, liquid water content) were scaled using z-score normalization (subtracting the mean and dividing by the standard deviation). Bounded variables, such as relative humidity, were scaled between 0 and 1. This ensured comparability across features and prevented dominant influence from variables with larger numerical ranges.

Cross-source harmonization was a critical step, as definitions of icing events and reference conditions varied. For example, power output from field measurements was normalized by the turbine's rated power, whereas CFD simulations provided aerodynamic coefficients directly. These were converted into consistent performance indicators to allow direct comparison. Literature-derived values were adjusted when possible, using reported turbine specifications.

3.4 Integration and Final Dataset Description

After harmonization and cleaning, the various data sources were integrated into a single structured dataset. Each row corresponds to a unique timestamp, with columns representing meteorological conditions, geometric parameters, operational variables, icing labels, and performance indicators.

3.4.1 Size, Balance of Classes, Time Span

Overall, the database contains approximately 15,000 individual records spanning a wide range of meteorological, operational, and environmental conditions. Meteorological parameters such as air temperature, wind speed, and relative humidity are consistently represented, whereas specialized variables such as LWC are sparser due to sensor and reporting limitations. The final dataset includes:

- Total entries 4736 rows: 4673 rows from in-situ measurements, and 63 simulation cases from the literature.
- **Class distribution**:
    - Rime: 394 rows (8,3%)
    - Glaze: 1308 rows (27,6%)
    - Mixed: 3034 rows (64,1%)

Efforts were made to ensure a balanced representation across ice types, although naturally occurring rime events were less frequent in the measured dataset and thus partially supplemented via CFD scenarios.

3.4.2 Limitations of the Dataset and Assumptions

Despite its comprehensiveness, the database has some limitations. First, field data remain geographically limited to a handful of cold-climate test sites, potentially constraining generalizability to other regions. Second, CFD-derived cases, while useful, depend on modeling assumptions that may not fully replicate real-world conditions. Third, literature-derived entries are heterogeneous, reflecting different experimental protocols and reporting standards. Finally, the representation of extreme icing events (very low temperatures and high wind speeds) is sparse, which reduces statistical robustness in this domain.

In summary, the final database provides a robust and well-balanced foundation for the dimensional analysis and predictive modeling developed in Chapters 4 and 5, while acknowledging the inherent limitations of working with heterogeneous sources.

3.5 Conclusion

This chapter has presented a comprehensive account of the methodology employed to construct the icing and power loss database, integrating multi-source data from in situ measurement campaigns, high-fidelity CFD simulations using FENSAP-ICE, and relevant literature findings. The integration of these diverse sources has enabled the creation of a physically consistent and operationally relevant dataset suitable for analyzing the impact of atmospheric icing on wind turbine performance.

Critical steps in this process included identifying and selecting meteorological and performance-related features, classifying ice types using both observational and model-based criteria, and rigorously cleaning and aligning the data temporally. The use of FENSAP-ICE simulations, focused on the S809 airfoil and employing Eulerian droplet tracking, provided valuable insights into the aerodynamic penalties associated with different icing morphologies. These simulations not only enhanced the physical interpretability of the dataset but also complemented observational gaps, particularly in regimes prone to glaze or mixed-ice formation.

The resulting dataset, characterized by its temporal depth, physical fidelity, and label diversity, establishes a robust foundation for subsequent modeling and analysis. While certain assumptions, such as steady-state conditions in CFD simulations and the idealized blade geometry, impose limitations, these have been delineated and will be addressed in the validation and uncertainty quantification phases to follow.

In the forthcoming chapter, the focus will shift to the development of data-driven models for ice classification and power-loss prediction. These models will leverage the structured dataset presented herein to enhance forecasting and mitigate icing-related performance degradation in wind energy systems.

CHAPTER 4

DIMENSIONAL ANALYSIS-DRIVEN CORRELATIONS FOR PREDICTING POWER LOSS ON WIND TURBINES UNDER ICING CONDITIONS

4.1 Introduction

The interaction of multiple meteorological, operational, and geometric parameters governs the performance of wind turbines under icing conditions. While the database developed in Chapter 3 provides comprehensive access to these variables, their high dimensionality complicates direct analysis and predictive modeling. To address this challenge, the present chapter applies dimensional analysis using the Buckingham π theorem to systematically identify the most influential non-dimensional groups that characterize icing dynamics and their impact on turbine performance.

The physics of ice accretion on wind turbine rotors is a complex process involving several key factors. Supercooled water droplets in the air collide with the blade surfaces and freeze upon impact. The collection efficiency of these droplets depends on factors such as droplet size, air velocity, and blade geometry (Pedersen & Yin, 2014). The icing process is influenced by ambient temperature, liquid water content (LWC), and heat transfer conditions at the blade surface (Özgen, Akyildiz, Berker. As ice accumulates, it alters the blade's aerodynamic profile, increasing drag and reducing lift, which significantly impacts the turbine's power output (Yirtici et al., 2016).

Different types of ice can form depending on atmospheric conditions. Rime ice, which is opaque and brittle, forms in colder conditions with lower LWC, while glaze ice, which is clear and dense, occurs in warmer conditions with higher LWC (Özgen; et al., 2019). The rotational effects of the turbine blades add another layer of complexity, as centrifugal forces affect ice accretion patterns and can lead to ice shedding when adhesion strength is exceeded (Özgen; et al., 2019).

Dimensional analysis offers two main advantages in this context. First, it reduces the number of independent variables by consolidating them into physically meaningful dimensionless groups. This simplification helps to reveal underlying physical relationships that may otherwise remain obscured in raw data (White, 2008; Zohuri, 2017). Second, the resulting π groups provide a framework for comparing observations and simulations across scales, turbines, and climatic contexts, thereby enabling more generalizable insights than purely dimensional variables.

This approach considers key physical variables that are typically monitored or known in wind farms, including ambient temperature, air density, wind speed, duration of the icing event, rotational speed, and turbine radius. The goal of this chapter is therefore to apply dimensional analysis to the curated dataset and derive dimensionless groups that best capture the relationship between meteorological conditions, ice accretion, and wind turbine power loss. Special attention is given to identifying groups that reflect key processes, including droplet collection efficiency, heat exchange at the blade surface, and aerodynamic penalties due to surface roughness. These π groups will form the basis for both the interpretative analysis presented here and the predictive modeling developed in Chapter 5.

This chapter is organized as follows. Section 4.2 reviews the theoretical framework of the Buckingham π theorem and its relevance to icing studies and describes the selection of fundamental variables from the database and the derivation of corresponding π groups. Section 4.3 analyzes the physical meaning and statistical significance of these groups with respect to the observed power loss. Finally, Section 4.4 summarizes the key findings and outlines their implications for subsequent modeling efforts.

4.2 Methodology

The methodology for predicting the power output of a wind turbine under icing conditions involves a multi-step approach that integrates dimensional analysis, correlation analysis, and machine learning validation. This comprehensive approach aims to simplify the complex physical processes underlying ice accretion and accurately predict turbine performance.

Dimensional analysis is used to reduce the number of physical variables and to establish relationships among dimensionless parameters. Using the Buckingham π theorem, we derive a set of dimensionless parameters that govern the relationship between the initial variables and the turbine's power output under icing conditions. These dimensionless parameters help in understanding the influence of each variable on ice accretion and power output.

To understand the individual and combined effects of the dimensionless parameters on ice accretion and power output, a correlation analysis is performed. This analysis involves:

- Calculating the correlation coefficients between the dimensionless parameters and the power output.
- Evaluating the significance of each parameter in influencing the power coefficient.

This step enables the identification of the most critical factors influencing turbine performance under icing conditions.

To validate the predictions of the wind turbine's power coefficient in the presence of ice, machine learning techniques are employed. Specifically, decision trees, random forests, and neural networks are used. These models are trained using the collected field data, along with dimensionless parameters derived from dimensional analysis. The performance of each model is assessed using metrics such as the mean squared error (MSE) and the coefficient of determination (R-squared), enabling a rigorous evaluation of its predictive performance.

4.2.1 Variable Selection

The most effective technique for forecasting icing in wind turbines is to combine meteorological information (e.g., numerical weather models or weather station measurements) with an ice accretion model (Battisti, 2015). If the wind turbine is covered in ice, meteorological and climatic data aren't enough to figure out how the turbine will work. They serve only as a first warning of potential risks (Battisti, 2015).

For the correct development of the π Theorem, it is important to identify the correct variables, i.e., those that most influence the phenomenon of ice accretion in wind turbines and their performance. Several studies have been conducted in recent decades to identify the influence of various variables on ice accretion (including collection efficiency, sticking efficiency, accretion efficiency, and ice shape). However, their impact on wind turbine performance has been studied at the level of airfoils or blades (lift, drag, and power coefficients). Table 4.1 summarizes some of the main findings.

Table 4.1 Summary of variables affecting the ice accretion in Wind Turbines.

Variable	Reference
Droplet size or Median Volume Diameter (MVD)	(Etemaddar et al., 2014; Homola, Virk, et al., 2010; Jia Yi Jin & Virk, 2018; J. Y. Jin et al., 2020; L. Makkonen, 2000; L. Makkonen et al., 2001; M. C. Pedersen & H. Sørensen, 2016)
Wind Speed	(Dimitrova, 2009; W. Han et al., 2018; Jia Yi Jin & Virk, 2018; L. Makkonen, 2000; M. C. Pedersen & H. Sørensen, 2016; Virk et al., 2016)
Relative Velocity	(Barber et al., 2010; Dimitrova, 2009; Hochart, Fortin, Perron, & Ilinca, 2008; Homola, Virk, et al., 2010; Jia Yi Jin & Virk, 2018; J. Y. Jin et al., 2020; Virk et al., 2016)
Blade geometry*	(W. Han et al., 2018; Jia Yi Jin & Virk, 2018; J. Y. Jin et al., 2020; Virk et al., 2012; Virk et al., 2016)
Air Temperature	(Homola, Virk, et al., 2010; Jia Yi Jin & Virk, 2018; J. Y. Jin et al., 2020; Li et al., 2019; L. Makkonen, 2000; L. Makkonen et al., 2001; M. C. Pedersen & H. Sørensen, 2016; Shu et al., 2018; Virk et al., 2016)
Humidity	(L. Makkonen, 2000)
Liquid Water Content (LWC)	(Etemaddar et al., 2014; Homola, Virk, et al., 2010; J. Y. Jin et al., 2020; Li et al., 2019; L. Makkonen, 2000; M. C. Pedersen & H. Sørensen, 2016)
Roughness	(Homola, Virk, et al., 2010; Jasinski et al., 1998; L. Makkonen, 2000)
Operation Point	(Virk et al., 2012)
Reynolds number	(Jasinski et al., 1998)
Tip Speed Ratio	(Barber et al., 2010; Homola et al., 2012; Shu et al., 2018)

* Includes: profile type (symmetric or asymmetric), chord, angle of attack, length, twist angle, and thickness.

Considering the above and that the study is focused on the turbine, some of the variables mentioned in Table 4.1 will not be considered, for example, variables that depend directly on the type of airfoil, such as relative speed, angle of attack, angle of twist, chord, and thickness. This reduction of variables is assumed due to the complexity of having too many variables that are difficult to estimate or unavailable. Indeed, wind turbine manufacturers typically do not disclose the type or types of profile (s) used along the blade. Therefore, for calculation purposes and given the available information, the turbine radius, rotational speed, and wind speed will be used. Table 4.2 summarizes the variables chosen for the π theorem.

Table 4.2 Summary of variables chosen for the application of the π theorem.

Meteorological Variables	**Operational Variables**	**Geometrical Variables**
Air Temperature (T)	Rotational Speed (Ω)	Turbine Radius (R)
Air Density (ρ)	Turbine Power (P)	Profile Chord (c)
Wind Speed (U)		
Liquid Water Content (LWC)		
Droplet size (MVD)		
Duration of the icing event (t)		

Additionally, three more variables were added to those in Table 4.2, related to the fluid's thermodynamic properties. The inclusion of these variables accounts for the mass and heat transfer processes involved in the icing phenomenon (L. Makkonen, 2000). Therefore, air viscosity (μ_a), air thermal conductivity (k), and the convection coefficient (h) were added.

The π theorem was applied in two parts. In the first part, the variables in Table 4.2 were used to identify the π groups for estimating the ice mass that accumulates on the turbine rotor. In the second part, the π number for the ice mass was correlated with the turbine power. All the variables and their dimensions are listed in Table 4.3.

Table 4.3 List of the n variables involved in the problem with their respective dimension.

Nº	Variable	Symbol	Mass (M)	Length (L)	Time (T)	Temperature (Θ)
1	Air Temperature	T	0	0	0	1
2	Liquid Water Content	LWC	1	-3	0	0
3	Droplet Size	MVD	1	0	0	0
4	Characteristic length	L	1	0	0	0
5	Wind Speed	U	0	1	-1	0
6	Rotational Speed	Ω	0	0	-1	0
7	Duration of the icing event	t	0	0	1	0
8	Air Density	ρ_a	1	-3	0	0
9	Air Dynamic Viscosity	μ_a	1	-1	-1	0
10	Air Thermal Conductivity	k	1	1	-3	-1
11	Convection Coefficient	h	1	0	-3	-1
12	Mass of Ice	M_{ice}	1	0	0	0
13	Turbine Power	P	1	2	-3	0

Hence, the mass of ice will be a function of:

$$M_{ice} = f(T, LWC, MVD, L, U, \Omega, t, \rho_a, \mu_a, k, h) \tag{4.1}$$

And the turbine power will be a function of:

$$P = f(M_{ice}, L, U, \Omega, \rho_a) = f(T, LWC, MVD, L, U, \Omega, t, \rho_a, \mu_a, k, h) \tag{4.2}$$

4.2.2 Estimation of LWC and MVD

As shown in Table 3.2, LWC and MVD are typically not monitored due to a lack of suitable sensors. As a result, the following subsections provide concise explanations of the methods used to determine these values, either using known data or empirical approximations.

Since the 1940's, scientists have been interested in measuring LWC. However, this is a time-consuming and expensive process, and the resulting uncertainties might be significant. The three main measurement methods are ice accretion methods, hot-wire methods, and droplet size and counting methods (Roberge, Lemay, Ruel, & Bégin-Drolet, 2021). This parameter has a significant impact on the cloud dynamics and radiative properties. The heat budget of the atmosphere is greatly influenced by its vertical distribution and temperature correlation (Gultepe & Isaac, 1997).

In response to the above, various researchers have developed alternative methodologies to estimate LWC from easily measurable parameters, such as air temperature and atmospheric pressure.

Gultepe et Isaac (1997) conducted airborne observations within clouds (primarily thin, thick, and low-level stratiform clouds) over several Canadian field projects during the 1984-1993 period to examine the relationship between LWC and T in northern latitudes. Frequency distributions of LWC were approximated using lognormal curves, with a focus on calculating median LWC values to represent the central tendency at different temperature intervals. Statistical analysis, such as curve fitting and regression, was utilized to establish the LWC-temperature relationship and compare findings with earlier studies, highlighting differences due to probe design and dataset limitations.

Another attempt to establish a relationship between atmospheric icing and routinely measured meteorological data was made by Drage and Hauge (2008). The study was conducted in a coastal, mountainous region of Norway (Brosviksåta), where four weather stations were installed at three different levels. All stations measured air temperature, relative humidity, wind speed, and wind direction. They developed a methodology to determine LWC from air temperature and pressure at different heights. The heights were defined as unsaturated (below the cloud) and saturated (inside the cloud). In the case where the temperature is not measured, they assumed that the air temperatures at different heights follow equations (4.3) and (4.4), where the subscript “1” indicates the parameters at unsaturated conditions, and the subscript “c” indicates the saturated conditions. γ is defined as the temperature gradient ($-\frac{dT}{dz}$), where γ_d is the temperature gradient for unsaturated conditions and γ_w is the temperature gradient for saturated conditions. The literature suggests γ_d= 0.85°C/100m and γ_w=0.54°C/100m, however, the measurements at Brosviksåta suggested γ_d=0.92°C/100m and γ_w=0.62°C/100m.

$$T(z) = T_1 - \gamma_d(z - z_1) \ ; \quad z \leq z_c \tag{4.3}$$

$$T(z) = T_1 - \gamma_d(z_c - z_1) - \gamma_w(z - z_c) \ ; \quad z \geq z_c \tag{4.4}$$

Continuing with the analysis made by Drage and Hauge (2008), the equation proposed to estimate the cloud LWC was based on the mixing ratio (w) which is defined as the mass of water vapor (M_v) per unit mass of dry air (M_d);

$$w = \frac{M_v}{M_d} = \frac{\rho_v}{\rho_d} \approx \varepsilon \frac{e}{p} \tag{4.5}$$

Where p is the air pressure, e is the water vapor pressure, ρ_v is the water vapor density, ρ_d is the density of dry air, and ε is the constant ratio of molecular weight for water vapor and dry air, equal to 0.622.

The authors made some assumptions. The total water content of the air and the mixing ratio are constant with height along the mountain slope. Hence, at the saturation level, the total mixing ratio (w_{tot}) is the sum of the saturation mixing ratio (w_2) and the liquid water content mixing ratio (w_{LWC}) (see equation (4.6)); while at the unsaturated level, the total mixing ratio equals the mixing ratio at unsaturated conditions (w_1) (see equation (4.7)), which means no fallout by rain and no exchange of water vapor between the air masses and the slope of the mountain.

At saturated conditions: $w_2 = w_{tot} - w_{LWC}$ (4.6)

At saturated conditions: $w_{tot} = w_1$ (4.7)

Where:

$$w_{LWC} = \frac{\rho_{LWC}}{\rho_d}; \tag{4.8}$$

$$w_1 = 0.622 \frac{e_1}{p_1} \tag{4.9}$$

$$w_2 = 0.622 \frac{e_2}{p_2} \tag{4.10}$$

Combining equations (4.6) to (4.10), the ρ_{LWC} in a cloud is given by:

$$\rho_{LWC} = 0.622 \rho_{d2} \left(\frac{e_1}{p_1} - \frac{e_2}{p_2} \right) \tag{4.11}$$

Where the water vapor pressure e_1 (unsaturated conditions) and e_2 (saturated conditions) can be fitted over the temperature range $-30°C \leq T \leq 35°C$ by the empirical formula (Drage & Hauge, 2008):

$$e = 6.112 \exp\left(\frac{17.67 \cdot T}{T + 243.5} \right) \; in \; [mb] \tag{4.12}$$

The pressure p_1, in this case, is equal to the pressure measured at the meteorological mast located at 78 m height at Nergica's facilities. And the pressure p_2 was estimated with the ideal gas equation, taking as T the temperature calculated at height z (equation (4.3) or (4.4)), that is, at the height of the blade's tip.

Below the cloud base (subscript 1), water in the air consists of only water vapor. Inside the cloud (subscript 2), the water in the air consists of a mixture of water vapor and cloud liquid water. The LWC estimated using this method ranged from 0.05 to 0.38 g/m^3.

The variation of the LWC found by Gultepe et Isaac (1997) was between 0.04 and 0.23 g/m^3, and the estimations made by Drage et Hauge (2008) were between 0.003 and 0.5 g/m^3. As can be seen, the variation between the two methods is quite high. These differences may be associated with the fact that the data collected by Gultepe et Isaac (1997) were acquired from high-altitude data rather than localized wind turbines and may be more suited for aircraft. Also, as mentioned before, the LWC is a parameter that is affected by altitude. Drage et Hauge (2008) approach focuses on estimating LWC within clouds while considering parameters such as cloud height, altitude, water vapor, and the masses of air surrounding the wind turbines; a circumstance that is more likely to occur in locations where wind farms are installed. Therefore, calculations involving LWC will be performed by the methodology proposed by Drage et Hauge (2008), as it considers more factors influencing LWC from parameters easily obtainable in a wind farm.

For the MVD, this parameter depends on the type of precipitation being studied. For example, the cases of “freezing fog” and “freezing rain” are described in terms of LWC and the diameter spectrum of supercooled water droplets. This spectrum is often complex and challenging to work with, so the MVD is used for simplicity. The median distribution is the diameter that divides the volume spectrum of supercooled water droplets into two equal parts and is expressed in µm (Fortin, 2009a).

4.2.2.1 Freezing Fog

The freezing fog was studied by Best in 1951. He used an experimental dataset to fit an equation for LWC. As a result, Best proposed LWC as a power function depending on the maximum water droplet diameter (D_{max}), where C and N are two empirically obtained constants. For LWC, the units are g/m^3, and for D_{max}, the units are µm.

$$LWC = C \cdot D_{max}^{N}; \qquad C = 0.0003181 \; and \; N = 1.79 \tag{4.13}$$

The freezing fog has a LWC of 0.3 g/m^3, which corresponds to a maximum droplet diameter of 45.9 µm.

4.2.2.2 Freezing Rain

Following the same methodology as in the previous paragraph, Best proposed an equation for LWC depending on the precipitation intensity (P) in mmH_2O/h and two other constants, E and F (Fortin, 2009a).

$$LWC = E \cdot P^{F} \tag{4.14}$$

He also derived an equation for MVD in mm (Fortin, 2009a).

$$MVD = 0.69^{\frac{1}{n}} \cdot \alpha P^{\beta} \tag{4.15}$$

MVD depends on the precipitation intensity and the constants α and β obtained from the smoothing of the experimental data, see Table 4.4 (Fortin, 2009a).

Because no information is available on the type of precipitation that led to the icing events measured by Nergica, we assumed “freezing fog” to estimate the MVD.

Table 4.4 Constants and smoothing parameters
Taken from Fortin (2009a)

	n	α	β	E	F
Best (1949)	2.25	1.30	0.232	0.067	0.846
Best (1950)	2.29	1.56	0.209	0.059	0.816
Marshall-Palmer (1947) Freezing Rain	1.85	1.00	0.240	0.072	0.880
Marshall-Palmer (1948) Continuous Rain		0.91	0.210	0.072	0.880
Marshall-Palmer Continuous Light Rain				0.054	0.840
Marshall-Palmer Storm				0.089	0.840

4.3 Results

4.3.1 Results of the Estimation of LWC and MVD

After implementing Drage's and Best's methodologies for the estimation of LWC and MVD, a LWC above 0.20 g/m^3 at temperatures between 0°C and -5°C was obtained, which implies the presence of wet ice (or glaze ice). At the same time, LWC below 0.10 g/m^3 was found at temperatures below -5°C, which implies that the ice type is dry (rime ice). These findings agree with the literature. However, the presence of both types of ice throughout the temperature range studied makes the study of icing more complex.

The LWC range obtained with this methodology is consistent with the type of clouds that can be found at low latitudes (see Figure 4.1). For example, “stratus” clouds are distinguished by their horizontal development, and LWC between 0.05 and 0.25 g/m^3 (Yau & Rogers, 1989); they may be precipitation-free or generate periods of light precipitation or fog. In the cumulus clouds, the development is vertical. Stratocumulus clouds are a cross of layered stratus and individual clouds. Stratocumulus can also be considered a layer of cloud clumps with thick and thin sections. These clouds can be seen in the sky regularly, either before or behind a frontal system. Nimbostratus clouds are thick, dense stratus or stratocumulus clouds that provide constant rain or snow (Funk, 2022), hence the LWC in this type of clouds is near or higher than 1 g/m^3 (Yau & Rogers, 1989).

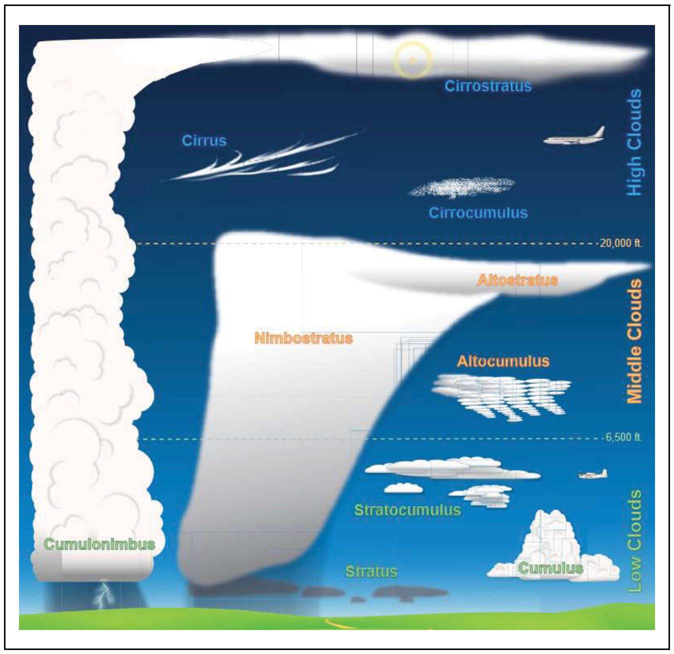

Figure 4.1 Clouds classification
Taken from: NOAA (2019).

It should be noted that the Drage et Hauge (2008) methodology reached a value of LWC equal to or higher than 0.2 g/m^3, which is the value most used in CFD simulations. So, it could be stated that although some studies claim to focus on “rime ice” based on temperature, when reviewing the assumed LWC, they were evaluating “glaze ice”. This shows that it is not possible to determine the type of ice present in the icing process by temperature alone.

Nowadays, most CFD software uses this parameter to determine the ice accretion in different structures (airplanes, electric cables, wind turbines), and from the simulated information, strategies are designed to mitigate the effects of icing. If the accretion is simulated inaccurately, errors can be made in the design of the protection systems or wind turbine operation strategies that may compromise the integrity of the wind turbine.

The estimated values for MVD range from 18 to 44 µm, which agrees with what was found in the literature. In general, in the CFD simulations, the authors used a MVD of 20 µm but without going into much detail as to why this value was chosen, if it had any relation or dependence with the LWC or some other environmental parameter, or if it was realistic.

In many CFD studies, a LWC of 0.20 g/m³ combined with a MVD of 20 µm is frequently adopted as a reference case. However, verification using the methodology of Drage et Hauge (2008) shows that such a combination is physically inconsistent. An MVD of 20 µm corresponds to rime ice conditions, which are typically characterized by low LWC values (0.06–0.07 g/m³) and air temperatures below −10 °C. Conversely, an LWC of 0.20 g/m³ is representative of glaze ice conditions, which require larger droplet sizes (MVD > 35 µm) and occur within a higher temperature range, generally between 0 and −5 °C. This mismatch highlights a recurrent issue in the literature: the use of meteorological parameter combinations that do not respect the underlying physical relationships of the icing process. Consequently, such inconsistencies can introduce systematic errors in ice accretion predictions and, ultimately, in the estimation of icing-induced performance losses on wind turbines.

4.3.2 Dimensionless Groups for the Mass of Ice (M_{ice})

Following the steps listed in the methodology, the number of variables (n) is twelve, and the number of dimensions (j) is four; hence, the number of π groups is eight. The selected repeating variables were: $\rho_a, U, L, and\ T$ because these variables include all the dimensions in the problem, do not form a π product between them, and they are usually measured (temperature and wind speed) or easily estimated (air density can be obtained from tables). After the algebraic development for each of the π groups for the remaining variables ($\Omega, \mu_a, h, k, t, MVD, LWC,$ and M_{ice}), the following dimensionless groups were obtained (see APPENDIX C for the entire algebraic development):

$\prod 1 = \frac{\Omega L}{U}$ or TSR $\qquad \prod 2 = \left(\frac{\mu_a}{\rho U L}\right)^{-1}$ or Re number $\qquad \prod 3 = \frac{hT_\infty}{\rho U^3}$

$\prod 4 = \frac{kT_\infty}{\rho U^3 L} \qquad \prod 5 = \frac{tU}{L} \qquad \prod 6 = \frac{MVD}{L}$

$\prod 7 = \frac{LWC}{\rho} \qquad \prod 8 = \frac{M_{ice}}{\rho L^3}$

Π_3 dimensionless group contains a variable that is difficult to estimate, h, the convective heat transfer coefficient. This coefficient can be obtained from Newton's cooling law (see equation (4.16)).

$$\dot{q}_{cond} = hA(T_s - T_\infty) \tag{4.16}$$

where A is the surface area, T_s the surface temperature, and T_∞ the fluid temperature, in this case air, away from the surface. In no-slip conditions, as in the boundary layer formed by the turbine blades and rotor, the heat transfer from the surface to the fluid layer adjacent to the surface is by pure conduction, since in that zone the fluid is not moving (velocity equal to zero), and can be expressed as follows (Çengel & Cimbala, 2013):

$$\dot{q}_{conv} = \dot{q}_{cond} = -k\frac{\partial T}{\partial y}\bigg|_{y=0} \tag{4.17}$$

Where $\frac{\partial T}{\partial y}\Big|_{y=0}$ is the surface temperature gradient. As a result of the fluid motion, heat is convected away from the surface. It is important to understand that convection heat transfer from a solid surface to a fluid is simply conduction heat transfer from the solid surface to the fluid layer next to the surface. When the temperature distribution within the fluid is known, we may equate equations (4.16) and (4.17) for the heat flux to obtain equation (4.18) for determining the convection heat transfer coefficient.

$$h = \frac{-k\left(\left.\frac{\partial T}{\partial y}\right|_{y=0}\right)}{T_s - T_\infty} \tag{4.18}$$

Due to the complexity of finding each of the parameters of equation (4.18), it is very common to nondimensionalize the heat transfer coefficient, h, with the Nusselt number, defined as (see equation (4.19)).

$$Nu = \frac{hL_c}{k} \tag{4.19}$$

Where k is the thermal conductivity of the fluid and L_c is the characteristic length. This number represents the enhancement of heat transfer through a fluid layer as a result of convection relative to conduction across the same fluid layer (Çengel & Cimbala, 2013).

The Nusselt number for a given geometry can be expressed in terms of the Reynolds number and the Prandtl number (Çengel & Cimbala, 2013), thus simplifying its calculation, since the estimation of these numbers requires variables associated with the fluid: density (ρ), dynamic viscosity (μ), specific heat (K_P), thermal conductivity (k) and velocity (U); and a variable related to the geometry of the surface (L_c).

The experimental data for heat transfer is often represented with reasonable accuracy by a simple power-law relation of the form:

$$Nu = C\mathrm{Re}^m\mathrm{Pr}^n \tag{4.20}$$

Where m and n are constant exponents (usually between 0 and 1), and the value of the constant C depends on geometry. Sometimes, more complex relations are used for better accuracy

(Çengel & Cimbala, 2013). The correlations used to estimate the Nusselt number in this research were for a cylindrical geometry; this shape was chosen due to data available in the literature and because most ice accretion models are based on or derived from this geometry. Table 4.5 summarizes the Nusselt number correlations proposed by various authors to account for roughness due to ice accretion.

Table 4.5 List of the Nusselt number correlations.

Cylinder type	**Nusselt Number**	**Range of Re**	**Equation**	**Ref.**
Rough	$Nu = 0.18\mathrm{Re}^{0.63}$; $\mathrm{Pr} = 0.72$	> 100000	(4.21)	(Achenbach, 1977)
Rough Heigh: 0.9 mm	$Nu = 0.032\mathrm{Re}^{0.83}$	7 x10^4 – 9 x10^5	(4.22)	(L. Makkonen, 1984)
Rough (Icing)	$Nu = 0.117\mathrm{Re}^{0.68}$	---	(4.23)	(Poots, 1996)
Rough	$Nu = 0.2\mathrm{Re}^{0.61}$	---	(4.24)	(Fortin, 2009b)

According to different studies performed on stationary and rotating cylinders (Achenbach, 1977; L. Makkonen, 1984; L. J. Makkonen & Stallabrass, 1984; Poots, 1996), there is a relation between the Reynolds number and the cylinder roughness, which is caused by ice accumulation. This is explained by the fact that the roughness affects the flow behavior, accelerating or retarding the transition from laminar to turbulent flow. However, so far, no general equation has been found that relates roughness, Reynolds number, and Nusselt number. The equations (4.21) and (4.22) are valid under specific conditions.

Because of the foregoing, Π_3 and Π_4, after equating, will form the Nusselt number. Hence, the problem is reduced to six independent parameters. The final expression for the mass of ice accumulated on the wind turbine will be the function in equation (4.25).

$$\Pi_8 = f(\Pi_1, \Pi_2, \Pi_3, \Pi_4, \Pi_5, \Pi_6, \Pi_7)$$

$$\frac{M_{ice}}{\rho L^3} = f\left(TSR, Re, Nu, \frac{tU}{L}, \frac{MVD}{L}, \frac{LWC}{\rho}\right) \tag{4.25}$$

Regarding equation (4.25), all the dimensionless parameters depend on a characteristic length, which is associated with the geometry. In this case, the geometry is the turbine blade; however, the ice accretion process is different along the blade, being greater at the tip of the blade (Burton et al., 2011). For this reason, the calculation of these parameters was performed using the airfoil chord (c) in the section corresponding to 85% of the blade. The chord estimation was performed following the methodology described in the APPENDIX E. Therefore, the equation (4.25) can be rewritten as:

$$\frac{M_{ice}}{\rho c^3} = f\left(TSR, Re, Nu, \frac{tU}{c}, \frac{MVD}{c}, \frac{LWC}{\rho}\right) \tag{4.26}$$

Regarding the final function for the ice mass, we found that these results are similar to those found by Homola, Virk, et al. (2010). In this study, the authors found that for a complete wind turbine, the relationship between turbine size and ice mass was inversely proportional, i.e., less severe for larger turbines. However, this analysis was conducted for rime ice, and further investigations are needed for glaze ice. The same authors also found that the dependence of ice mass on droplet size increases with turbine size; this indicates that knowledge of droplet size is important for estimating ice loads on larger turbines.

In terms of ice accretion, some authors found a relationship between LWC and MVD, which suggests that the increase of both variables implies the increase of ice mass along the chord, being more severe along the thickness of the airfoil (Etemaddar et al., 2014; Jia Yi Jin & Virk, 2019; Pedersen & Sørensen, 2016). Based on these findings, it is valid to confirm the use of the airfoil chord instead of the turbine radius in the dimensionless groups $\Pi_2 = Re$, $\Pi_5 = \frac{tU}{c}$ and $\Pi_6 = \frac{MVD}{c}$.

4.3.3 Dimensionless Groups for the Turbine Power (P)

The same methodology was used to determine the dimensionless groups for the turbine power. In this case, the number of variables (n) is six, and the number of dimensions (j) is three; hence, the number of π groups is three. The selected repeating variables were: $\rho_a, U,\ and\ L$, again, these variables were chosen because they include all the dimensions in the problem, and they do not form a π product between them. After the algebraic development for each of the π groups for the remaining variables ($\Omega, P\ and\ M_{ice}$ see APPENDIX D), the following dimensionless groups were obtained:

$\prod 1' = \frac{\Omega L}{U}$ or TSR $\qquad \prod 2' = \frac{M_{ice}}{\rho L^3} \qquad \prod 3' = \frac{P}{\rho U^3 L^2}$

For calculations on the final expression for the wind turbine power, the $\Pi_{2'}$ was used according to equation (4.26). Hence, the final expression for the wind turbine power under icing conditions will be the function in equation (4.27).

$$\frac{P}{\rho U^3 L^2} = f\left(TSR, Re, Nu, \frac{tU}{c}, \frac{MVD}{c}, \frac{LWC}{\rho}\right) \tag{4.27}$$

This expression allows us to express turbine power directly in terms of the variables that influence ice mass (see equation (4.27)).

As expected, the power turbine will be a function of the TSR. This parameter is essential in wind turbine design, and it refers to the ratio between the wind speed and the tangential velocity of the rotor blades (Burton et al., 2011; Contreras Montoya et al., 2021; Manwell et al., 2010), thus it allows for ensuring that the maximum amount of energy can be extracted from the wind.

Turkia et al. (2013) showed that as the ice mass was increased, the reduction in the power production was 18% for a short icing event and 24% for a long icing event. According to this research, the anticipated correlation with the π theorem methodology, in which turbine power is a function of ice mass, which in turn depends on the event duration, will also be valid.

Observing in detail, the form of the dimensionless parameter of the power agrees with the wind energy theory, where the power coefficient is defined as (Burton et al., 2011):

$$C_P = \frac{P}{\frac{1}{2}\rho U^3 A} \tag{4.28}$$

where A is the swept area of the turbine (πR^2), hence the equation (4.28) can be written in terms of the turbine size as:

$$C_P = \frac{P}{\frac{1}{2}\pi\rho U^3 R^2} \tag{4.29}$$

The above allows us to rewrite equation (4.27) to incorporate the pure constants (1/2 and π) present in the theoretical calculation of the wind turbine power:

$$C_P = \frac{P}{\frac{1}{2}\pi\rho U^3 R^2} = f\left(TSR, Re, Nu, \frac{tU}{c}, \frac{MVD}{c}, \frac{LWC}{\rho}\right) \tag{4.30}$$

4.3.4 Correlation Analysis

Before analyzing the function for turbine coefficient power, a correlation analysis was performed across the different Π groups in equation (4.30). In this analysis, the "Spearman rank method" was used, a nonparametric measure of the strength and direction of a monotonic but nonlinear relationship between two variables. Spearman's correlation coefficient ranges from -1 to +1 (Schober, Boer, & Schwarte, 2018). The sign of the correlation coefficient (r_s) indicates the direction of the relationship (increasing or decreasing), while the magnitude of the correlation (how close it is to -1 or +1) indicates the strength of the relationship (see Table 4.6).

Table 4.6 A guide to describe the strength of r_s
Taken from Weir (s. d.)

Absolute value of r_s	**Strength**
0.00 – 0.19	Very weak
0.20 – 0.39	Weak
0.40 – 0.59	Moderate
0.60 – 0.79	Strong
0.80 – 1.00	Very Strong

In the following tables, the significance of the π groups is as follows (from equation (4.30)).

$\prod 1 = TSR$ $\prod 2 = Re$ $\prod 3 = Nu$

$\prod 4 = \frac{tU}{c}$ $\prod 5 = \frac{MVD}{c}$ $\prod 6 = \frac{LWC}{\rho}$

$\prod 7 = C_P = \frac{P}{\frac{1}{2}\pi\rho U^3 R^2}$ $\prod 8 = \frac{M_{ice}}{\rho c^3}$

The correlation analysis was performed for four cases, a "general case" that includes all the temperatures ranges of the database; the "glace ice case" that includes the temperature range between 0°C and -3°C; the "mixed ice case" that includes the temperature range between -3°C and -10°C; and the "rime ice case" that includes the temperatures below -10°C.

Table 4.7 shows the correlation matrix obtained for the general case. As expected, the parameter that presents the strongest relation with the power coefficient is the TSR, with a value of 0.75, followed by the Reynolds number, the Nusselt numbers, and Π_4 (dimensionless accretion time). These parameters allow for the inclusion of heat transfer processes. In this case, Π_5 and Π_6 showed a very weak, negative relationship with the power coefficient, indicating that the higher the MVD and LWC, the lower the power coefficient. This observation is consistent with the literature: larger water droplets exhibit greater inertia, resulting in higher collection efficiency on the blade surface. As a result, the accumulated ice mass increases, reducing aerodynamic efficiency and lowering the power coefficient.

Regarding the Nusselt (Π_3), the three equations used to estimate it yield identical correlations; therefore, any of them may be used interchangeably in subsequent analyses. As the only correlation reported in the literature that accounts for icing-induced roughness is given by equation (4.23): $Nu = 0.117\text{Re}^{0.68}$, it will be assumed that this expression will be adopted for subsequent analyses. It should also be noted that the Reynolds and Nusselt numbers yield the same correlations, as expected, since the Nusselt number is directly derived from the Reynolds number. Nevertheless, the use of the Nusselt number is preferred, as it can be directly obtained from CFD-based formulations (see equations (4.18) and (4.19)), without requiring the assumption that the airfoil can be approximated as a cylindrical geometry.

The dimensionless ice mass (Π_8) exhibits a significant negative correlation with the power coefficient C_P across the general case, as shown in Table 4.7. This inverse relationship quantitatively confirms the detrimental impact of ice accumulation on wind turbine aerodynamic performance and power output.

Physically, ice accumulation on turbine blades alters the aerodynamic profile by increasing surface roughness and altering blade geometry, leading to increased drag and reduced lift. These aerodynamic degradations directly translate into a reduction of the turbine's power coefficient, consistent with the observed negative correlation coefficient of −0.60. This magnitude indicates a moderate to strong monotonic relationship, underscoring M_{ice}^* as a critical parameter for characterizing icing severity and its operational consequences.

Table 4.7 Correlation matrix for the general case

	Π_1 = TSR	Π_2 = Re	$\Pi_3 = Nu = 0.18Re^{0.63}$	$\Pi_3 = Nu = 0.117Re^{0.68}$	$\Pi_3 = Nu = 0.2Re^{0.61}$	Π_4 = tU/c	Π_5 = MVD/c	Π_6 = LWC/ρa	$\Pi_7 = C_P$	Π_8 = Mice*
Π_1 = TSR	1	0,44	0,44	0,44	0,44	0,40	-0,14	-0,15	0,75	-0.37
Π_2 = Re	0,44	1	1	1	1	0,98	-0,10	-0,09	0,67	-0.61
$\Pi_3 = Nu = 0.18Re^{0.63}$	0,44	1	1	1	1	0,98	-0,10	-0,09	0,67	-0.61
$\Pi_3 = Nu = 0.117Re^{0.68}$	0,44	1	1	1	1	0,98	-0,10	-0,09	0,67	-0.61
$\Pi_3 = Nu = 0.2Re^{0.61}$	0,44	1	1	1	1	0,98	-0,10	-0,09	0,67	-0.61
Π_4 = tU/c	0,40	0,98	0,98	0,98	0,98	1	0,00	0,01	0,64	-0.62
Π_5 = MVD/c	-0,14	-0,10	-0,10	-0,10	-0,10	0,00	1	1	-0,15	0.10
Π_6 = LWC/ρa	-0,15	-0,09	-0,09	-0,09	-0,09	0,01	1	1	-0,15	0.10
$\Pi_7 = C_P$	0,75	0,67	0,67	0,67	0,67	0,64	-0,15	-0,15	1	-0.60
Π_8 = Mice*	-0.37	-0.61	-0.61	-0.61	-0.61	-0.62	0.10	0.10	-0.60	1

Furthermore, M_{ice}* shows negative correlations with other dimensionless groups related to flow dynamics and heat transfer, such as the Reynolds and Nusselt numbers. This suggests that higher ice mass is associated with flow regimes and thermal conditions that exacerbate aerodynamic losses. The negative correlation with Reynolds number may reflect the influence of ice-induced roughness on boundary layer transition and flow separation, while the relationship with Nusselt number highlights the role of convective heat transfer in ice accretion dynamics.

Conversely, the correlations between M_{ice}* and meteorological parameters such as MVD and LWC are weakly positive and relatively low in magnitude. This indicates that, while these parameters govern the initial conditions for ice formation, their direct influence on the normalized ice mass is less pronounced than the integrated aerodynamic and thermodynamic effects captured by the other dimensionless groups.

Regarding the rime ice case (see Table 4.8), again, the parameter that most influences the power coefficient is the TSR. Re, Nu, and Π_4 show weak positive correlations, indicating lower relevance in this case. Regarding the low influence of the Nusselt number, Ibrahim et al. (2023a) reported in their study that during rime ice accretion, heat transfer is dominated by conduction rather than convection, making Nu less sensitive to changes in aerodynamic performance.

Table 4.8 Correlation matrix for the rime ice case

	Π_1 = TSR	Π_2 = Re	Π_3 = $Nu = 0.117\mathrm{Re}^{0.68}$	Π_4 = tU/c	Π_5 = MVD/c	Π_6 = LWC/ρ_a	Π_7 = C_P	Π_8 = Mice*
Π_1 = TSR	1	-0,31	-0,31	-0,31	0,13	0,16	0,68	0.34
Π_2 = Re	-0,31	1	1	1	-0,41	-0,46	0,25	-0.69
Π_3 = $Nu = 0.117\mathrm{Re}^{0.68}$	-0,31	1	1	1	-0,41	-0,46	0,25	-0.69
Π_4 = tU/c	-0,31	1	1	1	-0,38	-0,43	0,25	-0.69
Π_5 = MVD/c	0,13	-0,41	-0,41	-0,38	1	0,99	-0,17	0.29
Π_6 = LWC/ρ_a	0,16	-0,46	-0,46	-0,43	0,99	1	-0,17	0.36
Π_7 = C_P	0,68	0,25	0,25	0,25	-0,17	-0,17	1	-0.18
Π_8 = Mice*	0.34	-0.69	-0.69	-0.69	0.29	0.36	-0.18	1

The Nusselt number is also dependent on boundary layer characteristics, which are affected by surface roughness. Although rime ice increases roughness, it does not create significant turbulence or flow separation. As a result, changes in Nu due to roughness under rime conditions are relatively small and do not correlate strongly with variations in the power coefficient.

About the Reynolds number, under rime conditions, Re values may remain relatively stable because of low wind speeds or reduced turbulence near the blade surface. This stability minimized variations in Nu, reducing its correlation with the power coefficient.

This scenario also demonstrates that the MVD and LWC exhibit a very weak negative correlation with the power coefficient. The low correlation between LWC and the power coefficient under rime-ice conditions may be attributed to the unique characteristics of rime-ice formation and its effects on aerodynamic efficiency. Rime ice forms at low temperatures and low LWC, when supercooled water droplets freeze immediately upon contact with the blade surface. This produces a porous, frost-like ice structure characterized by low density and less aerodynamic disruption, because the alterations in the surface roughness, which increase drag and decrease lift, are not as drastic as those caused by thicker or more protruding glaze ice formations. Immediate freezing minimizes the spread of water across the blade, leading to less uniform ice coverage and a reduced impact on blade shape and airflow (Caccia & Guardone, 2023; Sista, Hu, & Hu, 2022). The observed correlation coefficient of approximately −0.18 between M_{ice}^* and C_P reflects this effect, though it is less pronounced than in glaze or mixed ice conditions.

In the rime ice regime, the M_{ice}^* maintains a negative correlation with the power coefficient C_P, consistent with the general case but with a reduced magnitude. This indicates that increased ice accumulation continues to adversely affect turbine performance, albeit with a somewhat weaker monotonic relationship compared to the overall dataset.

Moreover, M_{ice}^* exhibits stronger negative correlations with flow-related dimensionless groups such as the Reynolds number and the Nusselt number in the rime ice case. This suggests that aerodynamic and thermal flow characteristics play a significant role in modulating the impact of ice accumulation on turbine performance under rime conditions. The negative correlation with Reynolds number may indicate the influence of ice-induced surface roughness on boundary-layer behavior and flow separation, while the relationship with Nusselt number highlights the role of convective heat transfer in the ice accretion process.

Interestingly, the correlations between M_{ice}^* and meteorological parameters such as MVD and LWC are positive but remain relatively weak. This aligns with the understanding that although these parameters govern the initial ice-formation conditions, their direct influence on normalized ice mass and consequent power loss is mediated by complex aerodynamic and thermodynamic interactions.

In summary, within the rime ice regime, M_{ice}^* remains a relevant but less dominant predictor of power loss compared to other icing conditions. Its moderate negative correlation with C_P underscores the need to incorporate aerodynamic and heat-transfer parameters, alongside ice-mass metrics, to accurately model turbine performance degradation. This nuanced behavior highlights the importance of regime-specific modeling approaches to capture the distinct physical mechanisms governing ice accretion and its effects on wind turbine efficiency.

The power coefficient in the glaze ice case (see Table 4.9) has a strong relation with TSR, Re, Nu, and Π_4. This case is similar to the general case, since the parameter involving heat transfer phenomena has a strong influence on the power coefficient. The freezing process under glaze conditions involves significant latent heat release, which affects how quickly ice forms. However, this process is governed by convective heat transfer, which is related to the Nusselt number (Ibrahim et al., 2023a). Again, the MVD and the LWC have little influence on the power coefficient, which is lower than in the rime ice case. This may be explained by the fact that glaze ice formation requires a "threshold" of LWC and MVD to be met. Once this threshold is surpassed, the ice formed is relatively consistent, regardless of further increases in LWC and MVD. The blade may reach a saturation point where it can't effectively accrete any more ice; once the surface is fully covered with glaze ice, additional water content might run off or freeze in less aerodynamically impactful ways, weakening the correlation with the power coefficient.

Contrary to the rime and general cases, the correlation with LWC and MVD is positive and very weak. Variations in LWC and MVD might have a more proportional impact on roughness and ice accretion, thereby slightly increasing the correlation. In other words, a little more LWC and MVD leads to a little more performance degradation.

In the glaze ice regime, the M_{ice}* exhibits a strong negative correlation with the power coefficient C_P, similar to the general case. This indicates that ice accumulation under glaze conditions has a pronounced detrimental effect on turbine performance. Glaze ice formation involves significant convective heat transfer and latent heat release, intensifying ice accretion and its aerodynamic impact.

Additionally, M_{ice}* shows strong negative correlations with flow and heat-transfer parameters, such as Reynolds and Nusselt numbers, underscoring the interplay among aerodynamic roughness, thermal dynamics, and performance degradation in glaze-ice scenarios. Conversely, correlations with meteorological parameters MVD and LWC remain weak, indicating that once glaze ice formation thresholds are exceeded, further variations in MVD and LWC have a limited incremental effect on power loss.

Table 4.9 Correlation matrix for the glaze ice case

	Π_1 = TSR	**Π_2 = Re**	**Π_3 = Nu= $= 0.117Re^{0.68}$**	**Π_4 = tU/c**	**Π_5 = MVD/c**	**Π_6 = LWC/ρ_a**	**Π_7 = C_P**	**Π_8 = Mice***
Π_1 = TSR	1	0,39	0,39	0,36	0,14	0,13	0,72	-0.37
Π_2 = Re	0,39	1	1	0,99	-0,05	-0,04	0,66	-0.68
Π_3 = $Nu = 0.117Re^{0.68}$	0,39	1	1	0,99	-0,05	-0,04	0,66	-0.68
Π_4 = tU/c	0,36	0,99	0,99	1	-0,04	-0,03	0,64	-0.68
Π_5 = MVD/c	0,14	-0,05	-0,05	-0,04	1	0,99	0,04	0.04
Π_6 = LWC/ρ_a	0,13	-0,04	-0,04	-0,03	0,99	1	0,03	0.04
Π_7 = C_P	0,72	0,66	0,66	0,64	0,04	0,03	1	-0.60
Π_8 = **Mice***	-0.37	-0.68	-0.68	-0.68	0.04	0.04	-0.60	1

In the case of mixed ice (see Table 4.10), the TSR correlates strongly with the power coefficient at 0,76, slightly higher than in both glaze and general cases. This case showed the strongest correlations between Re, Nu, and Π4 and the power coefficient. This suggests that the power coefficient is more directly influenced by aerodynamic and heat-transfer dynamics than by the initial icing conditions.

Mixed ice conditions consist of both rime and glaze ice, forming under varying temperatures, LWC, and droplet sizes. This causes uneven ice buildup on the blade surface, leading to variations in ice type and distribution, making it challenging to directly relate LWC, MVD, and the power coefficient.

In summary, LWC and MVD show a low correlation with the power coefficient under mixed-ice conditions because their influence on turbine performance is indirect, mediated by complex interactions among rime and glaze ice formations, the spatial distribution of ice, and aerodynamic effects. Other factors, such as TSR, Re, and Nu, play a more dominant role in determining the power coefficient under these conditions.

Table 4.10 Correlation matrix for the mixed ice case

	Π_1 = TSR	Π_2 = Re	$\Pi_3 = Nu = 0.117Re^{0.68}$	Π_4 = tU/c	Π_5 = MVD/c	$\Pi_6 = LWC/\rho_a$	$\Pi_7 = C_P$	Π_8 = Mice*
Π_1 = TSR	1	0,51	0,51	0,48	-0,17	-0,18	0,76	-0.41
Π_2 = Re	0,51	1	1	0,99	-0,04	-0,03	0,67	-0.57
$\Pi_3 = Nu = 0.117Re^{0.68}$	0,51	1	1	0,99	-0,04	-0,03	0,67	-0.57
Π_4 = tU/c	0,48	0,99	0,99	1	0,00	0,01	0,66	-0.57
Π_5 = MVD/c	-0,17	-0,04	-0,04	0,00	1	1	-0,17	0.17
$\Pi_6 = LWC/\rho_a$	-0,18	-0,03	-0,03	0,01	1	1	-0,17	0.17
$\Pi_7 = C_P$	0,76	0,67	0,67	0,66	-0,17	-0,17	1	-0.63
Π_8 = Mice*	-0.41	-0.57	-0.57	-0.57	0.17	0.17	-0.63	1

In the mixed ice regime, the M_{ice}* exhibits a moderate negative correlation with the power coefficient, indicating that increased ice accumulation negatively impacts turbine performance, consistent with other icing regimes. This regime, characterized by the coexistence of rime and glaze ice, introduces complex spatial and temporal variations in ice morphology and distribution. Consequently, the influence of meteorological parameters, such as LWC and

MVD, on Mice∗ is less direct and weaker than that of aerodynamic and thermal flow parameters.

Notably, M_{ice}* shows stronger negative correlations with aerodynamic and heat-transfer dimensionless groups, such as the Reynolds and Nusselt numbers, underscoring the dominant role of flow dynamics and convective heat transfer in modulating power loss under mixed icing conditions.

4.4 Conclusion

This chapter examined the correlation structure of the derived Π groups to identify the most influential parameters governing wind turbine performance under icing conditions. The correlation matrices revealed clear patterns linking aerodynamic and heat-transfer dynamics to power loss, while also highlighting the varying importance of meteorological parameters across icing regimes. The main findings can be summarized as follows:

- Tip Speed Ratio shows a strong positive correlation with the power coefficient across all cases, underscoring its importance to turbine performance (Burton et al., 2011; Manwell et al., 2010). This correlation is strongest under glaze and mixed ice conditions and weaker in rime ice cases, reflecting the aerodynamic impact of different ice morphologies.
- Nusselt number correlations remained unchanged regardless of the equation used to calculate it, validating the robustness of this parameter and indicating that subsequent analyses can be carried out with a single formulation.
- Reynolds number, Nusselt number, and TSR all demonstrated stronger correlations with the power coefficient than liquid water content (LWC) or median volume diameter (MVD). While LWC and MVD govern the rate and nature of ice accretion, their direct effect on the power coefficient is limited compared to aerodynamic and heat-transfer dynamics.
- MVD and LWC are strongly correlated with one another across all icing conditions, reflecting their shared role in atmospheric icing processes. However, both exhibits consistently weak correlations with the power coefficient. This suggests that power losses

are more strongly influenced by variables such as wind speed, blade geometry, and temperature, rather than by LWC or MVD alone (Caccia & Guardone, 2023; Sista et al., 2022). Alternatively, this could indicate a need to refine dimensionless formulations to better capture their indirect influence.

- In summary, the dimensionless ice mass M_{ice}^* emerges as a robust and physically meaningful predictor of power loss in iced wind turbines. Its strong negative correlation with the power coefficient validates its inclusion in predictive models and supports the dimensional analysis framework employed in this study. The results emphasize the need to incorporate M_{ice}^* alongside aerodynamic and thermal dimensionless parameters to accurately capture the complex interplay of factors governing turbine performance degradation under icing conditions.
- The strength and direction of correlations vary by icing regime, underscoring the importance of distinguishing between rime, glaze, and mixed ice when analyzing turbine performance.

In summary, the performance of wind turbines under icing conditions results from a complex interplay of aerodynamic, thermodynamic, and environmental factors. While some parameters, such as TSR, consistently dominate, others exert their influence in ways that depend strongly on the prevailing icing regime. Notably, the results show that the type of ice formation exerts a more substantial influence on the power coefficient than LWC or MVD considered in isolation. These findings point to the need for advanced modeling approaches that move beyond single-parameter correlations and account for nonlinear interactions among multiple dimensionless groups and environmental conditions. Such models are essential for improving predictive capability and for developing mitigation strategies for icing-related performance degradation in wind turbines.

In order to generalize the present analysis to rotors with different geometries (blade length and chord), implies that the blade solidity (σ) should, in principle, be introduced as an additional non-dimensional parameter. Blade solidity can be defined as the blade planform area (number of blades (N) times radius times mean chord($\bar{c}$)) divided by the swept area, which makes it approximately proportional to the chord-to-radius ratio (see equation (4.31)). However, in this thesis only a single blade geometry with fixed chord and radius is considered, so the solidity remains constant and does not influence the observed trends among the other dimensionless groups. For this reason, solidity is acknowledged and discussed conceptually, but it is not explicitly included in the present non-dimensional formulation; its explicit treatment is left for future generalizations involving varying blade lengths and chord.

$$\sigma = \frac{NR\bar{c}}{\pi R^2} = \frac{N\bar{c}}{\pi R} \tag{4.31}$$

Even though the Reynolds and Nusselt numbers were interdependent, they were included in the analysis to capture, in a compact and general way, the combined effects of flow conditions and heat transfer on ice accretion. In the analysis, empirical relationships were used to estimate Nusselt number, MVD, and LWC, which makes these quantities interdependent within the specific data set examined. Nevertheless, by expressing the governing phenomena in terms of Reynolds and Nusselt numbers, the methodology remains applicable to other data sources where these parameters may be available independently, for example from detailed CFD-based calculations of convective heat transfer. This approach ensures that the framework is not limited to a single experimental configuration, but can be extended to different icing conditions as long as the relevant dimensionless groups are provided.

CHAPTER 5

METHODOLOGY VALIDATION USING MACHINE LEARNING METHODS

5.1 Introduction

The application of the Buckingham π theorem reduces complex physical phenomena to a set of dimensionless parameters, simplifying analysis and improving generalizability. This chapter focuses on validating these dimensionless parameters for wind turbine icing using machine learning.

The dimensionless correlations derived in Chapter 4 using the Buckingham π theorem provide a physically grounded framework for estimating power losses in wind turbines operating under icing conditions. These correlations reduce the complexity of the problem by transforming meteorological, geometrical, and operational variables into a set of dimensionless groups:

Input variables: $\prod 1 = TSR, \prod 2 = Re, \prod 3 = Nu, \prod 4 = \frac{tU}{c}, \prod 5 = \frac{MVD}{c}$ and $\prod 6 = \frac{LWC}{\rho}$

Output variables: $\prod 7 = C_P = \frac{P}{\frac{1}{2}\pi\rho U^3 R^2}$

The proposed formulation aims to preserve physical interpretability while enabling generalization across different turbines and environmental conditions. In this case, the dimensionless group $\prod_8 = \frac{M_{ice}}{\rho c^3}$, associated with the accreted ice mass, is not included in the final set of correlations. Although the correlation analysis revealed an expected relationship between Π_8 and the other dimensionless groups, it also evidenced a strong interdependence with multiple meteorological and operational parameters. This coupling makes it difficult to isolate the individual contribution of ice mass without introducing redundancy into the predictive framework. Consequently, to ensure the consistency, robustness, and applicability of the proposed methodology, all correlations are validated solely on the basis of the power coefficient. This choice aligns with the thesis's primary objective: directly relating measurable environmental and operational parameters to wind turbine performance degradation under icing conditions.

The objective of this chapter is to rigorously validate these correlations using supervised learning techniques. Machine learning techniques offer a powerful approach to modeling complex relationships in engineering problems. To assess the predictive capacity of these correlations, this chapter explores the application of three methods – decision trees (DT), random forests (RF), and neural networks (NN) – to validate the relationship between the dimensionless parameters and the wind turbine power coefficient under icing conditions. This chapter provides a comprehensive comparison of the three machine learning techniques, highlighting their strengths and weaknesses in capturing the complex interplay between the dimensionless parameters and the power coefficient. The findings advance wind energy in cold climates by providing insights into the effectiveness of these parameters and the suitability of different machine learning models for complex engineering problems. The subsequent sections detail the model architectures, training procedures, and a comparative analysis of their predictive capabilities.

Each model was trained to predict the dimensionless power coefficient (Π_7) based on the input π groups (Π_1 to Π_6), using the dataset mentioned in CHAPTER 3. The dataset was partitioned into a "training set" and a "test set". Seventy percent (70%) of the data was allocated to training the models, while thirty percent (30%) was reserved for testing and validation.

The performance of each model was evaluated using three metrics: the coefficient of determination or R–squared score (R^2), the Mean Absolute Error (MAE), and the Root Mean Squared Error (RMSE):

- **R^2:** Measured the proportion of variance in the target variable explained by the model, i.e., this metric indicates how well the predicted values fit the actual data. A value close to 1 indicates a good fit.

- **MAE:** Quantifies the average magnitude of errors between predicted and actual values.
- **RMSE:** Penalizes larger errors more heavily, providing insight into model robustness.

While the coefficient of determination (R^2) provides a global measure of explained variance, MAE and RMSE offer complementary insights into model accuracy and robustness. MAE reflects the average magnitude of prediction errors and is directly interpretable in terms of expected deviation from the true power coefficient. RMSE, by penalizing larger errors more strongly, is particularly sensitive to outliers and extreme operating conditions, which are of high relevance in icing scenarios where sudden aerodynamic degradation may occur.

A combined analysis of MAE and RMSE, therefore, allows for distinguishing between models that perform well on average and those that are robust under adverse or extreme conditions.

Two input configurations were tested for each model:

1) A full feature set comprising all π groups (Π_1 to Π_6).
2) A reduced feature set including only those π groups with a correlation coefficient greater than 0.39 with respect to Π_7.

Additionally, the impact of data normalization using "MinMax Scaling" was evaluated for the decision tree and the random forest models. The main idea behind this method is that variables measured at different scales do not contribute equally to model fitting and the learned function, and this can introduce bias. Also, when comparing different models, data normalization helps maintain consistency across models. Thus, to deal with this potential problem, data normalization, such as "MinMax Scaling," is usually used before model fitting. This method consists of transforming all features to the range (0, 1), meaning that the minimum and maximum values of each variable are 0 and 1, respectively.

$$x_{scaled} = \frac{x - x_{min}}{x_{max} - x_{min}} \tag{5.1}$$

This structure allows for a detailed comparison not only between models, but also between physical regimes and preprocessing strategies, which is particularly relevant for engineering applications and for the assessment of physical robustness.

5.1.1 Decision Tree Results

The Decision Tree model was implemented using the *DecisionTreeRegressor* class from the scikit-learn library in the "**google colaboratory**" environment. Algorithm 5.1 presents the implementation code for the decision tree without preprocessing, and Algorithm 5.2 presents the implementation code for the decision tree with preprocessing.

Algorithm 5.1 Implementation code for the decision tree without preprocessing

```
#Call the dataset
df=pd.read_excel("BD_Complete_Nu2-Relevant.xlsx") #dataset with correlation
coefficient higher than 0.39
#df=pd.read_excel("BD_Complete.xlsx") #dataset of with all pi parameters
dataset=df.values
X=dataset[:,0:6] # input variables
Y=dataset[:,6] # Output variable (power coefficient)

#Split of the dataset
X_train, X_test, Y_train, Y_test = train_test_split(X, Y, test_size=0.3)

#Decision tree model
dt = DecisionTreeRegressor(max_depth=5, min_samples_leaf=3,
min_samples_split=50, random_state=42)
dt.fit(X_train, Y_train)

#Model testing
yhat = dt.predict(X_test)
print("R2_SCORE: ",r2_score(Y_test, yhat))
print("MAE: ",mean_absolute_error(Y_test, yhat))
print("RMSE: ",np.sqrt(mean_squared_error(Y_test, yhat)))
```

The selected hyperparameters (*max_depth, min_samples_leaf, and min_samples_split)* balance model complexity and reproducibility: limiting *max_depth to 5* prevents the tree from overfitting to training-specific patterns. Requiring at least 50 samples per split and at least 3 per leaf reduces noisy, unstable splits, resulting in smoother predictions. These constraints, taken together, reduce variance and enhance the model's ability to generalize to new data. Additionally, setting the random state to 42 makes the training process deterministic, ensuring consistent results across runs, which is valuable for debugging and hyperparameter tuning.

Algorithm 5.2 Implementation code for the decision tree with preprocessing

```
#Call the dataset
df=pd.read_excel("BD_Complete_Nu2-Relevant.xlsx") #dataset with correlation
coefficient higher than 0.39
#df=pd.read_excel("BD_Complete.xlsx") #dataset of with all pi parameters
dataset=df.values
X=dataset[:,0:6] # input variables
Y=dataset[:,6] # Output variable (power coefficient)

#Preprocessing
min_max_scaler = preprocessing.MinMaxScaler()
X_scale = min_max_scaler.fit_transform(X)

#Split of the dataset
X_train, X_test, Y_train, Y_test = train_test_split(X_scale, Y, test_size=0.3)

#Decision tree model
dt = DecisionTreeRegressor(max_depth=5, min_samples_leaf=3,
min_samples_split=50, random_state=42)
dt.fit(X_train, Y_train)

#Model testing
yhat = dt.predict(X_test)
print("R2_SCORE: ",r2_score(Y_test, yhat))
print("MAE: ",mean_absolute_error(Y_test, yhat))
print("RMSE: ",np.sqrt(mean_squared_error(Y_test, yhat)))
```

Figure 5.1 presents the R^2 scores obtained across eight scenarios, combining ice types (rime, glazed, mixed, and general) and input configurations (all π groups vs. relevant π groups), with and without data normalization.

In general, the R^2 results summarized in Figure 5.1 reveal a moderate but consistent predictive capability. According to Figure 5.1, the model exhibited its highest predictive performance under glaze ice conditions when trained with the relevant π groups (R^2 = 0.759). Conversely, the lowest performance was observed under rime-ice conditions with the full feature set (R^2 =

0.626), suggesting that the model or the input parameters may not capture the target variable's variance effectively.

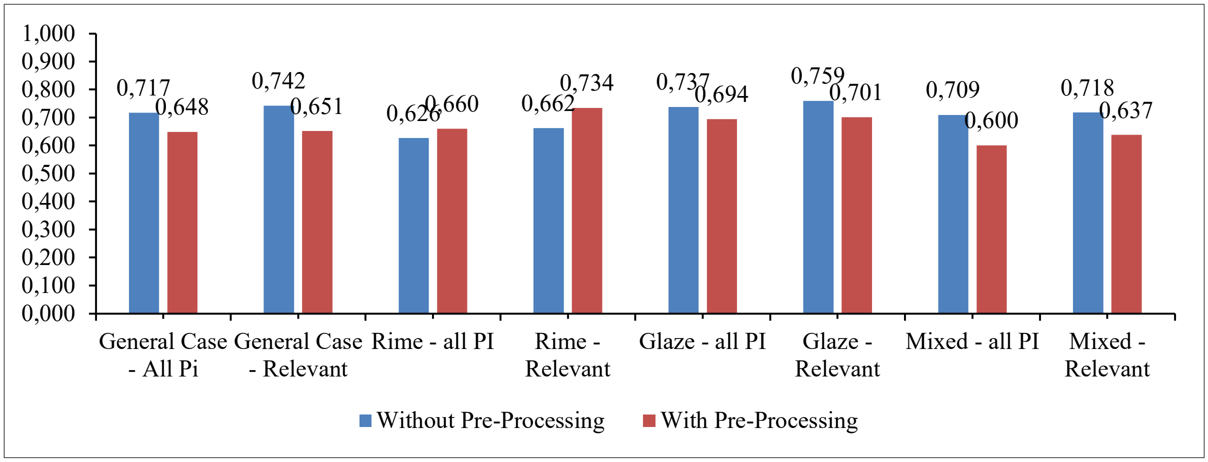

Figure 5.1 Results of the R^2 for all the cases using Decision Trees

The impact of Min-Max normalization is strongly case-dependent. For rime ice, normalization improves performance (R^2 increases from 0.626 to 0.660 across all π groups and from 0.662 to 0.734 across the relevant π groups), indicating that scaling helps balance the influence of multiple moderate predictors. In contrast, for glaze, mixed, and general cases, normalization degrades performance. This suggests that, in these regimes, the absolute magnitude of certain π groups carries physical significance that should not be suppressed by normalization. The corresponding MAE and RMSE trends (Figure 5.2 and Figure 5.3) confirm these observations, with lower errors aligning with higher R^2 values.

According to Figure 5.2, lower errors are observed for glaze ice conditions using the relevant π groups. In rime ice cases, applying Min–Max normalization results in a measurable reduction in both MAE and RMSE, indicating improved average accuracy and reduced sensitivity to extreme deviations.

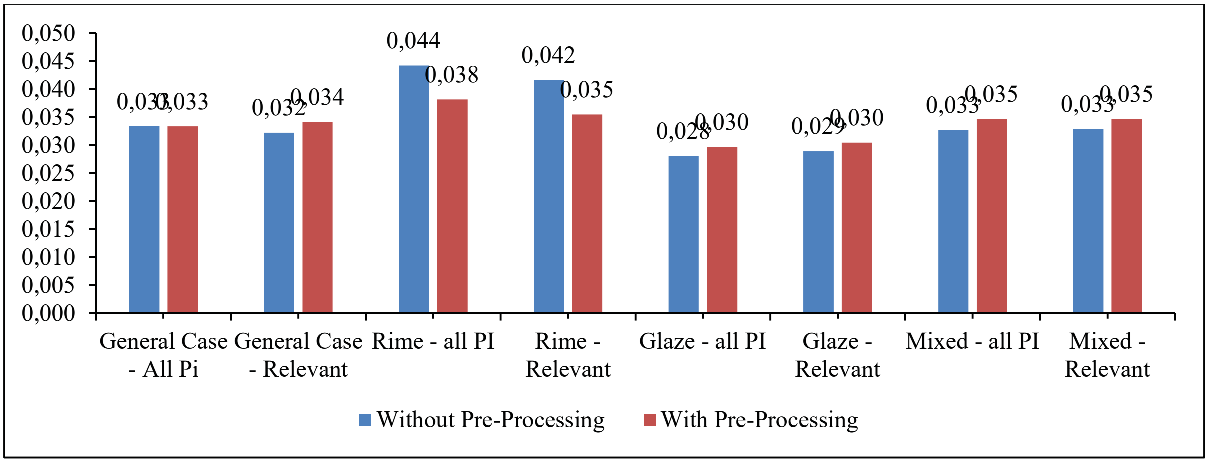

Figure 5.2 Results of the MAE for all the cases using Decision Trees

Conversely, for mixed and general ice conditions, normalization increases RMSE (see Figure 5.3), despite marginal changes in MAE. This divergence suggests that although average errors remain similar, the model exhibits larger deviations at specific operating points, particularly at higher tip-speed ratios. Physically, this reflects the inability of shallow tree structures to capture abrupt transitions and compounded aerodynamic effects present in heterogeneous ice regimes.

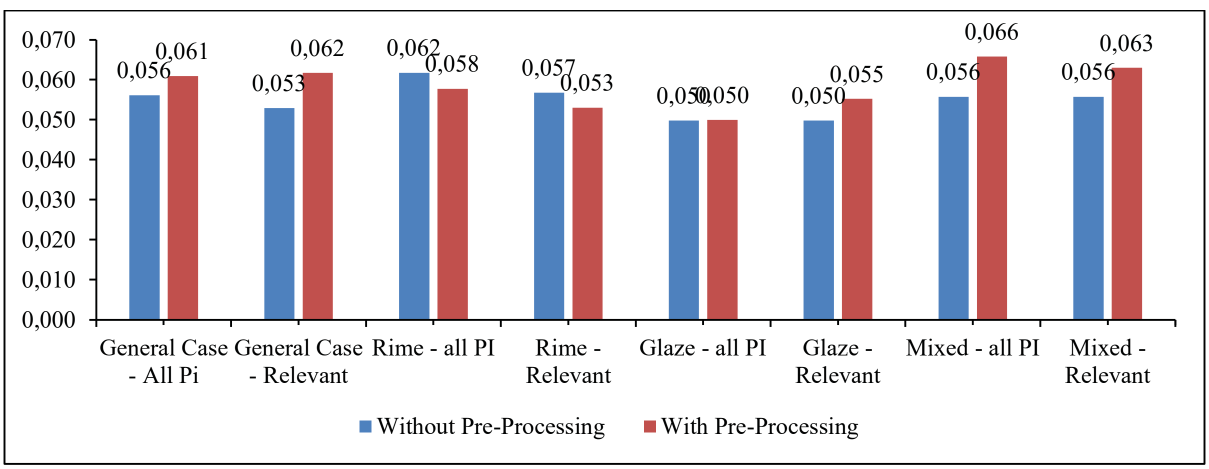

Figure 5.3 Results of the RMSE for all the cases using Decision Trees

The CP-TSR curves shown in Figure 5.4 further illustrate the limitations and strengths of the decision tree model by comparing the validation power coefficient (blue) and the predicted power coefficient (red), showing the model behavior before and after MinMax scaling. MinMax scaling rescales each input feature to the same range (between 0 and 1), which can prevent a large-range feature from dominating early splits and can help when useful information is spread across many features. Conversely, when the absolute scale or spread is itself informative, MinMax can remove that advantage. The plots, therefore, highlight how scaling affects prediction alignment, bias, and spread across the three ice types.

In general, for TSR values below approximately 2, predictions of the power coefficient closely match the validation data in all cases. At higher TSR values, unnormalized models exhibit clustered or segmented predictions, reflecting the piecewise-constant nature of tree-based regressors. In contrast, normalization partially mitigates this effect in the rime case but does not provide systematic improvements elsewhere.

These results suggest that the Decision Tree model is sensitive to both feature selection and feature scaling. This happens because tree splits depending on the relative distribution and importance of numeric variables. When scaling every feature to similar ranges, no single variable can dominate splits solely because of its large numeric range, so in the rime ice case, the model could make better use of multiple moderate predictors, and performance improved. In the other cases (glaze, mixed, and general), scaling reduced the natural differences in magnitude that encoded real, meaningful influence (for example, a physical variable whose larger range actually signals stronger predictive power), so preserving the original scale kept those features prioritized by the split criterion and yielded better results. Overall, Decision Trees demonstrated that the π groups encode physically meaningful information, but their limited capacity restricts their ability to capture higher-order nonlinear interactions present in more complex icing scenarios.

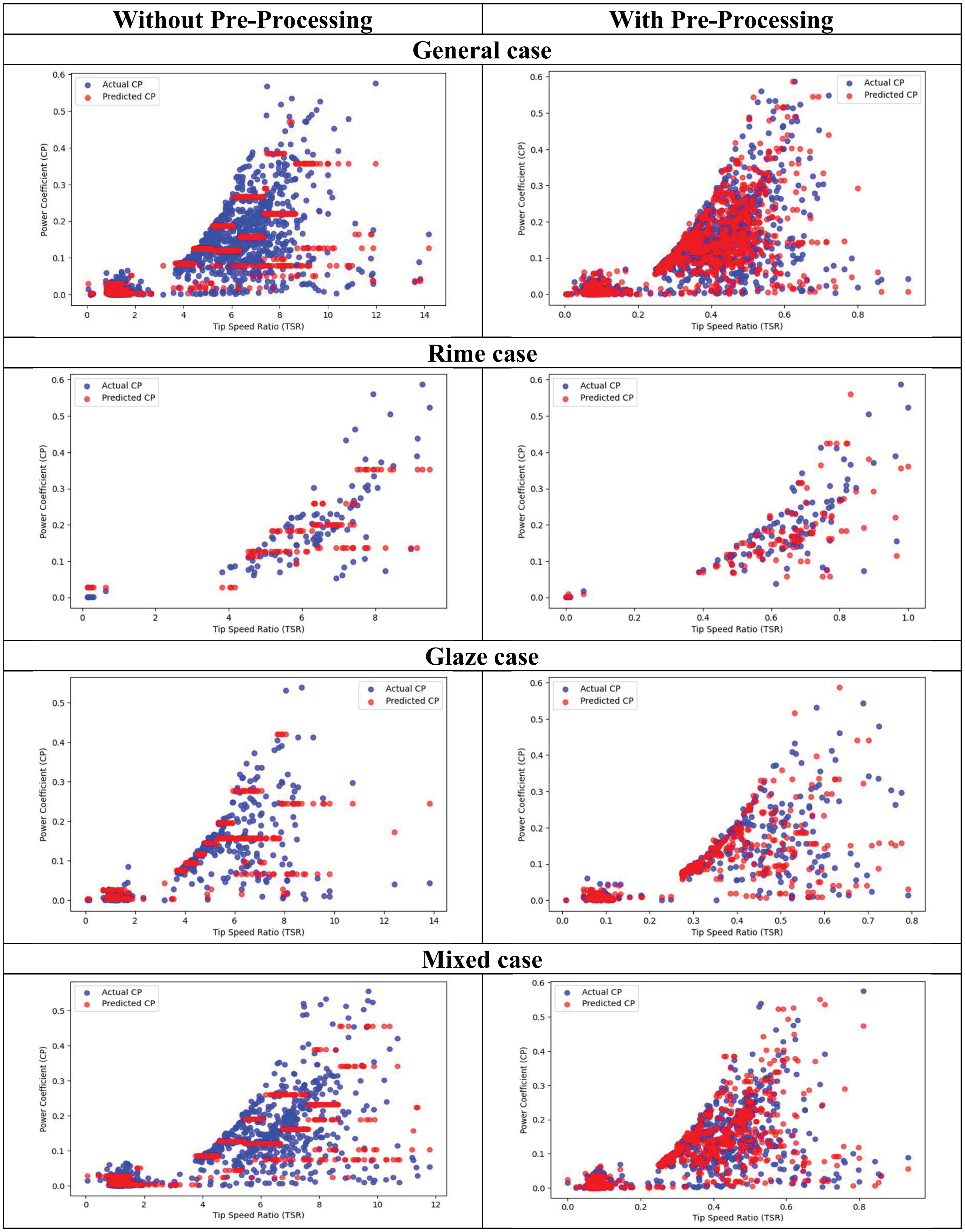

Figure 5.4 Comparison of the CP-TSR curves between the test and the predicted values of the relevant π groups, and between the implementation of normalization for all the ice types using Decision Trees

5.1.2 Random Forest Results

The Random Forest is a model that involves multiple Decision Trees on different random subsets of the training data and features and combines their outputs to produce a final prediction. This averaging reduces the variance associated with individual trees and often improves generalization, making it more robust than a single decision tree. The Random Forest model was implemented using the *RandomForestRegressor* class (see Algorithm 5.3 and Algorithm 5.4)

The hyperparameters specify an ensemble of 250 decision trees (*n_estimators*), each with a maximum depth of 200. Increasing the number of trees improves predictive stability and reduces variance, and a maximum depth of 200 enables each tree to model complex interactions and reduce bias. This architecture is particularly well-suited to problems where multiple weak predictors jointly contribute to the response.

Algorithm 5.3 Implementation code for the Random Forest without preprocessing

```
#Call the dataset
df=pd.read_excel("BD_Complete_Nu2-Relevant.xlsx") #dataset with correlation
coefficient higher than 0.39
#df=pd.read_excel("BD_Complete.xlsx") #dataset of with all pi parameters
dataset=df.values
X=dataset[:,0:6] # input variables
Y=dataset[:,6] # Output variable (power coefficient)

#Split of the dataset
X_train, X_test, Y_train, Y_test = train_test_split(X, Y, test_size=0.3)

#Random forest model
RF = RandomForestRegressor(n_estimators = 250, max_depth=200)
RF.fit(X_train, Y_train)

#Model testing
yphat = RF.predict(X_test)
r2_score(Y_test, yphat), mean_absolute_error(Y_test, yphat),
np.sqrt(mean_squared_error(Y_test, yphat))

print("R2_SCORE: ",r2_score(Y_test, yphat))
print("MAE: ",mean_absolute_error(Y_test, yphat))
print("RMSE: ",np.sqrt(mean_squared_error(Y_test, yphat)))
```

As shown in Figure 5.5, the R^2 score improves significantly across all cases, outperforming the decision tree for all ice types and configurations, as expected. Again, the highest R^2 score was achieved under rime ice conditions with the complete feature set (R^2 = 0.819). In contrast to the decision tree, the random forest model demonstrated a slight decrease in performance when trained with the reduced feature set, particularly in the general and mixed ice scenarios. This behavior suggests that even features with low individual correlation may contribute valuable information when aggregated across multiple decision trees. Removing these parameters may eliminate important patterns, making it harder for the model to explain the target variable's variance. Also, with fewer features, the Decision Trees in the Random Forest will have less information to split on, leading to simpler trees with lower predictive power and a lower R^2 score.

Algorithm 5.4 Implementation code for the Random Forest with preprocessing

```
#Call the dataset
df=pd.read_excel("BD_Complete_Nu2-Relevant.xlsx") #dataset with correlation
coefficient higher than 0.39
#df=pd.read_excel("BD_Complete.xlsx") #dataset of with all pi parameters
dataset=df.values
X=dataset[:,0:6] # input variables
Y=dataset[:,6] # Output variable (power coefficient)

#Preprocessing
min_max_scaler = preprocessing.MinMaxScaler()
X_scale = min_max_scaler.fit_transform(X)

#Split of the dataset
X_train, X_test, Y_train, Y_test = train_test_split(X_scale, Y, test_size=0.3)

#Random forest model
RF = RandomForestRegressor(n_estimators = 250, max_depth=200)
RF.fit(X_train, Y_train)

#Model testing
yphat = RF.predict(X_test)
r2_score(Y_test, yphat), mean_absolute_error(Y_test, yphat),
np.sqrt(mean_squared_error(Y_test, yphat))

print("R2_SCORE: ",r2_score(Y_test, yphat))
print("MAE: ",mean_absolute_error(Y_test, yphat))
print("RMSE: ",np.sqrt(mean_squared_error(Y_test, yphat)))
```

Random Forest models exhibit consistently low MAE and RMSE (Figure 5.6 and Figure 5.7) values across all ice types, confirming the superior accuracy and robustness of the Random Forest model. The relatively small gap between MAE and RMSE indicates that significant outliers are effectively mitigated by ensemble averaging. This behavior is particularly evident in mixed and general ice cases, where individual decision trees may fail locally but the ensemble prediction remains stable.

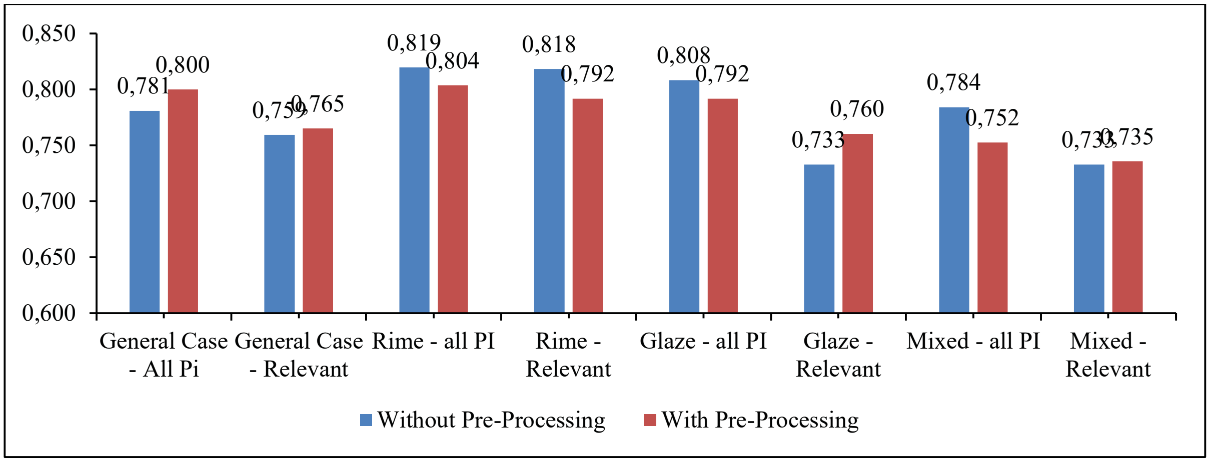

Figure 5.5 Results of the R^2 for all the cases using Random Forest

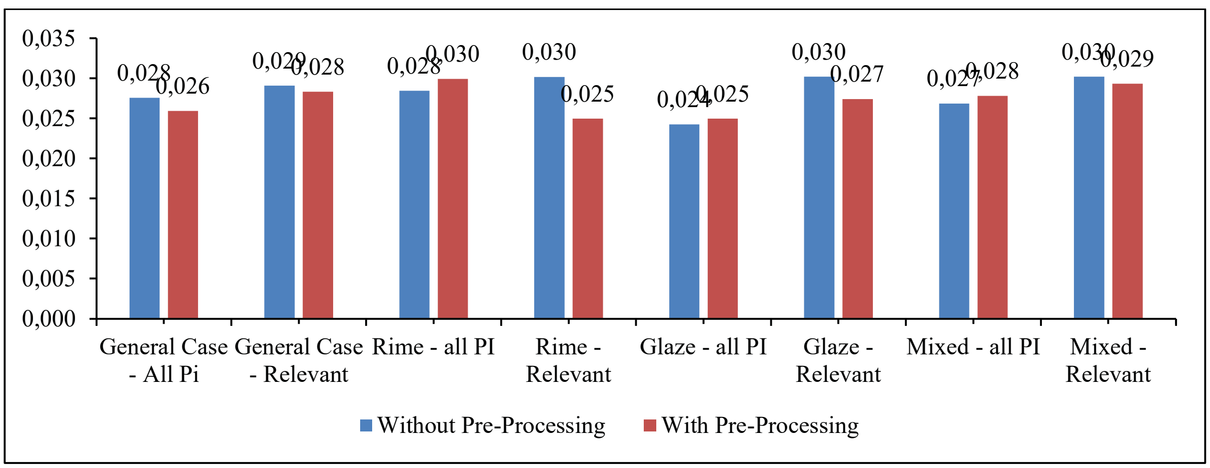

Figure 5.6 Results of the MAE for all the cases using Random Forest

The increase in errors observed with the reduced feature set is more pronounced in RMSE than in MAE, indicating that removing weakly correlated π groups primarily affects the model's ability to handle extreme cases rather than its overall performance. From a physical perspective, this confirms that secondary dimensionless parameters contribute to limiting worst-case prediction errors, even if their average influence appears small.

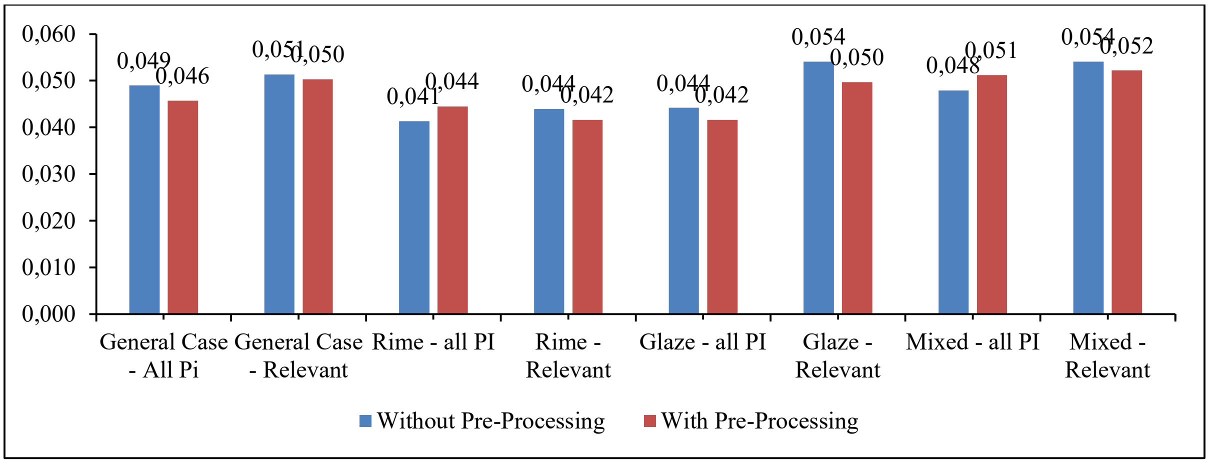

Figure 5.7 Results of the RMSE for all the cases using Random Forest

As expected, data normalization had a negligible impact on the Random Forest's performance, as shown in Figure 5.8. The predicted power coefficient (red dots) is close to the validation set (blue dots) and follows a similar pattern. This is consistent with the threshold-based nature of tree ensembles, which are insensitive to monotonic feature scaling. From a physical perspective, this robustness is advantageous, as it implies that the model can exploit both relative and absolute magnitudes of dimensionless parameters without requiring extensive preprocessing.

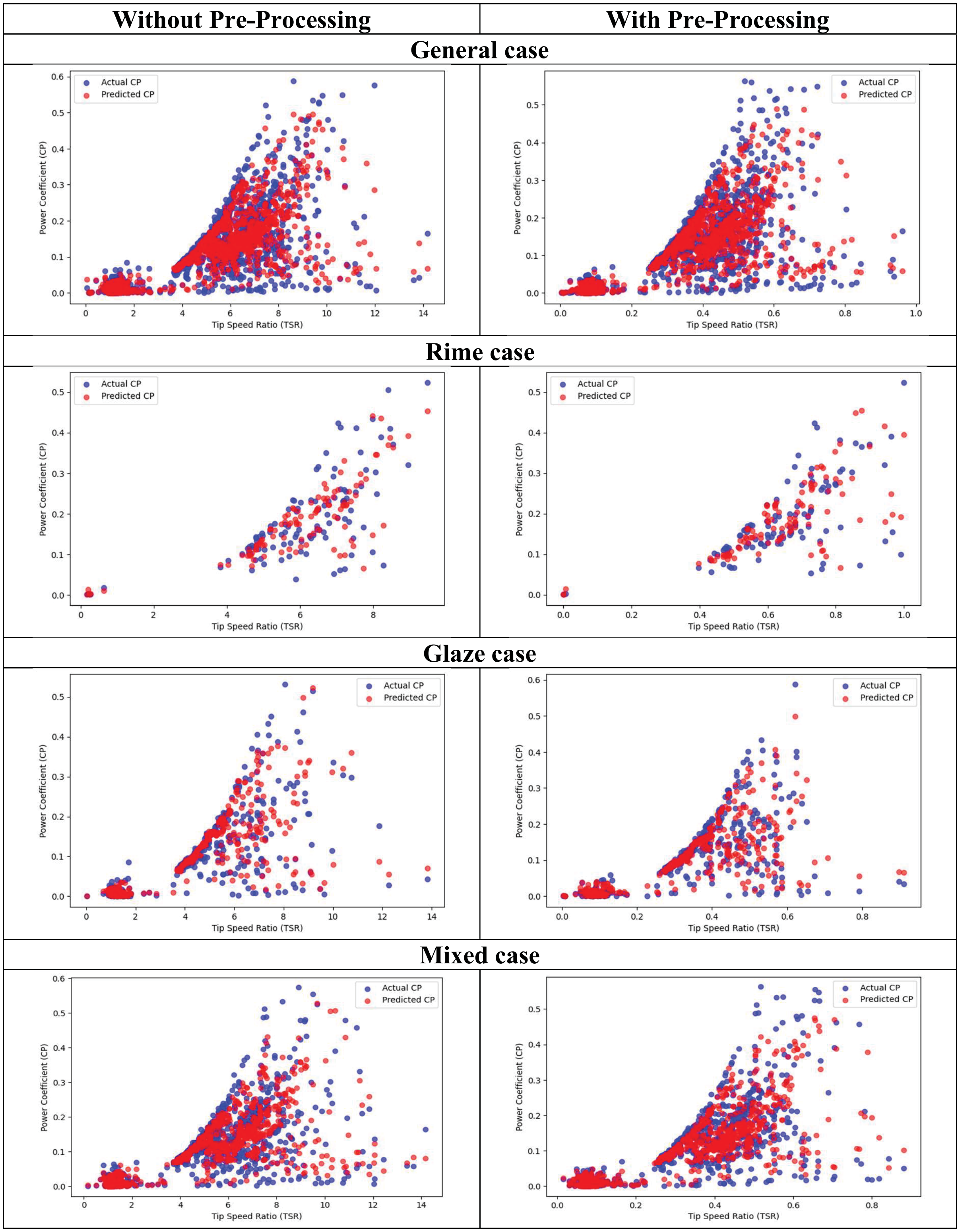

Figure 5.8 Comparison of the CP-TSR curves between the test and the predicted values for all the π groups, and between the implementations of normalization for all the ice types using Random Forest

5.1.3 Neural Network

Two neural network configurations were implemented using the Keras and TensorFlow libraries:

1) **Neural Network 1 (NN1):** A default configuration comprising three hidden layers, two layers of 256 neurons, and one layer of 64 neurons, the ReLU activation function for each, and a single output neuron using a sigmoid activation; and the SGD as optimizer. ReLU introduces nonlinearity, helping the network learn complex mappings, and the final sigmoid squashes the output to the (0, 1) interval.

Algorithm 5.5 Implementation code for the NN1

```
#Call the dataset
df=pd.read_excel("BD_Complete_Nu2-Relevant.xlsx") #dataset with correlation coefficient
higher than 0.39
#df=pd.read_excel("BD_Complete.xlsx") #dataset of with all pi parameters
dataset=df.values
X=dataset[:,0:6] # input variables
Y=dataset[:,6] # Output variable (power coefficient)

#Split of the dataset
X_train, X_val_and_test, Y_train, Y_val_and_test = train_test_split(X, Y, test_size=0.3)
X_val, X_test, Y_val, Y_test = train_test_split(X_val_and_test, Y_val_and_test,
test_size=0.5)

#Neural Network model
model = Sequential([
    Input(shape=(6,)),  # Explicitly define the input shape
    Dense(256, activation='relu'),
    Dense(256, activation='relu'),
    Dense(64, activation='relu'),
    Dense(1, activation='sigmoid'),
])
opt = SGD(learning_rate=0.01, momentum=0.9)
model.compile(optimizer='sgd', loss='mean_squared_error', metrics=['accuracy'])

hist = model.fit(X_train, Y_train, batch_size=32, epochs=100, validation_data=(X_val,
Y_val))

#Model testing
y_pred = model.predict(X_test)
print("R2_SCORE: ",r2_score(Y_test[:,0], y_pred[:,0]))
print("MAE: ",mean_absolute_error(Y_test[:,0], y_pred[:,0]))
print("RMSE: ",np.sqrt(mean_squared_error(Y_test[:,0], y_pred[:,0])))
```

2) **Neural Network 2 (NN2):** An optimized configuration obtained via "Grid Search" over optimizer, initializer, epoch count, and batch size:

Algorithm 5.6 Implementation code for the Grid Search

```
#Call the dataset
df=pd.read_excel("BD_Complete_Nu2-Relevant.xlsx") #dataset with correlation coefficient
higher than 0.39
#df=pd.read_excel("BD_Complete.xlsx") #dataset of with all pi parameters
dataset=df.values
X=dataset[:,0:6] # input variables
Y=dataset[:,6] # Output variable (power coefficient)

#Split of the dataset
X_train, X_test, Y_train, Y _test = train_test_split(X, Y, test_size=0.3,
random_state=42)

#Neural Network model
def create_model(optimizer='rmsprop', init='glorot_uniform'):
  model_3 = Sequential([
    Dense(64, activation='relu', input_shape=(6,)),
    Dense(64, activation='relu'),
    Dense(1),])
  model_3.compile(optimizer=optimizer,
              loss='mean_squared_error', metrics=['mean_squared_error'])
  return model_3

# grid search epochs, batch size and optimizer
optimizers = ['rmsprop', 'adam']
init = ['glorot_uniform', 'normal', 'uniform']
epochs = [50, 100, 150, 200, 400]
batches = [5, 10, 20]
param_grid = dict(optimizer=optimizers, nb_epoch=epochs, batch_size=batches,
init=init)
grid = GridSearchCV(estimator=model_3, param_grid=param_grid,
error_score='raise')
grid_result = grid.fit(X_train, Y_train)

print("Best: %f using %s" % (grid_result.best_score_, grid_result.best_params_))
means = grid_result.cv_results_['mean_test_score']
stds = grid_result.cv_results_['std_test_score']
params = grid_result.cv_results_['params']
for mean, stdev, param in zip(means, stds, params):
  print("%f (%f) with: %r" % (mean, stdev, param))

#Model testing
y_pred = model_3.predict(X_test)
print("R2_SCORE: ",r2_score(Y_test[:,0], y_pred[:,0]))
print("MAE: ",mean_absolute_error(Y_test[:,0], y_pred[:,0]))
print("RMSE: ",np.sqrt(mean_squared_error(Y_test[:,0], y_pred[:,0])))
```

The final neural network consisted of two hidden layers of 64 neurons each, with the ReLU activation function, and a single output neuron. RMSprop is an optimizer that uses an adaptive gradient method, scaling parameter updates by a running average of recent squared gradients to stabilize and accelerate training.

Algorithm 5.7 Implementation code for the NN2

```
#Call the dataset
df=pd.read_excel("BD_Complete_Nu2-Relevant.xlsx") #dataset with correlation coefficient
higher than 0.39
#df=pd.read_excel("BD_Complete.xlsx") #dataset of with all pi parameters
dataset=df.values
X=dataset[:,0:6] # input variables
Y=dataset[:,6] # Output variable (power coefficient)

#Split of the dataset
X_train, X_test, Y_train, Y _test = train_test_split(X, Y, test_size=0.3,
random_state=42)

#Neural Network model
model = Sequential([
    Input(shape=(6,)),  # Explicitly define the input shape
    Dense(64, activation='relu'),
    Dense(64, activation='relu'),
    Dense(1)
])
model.compile(optimizer="RMSprop", loss='mean_squared_error')

hist = model.fit(X_train, Y_train, batch_size=5, epochs=400, validation_data=(X_test,
Y_test))

#Model testing
y_pred = model.predict(X_test)
print("R2_SCORE: ",r2_score(Y_test[:,0], y_pred[:,0]))
print("MAE: ",mean_absolute_error(Y_test[:,0], y_pred[:,0]))
print("RMSE: ",np.sqrt(mean_squared_error(Y_test[:,0], y_pred[:,0])))
```

Figure 5.9 presents the R^2 scores for both configurations across all scenarios. The default network (NN1) yielded poor results, with negative R^2 values in several cases (e.g., Rime – All Pi: $R^2 = -0.362$), indicating that the model failed to capture the underlying relationships. In contrast, the optimized network (NN2), obtained through grid search over optimizers, initializers, batch size, and number of epochs, achieved significantly higher R^2 scores across all scenarios, with values exceeding 0.76 in most cases. The best performance was observed in the General Case – All π scenario ($R^2 = 0.763$).

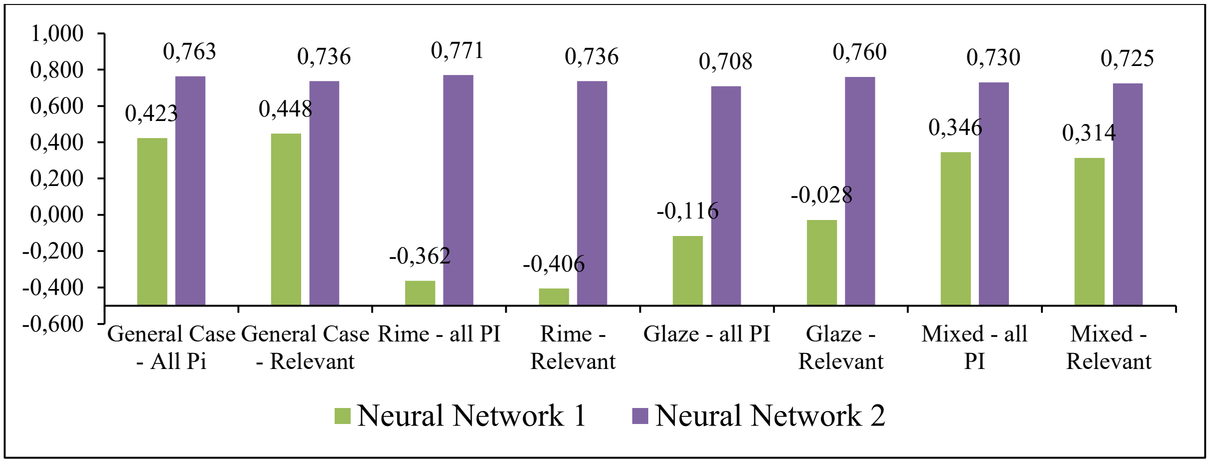

Figure 5.9 Results of the R^2 for all the cases using Neural Networks

Regarding Figure 5.10 and Figure 5.11, the baseline neural network (NN1) exhibits high MAE and RMSE values, consistent with its poor R^2 performance and lack of generalization. In contrast, the optimized network (NN2) achieves MAE and RMSE levels comparable to those of the Random Forest model. The relatively larger RMSE compared to MAE in some scenarios suggests occasional large deviations, likely associated with extreme operating conditions. This sensitivity underscores the need for careful training, regularization, and dataset coverage when deploying neural networks for physically critical applications. Nevertheless, the low average errors achieved by NN2 confirm its ability to accurately represent nonlinear π-group interactions.

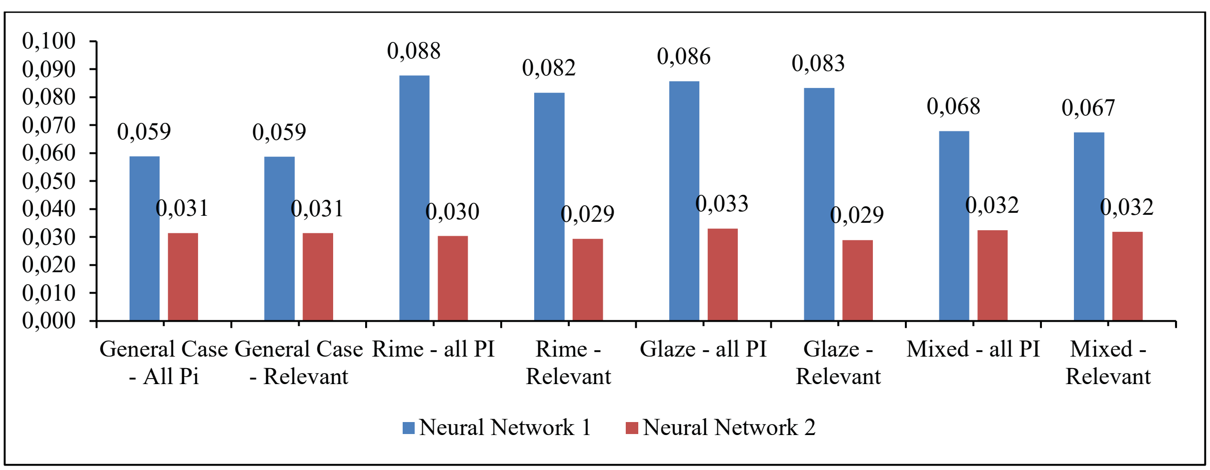

Figure 5.10 Results of the MAE for all the cases using Neural Networks

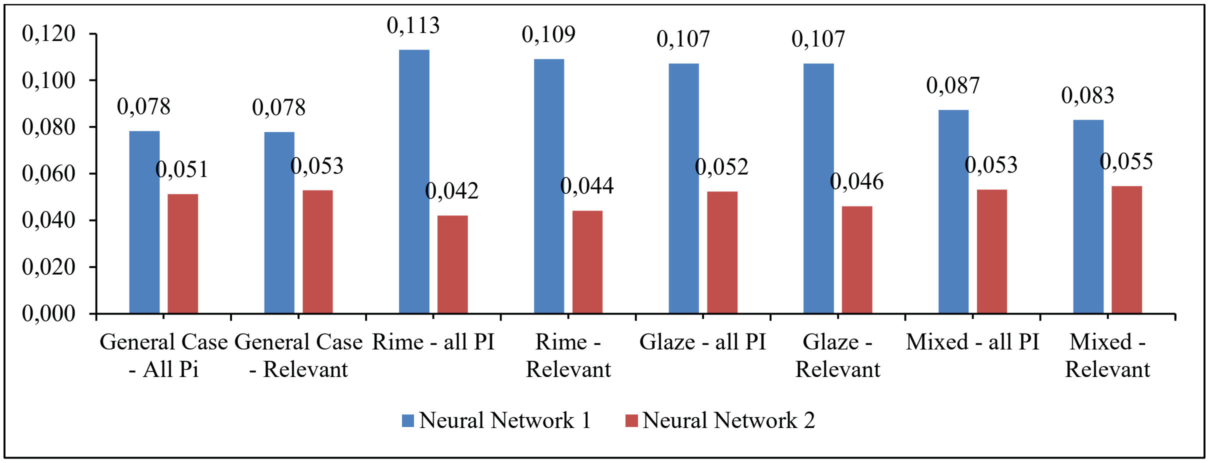

Figure 5.11 Results of the RMSE for all the cases using Neural Networks

These findings underscore the importance of hyperparameter tuning in neural networks. The substantial improvement observed with NN2 confirms that neural networks can model complex nonlinear relationships between the dimensionless input variables and the power coefficient, provided the architecture is appropriately configured.

5.2 Discussion

The comparative analysis of the three models reveals distinct strengths and limitations:

Model	Strengths	Limitations
Decision Tree	Interpretability, fast training	Sensitive to feature selection and scaling
Random Forest	Robustness, generalization, and low variance	Performance drops with a reduced feature set
Neural Network	High accuracy (with tuning), nonlinear modeling	Requires extensive data, sensitive to architecture

All three models successfully validated the physical relevance of the π-based correlations. The Random Forest model emerged as the most reliable and generalizable approach, offering consistent performance across all icing scenarios. The optimized neural network demonstrated strong predictive capabilities, particularly in capturing nonlinear dependencies. The Decision

Tree model, while less accurate, provided interpretable insights into feature importance and model behavior.

The results also highlight the importance of tailoring preprocessing strategies and model configurations to the specific ice regime and learning algorithm. In particular, the use of relevant π groups improved performance in simpler models, while more complex models benefited from the complete feature set. These findings reinforce the value of integrating physics-informed modeling with data-driven techniques to enhance predictive accuracy and operational reliability in wind energy systems.

5.3 Conclusions

This chapter presented a comprehensive validation of the dimensionless correlations derived in CHAPTER 4 using three supervised machine learning techniques applied across multiple icing regimes and preprocessing configurations.

A global synthesis of R^2, MAE, and RMSE metrics reveals a consistent and physically interpretable pattern. Simpler models perform adequately in regimes characterized by smoother, more uniform physical behavior (e.g., rime ice), while more complex models are required to accurately capture the compounded effects in mixed and general icing conditions.

The results confirm that the proposed π groups offer a physically consistent and predictive representation of wind turbine power losses under icing conditions, effectively capturing the relationships among meteorological conditions, turbine operation, and power losses.

The Random Forest model had the highest overall R^2 scores, offering the best global balance between accuracy, robustness, and stability across ice types, making it particularly suitable for engineering and operational applications. The optimized neural network achieved high predictive accuracy and effectively captured nonlinear relationships, though it was more sensitive to data quality and architecture choices. The Decision Tree model was interpretable but showed limited accuracy in complex scenarios.

Feature selection and normalization must be guided by both the physical characteristics of the icing regime and the inductive bias of the learning algorithm, rather than applied uniformly.

These findings confirm that the integration of dimensional analysis and machine learning constitutes a robust, scalable, and versatile framework for predicting wind turbine performance in cold climates. Future research could focus on including more physical parameters, applying ensemble learning methods, and developing real-time predictive systems using sensor data.

CONCLUSION

This doctoral research addressed the complex interactions between meteorological conditions, operational variables, and aerodynamic phenomena that influence power loss in wind turbines operating under icing conditions. By integrating dimensional analysis, multisource data collection, and supervised machine learning techniques, the thesis provides a comprehensive framework for understanding, modeling, and predicting icing-induced performance degradation in cold-climate wind energy systems.

A central contribution of this work is the construction of a harmonized, physically consistent database that integrates field measurements, CFD simulations, and peer-reviewed literature, serving as a foundation for identifying physically meaningful parameters and ensuring statistical robustness across a wide range of icing scenarios. The consistent treatment of meteorological variables, turbine operating conditions, and ice-type classification enabled a reliable comparison of heterogeneous datasets and strengthened the validity of the subsequent analyses. This multisource approach ensured that the derived conclusions are not restricted to a single turbine configuration or dataset, thereby reinforcing the generality and applicability of the proposed methodology.

Using dimensional analysis based on the Buckingham π theorem, seven key dimensionless groups were derived to represent the governing physics of ice accretion and turbine performance. This dimensional reduction constitutes a key scientific contribution, as it transforms a high-dimensional and turbine-specific problem into a compact, scale-independent representation. Among the derived parameters, the tip-speed ratio (TSR) consistently emerged as the dominant predictor of power-coefficient reductions across all icing regimes, confirming its central role in aerodynamics. Reynolds and Nusselt numbers demonstrated a secondary but still significant influence, especially under glaze and mixed icing conditions, where convective heat transfer and partial melting are more pronounced. In contrast, the liquid water content (LWC) and median volume diameter (MVD), while physically central to ice formation, exhibited weak direct correlations with the power loss. This outcome reinforces the idea that icing effects are mediated through aerodynamic and thermodynamic processes rather than through LWC or MVD alone.

Another key outcome of this thesis is the demonstration that the icing regime fundamentally modulates the relative importance of the governing parameters. Rime ice, characterized by colder temperatures and conduction-dominated heat transfer, exhibits smoother and more monotonic aerodynamic degradation, whereas glaze and mixed ice regimes introduce stronger nonlinearities associated with surface roughness evolution, runback water, and localized flow separation. These findings confirm that a single universal model cannot accurately represent icing-induced performance losses and must instead be interpreted through regime-dependent physical mechanisms.

The machine learning validation presented in Chapter 5 provides a critical link between physical modeling and data-driven analysis. Decision Trees, Random Forests, and Artificial Neural Networks, despite their fundamentally different inductive biases, were all capable of reconstructing wind turbine power losses using the same set of dimensionless input parameters. This convergence constitutes strong evidence of the physical relevance and completeness of the proposed π groups. Random Forest models achieved the most robust and consistent performance across all icing regimes, minimizing both average (MAE) and extreme (RMSE) prediction errors, and therefore represent the most suitable approach for engineering and operational applications. Optimized neural networks demonstrated comparable predictive accuracy and superior capability in capturing higher-order nonlinear interactions, particularly in mixed and transitional icing regimes, albeit at the cost of reduced interpretability and increased sensitivity to training configuration. Decision Trees, while less accurate, provided valuable interpretative insight into parameter dominance and regime transitions, reinforcing their role as diagnostic and validation tools.

The combined analysis of R^2, MAE, and RMSE metrics further strengthened the physical interpretation of the results. Low MAE values confirmed accurate average prediction of power losses, while RMSE trends revealed the ability, or limitations, of each model to handle extreme operating conditions, which are of particular relevance for turbine reliability and risk assessment in cold climates. The sensitivity of error metrics to feature selection and normalization underscored the importance of aligning preprocessing strategies with both the underlying physical regime and the chosen learning algorithm, rather than adopting uniform data-driven practices.

Overall, this research makes the following key contributions to the field of climate wind energy: (1) the development of a physically interpretable, dimensionless framework for modeling wind turbine power losses under icing conditions; (2) the unification and validation of heterogeneous experimental, numerical, and literature-based datasets through dimensional analysis; (3) the demonstration that physics-informed machine learning can serve as a rigorous validation tool rather than a purely empirical alternative; and (4) the identification of Random Forest and optimized Neural Network models as reliable predictors of icing-induced performance degradation, with clear guidance on their applicability and limitations.

From a practical perspective, the proposed methodology offers a scalable, computationally efficient basis for performance forecasting, operational decision-making, and the development of wind turbines for cold-climate operation. Future research directions include integrating real-time sensor data, quantifying uncertainties in predicted power losses, extending to dynamic icing and de-icing processes, and coupling with control strategies to mitigate icing impacts. Collectively, these advances enhance the reliability, resilience, and economic viability of wind energy systems deployed in cold, icing-prone environments.

RECOMMENDATIONS AND FUTURE WORK

While this thesis offers a solid analytical and predictive basis for understanding how icing affects wind turbine performance, it also suggests several directions for future research to further develop and implement these findings.

Integration of Three-Dimensional Aerodynamic and Thermodynamic Effects

Most aerodynamic analyses in the dimensional studies relied on two-dimensional airfoil simulations. Yet, actual wind turbine blades have intricate 3D shapes that feature twist, taper, and radial flow effects. Future research should include 3D CFD simulations that account for rotational dynamics, secondary flows, and ice accumulation along the span. Such simulations would improve the accuracy of icing-related penalty estimates and enhance the applicability of the dimensionless framework.

Improved Modeling of Surface Roughness and Ice Morphology

Results from the literature and the thesis highlight significant uncertainties in roughness modeling, particularly when relying on aeronautical-derived empirical correlations. Field-based roughness measurements and more physically accurate roughness distribution models (e.g., beading models) should be integrated into future simulations. These improvements could enhance predictive fidelity in glaze ice conditions, where heterogeneous roughness plays a critical role.

Expansion of the Database with High-Resolution Field Measurements

While the constructed database incorporates diverse sources, additional high-frequency measurements of ice mass, roughness, droplet size spectra, and blade temperatures would improve the robustness of machine learning models. Collaborations with wind farm operators could facilitate the acquisition of enriched SCADA datasets and the execution of targeted icing campaigns.

Exploration of Hybrid Physics–Machine Learning Models

Given the demonstrated importance of physical interpretability and the strengths of machine learning, future research should investigate hybrid approaches that combine π-based physical formulations with neural architectures. This would allow for maintaining physical consistency while leveraging data-driven flexibility.

APPENDIX A

SUMMARY OF THE ATMOSPHERIC CONDITIONS, SIMULATION CONFIGURATION, AND OUTPUT PARAMETERS OF THE REVIEWED ARTICLES

		Software			Atmospheric Conditions				Simulation Set-Up							
Ref.	**IT**	**BEM**	**CFD**	**WT/Prof**	**T (°C)**	**U (m/s)**	**LWC (g/m^3)**	**MVD (µm)**	**Ω (RPM)**	**AoA (°)**	**BC**	**RM**	**AT**	**TM**	**OP**	**Val.**
Jasinski et al. (1998)	R	PROPID	LEWICE	450-kW/S809	−10	65.2	0.1	15 35	48	5	N/A	N/A	3 h 7 h	N/A	AC, PC	Exp.
Dimitrova (2009)	RG	PROICET (CIRALIMA, XFOIL and PROPID)		Vestas V80 1.8 MW/NACA63415	−6 −2	8	0.05	20	15.2	6	N/A	N/A	6 h 4 h	N/A	AC, PC, IS, IM, PL	Num.
Barber et al. (2010)	R	N/A	LEWICE CFX	NREL Phase VI	−6	1.6 to 3.1	0.1	35	800	N/A	I: Velocity O: Pressure W: Periodic (120°)	N/A	10 h	k-ε	IS, CP	Exp.
Homola et al. (2012)	R	In-house code	FENSAP-ICE	NREL 5 MW	−10	10	0.22	20	11.4	5.824	N/A	Shin et al. (1991)	1 h	S-A	IS, AC, CP, PC, PL	No

Ref.	IT	BEM	CFD	WT/Prof	T (°C)	U (m/s)	LWC (g/m^3)	MVD (μm)	Ω (RPM)	AoA (°)	BC	RM	AT	TM	OP	Val.
	Software				Atmospheric Conditions				Simulation Set-Up							
Reid et al. (2013)	RG	N/A	FENSAP-ICE	NREL Phase VI	−3 −15	7 22	0.5	20	72	N/A	I: Velocity O: Pressure W: Slip	N/A	10 min 20 min 1 h	S-A	IS, PL	Exp. & Num.
Turkia et al. (2013)	R	FAST	TURBICE FLUENT	NREL 5 MW	−7	7	0.2	25	11.5	N/A	N/A	Shin et al. (1991)	19 min 3 h 10 h	S-A	IS, AC, PC, IM, PL	Exp.
Sagol (2014)	R	In-house code	FLUENT	NREL Phase VI	−15	7	1	20	72	N/A	I: Velocity O: Pressure W: Periodic (180°) RRF	0.1 mm to 2 mm	1 h	k-ω SST	IS, AC, PL	Exp.
Switchenko et al. (2014)	RG	N/A	FENSAP-ICE	NREL Phase VI	−1 to −13	7	0.1	20 50 100	72	N/A	I: Velocity O: Pressure W: Slip	1, 3, and 10 mm	17 h	S-A	IS, PC	Real
Etemaddar et al. (2014)	RG	WT-Perf	LEWICE FLUENT	NREL 5 MW	0 −1.25 −2.5 −3.75 −5	8 12 16 20	0.05 0.075 0.1 0.125 0.15	8 10 12 14 16	N/A	5	N/A	0.5 mm	24 h to obtain the	k-ε	IS, IM, AC, CP	Exp.

Ref.	IT	BEM	CFD	WT/Prof	T (°C)	U (m/s)	LWC (g/m^3)	MVD (µm)	Ω (RPM)	AoA (°)	BC	RM	AT	TM	OP	Val.
	Software				Atmospheric Conditions				Simulation Set-Up							
					−6.25 −7.5 −8.75 −10		0.175 0.2 0.225 0.25	18 20 22 24					iced profile			
Yirtici et al. (2016)	R	XFOIL	In-house model (ice accretion)	Aeolos 30 kW/NACA64618 and S809	−8	11	0.05	27	120	5	N/A	N/A	3 h	N/A	IS, PC	Exp. & Num.
Shu et al. (2017)	G	N/A	FLUENT MATLAB (Ice accretion)	Small HAWT/NACA4409	−3 −6 −8	5 6 8	0.71	20	N/A	N/A	MRF	Exp.	500 s	k-ε	IS, CP	Exp.
Ebrahimi (2018)	RG	In-house code	LEWICE FLUENT	600 kW/S816	−1.4 −5.7	9.2 18.1 27.1	0.218 0.242	38.3 40.5	N/A	8	N/A	N/A	G: 360 s R: 264 s	k-ω SST	IS, AC, PC	Exp.
W. Han et al. (2018)	R	BLADED	STAR-CCM+	NREL 5 MW/NACA64618	−8	4 to 25	0.22	25	12.1	N/A	N/A	Shin et al. (1991)	1 h	k-ω SST	IS, IM, AC, PC	Exp.
Hu et al. (2018)	R	N/A	FLUENT	NREL Phase VI	−15	7	1	20	72	N/A	I: Velocity O: Pressure W: Periodic MRF	N/A	30 min	k-ω SST	PC, IS, IM	No

		Software			Atmospheric Conditions				Simulation Set-Up						
Ref.	IT	BEM	CFD	WT/Prof	T (°C)	U (m/s)	LWC (g/m^3)	MVD (µm)	Ω (RPM)	AoA (°)	BC	RM	AT	TM	OP	Val.
Shu et al. (2018)	RG	N/A	FLUENT	300-kW/S819	−11.3 −1	4 to 13	N/A	N/A	24 to 45	N/A	I: Velocity O: Pressure W: Periodic MRF	N/A	2 h 3 h	k-ω SST	IS, CP, PC	Exp.
Zanon et al. (2018)	RG	BEM WT-Perf	CFX ICEAC2D	NREL 5 MW	−10 −2	10	0.22 0.1605	20 14.36	TSR: 7.68 TSR: 7.32 TSR: 7.55	N/A	N/A	Shin et al. (1991)	8 h	k-ω SST	IS, AC, PC, CP	Exp. & Num.
Tabatabaei et al. (2019)	R	In-house code	CFX	NREL 5 MW/NACA64618	N/A	11.4	N/A	N/A	12.1	N/A	I: Velocity O: Pressure W: Periodic (120°)	N/A	N/A	k-ω SST	CP	No
Yirtici, Ozgen, et al. (2019)	R	XFOIL	In-house model (ice accretion) SU2	Aeolos 30 kW NREL 5 MW	−5 −10 −15	11	0.05 0.15 0.25	18 27 35	120 12.1	5	N/A	N/A	20 min 40 min 1 h 80 min	k-ω SST	IS, PC, PL	Exp.

		Software			Atmospheric Conditions						Simulation Set-Up					
Ref.	IT	BEM	CFD	WT/Prof	T (°C)	U (m/s)	LWC (g/m^3)	MVD (μm)	Ω (RPM)	AoA (°)	BC	RM	AT	TM	OP	Val.
Hildebrandt et Sun (2021)	RG	Xturb-PSU	FENSAP-ICE	WindPACT 1.5 MW/NACA64618	−8 −1	8 12	0.2 0.48	30 33	0	0	N/A	Shin et al. (1991)	2 h	S-A	IS, AC, PC	Exp.

Note: IC: Ice Type; R: Rime; G: Glaze; RG: Rime and Glaze; WT/Prof: Wind Turbine/Profile; AoA: Angle of Attack; TSR: Tip Speed Ratio; BC: Boundary Conditions; I: inlet; O: Outlet; W: Walls; RRF: Rotating Reference Frame; MRF: Multiple Reference Frame; RM: Roughness Model; BS: Beading Surface Roughness Model; AT: Accretion time; TM: Turbulence Model; S-A: Spalart-Allmaras; OP: Output Parameters; AC: Aerodynamic Coefficients; PC: Power Curve; IS: Ice shape; IM: Ice mass; PL: Power Loss; CP: Power Coefficient; Val.: Validation; Exp.: Experimental; Num: Numerical

APPENDIX B

SUMMARY OF THE STUDIES FROM THE LITERATURE INCLUDED IN THE DATASET

Ref.	Ref. WT	Rotor Diameter (m)	Airfoil	Ice Type	CP	Ω (rpm)	U (m/s)	T (°C)	LWC (g/m³)	MVD (µm)	Icing duration (min)	c (m)	Spanwise airfoil position
W. Han et al. (2018)	NREL 5MW	126	DU91-W2–250 DU91-W-210 NACA 64618	R	A	12.1	11.1	-8	0.22	25	60	2.518 2.313 1.419	83% 89% 97%
Homola et al. (2012)	NREL 5MW	126	NACA64-A17	R	A	N/A	10	-10	0.22	20	60	1.419	100%
Homola, Virk, et al. (2010)	NREL 5MW	126	NACA 64618	R, G	A	N/A	N/A	-2,5 -5 -7,5	0.2	12 17 30	120	2.518	85%
Turkia et al. (2013)	A typical 3 MW WT	90	NACA 64618	R	A	11.5	7	-7	0.2	25	19 200 600	2.111 1.622	67% 90%
Etemaddar et al. (2014)	NREL 5MW	126	NACA 64618	G	A	12.1	14	-7	0.2	13	120	1	93%
Zanon et al. (2018)	NREL 5MW	63	NACA 64618	R, G	A	9 11.6	6	-10 -2	0.22 0.16	20 14.36	600	2.764 2.518	From 45% to 100%

Ref.	Ref. WT	Rotor Diameter (m)	Airfoil	Ice Type	CP	Ω (rpm)	U (m/s)	T (°C)	LWC (g/m^3)	MVD (µm)	Icing duration (min)	c (m)	Spanwise airfoil position
												2.313 2.086 1.419	
Hildebrandt et Sun (2021)	WindPACT NREL 1.5 MW	N/A	S825 NACA 64-618	R, G	A	N/A	8 12	-8 -1	0.2 0.48	30 33	120	1.24	85%
Barber et al. (2010)	NREL Phase VI	44	S809	R	A	15	4	-6	0.1	35	600	N/A	N/A
Reid et al. (2013)	NREL Phase VI	10	S809	R, G	A	72	7 10 12 15 17 20 22 25	-3 -15	0.5	20 30	10 20 60	N/A	30% 46.6% 63.3% 80%
Shu et al. (2017)	N/A	1	NACA 4409	G	A	30	5 6 8	-3 -6 -8	0.71	20	8	0.03 0.035 0.045	100% 80% 60%
Shu et al. (2018)	N/A	31	S819	R, G	A	24 25 26 27	4 5 7 9	-1 -11.3	N/A	N/A	120 180	0.363	99%

Ref.	**Ref. WT**	**Rotor Diameter (m)**	**Airfoil**	**Ice Type**	**CP**	**Ω (rpm)**	**U (m/s)**	**T (°C)**	**LWC (g/m³)**	**MVD (μm)**	**Icing duration (min)**	**c (m)**	**Spanwise airfoil position**
						29 30 32	11 13						
Hu et al. (2018)	NREL Phase VI	5.029	S809	R	A	72	5 7 9	-15	0.6 1 1.4	15 20 25	30	0.267	80% 95%
Tabatabaei et al. (2019)	NREL 5MW	126	NACA 64618	R, G	A	12.1	11.4	-5.7 -11.1	0.48 1	20 27.6	3.85 19.6	0.2	N/A

Note: A – Available, R – Rime, G – Glaze.

APPENDIX C

ALGEBRAIC DEVELOPMENT TO DERIVING THE π GROUPS FOR THE MASS OF ICE

The following is the algebraic development for each of the π groups for the remaining variables: $\Omega, \mu_a, h, k, t, MVD, LWC$ and M_{ice}.

$$\prod 1 = \rho^a U^b L^c {T_\infty}^d \Omega = M^0 L^0 T^0 \theta^0$$

$$\prod 1 = [ML^{-3}]^a [LT^{-1}]^b [L]^c [\theta]^d [T^{-1}] = M^0 L^0 T^0 \theta^0$$

$M: a = 0$

$L: -3a + b + c = 0 \rightarrow c = 1$

$T: -b - 1 = 0 \rightarrow b = -1$

$\theta: d = 0$

$$\prod 1 = \rho^0 U^{-1} L^1 {T_\infty}^0 \Omega$$

$$\boxed{\prod 1 = \frac{\Omega L}{U} = TSR\ (Tip\ Speed\ Ratio)}$$

$$\prod 2 = \rho^a U^b L^c {T_\infty}^d \mu_a = M^0 L^0 T^0 \theta^0$$

$$\prod 2 = [ML^{-3}]^a [LT^{-1}]^b [L]^c [\theta]^d [ML^{-1}T^{-1}] = M^0 L^0 T^0 \theta^0$$

$M: a + 1 = 0 \rightarrow a = -1$

$L: -3a + b + c = 1 \rightarrow c = -1$

$T: -b - 1 = 0 \rightarrow b = -1$

$\theta: d = 0$

$$\prod 2 = \rho^{-1}U^{-1}L^{-1}{T_\infty}^{0}\mu_a$$

$$\boxed{\prod 2 = \left(\frac{\mu_a}{\rho UL}\right)^{-1} = Re}$$

$$\prod 3 = \rho^{a}U^{b}L^{c}{T_\infty}^{d}h = M^0L^0T^0\theta^0$$

$$\prod 3 = [ML^{-3}]^{a}[LT^{-1}]^{b}[L]^{c}[\theta]^{d}[MT^{-3}\theta^{-1}] = M^0L^0T^0\theta^0$$

$M: a + 1 = 0 \rightarrow a = -1$

$L: -3a + b + c = 0 \rightarrow c = 0$

$T: -b - 3 = 0 \rightarrow b = -3$

$\theta: d - 1 = 0 \rightarrow d = 1$

$$\prod 3 = \rho^{-1}U^{-3}L^{0}{T_\infty}^{1}h$$

$$\boxed{\prod 3 = \frac{hT_\infty}{\rho U^3}}$$

$$\prod 4 = \rho^{a}U^{b}L^{c}{T_\infty}^{d}k = M^0L^0T^0\theta^0$$

$$\prod 4 = [ML^{-3}]^{a}[LT^{-1}]^{b}[L]^{c}[\theta]^{d}[MLT^{-3}\theta^{-1}] = M^0L^0T^0\theta^0$$

$M: a + 1 = 0 \rightarrow a = -1$

$L: -3a + b + c + 1 = 0 \rightarrow c = -1$

$T: -b - 3 = 0 \rightarrow b = -3$

$\theta: d - 1 = 0 \rightarrow d = 1$

$$\prod 4 = \rho^{-1}U^{-3}L^{-1}{T_\infty}^{1}k$$

$$\boxed{\prod 4 = \frac{kT_{\infty}}{\rho U^3 L}}$$

$$\prod 5 = \rho^a U^b L^c {T_{\infty}}^d t = M^0 L^0 T^0 \theta^0$$

$$\prod 5 = [ML^{-3}]^a [LT^{-1}]^b [L]^c [\theta]^d [T] = M^0 L^0 T^0 \theta^0$$

$M: a = 0$

$L: -3a + b + c = 0 \rightarrow c = -1$

$T: -b + 1 = 0 \rightarrow b = 1$

$\theta: d = 0$

$$\prod 5 = \rho^0 U^1 L^{-1} {T_{\infty}}^0 t$$

$$\boxed{\prod 5 = \frac{tU}{L}}$$

$$\prod 6 = \rho^a U^b L^c {T_{\infty}}^d MVD = M^0 L^0 T^0 \theta^0$$

$$\prod 6 = [ML^{-3}]^a [LT^{-1}]^b [L]^c [\theta]^d [L] = M^0 L^0 T^0 \theta^0$$

$M: a = 0$

$L: -3a + b + c + 1 = 0 \rightarrow c = -1$

$T: -b = 0$

$\theta: d = 0$

$$\prod 6 = \rho^0 U^0 L^{-1} {T_{\infty}}^0 MVD$$

$$\boxed{\prod 6 = \frac{MVD}{L}}$$

$$\prod 7 = \rho^a U^b L^c {T_\infty}^d LWC = M^0 L^0 T^0 \theta^0$$

$$\prod 7 = [ML^{-3}]^a [LT^{-1}]^b [L]^c [\theta]^d [ML^{-3}] = M^0 L^0 T^0 \theta^0$$

$M: a + 1 = 0 \rightarrow a = -1$

$L: -3a + b + c - 3 = 0 \rightarrow c = 0$

$T: -b = 0$

$\theta: d = 0$

$$\prod 7 = \rho^{-1} U^0 L^0 {T_\infty}^0 LWC$$

$$\boxed{\prod 7 = \frac{LWC}{\rho}}$$

$$\prod 8 = \rho^a U^b L^c {T_\infty}^d M_{ice} = M^0 L^0 T^0 \theta^0$$

$$\prod 8 = [ML^{-3}]^a [LT^{-1}]^b [L]^c [\theta]^d [M] = M^0 L^0 T^0 \theta^0$$

$M: a + 1 = 0 \rightarrow a = -1$

$L: -3a + b + c = 0 \rightarrow c = -3$

$T: -b = 0$

$\theta: d = 0$

$$\prod 8 = \rho^{-1} U^0 L^{-3} {T_\infty}^0 M_{ice}$$

$$\boxed{\prod 8 = \frac{M_{ice}}{\rho L^3}}$$

$$\frac{M_{ice}}{\rho L^3} = f\left(\frac{\Omega L}{U}, \frac{\mu_a}{\rho U L}, \frac{h T_\infty}{\rho U^3}, \frac{k T_\infty}{\rho U^3 L}, \frac{tU}{L}, \frac{MVD}{L}, \frac{LWC}{\rho}\right)$$

$$\frac{M_{ice}}{\rho L^3} = f\left(TSR, Re, Nu, \frac{tU}{L}, \frac{MVD}{L}, \frac{LWC}{\rho}\right)$$

APPENDIX D

ALGEBRAIC DEVELOPMENT TO DERIVING THE π GROUPS FOR THE TURBINE POWER

The following is the algebraic development for each of the π groups for the remaining variables

The following is the algebraic development for each of the π groups for the remaining variables: Ω, M_{ice} and P.

$$\prod 1' = \rho^a U^b L^c \Omega = M^0 L^0 T^0 \theta^0$$

$$\prod 1' = [ML^{-3}]^a [LT^{-1}]^b [L]^c [T^{-1}] = M^0 L^0 T^0 \theta^0$$

$M: a = 0$

$L: -3a + b + c = 0 \rightarrow c = 1$

$T: -b - 1 = 0 \rightarrow b = -1$

$$\prod 1' = \rho^0 U^{-1} L^1 \Omega$$

$$\boxed{\prod 1' = \frac{\Omega L}{U}}$$

$$\prod 2' = \rho^a U^b L^c M_{ice} = M^0 L^0 T^0 \theta^0$$

$$\prod 2' = [ML^{-3}]^a [LT^{-1}]^b [L]^c [M] = M^0 L^0 T^0 \theta^0$$

$M: a + 1 = 0 \rightarrow a = -1$

$L: -3a + b + c = 0 \rightarrow c = -3$

$T: -b = 0$

$$\prod 2' = \rho^{-1} U^0 L^{-3} M_{ice}$$

$$\boxed{\prod 2' = \frac{M_{ice}}{\rho L^3}}$$

$$\prod 3' = \rho^a U^b L^c P = M^0 L^0 T^0 \theta^0$$

$$\prod 3' = [ML^{-3}]^a [LT^{-1}]^b [L]^c [ML^2 T^{-3}] = M^0 L^0 T^0 \theta^0$$

$M: a + 1 = 0 \rightarrow a = -1$

$L: -3a + b + c + 2 = 0 \rightarrow c = -2$

$T: b = -3$

$$\prod 3' = \rho^{-1} U^3 L^{-2} P$$

$$\boxed{\prod 3' = \frac{P}{\rho U^3 L^2}}$$

$$\frac{P}{\rho U^3 L^2} = f\left(\frac{\Omega L}{U}, \frac{M_{ice}}{\rho L^3}\right)$$

$$\frac{P}{\rho U^3 L^2} = f\left(TSR, \frac{M_{ice}}{\rho L^3}\right)$$

$$\frac{P}{\rho U^3 L^2} = f\left(TSR, \left[TSR, Re, Nu, \frac{tU}{c}, \frac{MVD}{c}, \frac{LWC}{\rho}\right]\right)$$

APPENDIX E

ALGEBRAIC DEVELOPMENT FOR DERIVING THE CORD OF THE AIRFOIL

The following is the algebraic development for the estimation of the chord of the airfoil at 85% of the blade length.

Assumptions to use the formulas from the BEM theory (Manwell et al., 2010):

- No wake rotation: $\boldsymbol{a' = 0}$
- No drag: $\boldsymbol{C_D \approx 0}$
- No losses from a finite number of blades
- Three-bladed turbine
- Maximum power coefficient of the turbine: 0.46 at:
- $\boldsymbol{TSR = 7.26}$
- $\boldsymbol{U = 8\frac{m}{s}}$
- $\boldsymbol{\Omega = 11.5\ rpm}$
- Airfoil: S809, this airfoil has the minimum ratio $\frac{C_D}{C_L}$ at an angle of attack of 5.15°. For this angle of attack, the aerodynamic coefficients are (Somers, 1997):

  $\boldsymbol{C_L = 0.743975}$ and $\boldsymbol{C_D = 0.007055}$

Equations from Manwell et al. (2010):

$$c = \frac{8\pi r \sin\varphi}{3BC_L} \tag{5.2}$$

$$\varphi = \tan^{-1}\left(\frac{2}{3TSR_r}\right) \tag{5.3}$$

$$TSR_r = TSR\left(\frac{r}{R}\right) \tag{5.4}$$

1) Estimation of the Tip Speed Ratio at 85% of the blade length:

$$TSR_r = 7.26\left(\frac{39.31\ m}{46.25\ m}\right) \rightarrow \boxed{\boldsymbol{TSR_r = 6.17}}$$

2) Estimation of the pitch angle for the airfoil at the position evaluated:

$$\varphi = \tan^{-1}\left(\frac{2}{3(6.17)}\right) \rightarrow \boxed{\boldsymbol{\varphi = 6.17°}}$$

3) Estimation of the chord of the airfoil:

$$c = \frac{8\pi(39.31m)\sin(6.17°)}{3(3)(0.743975)} \rightarrow \boxed{\boldsymbol{c = 2.5702\ m}}$$

APPENDIX F

LIST OF PUBLICATIONS

Within the scope of this thesis, the following publications were made:

1) **Contreras Montoya, Leidy Tatiana**; Laín, Santiago; Issa, Mohamad; Ilinca, Adrian. (2021). 4-Renewable Energy Systems. Hybrid Renewable Energy Systems and Microgrids. Academic Press, pages 103-177. https://doi.org/10.1016/B978-0-12-821724-5.00013-1
2) **Contreras Montoya, Leidy Tatiana**; Hayyani, Mohamed Yasser; Issa, Mohamad; Ilinca, Adrian; Ibrahim, Hussein; Rezkallah, Miloud. (2021). 8-Wind Power Plant Planning and Modeling. Hybrid Renewable Energy Systems and Microgrids. Academic Press, pages 259-312. https://doi.org/10.1016/B978-0-12-821724-5.00012-X
3) Martini, F., **Contreras Montoya, L. T.**, & Ilinca, A. (2021). Review of Wind Turbine Icing Modeling Approaches. Energies, 14(16), 5207. MDPI AG. Retrieved from http://dx.doi.org/10.3390/en14165207
4) Fahed Martini, **Leidy Tatiana Contreras Montoya**, Adrian Ilinca, and Ali Awada (2021); REVIEW OF STUDIES ON THE CFD-BEM APPROACH FOR ESTIMATING POWER LOSSES OF ICED-UP WIND TURBINES Int. J. of Adv. Res. 9 (Sep). 633-652] (ISSN 2320-5407).
5) Martini, F., Ibrahim, H., **Contreras Montoya, L. T**., Rizk, P., & Ilinca, A. (2022). Turbulence Modeling of Iced Wind Turbine Airfoils. Energies, 15(22), 8325. MDPI AG. Retrieved from http://dx.doi.org/10.3390/en15228325

This project was also selected for the final in the 4th edition of the science popularization contest "Transition énergétique: 3 minutes pour changer le monde" organized by the AQPER in partnership with TEQ. The contest took place during the AQPER's Annual Symposium (virtual edition) in February 2021.

LIST OF BIBLIOGRAPHICAL REFERENCES

Abbadi, M., Mussa, I., Lin, Y., & Wang, J. (2020, 6-10 January 2020). *Preliminary Analysis of Ice Accretion Prediction on Wind Turbine Blades* présentée à AIAA Scitech 2020 Forum, Orlando, FL, USA. doi: 10.2514/6.2020-0619

Achenbach, E. (1977). The effect of surface roughness on the heat transfer from a circular cylinder to the cross flow of air. *International Journal of Heat and Mass Transfer, 20*(4), 359-369. doi: https://doi.org/10.1016/0017-9310(77)90157-0. Repéré à https://www.sciencedirect.com/science/article/pii/0017931077901570

Ahmed H. Abdulaziz, Adel M. Elsabbagh, & Akl, W. N. (2015). Dynamic and Static Characterization of Horizontal Axis Wind Turbine Blades Using Dimensionless Analysis of Scaled-Down Models. *International Journal of Renewable Energy Research-IJRER, 5*(2), 14. doi: https://doi.org/10.20508/ijrer.v5i2.2057.g6620

Airfoil Tools. NREL's S809 Airfoil (s809-nr). Repéré le February 4, 2023 à http://airfoiltools.com/airfoil/details?airfoil=s809-nr

ANSYS Inc. (2013). *ANSYS Fluent User's Guide Release 15.0*.

ANSYS Inc. (2016). In-Flight Icing Simulation. Repéré le October 19, 2023 sur ANSYS FENSAP-ICE à https://www.ansys.com/products/fluids/ansys-fensap-ice

ANSYS Inc. (2017). ANSYS FENSAP-ICE 18.1 User Manual. Repéré à http://www.ansys.com

ANSYS Inc. (2020). Multiphase Flows Models and Capabilities. Repéré le August 19, 2019 à https://www.ansys.com/products/fluids/multiphase-flows/multiphase-flows-models

Ayabakan, S. (2013, Feb. 12-13, 2013). *TURBICE-The Turbine Blade Icing Model, and its further development via a new interface* présentée à Winterwind International Wind Energy Conference, Ostersund, Sweden. Repéré à http://www.winterwind.se/sundsvall-2014/wp-content/uploads/03_Ayabakan_Saygin_Winterwind_2013.pdf

Bai, C.-J., & Wang, W.-C. (2016). Review of computational and experimental approaches to analysis of aerodynamic performance in horizontal-axis wind turbines (HAWTs). *Renewable and Sustainable Energy Reviews, 63*, 506-519. doi: https://doi.org/10.1016/j.rser.2016.05.078. Repéré à https://www.sciencedirect.com/science/article/pii/S1364032116301903

Barber, S., Wang, Y., Jafari, S., Chokani, N., & Abhari, R. S. (2010). The Effect of Icing on Wind Turbine Performance and Aerodynamics. Dans *European Wind Energy Conference (EWEC)* (pp. 11).

Battisti, L. (2015). 3. Aerodynamic Performances on Ice Contaminated Rotors. Dans *Wind Turbines in Cold Climates* (1 éd., pp. 341). Springer International Publishing. doi: 10.1007/978-3-319-05191-8

Bhatia, D., & Wahaibi, A. Y. S. a. (2019). A Numerical Investigation into the Impact of Icing on the Aerodynamic Performance of Aerofoils. Dans *The 7th International Conference on Mechanical, Automotive and Materials Engineering* (Vol. 831, pp. 8). IOP Conference Series: Materials Science and Engineering. Repéré à https://iopscience.iop.org/article/10.1088/1757-899X/831/1/012007

Blasco, P., Palacios, J., & Schmitz, S. (2017). Effect of icing roughness on wind turbine power production. *Wind Energy, 20*(4), 601-617. doi: https://doi.org/10.1002/we.2026. Repéré à https://onlinelibrary.wiley.com/doi/abs/10.1002/we.2026

Bodenlle-Toral, D., García-Regodeseves, P., & Pandal-Blanco, A. (2022). Performance evaluation of an airfoil under ice accretion using CFD simulations. *Journal of Physics: Conference Series, 2217*(1), 012088. doi: 10.1088/1742-6596/2217/1/012088. Repéré à https://dx.doi.org/10.1088/1742-6596/2217/1/012088

Bragg, M. B. (1982). *Rime Ice Accretion and Its Effect on Airfoil Performance* (Doctoral dissertation, The Ohio State University). Repéré à https://ntrs.nasa.gov/citations/19820016290

Burton, T., Jenkins, N., Sharpe, D., & Bossanyi, E. (2011). Aerodynamics of Horizontal Axis Wind Turbines. Dans *Wind Energy Handbook* (pp. 39-136). doi: https://doi.org/10.1002/9781119992714.ch3. Repéré à https://onlinelibrary.wiley.com/doi/abs/10.1002/9781119992714.ch3

Caccia, F., & Guardone, A. (2023). Numerical simulation of ice accretion on wind turbine blades: are performance losses due to ice shape or surface roughness? *Wind Energy Science, 8*(3), 341-362. doi: https://doi.org/10.5194/wes-8-341-2023. Repéré à https://wes.copernicus.org/preprints/wes-2022-43/

Çengel, Y. A., & Cimbala, J. M. (2013). *Fluid Mechanics: Fundamentals and Applications* (Third Edition éd.). McGraw Hill.

Chen, J.-Y., Feng, Y.-W., Teng, D., Lu, C., & Fei, C.-W. (2022). Support vector machine-based similarity selection method for structural transient reliability analysis. *Reliability Engineering & System Safety, 223*, 108513. doi: https://doi.org/10.1016/j.ress.2022.108513. Repéré à https://www.sciencedirect.com/science/article/pii/S0951832022001715

Coderoni, M. (2020). The Buckingham-Pi Theorem - Lesson 3. Repéré le October 19, 2020 sur Dimensional Analysis and Similarity à https://courses.ansys.com/index.php/courses/dimensional-analysis-and-similarity/lessons/the-buckingham-pi-theorem-lesson-3/

Contreras Montoya, L. T., Hayyani, M. Y., Issa, M., Ilinca, A., Ibrahim, H., & Rezkallah, M. (2021). 8 - Wind power plant planning and modeling. Dans E. Kabalci (Éd.), *Hybrid Renewable Energy Systems and Microgrids* (pp. 259-312). Academic Press. doi: https://doi.org/10.1016/B978-0-12-821724-5.00012-X. Repéré à https://www.sciencedirect.com/science/article/pii/B978012821724500012X

Contreras Montoya, L. T., Ilinca, A., & Lain, S. (2023). Influence of Surface Roughness Modeling on the Aerodynamics of an Iced Wind Turbine S809 Airfoil. *Processes, 11*(12), 3371. Repéré à https://www.mdpi.com/2227-9717/11/12/3371

Contreras Montoya, L. T., Lain, S., & Ilinca, A. (2022). A Review on the Estimation of Power Loss Due to Icing in Wind Turbines. *Energies, 15*(3), 1083. Repéré à https://www.mdpi.com/1996-1073/15/3/1083

Dai, J., Rotea, M. A.-O., & Kehtarnavaz, N. A.-O. (2024). An Ensemble Network for High-Accuracy and Long-Term Forecasting of Icing on Wind Turbines. LID - 10.3390/s24248167 [doi] LID - 8167. *Sensors, 24*(24). doi: https://doi.org/10.3390/s24248167

Dai, J., Zhang, Y., Rotea, M., & Kehtarnavaz, N. (2024). A Review of Machine Learning Approaches for Prediction of Icing on Wind Turbines. Dans *2024 IEEE 19th Conference on Industrial Electronics and Applications (ICIEA)* (pp. 1-7). doi: 10.1109/ICIEA61579.2024.10664786

Dimitrova, M. H. (2009). *Pertes énergétiques d'une éolienne à partir des formes de glace simulées numériquement* (Mémoire, Université du Québec à Rimouski). Repéré à http://semaphore.uqar.ca/id/eprint/275/1/Mariya_Hristova_Dimitrova_aout2009.pdf

Drage, M. A., & Hauge, G. (2008). Atmospheric icing in a coastal mountainous terrain. Measurements and numerical simulations, a case study. *Cold Regions Science and Technology, 53*(2), 150-161. doi: https://doi.org/10.1016/j.coldregions.2007.12.003. Repéré à https://www.sciencedirect.com/science/article/pii/S0165232X07002121

Ebrahimi, A. (2018). Atmospheric Icing Effects of S816 Airfoil on a 600 kW Wind Turbine Performance. *Scientia Iranica, 25*(5), 2693-2705. doi: 10.24200/sci.2017.4521

Etemaddar, M., Hansen, M. O. L., & Moan, T. (2014). Wind turbine aerodynamic response under atmospheric icing conditions. *Wind Energy, 17*(2), 241-265. doi: 10.1002/we.1573

Fakorede, O., Feger, Z., Ibrahim, H., Ilinca, A., Perron, J., & Masson, C. (2016). Ice protection systems for wind turbines in cold climate: characteristics, comparisons and analysis. *Renewable and Sustainable Energy Reviews, 65*, 662-675. doi: https://doi.org/10.1016/j.rser.2016.06.080. Repéré à https://www.sciencedirect.com/science/article/pii/S1364032116303124

Farzaneh, M. (2008). *Atmospheric Icing of Power Networks* (1 éd.). Berlin/Heidelberg, Germany: Springer Dordrecht. doi: https://doi.org/10.1007/978-1-4020-8531-4. Repéré à https://link.springer.com/book/10.1007/978-1-4020-8531-4

Fei, C.-W., Han, Y.-J., Wen, J.-R., Li, C., Han, L., & Choy, Y.-S. (2023). Deep learning-based modeling method for probabilistic LCF life prediction of turbine blisk. *Propulsion and Power Research*. doi: https://doi.org/10.1016/j.jppr.2023.08.005. Repéré à https://www.sciencedirect.com/science/article/pii/S2212540X23000548

Fortin, G. (2009a). *Thermodynamique de la glace atmosphérique - Chapitre 02*. Note de cours 6DIG966, Département des sciences appliquées, Université du Québec à Chicoutimi.

Fortin, G. (2009b). *Thermodynamique de la glace atmosphérique - Chapitre 03*. Note de cours 6DIG966, Département des sciences appliquées, Université du Québec à Chicoutimi.

Fortin, G., & Perron, J. (2009a, 22-25 june 2009). *Spinning Rotor Blade Tests in Icing Wind Tunnel* présentée à 1st AIAA Atmospheric and Space Environments Conference, San Antonio, Texas. doi: 10.2514/6.2009-4260. Repéré à https://arc.aiaa.org/doi/abs/10.2514/6.2009-4260

Fortin, G., & Perron, J. (2009b). Wind Turbine Icing and De-Icing. Dans *47th AIAA Aerospace Sciences Meeting including The New Horizons Forum and Aerospace Exposition*. American Institute of Aeronautics and Astronautics. doi: doi:10.2514/6.2009-274 10.2514/6.2009-274. Repéré à https://doi.org/10.2514/6.2009-274

Fu, P., & Farzaneh, M. (2010). A CFD approach for modeling the rime-ice accretion process on a horizontal-axis wind turbine. *Journal of Wind Engineering and Industrial Aerodynamics, 98*(4-5), 181-188. doi: https://doi.org/10.1016/j.jweia.2009.10.014. Repéré à https://www.sciencedirect.com/science/article/pii/S016761050900124X

Funk, T. (2022). Cloud Classifications and Characteristics. Repéré le February 2, 2023 à https://www.weather.gov/media/lmk/soo/cloudchart.pdf

Géron, A. (2019). *Hands-On Machine Learning with Scikit-Learn, Keras, and TensorFlow* (Second éd.). O'Reilly Media, Inc.

Gultepe, I., & Isaac, G. A. (1997). Liquid Water Content and Temperature Relationship from Aircraft Observations and Its Applicability to GCMs. *Journal of Climate, 10*(3), 446-

452. doi: 10.1175/1520-0442(1997)010<0446:Lwcatr>2.0.Co;2. Repéré à https://journals.ametsoc.org/view/journals/clim/10/3/1520-0442_1997_010_0446_lwcatr_2.0.co_2.xml

Hacıefendioğlu, K., Başağa, H. B., Yavuz, Z., & Karimi, M. T. (2022). Intelligent ice detection on wind turbine blades using semantic segmentation and class activation map approaches based on deep learning method. *Renewable Energy, 182*, 1-16. doi: https://doi.org/10.1016/j.renene.2021.10.025. Repéré à https://www.sciencedirect.com/science/article/pii/S0960148121014828

Han, W., Kim, J., & Kim, B. (2018). Study on correlation between wind turbine performance and ice accretion along a blade tip airfoil using CFD. *Journal of Renewable and Sustainable Energy, 10*(2), 023306. doi: 10.1063/1.5012802

Han, Y., Palacios, J., & Schmitz, S. (2012). Scaled ice accretion experiments on a rotating wind turbine blade. *Journal of Wind Engineering and Industrial Aerodynamics, 109*, 55-67. doi: 10.1016/j.jweia.2012.06.001

Hand, M. M., Simms, D. A., Fingersh, L. J., Jager, D. W., Cotrell, J. R., Schreck, S., & Larwood, S. M. (2001). *Unsteady Aerodynamics Experiment Phase VI WindTunnel Test Configurations and Available Data Campaigns* (nº NREL/TP-500-29955). National Renewable Energy Laboratory - NREL. Repéré à https://www.nrel.gov/docs/fy02osti/29955.pdf

Hann, R., Hearst, R. J., Sætran, L. R., & Bracchi, T. (2020). Experimental and Numerical Icing Penalties of an S826 Airfoil at Low Reynolds Numbers. *Aerospace, 7*(4), 46. Repéré à https://www.mdpi.com/2226-4310/7/4/46

Heavy.AI. (2024). Feature Selection. Repéré le April 13, 2025 à https://www.heavy.ai/technical-glossary/feature-selection

Hex. (2025). Feature Selection. Repéré le April 13, 2025 à https://hex.tech/templates/feature-selection/

Hildebrandt, S., & Sun, Q. (2021). Evaluation of operational strategies on wind turbine power production during short icing events. *Journal of Wind Engineering and Industrial Aerodynamics, 219*, 104795. doi: https://doi.org/10.1016/j.jweia.2021.104795. Repéré à https://www.sciencedirect.com/science/article/pii/S0167610521002725

Hochart, C., Fortin, G., Perron, J., & Ilinca, A. (2008). Wind turbine performance under icing conditions. *Wind Energy, 11*(4), 319-333. doi: https://doi.org/10.1002/we.258. Repéré à https://onlinelibrary.wiley.com/doi/abs/10.1002/we.258

Homola, M. C., Virk, M. S., Nicklasson, P. J., & Sundsbø, P. A. (2012). Performance losses due to ice accretion for a 5 MW wind turbine. *Wind Energy, 15*(3), 379-389. doi: 10.1002/we.477

Homola, M. C., Virk, M. S., Wallenius, T., Nicklasson, P. J., & Sundsbø, P. A. (2010). Effect of atmospheric temperature and droplet size variation on ice accretion of wind turbine blades. *Journal of Wind Engineering and Industrial Aerodynamics, 98*(12), 724-729. doi: https://doi.org/10.1016/j.jweia.2010.06.007. Repéré à http://www.sciencedirect.com/science/article/pii/S0167610510000693

Homola, M. C., Wallenius, T., Makkonen, L., Nicklasson, P. J., & Sundsbø, P. A. (2010). The relationship between chord length and rime icing on wind turbines. *Wind Energy, 13*(7), 627-632. doi: 10.1002/we.383

Hu, L., Zhu, X., Chen, J., Shen, X., & Du, Z. (2018). Numerical simulation of rime ice on NREL Phase VI blade. *Journal of Wind Engineering and Industrial Aerodynamics, 178*, 57-68. doi: 10.1016/j.jweia.2018.05.007

Hu, L., Zhu, X., Hu, C., Chen, J., & Du, Z. (2017). Wind turbines ice distribution and load response under icing conditions. *Renewable Energy, 113*, 608-619. doi: 10.1016/j.renene.2017.05.059

Hudecz, A., Koss, H., & Laver, M. O. (2013). Ice Accretion on Wind Turbine Blades. Dans *15th International Workshop on Atmospheric Icing of Structures (IWAIS XV)* (pp. 8). Proceeding of the 15th International Workshop on Atmospheric Icing of Structures (IWAIS XV).

Ibrahim, G. M., Pope, K., & Muzychka, Y. S. (2018). Transient atmospheric ice accretion on wind turbine blades. *Wind Engineering, 42*(6), 596-606. doi: 10.1177/0309524x18780380

Ibrahim, G. M., Pope, K., & Naterer, G. F. (2023a). Extended scaling approach for droplet flow and glaze ice accretion on a rotating wind turbine blade. *Journal of Wind Engineering and Industrial Aerodynamics, 233*, 105296. doi: https://doi.org/10.1016/j.jweia.2022.105296. Repéré à https://www.sciencedirect.com/science/article/pii/S0167610522003920

Ibrahim, G. M., Pope, K., & Naterer, G. F. (2023b). Scaling formulation of multiphase flow and droplet trajectories with rime ice accretion on a rotating wind turbine blade. *Journal of Wind Engineering and Industrial Aerodynamics, 232*, 105247. doi: https://doi.org/10.1016/j.jweia.2022.105247. Repéré à https://www.sciencedirect.com/science/article/pii/S0167610522003439

IEA Wind. (2016). *Wind Energy in Cold Climates Available Technologies - Report*. VTT Technical Research Centre on Finland Ltd. Repéré à https://www.vaisala.com/sites/default/files/documents/Task%2019_Available_Technologies_report_WEinCC_May2016_approved.pdf

IEA Wind TCP TASK. (2020). *Task 19 Report 2020: Wind Energy in Cold Climates*. Repéré à https://www.epaper.dk/dtupaper/rapport/task-19/

Iswahyudi, S., Sutrisno, & Prajitno. (2019). Dimensional analysis of horizontal axis wind turbine scaling design. *AIP Conference Proceedings, 2097*(1). doi: 10.1063/1.5098202. Repéré à https://doi.org/10.1063/1.5098202

Jasinski, W. J., Noe, S. C., Selig, M. S., & Bragg, M. B. (1998). Wind Turbine Performance Under Icing Conditions. *Journal of Solar Energy Engineering, 120*(1), 60-65. doi: 10.1115/1.2888048. Repéré à https://doi.org/10.1115/1.2888048

Jian Liang, Maolian Liu, Ruiqi Wang, & Wang, Y. (2018). Study on the glaze ice accretion of wind turbine with various chord lengths. *IOP Conference Series: Earth and Environmental Science, 121*(4), 7. doi: doi :10.1088/1755-1315/121/4/042026. Repéré à https://iopscience.iop.org/article/10.1088/1755-1315/121/4/042026/meta

Jin, J. Y., & Virk, M. S. (2018). Study of ice accretion along symmetric and asymmetric airfoils. *Journal of Wind Engineering and Industrial Aerodynamics, 179*, 240-249. doi: https://doi.org/10.1016/j.jweia.2018.06.004. Repéré à http://www.sciencedirect.com/science/article/pii/S0167610518301740

Jin, J. Y., & Virk, M. S. (2019). Study of ice accretion and icing effects on aerodynamic characteristics of DU96 wind turbine blade profile. *Cold Regions Science and Technology, 160*, 119-127. doi: 10.1016/j.coldregions.2019.01.011

Jin, J. Y., Virk, M. S., Hu, Q., & Jiang, X. (2020). Study of Ice Accretion on Horizontal Axis Wind Turbine Blade Using 2D and 3D Numerical Approach. *IEEE Access, 8*, 166236-166245. doi: 10.1109/ACCESS.2020.3022458

Jonkman, J., Butterfield, S., Musial, W., & Scott, G. (2009). *Definition of a 5-MW Reference Wind Turbine for Offshore System Development*. ; National Renewable Energy Lab. (NREL), Golden, CO (United States). Repéré à https://www.osti.gov/servlets/purl/947422

Knobbe-Eschen, H., Stemberg, J., Abdellaoui, K., Altmikus, A., Knop, I., Bansmer, S., . . . Suhr, J. (2019, 7-11 January 2019). *Numerical and experimental investigations of wind-turbine blade aerodynamics in the presence of ice accretion* présentée à AIAA Scitech 2019 Forum, San Diego, CA, USA. doi: 10.2514/6.2019-0805

Kreutz, M., Ait-Alla, A., Varasteh, K., Oelker, S., Greulich, A., Freitag, M., & Thoben, K.-D. (2019). Machine learning-based icing prediction on wind turbines. *Procedia CIRP, 81*, 423-428. doi: https://doi.org/10.1016/j.procir.2019.03.073. Repéré à https://www.sciencedirect.com/science/article/pii/S2212827119303786

Laín, S., & Aliod, R. (2000). Study on the Eulerian dispersed phase equations in non-uniform turbulent two-phase flows: discussion and comparison with experiments. *International Journal of Heat and Fluid Flow, 21*(3), 374-380. doi: 10.1016/S0142-727X(00)00023-0

Laín, S., Contreras, L. T., & López, O. (2019). A review on computational fluid dynamics modeling and simulation of horizontal axis hydrokinetic turbines. *Journal of the Brazilian Society of Mechanical Sciences and Engineering, 41*(9), 375. doi: 10.1007/s40430-019-1877-6. Repéré à https://doi.org/10.1007/s40430-019-1877-6

Lamraoui, F., Fortin, G., Benoit, R., Perron, J., & Masson, C. (2014). Atmospheric icing impact on wind turbine production. *Cold Regions Science and Technology, 100*, 36-49. doi: 10.1016/j.coldregions.2013.12.008

Li, Y., Sun, C., Jiang, Y., Yi, X., Xu, Z., & Guo, W. (2018). Temperature effect on icing distribution near blade tip of large-scale horizontal-axis wind turbine by numerical simulation. *Advances in Mechanical Engineering, 10*(11). doi: 10.1177/1687814018812247

Li, Y., Sun, C., Jiang, Y., Yi, X., & Zhang, Y. (2019). Effect of liquid water content on blade icing shape of horizontal axis wind turbine by numerical simulation. *Thermal Science, 23*(3 Part A), 1637-1645. doi: 10.2298/tsci180627234l

Li, Y., Wang, S., Sun, C., Yi, X., Guo, W., Zhou, Z., & Feng, F. (2018). Icing distribution of rotating blade of horizontal axis wind turbine based on Quasi-3D numerical simulation. *Thermal Science, 22*(Suppl. 2), 681-691. doi: 10.2298/tsci170821053l

Liang, J., An, S., Liu, S., Wang, R., & Lv, W. (2019). Wind Turbine Simulation Based on CFD Optimization Algorithm. *IOP Conference Series: Earth and Environmental Science, 234*, 6. doi: doi:10.1088/1755-1315/234/1/012067. Repéré à https://iopscience.iop.org/article/10.1088/1755-1315/234/1/012067

Lidong, Z., Yimin, X., & Yuze, Z. (2023). A Review of Wind Turbine Icing Prediction Technology. Dans L. Yan (Éd.), *Wind Turbine Icing* (pp. Ch. 3). Rijeka: IntechOpen. doi: 10.5772/intechopen.111975. Repéré à https://doi.org/10.5772/intechopen.111975

Lozowski, E. P., Stallabrass, J. R., & Hearty, P. F. (1983a). The Icing of an Unheated, Nonrotating Cylinder. Part I: A Simulation Model. *Journal of Applied Meteorology and Climatology, 22*(12), 2053-2062. doi: 10.1175/1520-0450(1983)022<2053:Tioaun>2.0.Co;2. Repéré à https://journals.ametsoc.org/view/journals/apme/22/12/1520-0450_1983_022_2053_tioaun_2_0_co_2.xml

Lozowski, E. P., Stallabrass, J. R., & Hearty, P. F. (1983b). The Icing of an Unheated, Nonrotating Cylinder. Part II. Icing Wind Tunnel Experiments. *Journal of Applied Meteorology and Climatology, 22*(12), 2063-2074. doi: 10.1175/1520-0450(1983)022<2063:Tioaun>2.0.Co;2. Repéré à https://journals.ametsoc.org/view/journals/apme/22/12/1520-0450_1983_022_2063_tioaun_2_0_co_2.xml

Makkonen, L. (1984). Modeling of Ice Accretion on Wires. *Journal of Climate and Applied Meteorology, 23*(6), 929-939. Repéré à http://www.jstor.org/stable/26180954

Makkonen, L. (2000). Models for the growth of rime, glaze, icicles and wet snow on structures. *Philosophical Transactions of the Royal Society of London. Series A: Mathematical, Physical and Engineering Sciences, 358*(1776), 2913-2939. doi: 10.1098/rsta.2000.0690

Makkonen, L., Laakso, T., Marjaniemi, M., & Finstad, K. J. (2001). Modeling and Prevention of Ice Accretion on Wind Turbines. *Wind Engineering, 25*(1), 3-21. doi: 10.1260/0309524011495791

Makkonen, L., Zhang, J., Karlsson, T., & Tiihonen, M. (2018). Modeling the growth of large rime ice accretions. *Cold Regions Science and Technology, 151*, 133-137. doi: 10.1016/j.coldregions.2018.03.014

Makkonen, L. J., & Stallabrass, J. R. (1984). Ice accretion on cylinders and wires - Technical report TR-LT-005. *National Research Council of Canada. Division of Mechanical Engineering*. doi: https://doi.org/10.4224/40002646

Manwell, J. F., McGowan, J. G., & Rogers, A. L. (2010). *Wind Energy Explained: Theory, Design and Application* (Second éd.). Wiley. Repéré à https://books.google.ca/books?id=roaTx_Of0vAC

Martínez, J., Bernabini, L., Probst, O., & Rodríguez, C. (2005). An improved BEM model for the power curve prediction of stall-regulated wind turbines. *Wind Energy, 8*(4), 385-402. doi: https://doi.org/10.1002/we.147. Repéré à https://onlinelibrary.wiley.com/doi/abs/10.1002/we.147

Martini, F., Contreras, L. T., & Ilinca, A. (2021). Review of Wind Turbine Icing Modeling Approaches. *Energies, 14*(16), 5207. Repéré à https://www.mdpi.com/1996-1073/14/16/5207

Martini, F., Contreras, L. T., Ilinca, A., & Awada, A. (2021). Review of Studios on the CFD-BEM Approach for Estimating Power Losses of Iced-Up Wind Turbines. *International Journal of Advanced Research, 9*(9), 633-652. doi: http://dx.doi.org/10.21474/IJAR01/13462

Martini, F., Ibrahim, H., Contreras M, L. T., Rizk, P., & Ilinca, A. (2022). Turbulence Modeling of Iced Wind Turbine Airfoils. *Energies, 15*(22), 8325. Repéré à https://www.mdpi.com/1996-1073/15/22/8325

MathWorks. (2020). What Is Deep Learning? 3 things you need to know. Repéré le October 21, 2020 à https://www.mathworks.com/discovery/deep-learning.html#howitworks

Matthew C. Homola, Tomas Wallenius, Lasse Makkonen, Per J. Nicklassona, & Per A. Sundsbøa. (2010). Turbine Size and Temperature Dependence of Icing on Wind Turbine Blades. *Wind Engineering, 34*(6), 615–628.

Menter, F. (1993, 6-9 July 1993). *Zonal Two Equation k-w Turbulence Models For Aerodynamic Flows* présentée à 23rd Fluid Dynamics, Plasmadynamics, and Lasers Conference, Orlando, FL, USA. doi: 10.2514/6.1993-2906. Repéré à https://arc.aiaa.org/doi/abs/10.2514/6.1993-2906

Messinger, B. L. (1953). Equilibrium Temperature of an Unheated Icing Surface as a Function of Air Speed. *Journal of the Aeronautical Sciences, 20*(1), 29-42. doi: 10.2514/8.2520. Repéré à https://arc.aiaa.org/doi/abs/10.2514/8.2520

Muhammad S. Virk, Matthew C. Homola, & Per J. Nicklasson. (2010a). Effect of rime ice accretion on aerodynamic characteristics of wind turbine blade profiles. *WIND ENGINEERING 34*(2), 207-218.

Muhammad S. Virk, Matthew C. Homola, & Per J. Nicklasson. (2010b). Relation Between Angle of Attack and Atmospheric Ice Accretion on Large Wind Turbine's Blade. *Wind Engineering, 34*(6), 607–614.

Nergica. (2022a). About us. Repéré le April 14 à https://nergica.com/en/infrastructures/

Nergica. (2022b). Wind Farm. Repéré le April 14 à https://nergica.com/en/infrastructure/wind-farm/

NOAA. (2019, 08/29/2019). NOAA Cloudwise. Repéré le June à https://www.weather.gov/media/owlie/cloud_chart.pdf

O'Brien, J. M., Young, T. M., O'Mahoney, D. C., & Griffin, P. C. (2017). Horizontal axis wind turbine research: A review of commercial CFD, FE codes and experimental practices. *Progress in Aerospace Sciences, 92*, 1-24. doi: https://doi.org/10.1016/j.paerosci.2017.05.001. Repéré à https://www.sciencedirect.com/science/article/pii/S0376042116301579

Özgen;, S., Akyildiz;, E., Berker;, A. M., & Çakmak, A. (2019, 1st to 4th July). *Numerical simulation of ice accretion and consequent power loss estimation in wind turbine* *blades* présentée à 8th European Conference for Aeronautics and Space Sciences (EUCASS), Madrid, Spain. doi: 10.13009/EUCASS2019-83

Pallarol, J. G., Sunden, B., & Wu, Z. (2014). On Ice Accretion for Wind Turbines and Influence of Some Parameters. Dans *Aerodynamics of Wind Turbines* (Vol. 81, pp. 129-159). WIT Press. doi: 10.2495/978-1-78466-004-8/006

Pedersen, & Sørensen. (2016, Apr 2016). *Towards a CFD Model for Prediction of Wind Turbine Power Losses due to Icing in Cold Climate* présentée à 16th International Symposium on Transport Phenomena and Dynamics of Rotating Machinery, Honolulu, United States.

Pedersen, M. C. (2018). *Modeling Icing on Structures for Wind Power Applications* (Ph.D dissertation, Aalborg University). Repéré à https://vbn.aau.dk/en/publications/modellering-af-isdannelse-p%C3%A5-strukturer-for-applikationer-indenfo

Pedersen, M. C., & Sørensen, H. (2016). *Towards a CFD Model for Prediction of Wind Turbine Power Losses due to Icing in Cold Climate* présentée à 16th International Symposium on Transport Phenomena and Dynamics of Rotating Machinery, Honolulu, United States. Repéré à http://isromac-isimet.univ-lille1.fr/upload_dir/finalpaper/359.FINALmarie_cecilie_pedersen_ISROMAC16.pdf

Pedersen, M. C., & Yin, C. (2014). Preliminary Modeling Study of Ice Accretion on Wind Turbines. *Energy Procedia, 61*, 258-261. doi: https://doi.org/10.1016/j.egypro.2014.11.1102

Poots, G. (1996). *Ice and Snow Accretion on Structures*. Research Studies Press LTD.

Reid, T., Baruzzi, G., Ozcer, I., Switchenko, D., & Habashi, W. (2013, 7-10 January 2013). *FENSAP-ICE Simulation of Icing on Wind Turbine Blades, Part 1: Performance Degradation* présentée à 51st AIAA Aerospace Sciences Meeting including the New Horizons Forum and Aerospace Exposition, Grapevine, TX, USA. doi: 10.2514/6.2013-750

REPower Systems. (2010). *Power Curve & Sound Power Level REpower MM92 [kW]*. Repéré à http://ventderaison.eu/estaimpuis/estaimpuis_eie_windvision_2012/Annexes/Annexe_S1_Courbes_acoustique_MM92,_E-82_E2,_V100.pdf

Rizk, P., Younes, R., Ilinca, A., & Khoder, J. (2022). Wind turbine ice detection using hyperspectral imaging. *Remote Sensing Applications: Society and Environment, 26*, 100711. doi: https://doi.org/10.1016/j.rsase.2022.100711. Repéré à https://www.sciencedirect.com/science/article/pii/S2352938522000192

Roberge, P., Lemay, J., Ruel, J., & Bégin-Drolet, A. (2021). In situ estimation of effective liquid water content on a wind turbine using a thermal based sensor. *Cold Regions Science and Technology, 184*, 103235. doi: https://doi.org/10.1016/j.coldregions.2021.103235. Repéré à https://www.sciencedirect.com/science/article/pii/S0165232X21000161

Sagol, E. (2014). *THREE DIMENSIONAL NUMERICAL PREDICTION OF ICING RELATED POWER AND ENERGY LOSSES ON A WIND TURBINE* (Thèse de doctorat, École Polytechnique de Montréal, PolyPublie Polytechnique Montréal). Repéré à https://publications.polymtl.ca/1476/

Sagol, E., Reggio, M., & Ilinca, A. (2012). Assessment of Two-Equation Turbulence Models and Validation of the Performance Characteristics of an Experimental Wind Turbine by CFD. *ISRN Mechanical Engineering, 2012*, 428671. doi: 10.5402/2012/428671. Repéré à https://doi.org/10.5402/2012/428671

Scher, S., & Molinder, J. (2019). Machine Learning-Based Prediction of Icing-Related Wind Power Production Loss. *IEEE Access, 7*, 129421-129429. doi: 10.1109/ACCESS.2019.2939657

Schober, P., Boer, C., & Schwarte, L. A. (2018). Correlation Coefficients: Appropriate Use and Interpretation. *Anesthesia & Analgesia, 126*(5), 1763-1768. doi: 10.1213/ane.0000000000002864. Repéré à https://journals.lww.com/anesthesia-analgesia/fulltext/2018/05000/correlation_coefficients__appropriate_use_and.50.aspx

Shin, J., Berkowitz, B., Chen, H., & Cebeci, T. (1991). Prediction of ice shapes and their effect on airfoil performance. Dans *29th Aerospace Sciences Meeting* (pp. 264).

Shu, L., Li, H., Hu, Q., Jiang, X., Qiu, G., He, G., & Liu, Y. (2018). 3D numerical simulation of aerodynamic performance of iced contaminated wind turbine rotors. *Cold Regions Science and Technology, 148*, 50-62. doi: https://doi.org/10.1016/j.coldregions.2018.01.008

Shu, L., Liang, J., Hu, Q., Jiang, X., Ren, X., & Qiu, G. (2017). Study on small wind turbine icing and its performance. *Cold Regions Science and Technology, 134*, 11-19. doi: 10.1016/j.coldregions.2016.11.004

Sista, H., Hu, H., & Hu, H. (2022). *Qualification of Ice Accretion Characteristics on a Wind Turbine Blade Model at High Liquid Water Content Levels Pertinent to Offshore Wind Turbine Icing Phenomena* présentée à AIAA AVIATION 2022 Forum. doi: 10.2514/6.2022-4070. Repéré à https://arc.aiaa.org/doi/abs/10.2514/6.2022-4070

Solheim Haugen, H. (2025). *Forecasting Icing Induced Production Loss on Wind Turbines : a Machine Learning Approach* (Student thesis). Repéré à DiVA. (2025:389). Repéré à http://urn.kb.se/resolve?urn=urn:nbn:se:kth:diva-369388

Somers, D. M. (1997). *Design and Experimental Results for the S809 Airfoil* (nº NREL/SR-440-6918 ON: DE97000206; TRN: 97:001243). U.S. Department of Energy, Office of Scientific and Technical Information: National Renewable Energy Laboratory (NREL). doi: 10.2172/437668

Other Information: PBD: Jan 1997. Repéré à https://www.osti.gov/biblio/437668

Son, C., & Kim, T. (2020). Development of an icing simulation code for rotating wind turbines. *Journal of Wind Engineering and Industrial Aerodynamics, 203*. doi: 10.1016/j.jweia.2020.104239

Sutrisno, Iswahyudi, S., & Wibowo, S. B. (2018). Dimensional Analysis of Power Prediction of a Real-Scale Wind Turbine Based on Wind-Tunnel Torque Measurement of Small-Scaled Models. *Energies, 11*(9), 2374. Repéré à https://www.mdpi.com/1996-1073/11/9/2374

Switchenko, D., Habashi, W., Reid, T., Ozcer, I., & Baruzzi, G. (2014, 13-17 January 2014). *FENSAP-ICE Simulation of Complex Wind Turbine Icing Events, and Comparison to Observed Performance Data* présentée à 32nd ASME Wind Energy Symposium, National Harbor, MD, USA. doi: 10.2514/6.2014-1399

Tabatabaei, N., Gantasala, S., & Cervantes, M. J. (2019). Wind Turbine Aerodynamic Modeling in Icing Condition: Three-Dimensional RANS-CFD Versus Blade Element Momentum Method. *Journal of Energy Resources Technology, 141*(7). doi: 10.1115/1.4042713

Taborda Ceballos, M. A. (2015). *Simulación tridimensional transitoria de flujo turbulento en configuraciones de interés industrial* (Master Thesis, Universidad Autónoma de Occidente). Repéré à http://hdl.handle.net/10614/8162

Tan, H. (2020). *CFD Analysis of a Wind Turbine Airfoil with Flap* (Master Degree, Washinton University in St. Louis).

Tardif d'Hamonville, T. (2009). *Modélisation et analyse des phénomènes aéroélastiques pour une pale d'éolienne* (Université du Québec à Chicoutimi). Repéré à https://constellation.uqac.ca/id/eprint/263/1/030151364.pdf

Toloka. (2023). Machine learning label vs feature, and other common terms. Repéré le April à https://toloka.ai/blog/machine-learning-labels-and-features/

Turkia, V., Huttunen, S., & Wallenius, T. (2013). Method for estimating wind turbine production losses due to icing. *VTT Technical Research Centre of Finland, 114*, 44. Repéré à https://www.vttresearch.com/sites/default/files/pdf/technology/2013/T114.pdf

Van Wachem, B. G. M., & Almstedt, A. E. (2003). Methods for multiphase computational fluid dynamics. *Chemical Engineering Journal, 96*(1), 81-98. doi: https://doi.org/10.1016/j.cej.2003.08.025

Villalpando, F., Reggio, M., & Ilinca, A. (2011). Assessment of Turbulence Models for Flow Simulation around a Wind Turbine Airfoil. *Modeling and Simulation in Engineering, 2011*, 714146. doi: 10.1155/2011/714146. Repéré à https://doi.org/10.1155/2011/714146

Villalpando, F., Reggio, M., & Ilinca, A. (2016). Prediction of ice accretion and anti-icing heating power on wind turbine blades using standard commercial software. *Energy, 114*, 1041-1052. doi: 10.1016/j.energy.2016.08.047

Virk, M., Homola, M., & Nicklasson, P. J. (2012). Atmospheric icing on large wind turbine blades. *International Journal of Energy and Environment, 3*(1), 1-8. Repéré à http://www.ijee.ieefoundation.org/vol3/issue1/IJEE_01_v3n1.pdf

Virk, M., Mughal, U., Hu, Q., & Jiang, X. (2016). Multiphysics Based Numerical Study of Atmospheric Ice Accretion on a Full Scale Horizontal Axis Wind Turbine Blade. *The International Journal of Multiphysics, 10*(3), 237-246. doi: 10.21152/1750-9548.10.3.237

Volker Simon, B., & Weigand, H. G. (2017). *Dimensional Analysis for Engineers*. Springer International Publishing AG. doi: https://doi.org/10.1007/978-3-319-52028-5

Wang, Q., Yi, X., Liu, Y., Ren, J., Li, W., Wang, Q., & Lai, Q. (2020). Simulation and analysis of wind turbine ice accretion under yaw condition via an Improved Multi-Shot Icing Computational Model. *Renewable Energy, 162*, 1854-1873. doi: 10.1016/j.renene.2020.09.107

Weir, I. (s. d.). Spearman's Rank Correlation - Introduction. Repéré à https://www.statstutor.ac.uk/resources/uploaded/spearmans.pdf

White, F. M. (2008). *Fluid mechanics* (6th ed. éd.). Boston, Mass. ;: McGraw-Hill Higher Education.

YAN LI, CE SUN, YU JIANG, XIAN YI, WENFENG GUO, SHAOLONG WANG, & FENG, F. (2017, 18-20 October 2017). *Ambient Temperature Effect on Wind Turbine Blade Icing Shape by Numerical Simulation* présentée à 2nd International Conference on Industrial Aerodynamics (ICIA 2017), Qingdao, China. doi: 10.12783/dtetr/icia2017/15651

Yau, M. K., & Rogers, R. R. (1989). *A short course in cloud physics*. Elsevier.

Yirtici, O., Cengiz, K., Ozgen, S., & Tuncer, I. H. (2019). Aerodynamic validation studies on the performance analysis of iced wind turbine blades. *Computers & Fluids, 192*. doi: 10.1016/j.compfluid.2019.104271

Yirtici, O., Ozgen, S., & Tuncer, I. H. (2019). Predictions of ice formations on wind turbine blades and power production losses due to icing. *Wind Energy*. doi: 10.1002/we.2333

Yirtici, O., Tuncer, I. H., & Ozgen, S. (2016). Ice Accretion Prediction on Wind Turbines and Consequent Power Losses. *Journal of Physics: Conference Series, 753*(022022), 11. doi: 10.1088/1742-6596/753/2/022022

Zanon, A., De Gennaro, M., & Kühnelt, H. (2018). Wind energy harnessing of the NREL 5 MW reference wind turbine in icing conditions under different operational strategies. *Renewable Energy, 115*, 760-772. doi: 10.1016/j.renene.2017.08.076

Zhang, L., Zhao, Y., Guo, Y., Hu, T., Xu, X., Zhang, D., . . . Ma, Y. (2024). Research on wind turbine icing prediction data processing and accuracy of machine learning algorithm. *Renewable Energy, 237*, 121566. doi: https://doi.org/10.1016/j.renene.2024.121566. Repéré à https://www.sciencedirect.com/science/article/pii/S0960148124016343

Zimnickas, V., Gecevičius, G., & Markevičius, A. (2016). A Literature Review of Wind Turbines Icing Problems. Dans L. E. Institute (Éd.), *13th International Conference of Young Scientists on Energy Issues - CYSENI 2016* (pp. 109 - 115). CYSENI 2016.

Zohuri, B. (2017). *Dimensional Analysis Beyond The PI Theorem*. Cham, Switzerland: Springer. doi: 10.1007/978-3-319-45726-0